Studies of Runaway Electrons in COMPASS Tokamak

Miloš Vlainić

August 2017

This research was performed at:
Dit onderzoek werd uitgevoerd in:
Tento výzkum byl proveden na:

Institute of Plasma Physics of the CAS
Za Slovankou 1782/3
182 00 Prague 8, Czech Republic

In collaboration with:
In samenwerking met:
Ve spolupáci s:

Ghent University
Faculty of Engineering and Architecture
Department of Applied Physics
Sint-Pietersnieuwstraat 41
9000 Ghent, Belgium

Czech Technical University
Faculty of Nuclear Sciences
and Physical Engineering
Břehová 7
115 19 Prague 1, Czech Republic

FUSION-DC - International Doctoral
College in Fusion Science and Engineering
Erasmus Mundus Programme
Coordinated by Ghent University

Examination Board

Em. Prof. Dr. ir. D. De Zutter, Chairman of the Examination Board
Ghent University

Prof. Ing. J. Limpouch, CSc., Co-Chairman of the Examination Board
Czech Technical University

Prof. Dr. ir. F. Beunis, Secretary of the Examination Board
Ghent University

Ing. V. Svoboda, CSc.
Czech Technical University

RNDr. R. Pánek, Ph.D.
Institute of Plasma Physics of the Czech Academy of Science

Prof. J. R. Martín Solís
Charles III University of Madrid

Prof. Dr. ir. J.-M. Noterdaeme, Promoter
Ghent University
Max Planck Institute of Plasma Physics

Ereprof. Dr. ir. G. Van Oost, Promoter
Ghent University

Dean Prof. Dr. Ing. I. Jex, Promoter
Czech Technical University

doc. RNDr. J. Mlynář, Ph.D., Mentor
Czech Technical University
Institute of Plasma Physics of the Czech Academy of Science

To Tatjana and my unborn child

Table of Contents

List of Figures

List of Tables

List of Symbols and Abbreviations

Symbols and Variables

$\langle \quad \rangle$	Average over spatial and momentum space
$\langle \quad \rangle_V$	Volume average
$\mathrm{d}\sigma/\mathrm{d}\Omega$	Differential cross section
$\mathrm{d}N/\mathrm{d}t$	Particle flow rate
$\mathrm{d}P/\mathrm{d}\Omega$	Scattered power per solid angle
$\mathrm{d}P_{geom}$	Geometrical factor of $\mathrm{d}P/\mathrm{d}\Omega$
α	Angle between $\vec{B}$ and the observation line
α_{sG}	Skewness of f_{sG}
β, $\vec{\beta}$	Normalised electron velocity to the speed of light
$\beta_\parallel$	β component parallel to $\vec{B}$
$\beta_\perp$	β component perpendicular to $\vec{B}$
β_n	Normalised beta
β_p	Plasma beta
β_{pol}	Poloidal beta
β_{tor}	Toroidal beta
γ	Relativistic Lorentz factor
$\gamma_\parallel$	γ component parallel to $\vec{B}$
$\Delta\tau_v$	Time for which the valve is opened
$\Delta_S(\rho)$	Profile of plasma surface displacement
Δ_{sh}	Shafranov shift
$\Delta\Phi$	Flux change
Δr	Difference between observed RE beam width and height
ΔV_{jump}	Amplitude of the negative voltage spike
$\delta(x)$	Dirac function, i.e. the delta-function
$\delta_r(x)$	Relative error of x
$\delta^W_{x,y}$	Symmetric mean absolute error between W_x and W_y
ϵ	Parameter for f_{exp}
ε_0	Vacuum permittivity

ζ	Scale parameter for f_{sG}
η	$= \Omega R_0 v_\perp / \gamma v_\parallel^2$
η_a	$= \xi\eta/(1+\eta^2)$
η_{res}	Resistivity
θ	Pitch angle
θ_i	Incident θ_{ts}
θ_s	Scattered θ_{ts}
θ_{ts}	Polar angle
κ	Elongation
Λ	Shafranov lambda
λ	Photon wavelength
λ_{1l}	Lower wavelength limit for $\mathcal{P}_1$ validity
λ_{1u}	Upper wavelength limit for $\mathcal{P}_1$ validity
λ_{2u}	Upper wavelength limit for $\mathcal{P}_2$ validity
λ_c	$= (4\pi m_e c \gamma_\parallel)/(3eB_{tor}\gamma)$
λ_D	Debye length
λ_i	Wavelength of an incident photon
λ_{peak}	Wavelength where SR has maximum radiated power
μ_0	Vacuum permeability
$\mu_{x,y}^W$	Mean value of $\delta_{x,y}^W$
ν	Photon frequency
ν_0	Plasma collisionality before disruption
ν_{peak}	Frequency where SR has maximum radiated power
ξ	Streaming parameter
ξ_{SR}	$= (4\pi R_p)/(3\lambda\gamma^3\sqrt{1+\eta^2})$
ρ	Normalised minor radius, $\rho = r/a_p$
ρ_{max}	Maximum ρ for RE existence
ρ_{min}	Minimum ρ for RE existence
σ_r	$= \frac{2}{3\ln\Lambda}\left(\frac{\Omega}{\omega_{pe}}\right)^2$
σ_{ts}	TS cross section
$\sigma_{x,y}^W$	Standard deviation of $\delta_{x,y}^W$
τ_E	Energy confinement time
τ_v	Duration of rectangular burst that opens valve
$\tau_{v,min}$	Minimum τ_v necessary for valve to get open
ϕ_{FL}	Flux through FL
ϕ_{PFCC}	Flux through PFCC
ϕ_{ts}	Azimuth angle
Ω	Fundamental cyclotron angular frequency
Ω_{SR}	Solid angle at which SR is emitted
ω	Photon angular frequency
ω_i	Angular frequency of incident photon
ω_l	Cyclotron angular frequency for harmonic l
ω_{pe}	Plasma angular frequency for electrons
ω_s	Angular frequency of scattered photon

A_{RE}	Surface of RE beam
a_p	Minor radius of plasma
a_{RE}	Minor radius of the RE beam
a_v	Coefficient in Eq. C.4
B, $\vec{B}$	Magnetic field
B_{bb}	Radiance of black body radiation
B_{EFPS}	Magnetic field of EFPS
B_{pol}	Poloidal magnetic field
B_{SR}	Radiance of SR
B_{tor}	Toroidal magnetic field
B_v	Vertical magnetic field
b	Minor radius of flux loop
b_v	Coefficient in Eq. C.4
C_v	Capacitance of valve-piping system
c	Speed of light
c_z	$= \sqrt{3(Z_{eff}+5)/\pi}$
d	$= R_c - \Delta r$
d_{IR}	Diameter of observed plasma region by the IR camera
E	Electric field
$\hat{E}$	$= (\mathcal{E}_{crit}-1)/(1+Z_{eff})$
E_{crit}	Critical field
E_D	Dreicer field
E_{disr}	E_{tor} just before TQ
$E_{i,o}$	Electric field of an incident photon
E_{max}	Maximum E_{tor} after TQ
E_{tor}	Toroidal electric field
e	Elementary charge
e_I	I_p profile power factor
e_p	p_{pl} profile power factor
$\mathrm{erf}(x)$	Error function
$\mathcal{E}_{crit}$	E normalised to E_{crit}
$\mathcal{E}_{\mathcal{D}}$	E_D normalised to E
F	Function in Zehrfeld's drift theory
$F_{\parallel}$	Probability distribution function of bulk electrons parallel to $\vec{B}$
$F_{\perp}$	Probability distribution function of bulk electrons perpendicular to $\vec{B}$
F_{drag}	Drag or friction force
F_E	Accelerating force due to E
F_x	Parameter in Zehrfeld's drift theory
f_{bulk}	EDF of bulk plasma
f_{E-low}	Frequencies of the COMPASS ECE detector chords in low E-band
f_{exp}	Exponential REDF
f_{Gcdf}	Gaussian cumulative distribution function

f_{Gpdf}	Gaussian probability distribution function
f_{lin}	Linear REDF
f_{MJ}	Maxwell-Jüttner REDF
f_{mono}	Monoenergetic REDF
f_p	Plasma frequency
f_{quad}	Quadriatic REDF
f_{RE}	Analytical REDF
f_{REDF}	Any REDF
f_{sG}	Skewed Gaussian REDF
f_{uni}	Uniform REDF
h	Planck constant
h_{RE}	Height of the RE beam observed with the IR camera
I_γ	Normalised derivative of I_p during CQ
$I(\rho)$	Current profile
I_A	Alfvén current
I_{BV}	Current through the fast vertical magnetic field circuit
I_{disr}	I_p just before TQ
I_{EFPS}	Current through the slow vertical magnetic field circuit
$I_n(y)$	Modified Bessel function of the first kind of an n^{th} order
I_p	Plasma current
I_p^{max}	Plasma current at the end of the I_p ramp-up phase
I_{PFCC}	Current through PFCC
I_{RE}	RE current
$\vec{i}$	Unit vector for an incident direction
$J_n(y)$	Bessel function of the first kind of an n^{th} order
j	Current density
j_l	Electron cyclotron emissivity for harmonic l
j_p	Plasma current density
K	$= \omega_p \Omega \omega / [(\omega^2 - \omega_p^2)^2 - \Omega^2 \omega^2]$
k_B	Boltzmann constant
$K_n(y)$	Modified Bessel function of the second kind of an n^{th} order
L	Self-inductance
L_p	Plasma L
L_{PFCC}	L through PFCC
L_{ts}	Length of observed region with TS diagnostics
l	Cyclotron harmonic
l_i	Internal inductance
l_{IR}	Distance between IR camera and the plasma core observed
l_{sG}	Location parameter for f_{sG}
$\ln \Lambda$	Coulomb logarithm
M	Mutual inductance
m	Toroidal mode number
m_e	Electron mass

N_{coil}	Number of toroidal coils
N_{GP}	Number of the injected particles
N_{GP}^{ru}	N_{GP} during the I_p ramp-up
N_{ITER}	Number of particles in ITER plasma
N_p	Number of photons
N_r	Refractive index
N_{r+}	N_r of ordinary wave
N_{r-}	N_r of extraordinary wave
N_{ray}	Ray N_r
N_{RE}	Number of REs
N_{vv}	Number of particles in the vacuum vessel
n	Poloidal mode number
n_{bulk}	n_e of bulk plasma
n_e	Electron density
$\bar{n}_e$	Line-averaged electron density
$n_{e,c}$	n_e at the plasma core
$\bar{n}_{e,ts}$	$\bar{n}_e$ from TS
n_i	Ion density
n_{MR}	Magnetic ripple harmonic
n_{RE}	RE density
n_{RE}^{synch}	n_{RE} observed with the IR camera
P_{back}	Back pressure
P_{brems}	Power lost due to the bremsstrahlung radiation
P_E	Power gained due to the electric field
P_{RE}	Volume-averaged p_{RE}
P_{synch}	Power lost due to the synchrotron radiation
P_{th}	Momentum of thermal (bulk) electrons
P_{vv}	Pressure in vacuum vessel
$p_{\parallel}$	Momentum parallel to $\vec{B}$
$p_{\perp}$	Momentum perpendicular to $\vec{B}$
$\bar{p}_{\parallel}$	Momentum parallel to $\vec{B}$ normalised to $m_e c$
$\bar{p}_{\parallel,b}$	$\bar{p}_{\parallel}$ of the REDF bump
p_{min}	Momentum RE threshold
p_{pl}	Bulk plasma pressure
$p_{pl,c}$	p_{pl} at the plasma core
p_{RE}	RE pressure
p_{re}	RE momentum
p_{tot}	Total pressure, i.e. sum of p_{pl} and p_{RE}
$\mathcal{P}$	Spectral density of emitted SR power
$\mathcal{P}_1$	Approximation 1 of $\mathcal{P}_f$
$\mathcal{P}_2$	Approximation 2 of $\mathcal{P}_f$
$\mathcal{P}_c$	$\mathcal{P}$ for cylindrical plasma
$\mathcal{P}_f$	Full formula for $\mathcal{P}$ for tokamak plasma
$\mathcal{P}_{peak}$	Maximum $\mathcal{P}$
Q_{eff}	Effective volumetric flow rate

q	Safety factor
q_0	Safety factor on the magnetic axis
q_{95}	Safety factor at $\rho = 0.95$
q_a	Safety factor at a plasma edge ($r = a_p$)
q_{eff}	Effective safety factor
q_{RE}	Safety factor if magnetic surface before TQ that had same current as initial I_{RE}
R_0	Major radius of a torus or any fusion device (e.g. tokamak, stellarator)
R_{bc}	Major radius of I_p barycenter
R_c	Curvature radius
R_{geom}	Geometrical major radius of plasma
R_{max}	Maximum major radius for RE existence
R_{min}	Minimum major radius for RE existence
R_{out}	Major radius of the LFS border point in equatorial plane
R_p	Major radius of the plasma
R_{sh}	Major radius of Shafranov shifted magnetic surface
r	Minor radius
r_e	Classical electron radius
$\mathcal{R}$	Relative SR intensity measured via IR camera
$\mathcal{R}_{max}$	Maximum $\mathcal{R}$
S	Brightness
s	$= (w - \xi)/\zeta$
$\vec{s}$	Unit vector of scattering direction
$T_\parallel$	T_e in direction parallel to $\vec{B}$
$T_\perp$	T_e in direction perpendicular to $\vec{B}$
$T(\lambda)$	Transparency
T_e	Electron temperature
$T_{e,c}$	T_e at the plasma core
$T_{e,ts}$	T_e from TS
T_i	Ion temperature
T_{vv}	Temperature in vacuum vessel
T_{wall}	Vacuum vessel wall temperature
t	Time
t_0	Decay time of T_e during TQ
$t_{opening}$	Time needed for solenoid valve to open
t_{ru}	Ending time of I_p ramp-up phase
U	Any function
V	Electric potential
V_{ITER}	Volume of ITER plasma
V_{loop}	Loop voltage
V_{plasma}	Plasma voltage
V_{vv}	Volume of vacuum vessel
v, $\vec{v}$	Velocity
$v_\parallel$	Velocity component parallel to $\vec{B}$

$v_\perp$	Velocity component perpendicular to $\vec{B}$
v_{dr}	Drift velocity
v_e	Electron velocity
v_{osc}	Relativistic oscillation velocity
v_{RE}	RE velocity
$v_{th,e}$	Thermal velocity of an electron
W_{bump}	Energy of REDF bump
W_{crit}	Critical RE energy
W_{drift}	RE energy limit due to drift
W_{laser}	Energy of laser
W_{max}	Maximum RE energy
W_{RE}	RE energy
w	Energy
$\mathcal{W}$	Normalised w to $m_e c^2$
x	$= 1 - \rho^2$
Z	Atomic number
Z_{eff}	Effective charge of the plasma ions, $Z_{eff} = \sum_i \frac{n_i Z_i^2}{n_e}$
Z_i	Charge of ion i
Z_p	Vertical plasma position

Abbreviations and Names

ANTS	plasmA simulatioN with drifT and collisionS, a 3D numerical Monte Carlo code
AUG	ASDEX UpGrade (Axially Symmetric Divertor EXperiment), a tokamak in Max-Planck IPP (Garching, Germany)
AXUV	Absolute eXtreme UV ($10 - 124\,\mathrm{nm}$)
a.u.	Arbitrary Units
CASTOR	Czech Academy of Science TORus, a decommissioned tokamak in IPP Prague (Prague, Czech Republic) – now GOLEM at CTU
CEA	Commissariat à l'Énergie Atomique et aux énergies alternatives (eng. Atomic Energy and Alternative Energy Commission)
CODE	COllisional Distribution of Electrons, a 2D numerical code for kinetic equations
COMPASS	COMpact ASSembly, a tokamak in IPP Prague (Prague, Czech Republic)
CQ	Current Quench
CQL3D	Collisional Quasi-Linear 3D, a 3D numerical code for kinetic equations
CTU	Czech Technical University
DAQ	Data AcQuisition

DEMO	Demonstration fusion power plant
DIII-D	Doublet III Divertor, a tokamak developed by General Atomics in San Diego (USA)
DINA	A 2D simulator of tokamak discharge
DT	Deuterium-Tritium
ECRH	Electron Cyclotron Resonance Heating
ECE	Electron Cyclotron Emission
EDF	Electron Distribution Function
EFIT	Equilibrium FITting, a numerical code for MHD equilibrium
EFPS	Equilibrium Field Power Supply
ELM	Edge Localised Mode
EM	Electromagnetic
ENEA	Agenzia nazionale per le nuove tecnologie, l'energia e lo sviluppo economico sostenibile (eng. Italian National Agency for New Technologies, Energy and Sustainable Economic Development), while abbreviation stands for "Energia Nucleare ed Energie Alternative" (eng. Atomic Energy and Alternative Energy)
EPR	External Partial Rogowski
EUROfusion	EUROpean consortium for the development of FUSION energy
FEB	Fast Electron Bremsstrahlung
FL	Flux Loop
FSR	Former Soviet Republics
FT	Frascati Tokamak, a decommissioned tokamak in ENEA Frascati (Frascati, Italy)
FT-1	A decommissioned tokamak in Ioffe Institute (St. Petersburg, Russia – the then USSR)
FTU	Frascati Tokamak Upgrade, a tokamak in ENEA Frascati (Frascati, Italy)
ft	Flat-Top phase of the plasma current
GDP	Gross Domestic Product
GO	A 1D numerical code for fluid system of equations
GOLEM	A tokamak in Czech Technical University (Prague, Czech Republic)
GP	Gas Puff
grad-B	Gradient of magnetic field
H_α	The first spectral line in the hydrogen Balmer series
HFS	High Field Side
HT-7	Hefei Tokamak-7, a decommissioned tokamak in IPP Hefei (Hefei, China)
HXR	Hard X-Ray
IAEA	International Atomic Energy Agancy
ICF	Inertial Confinement Fusion

IMAGINE	A numerical simulator of gas injection into (fusion) plasma
IPC	ITER Party Contributor
IPP	Institute of Plasma Physics
IPR	Internal Partial Rogowski
IR	InfraRed
ISTTOK	Instituto Superior Técnico TOKamak, a tokamak in Instituto Superior Técnico (Lisbon, Portugal)
ITER	International Thermonuclear Experimental Reactor, a tokamak under construction next to CEA Cadarache (Saint Paul-dez-Durance, France)
ITPA	International Tokamak Physics Activity
ITS	Incoherent Thomson Scattering
JET	Joint Europen Torus, a tokamak in Culham Center for Fusion Energy (Culham, UK)
JOREK	A 3D numerical code for MHD equations
JT-60	Japan Torus-60, a decommissioned tokamak in Naka Fusion Institute (Naka, Japan)
JT-60U	Japan Torus-60 Upgrade, a decommissioned tokamak in Naka Fusion Institute (Naka, Japan)
KSTAR	Korea Superconducting Tokamak Advanced Research, a tokamak in National Fusion Research Institute (Daejeon, South Korea)
LFS	Low Field Side
LT-1	A decommissioned tokamak in Australian National University (Canberra, Australia)
LUKE	LU solver for Kinetic Equation, a 3D numerical code for kinetic equations
MAST	Mega Amp Spherical Tokamak, a spherical tokamak in Culham Center for Fusion Energy (Culham, UK)
MCF	Magnetic Confinement Fusion
METIS	Multi-Element Tokamak-oriented Integrated Simulator, a numerical simulator of a tokamak discharge
MGI	Massive Gas Injection
MHD	MagnetoHydroDynamics
MIT	Massachusetts Intistute of Technology (Cambridge, USA)
MST	Medium Size Tokamak
NBI	Neutral Beam Injector
NCBJ	National Center for Nuclear Research (a few locations in Poland)
NORSE	NOn-linear Relativistic Solver for Electrons, a 2D numerical code for RE generation equations
PFC	Plasma Facing Component
PFCC	Poloidal Field Coil Circuit

PMT	PhotoMultiplier Tube
PN	PhotoNeutron
p.d.u.	Procedure Defined Units
R&D	Research and Development
RE	Runaway Electron
REDF	RE Distribution Function
RMP	Resonant Magnetic Perturbation
RotW	Rest of the World
ru	Ramp-Up phase of the plasma current
SOL	Scrape-Off-Layer
SR	Synchrotron Radiation
SXR	Soft X-Ray
SYRUP	SYnchrotron spectra from RUnaway Particles, a numerical code for synchrotron radiation power spectrum
TCV	Tokamak à Configuration Variable (eng. Variable Configuration Tokamak), a tokamak in École Polytechnique Fédérale de Lausanne (Lausanne, Switzerland)
TEXTOR	Tokamak EXperiment for Technology Oriented Research, a decommissioned tokamak in Forschungszentrum Jülich (Jülich, Germany)
TF	Toroidal Field
TFTR	Tokamak Fusion Test Reactor, a decommissioned tokamak in Princeton Plasma Physics Laboratory (Princeton, USA)
TJ-II	A stellarator in CIEMAT (Madrid, Spain)
ToriX	A magnetised plasma toroidal device in French École Polytechnique (Paris, France)
TORPEX	A toroidal plasma device in École Polytechnique Fédérale de Lausanne (Lausanne, Switzerland)
TORTUR	A decommissioned tokamak in FOM IPP Rijnhuizen (Nieuwegein, The Netherlands) – now ISTTOK
TQ	Thermal Quench
TS	Thomson Scattering
UKAEA	UK Atomic Energy Authority
UV	UltraViolet
W7-X	Wendelstein 7-X, a stellarator in Max-Planck IPP (Greifswald, Germany)
WEGA	A decommissioned stellarator and a tokamak in Max-Planck IPP (Greifswald, Germany)

Abstract

Relativistic (up to tens of MeV) runaway electrons carrying about 10 MA are predicted to be generated after disruptions in ITER. Therefore, researching methods for mitigation of runaway electrons is one of the highest priorities for ITER's safety. As part of the EUROfusion consortium, a project on runaway electron studies was granted to the COMPASS tokamak due to, among others, its relatively low safety issues regarding potential runaway electron damage and flexibility of various plasma parameters (e.g. shaping, electron density, plasma current, etc.). Such features with a significant, but still safe, runaway electron population make COMPASS suitable for runaway electron model validation and scaling towards ITER. In this thesis, pioneering experimental work on runaway electrons performed in the COMPASS tokamak is presented, accompanied with the implementation of the corresponding theoretical models.

Firstly, for more ITER-relevant runaway electron studies, such as suppression, mitigation, termination and/or control of runaway electron beam, it is important to obtain runaway electrons after the disruption. In this thesis, the author shows the recipe for runaway electron beam generation that he obtained during his studies on the COMPASS tokamak. Consequently, parametrisation of the runaway electron beam was performed to characterise its occurrence. These parameters include the plasma current, the toroidal electric field, the disruption speed, the effective safety factor, magnetic fluctuations and the loop voltage spike. It was found that the lower the plasma current before the disruption the more probable it is for the runaway electron beam to be generated. We also show that the runaway electron beams are generated in a relatively narrow range ($0.6 - 0.8\,\mathrm{V/m}$) of the toroidal electric field before the disruption. Next, the higher the disruption speed and the effective safety factor, the more probable for runaway electron beam to be generated. A linear connection between the magnetic fluctuations and the loop voltage spike is reported and lower values are more favourable for runaway electron beam generation. In addition to thesis typical parameters, Abduallaev's hypothesis on the runaway electron beam generation was thoroughly investigated. Unfortunately, except for the connection of the runaway electron current with the pre-disruptive current inside certain rational surface, none of the other parameters and dependencies were suf-

ficiently clear in the COMPASS studies so far. The lack of synchrotron radiation during runaway electron beam existence after massive gas injection and the importance of long discharges for runaway electron mitigation studies are briefly reported.

Secondly, it is well known that synchrotron radiation is one of the most direct ways to measure confined runaway electrons. On the COMPASS tokamak, the very first synchrotron radiation was observed thanks to the author's studies. Henceforth, the synchrotron radiation measurements are presented. The data in the first three experimental campaigns was analysed. Different patterns were observed and a correlation between the synchrotron radiation and hard X-ray/neutron signals was found. Using the SYRUP code, we estimated typical pitch angles and runaway electron densities for runaway electrons having energies over $15-20\,\mathrm{MeV}$ from direct observation of synchrotron radiation in the COMPASS tokamak. The calculated pitch angles in the range $0.15-0.30\,\mathrm{rad}$ are very similar to the ones reported in other tokamaks. The runaway electron density for runaway electron having energies over $15-20\,\mathrm{MeV}$ is predicted to be of the order of a few $10^{15}\,\mathrm{m}^{-3}$. The latter result is compared with the Kruskal-Bernstein theory and the NORSE code. The Kruskal-Bernstein theory clearly overestimate the total runaway electron density, while the NORSE code predicts a density of runaway electron for energy above $15-20\,\mathrm{MeV}$ five orders of magnitude lower than estimated experimentally. However, the timing of synchrotron radiation observation and the rise of high-energy runaway electron density from the NORSE code are in excellent agreement.

Furthermore, one of the most crucial parameters for runaway electron studies in tokamaks is the toroidal electric field. Here we present the importance of its precise estimation for experimental runaway electron studies, as different approaches could give quite different results. Namely, the influence of the toroidal electric field from measurements (flux loops) and codes (EFIT and METIS) on the maximum runaway electron energy calculation is examined. It is found how the mid-plane high field side flux loop gives the runaway electron energy closest to the ones obtained from the EFIT code. In addition, the METIS code gave the closest runaway electron energy when the effective charge was set to 2.5, which is a reasonable value for the limited plasma of the COMPASS tokamak. This analysis is performed for different types of COMPASS runaway electron discharges, namely: standard COMPASS discharge, runaway electron discharge, runaway electron discharge in the Parail-Pogutse regime and slide-away discharge. In all the four cases EFIT predicts a runaway electron energy closer to the one from the measurements than METIS. However, in the case of the slide-away regime, the errors presented for both codes are over 50 %.

Finally, the knowledge of the runaway electron current or runaway electron density during the plasma discharge is one of the best ways to compare experiment and theory. For that reason, a method to estimate experimentally the runaway electron current is elaborated in this thesis for the COM-

PASS tokamak. In the particular case of the runaway electron discharge #7298, we estimated that at least 4 kA are driven by runaway electrons. The method is then applied to a set of experiments (a standard COMPASS discharge, a slide-away and an intermediate one) for which runaway electrons influenced the plasma current at the beginning of the discharge. The expected trend is clearly observed for the experimental runaway electron density estimations for the standard COMPASS discharge, the intermediate case and the slide-away regime: only $10^{15} - 10^{16}\,\mathrm{m}^{-3}$ at the discharge beginning, $10^{16} - 10^{17}\,\mathrm{m}^{-3}$ with a decrease after the discharge beginning and $10^{16} - 10^{17}\,\mathrm{m}^{-3}$ with an increase after the discharge beginning, respectively. The obtained experimental results are also compared with the Kruskal-Berstein theory and the NORSE code. Even though the exact orders of magnitude between models and experiment are not matching, the discrepancies with the observations are relatively low for both models. Furthermore, the runaway electron energy drift limit is identified as the most probable reason for the common runaway electron losses at the end of the plasma discharge in the COMPASS tokamak. Six different types of runaway electron distribution functions are used in all the aforementioned experimental estimations of runaway electron density. However, none of them is identified as the best option, though the results from all six of them are physically acceptable, i.e. are not contradictory with the observations.

Keywords: runaway electron, COMPASS tokamak, electric field, massive gas injection, disruption, synchrotron radiation

Samenvatting

– Summary in Dutch –

Relativistische (tot tientallen MeV) runaway elektronen met een stroom tot ongeveer 10 MA, worden naar schatting na dirupties in ITER genereerd. Daarom is het onderzoeken van methoden ter beperking van runaway elektronen één van de hoogste prioriteiten voor de veiligheid van ITER. In het kader van het EUROfusion consortium werd een project over runaway elektronen studies op de COMPASS tokamak toegekend onder andere omdat er relatief weinig veiligheidsproblemen zijn op COMPASS met betrekking tot mogelijke schade ten gevolge van runaway elektronen en aangezien zijn grote flexibiliteit voor verschillende plasmaparameters (bijv. plasma vorm, elektronen dichtheid, plasma stroom , enz.). Dergelijke mogelijkheden met een significante, maar nog steeds veilige, runaway elektronenpopulatie maken COMPASS geschikt voor de validatie van modellen van runaway elektronen en voor extrapolaties naar ITER. In dit proefschrift wordt baanbrekend experimenteel werk op runaway elektronen gepresenteerd dat uitgevoerd werd op de COMPASS tokamak, vergezeld van de implementatie van de bijbehorende theoretische modellen.

Ten eerste is het belangrijk runaway elektronen na een disruptie te kunnen genereren om ITER-relevante runaway elektronenstudies te kunnen doorvoeren; studies zoals de onderdrukking, mitigatie, beëindiging en/of controle van de runaway elektronenbundel. In dit proefschrift verklaart de auteur het recept voor de generatie van runaway elektronenbundel dat hij tijdens zijn studie op de COMPASS tokamak ontwikkelde. Vervolgens wordt het optreden van de runaway elektronenbundel gekarakteriseerd als functie van een aantal parameters. Deze omvatten de plasmastroom, het toroidale elektrische veld, de disruptiesnelheid, de effectieve veiligheidsfactor, magnetische turbulenties en de piek in de omvangsspanning. Hoe lager de plasmastroom vóór de disruptie, hoe hoger de waarschijnlijkheid dat een runaway elektronenbundel wordt gegenereerd. We tonen ook aan dat de runaway elektronenbundels worden gegenereerd in een relatief klein bereik $(0{,}6 - 0{,}8\,\mathrm{V/m})$ van het toroidale elektrische veld vóór de disruptie. Verder: hoe hoger de disruptiesnelheid en de effectieve veiligheidsfactor, hoe groter

de kans dat een runaway electronenbundel wordt gegenereerd. Een lineaire verbinding tussen de magnetische turbulentie en de piek in de omvangsspanning wordt gerapporteerd waarbij lagere waarden gunstiger zijn voor de productie van runaway electronen. Naast deze typische parameters werd de hypothese van Abduallaev op de generatie van runaway electronen grondig onderzocht. Behalve een correlatie tussen de runaway elektronen stroom en de plasma stroom voor de disruptie binnen een bepaald rationeel oppervlak, waren geen van de andere parameters en afhankelijkheden tot nog toe voldoende duidelijk in de COMPASS studies. Het ontbreken van synchrotronstraling tijdens runaway elektronenbundel na massale gasinjectie en het belang van lange ontladingen voor studies van runaway elektronen wordt kort gerapporteerd.

Ten tweede is het bekend dat synchrotronstraling één van de meest directe manieren is om geconfineerde elektronen te meten. Op de COMPASS tokamak werd de eerste synchrotronstraling gemeten dankzij de studies van de auteur. Deze metingen van de synchrotronstraling worden dan ook voorgesteld. De gegevens in de eerste drie experimentele campagnes hierover werden geanalyseerd. Verschillende patronen werden waargenomen en er werd een correlatie gevonden tussen de synchrotronstraling en de harde X-ray/neutron signalen. Met behulp van de SYRUP-code schatten we de typische pitchhoeken en runaway elektronendichtheid voor runaway elektronen met energieën van meer dan $15 - 20\,\mathrm{MeV}$ op basis van directe observatie van synchrotronstraling in de COMPASS tokamak. De berekende pitchhoeken van om en bij de $0.15 - 0.30\,\mathrm{rad}$, zijn zeer vergelijkbaar met die welke in andere tokamaks worden gerapporteerd. Voor de runway elektronen dichtheid, van runaway elektronen met energieën over $15 - 20\,\mathrm{MeV}$, wordt een grootteorde voorspeld van ongeveer $10^{15}\,\mathrm{m}^{-3}$. Dit laatste resultaat wordt vergeleken met de Kruskal-Bernstein theorie en de NORSE code. De Kruskal-Bernstein theorie overschat de totale runaway elektronentheeheid duidelijk, terwijl de NORSE-code een runaway elektronendichtheid voorspelt, voor energieën boven $15-20\,\mathrm{MeV}$, dat vijf orders van grootte lager ligt dan experimenteel geschat. Hiertegenover staat dat de timing van de observatie van de synchrotronstraling en het tijdsverloop van de stijging van de dichtheid van de hoge energie runaway elektronen in de NORSE-code in uitstekende overeenstemming zijn met het experimenteel gedrag.

Verder is één van de meest cruciale parameters voor onderzoek in runaway elektronen in tokamaks het toroidale elektrische veld. Hier presenteren we het belang van nauwkeurigheid van de schatting van het toroidale elektrische veld voor studies van experimentele runaway elektronen, aangezien verschillende benaderingen zeer verschillende resultaten geven. Hiervoor wordt de invloed van het toroidale elektrische veld uit metingen (op basis van flux lussen) en codes (EFIT en METIS) op de berekening van de maximale runaway elektronenergie onderzocht. Het gebruik van de meting van de flux lus in het midden vlak op de hoge veld zijde levert de elektronenergie die het dichtst bij de EFIT-code komt. Daarnaast levert de METIS-code

de beste benadering voor de runaway elektronenergie als de effectieve lading op 2.5 wordt ingesteld, wat een redelijke waarde is voor het plasma van de COMPASS tokamak als het plasma door een limiter beperkt is. Deze analyse werd uitgevoerd voor verschillende typen COMPASS runaway elektronen ontladingen: standaard COMPASS ontlading, runaway elektronen ontlading, runaway elektronen ontlading in het Parail-Pogutse regime en slide-away ontlading. In elk van deze vier gevallen voorspelt EFIT een runaway elektronenergie in betere overeenstemming met de metingen dan METIS. In het geval van de slide-away ontladingen zijn de fouten voor beide codes echter meer dan 50%.

Tenslotte zijn de kennis van de stroom door de runaway elektronen gedragen of de dichtheid van de runaway elektronen tijdens de plasma ontlading één van de beste manieren om experiment en theorie te vergelijken. Om deze reden werd in dit proefschrift een methode uitgewerkt om experimenteel de runaway elektronen stroom te bepalen voor de COMPASS tokamak. In het specifieke geval van de runaway elektronen ontlading #7298, schatten we dat tenminste 4 kA stroom door runaway-elektronen wordt gedragen. De methode wordt vervolgens toegepast op een reeks experimenten (een standaard COMPASS ontlading, een slide-away ontlading en een ontlading dat tussen beide ligt) waarvoor de runaway elektronen stroom aan het begin van de ontlading de plasma stroom beïnvloedde. De verwachte trend wordt duidelijk waargenomen voor de schatting van de experimentele runaway elektronische dichtheid respectievelijk voor de standaard COMPASS ontlading, het tussenliggende geval en het slide-away regime: alleen $10^{15} - 10^{16}\,\mathrm{m}^{-3}$ bij het begin van de ontlading, $10^{16} - 10^{17}\,\mathrm{m}^{-3}$ met een afname na het begin van de ontlading en $10^{16} - 10^{17}\,\mathrm{m}^{-3}$ met een toename na het begin van de ontlading. De verkregen experimentele resultaten worden ook vergeleken met de Kruskal-Berstein theorie en de NORSE code. Hoewel de exacte orders van grootte tussen modellen en experimenten niet overeenkomen, zijn de verschillen met de waarnemingen relatief laag voor beide modellen. Bovendien wordt de drift limiet van de energie van de runaway elektronen geïdentificeerd als de meest waarschijnlijke reden voor de verliezen van runaway elektronen op het einde van de plasma ontlading in de COMPASS tokamak. Zes verschillende soorten distributiefuncties voor de runaway elektronen worden gebruikt bij alle bovengenoemde experimentele schattingen van de elektronische dichtheid van de runaway elektronen. Geen van hen wordt echter geïdentificeerd als de beste optie, hoewel de resultaten van alle zes van hen fysiek aanvaardbaar zijn, met andere woorden niet in strijd zijn met de waarnemingen.

Trefwoorden: Runaway electron, COMPASS tokamak, elektrisch veld, massieve Gasinjectie, disruptie, synchrotronstraling

Resumé

– Summary in Czech –

Na ITER je při disrupcích plazmatu předpovídána generace relativistických ubíhajících elektronů (runaway electrons, zkráceně RE, s energiemi až desítky MeV), které ponesou proud kolem 10 MA. Nalezení metod pro jejich utlumení je proto jednou z nejvyšších priorit z hlediska technické bezpečnosti ITER. Tokamak COMPASS získal jako součást konsorcia EUROfusion projekt na studium ubíhajících elektronů, a to mj. z důvodů poměrně nízkých bezpečnostních rizik z hlediska možného poškození od RE. V této disertační práci prezentujeme průkopnickou experimentální práci zaměřenou na studium RE na tokamaku COMPASS.

Jedním ze základních parametrů pro studium RE je toroidální elektrické pole E_{tor} v tokamaku. V práci prezentujeme důležitost přesné definice tohoto parametru pro experimentální výzkum RE s ohledem na skutečnost, že rozdílné přístupy mohou vést na značně odlišné výsledky. Zejména je zkoumán vliv hodnot E_{tor} z měření a z výpočtů (EFIT a METIS) na výpočet maximální energie RE W_{max}. Tato analýza je provedena pro rozdílné typy výbojů s RE na tokamaku COMPASS.

Znalost elektrického proudu I_{RE} nebo hustoty n_{RE} charakterizujících RE během plazmatického výboje patří mezi nejlepší způsoby jak porovnat experiment s teorií. Proto byla pro tokamak COMPASS uzpůsobena metoda odhadu I_{RE}. Tato metoda je pak aplikována na sadu výbojů, ve kterých byl proud plazmatem I_p ovlivněn RE v počátku výboje. Získané experimentální výsledky jsou také porovnány s Kruskalovou-Bernsteinovou teorií a s kódem NORSE. Kromě toho je identifikována driftová mez pro energii RE, která je nejpravděpodobnější příčinou pro obvyklé ztráty RE na konci výboje v tokamaku COMPASS.

Synchrotronní záření patří mezi nejpřímější metody k měření RE udržovaných magnetickým polem. V této práci jsou prezentována první úspěšná měření synchrotronního záření na tokamaku COMPASS. Byla provedena analýza dat ze všech experimentálních kampaní. Přímé pozorování synchrotronního záření na tokamaku COMPASS bylo využito k odhadu typického úhlu stoupání částice na silokřivce θ a hustoty n_{RE} pro RE s en-

ergiemi přes $15 - 20\,\mathrm{MeV}$. Odhadnuté hustoty byly rovněž srovnány jak s Kruskalovou-Bersteinovou teorií, tak s kódem NORSE.

Konečně z hlediska více ITER-relevantního studia RE, jako např. studia potlačení, utlumení, ukončení a/nebo řízení svazku RE je důležité získat svazek RE po disrupci. Parametrizace svazku je provedena s ohledem na pravděpodobnost jeho výskytu. Tyto parametry zahrnují proud plazmatem, toroidální elektrické pole, rychlost disrupce, efektivní bezpečnostní faktor, magnetické fluktuace, a špičky v napětí na závit. Navíc k těmto typickým parametrům byla zevrubně testována Abduallaevova hypotéza ohledně produkce svazku RE. Krátká zpráva je dále věnována nepřítomnosti synchrotronního záření během existence RE svazku, a také významu dlouhých výbojů pro studium utlumování RE.

Klíčová slova: ubíhající elektron, COMPASS tokamak, elektrické pole, masivní vstřik plynu, disrupce, synchrotronní záření

Chapter 1

Introduction

1.1 Taming Nuclear Fusion

Mankind will soon be confronted to a difficult period. On one side, the rise of the human population and its rapid technological development increase the energy demand, while on the other side humanity will have to face the lack of oil and other carbon-based fuels, the fear of (fission) nuclear energy, intermittence of renewable energy sources and increase of greenhouse gasses (like CO_2) in the atmosphere.

The most promising solution that meets all the aforementioned requirements is controlled thermonuclear fusion (hereinafter refer to as *fusion*), as base-load electricity (renewable energy misses this requirement) and CO_2-emission-free (carbon-based fuels miss this requirement) energy source. Moreover, even though the fusion has 'nuclear' in its name, the level of radiation and radiation lifetime will be drastically lower than in nowaday fission nuclear power plants, featuring an intrinsic safety.

Nuclear fission is the splitting of a heavy radioactive nucleus into two lighter nuclei. The fission process is accompanied with formation of transuranium elements and other by-products creating the radioactive waste. On the other hand, nuclear fusion incorporates merging of light nuclei into a heavier one, where none of initial nuclei nor the reaction products have to be radioactive. However, the most promising fusion reactions usually involve tritium T and/or high energy neutrons. The half-life of tritium beta decay is 12.32 years, the time period which is shorter for more than three orders of magnitude than any main fission product, and tritium is only harmful to human being if ingested. Thus, confining tritium properly inside a fusion power reactor would be safe for people and environment. The high energy neutrons that result from the fusion reactions, can interact with the surrounding material and make the material radioactive (called activation process) for several hundred years, but even this time is orders of magnitude shorter than the one of the fission products and can be handled in

one human generation. Moreover, the activation process could be reduced with further development of fusion materials (plasma facing components or wall). Finally, at the present moment the most interesting nuclear reaction from the angle of the fusion power plant contains both, T and high energy neutron:

$$ {}^{2}_{1}D + {}^{3}_{1}T \rightarrow {}^{4}_{2}He(3.5\,\mathrm{MeV}) + n^{0}(14.1\,\mathrm{MeV}). \tag{1.1} $$

The reaction given in Eq. 1.1, between two hydrogen isotopes (so-called DT-reaction), has the largest cross-section among all possible fusion reactions, i.e. probability to happen and has one of the largest fusion energy outputs, making it twofold interesting. Despite the radioactive issues mentioned above, one additional problem is to be stressed out: the world tritium deficit due to its short decay half-life. For this reason, a technology of "breeding" tritium inside the machine involving another nuclear reaction where the neutron (that comes from the initial DT-reaction) interacts with lithium Li is being developed. It would then close the reaction cycle between relatively abundant fuels coming from seawater (D) and the Earth's crust (Li).

Up to now, the fusion power is a privilege of the stars, where extremely energetic nuclei are necessary to overcome the reflecting Coulomb force and make the fusion reactions to happen. The state of matter in the star's core is called plasma, which is practically an ionized gas, for which electrons are separated from the atoms. To achieve self-sustained energy production from DT-reactions, a plasma needs to be sufficiently hot and dense with low energy losses. The criteria that defines those plasma condition is so-called "triple product"

$$ n_i T_i \tau_E > 3 \times 10^{21}\,\mathrm{m^{-3}\,keV\,s^{-1}}, \tag{1.2} $$

where n_i is the ion density, T_i is the ion temperature in keV[1] and τ_E is the average time that heat energy stays in the system (i.e. plasma).

To reach this condition two main plasma confinements are proposed - Inertial Confinement Fusion (ICF) and Magnetic Confinement Fusion (MCF). The former achieves the necessary aforementioned condition using laser compression, hence making short-living (order of nanoseconds), but extremely dense plasma (order of $10^{30}\,\mathrm{m^{-3}}$). Contrary, the magnetically confined fusion confines plasma with magnets for significantly longer time (order of seconds), but with much lower densities (order of $10^{20}\,\mathrm{m^{-3}}$). In this Thesis the main focus is on magnetic confinement.

Magnetic confinement pioneers first made linear devices with various configurations of magnetic coils, hence making different magnetic field configurations inside the device. These methods were not very efficient, due to various instabilities as a result of the losses at the ends of the cylinder, leading to too small confinement time and the size of the power-plant devices was estimated to be on the order of hundreds meters [1, Chapter 3]. Those devices had open magnetic configuration inside the chamber, i.e. the magnetic field lines were not closed upon itself. Therefore, they were afterwards

[1] $1\,\mathrm{eV} = 11\,604,505\,\mathrm{K}$

referred as "open" MCF and they will not be the focus of this Thesis. The place where the field lines were exiting the device were called "ends", where the main losses occurred.

Next logical step for reducing the losses at the ends of the linear device was to join its ends and make a ring, an endless "closed" MCF. Closed MCF devices are usually called toroidal, coming from the name of the mathematical object "torus" that looks similar to the machines. Moreover, a toroidal surface is mathematically the only surface that can be covered by a non-zero vector field [2] (e.g. magnetic field). At the time, some of the toroidal devices were simply closed copies of their open predecessor, while some new concepts were introduced. For example, the success of the toroidal theta pinch was so great from the bare beginning, that it led Lev Artsimovich[2] to announce at the Geneva 1958 Conference how "every housewife should have her own theta pinch" [1, Section 5.2]. Further extensive researches on toroidal devices, made two of them the most prominent ones for realistic fusion power plants: stellarator and tokamak. Both of them will be briefly described in the next two paragraphs. The main feature for both is a strong twisting of the nested magnetic field lines that improves confinement. This twisting is necessary to compensate the grad-B drift[3]. The grad-B drift induces a vertical charge separation and a vertical electric field. The perpendicular vertical electric field and toroidal magnetic field produce a net outward force and particles get lost from the devices. Therefore, twisting the magnetic field lines short-circuits the charge separation induced by the grad-B. In addition, two more devices are showing high potential as a good fusion power plant candidate - spherical tokamak and reversed-field pinch, but their state-of-the-art is presently far beyond those of stellarators and tokamaks.

Stellarators are the best competitor towards steady-state long-time operating fusion device. Even in the class of stellarators there are several subclasses, but they all have in common completely externaly generated magnetic fields. This is achieved with a thorough choice of the magnetic coils. The main drawback of this approach is the design and/or construction of the magnetic coils, due to their complicated shapes and high request on the magnetic field precision (error should be smaller than 10^{-4} T or 0.01 %). Even though stellarators were invented before the tokamaks, the current stage of the stellarator state-of-the-art is trailing one generation behind the tokamak state-of-the-art. This is due to the huge success of tokamaks presented by Artsimovich in the 3^{rd} IAEA Fusion Energy Conference, held in Novosibirsk in 1968. Anyway, based on the present scientific knowledge, the stellarators are the best MCF alternative if the tokamaks fail to give economical power from fusion. Nonetheless, the confinement time of the stellarator plasma is still quite lower than for the tokamak plasma. There-

[2]The leader of Soviet fusion power program from 1951 to 1973.

[3]Gradient of the toroidal magnetic field is an intrinsic feature of the toroidal magnetic devices.

fore, the main goal of newly built stellarator Wendelstein-7X (Greifswald, Germany) is the improvement of the stellarator confinement.

Tokamaks are, at the present state, by far the best fusion devices with respect to the triple product Eq. 1.2 achievements. They are simpler to design and manufacture than stellarators, as toroidal field coils generating the toroidal component of magnetic field are planar and identical. The main difference with stellarators is the non-zero net plasma current, which induces the poloidal magnetic field. Besides the poloidal magnetic field, the plasma current heats the plasma by means of the Ohm's law. The plasma current is induced via a central solenoid coil that acts as the primary winding of a transformer, while plasma acts as the secondary loop. The tokamak is sometimes called *quasi-steady-state* device, as it has relatively long fusion plasma discharges in comparison with majority of the other fusion devices, but the discharge length is usually limited by the current ramp-up in the central solenoid coil swing. There are however, good results in prolongating the tokamak discharge length via electromagnetic (EM) wave driven current [3]. Additional problem to plasma current is that it introduces a wide span of plasma instabilities that lead to plasma control issues. Nonetheless, tokamaks were the first devices where the plasma state of improved high confinement, so-called H-mode, was discovered and operation in H-mode became a routine for majority of tokamaks. The understanding of physics of the H-mode occurrence is still developing, but it is widely accepted that it is the result of lower turbulent transport and energy losses. Furthermore, the H-mode operation is not achieved routinely in other types of MCF devices. In summary, tokamaks demonstrated so far the best fusion plasma performances and thus the efforts in making a first fusion device that will have larger output power than input power are devoted to build a giant tokamak called ITER (International Thermonuclear Experimental Reactor)[4], now under construction next to the CEA Cadarache (France) under world wide international collaboration.

The main goal of ITER is not to power the grid, but to clarify how the fusion power plant concept is technologically feasible for commercial use. Further major deliverable of ITER is to prove the feasibility of the tritium breeding blankets, as it should be sufficiently efficient and economical without any exterior leakage of tritium. Moreover, ITER should demonstrate how self-sustained discharges heated by the alpha particles (fully ionised helium He - the product of the fusion reaction, see Eq. 1.1) are possible with a reliable system to clean the plasma from the thermalised alpha particles (that already deliver their energy to the plasma), so-called alpha-ash. ITER should also show how divertor materials can survive extreme heat loads for sufficiently long time, as too frequent maintenance would be too expensive. Beside these new science and technology demands, ITER is already pushing existing technologies to their limits, such as computation science

[4]Note that *iter* also means 'the way' in Latin. Moreover, nowadays ITER is rarely mention as abbreviation, but more as a name for an organization.

for recording enormous amounts of data with high speed, huge amount of niobium-based superconducting material required for its coils and cryogenic technology for cooling the magnets. If ITER demonstrates that all of this is feasible, the connection to the grid of the fusion device is then foreseen with the first fusion power plant prototype named DEMO. According to the present plans each ITER partner shall build its own DEMO.

1.2 Is ITER "the ONLY *way*"?

During the '90s, the two largest tokamaks ever made (JET in EU and TFTR in USA) have proved the scientific principle of fusion power production with operating DT plasmas and getting output power in order of megawatts. Even though the output was lower than the input power, this was a colossal step for the MCF. The next logical step is to show the technological principle of fusion power production, which will be the main goal of ITER.

"The fusion is always 20-30 year ahead" is a very common joke about fusion as energy source and ITER is definitely the step that should put down this joke. If ITER is successful, then fusion power fed into the grid will be possible, while if ITER results are dissapointing, that could end the fusion research for many decades, as politicians (at least in EU and USA) are slowly loosing their patience. Moreover, in two-three decades some other energy-related technologies could have unexpected breakthrough, e.g. solar or wind power or even "compact" fusion. Furthermore, a discovery of room-temperature superconductor would have even larger energy-related impact than the renewable energy sources. Therefore, seen that the ITER's success/failure could influence the future of the fusion research, we raise the question - is it the **only** *way*? This Section will treat this issue systematically, and finally try to give an answer.

The reason why fusion energy is always 20-30 years ahead is simply because plasma has been behaving unexpectedly with plasma volume enlargement and stronger heating input. In other words, each new generation of tokamaks brought something new to the tokamak physics. The unexpected plasma features significantly slowed down the tokamak progress towards the fusion power plant. Still scientists managed to keep a good pace on increasing the triple product as can be seen in Fig. 1.1. It is clear from Fig. 1.1 that fusion power condition was growing faster than the famous Moore's law. However, the fusion opponents argue that this progress was made by enlarging the machine, while Moore's law implies constant size of the chip. This is why maximum energy of accelerators is also on the Figure for a more suitable comparison. Unfortunately for fusion, after 1997 the triple product stagnated while Moore's law grow continued. The halt in fusion power production is due to the (in)decision around building ITER, as the next logical step. This hesitation came rather from the politicians than from the fusion community, as ITER called for complex international

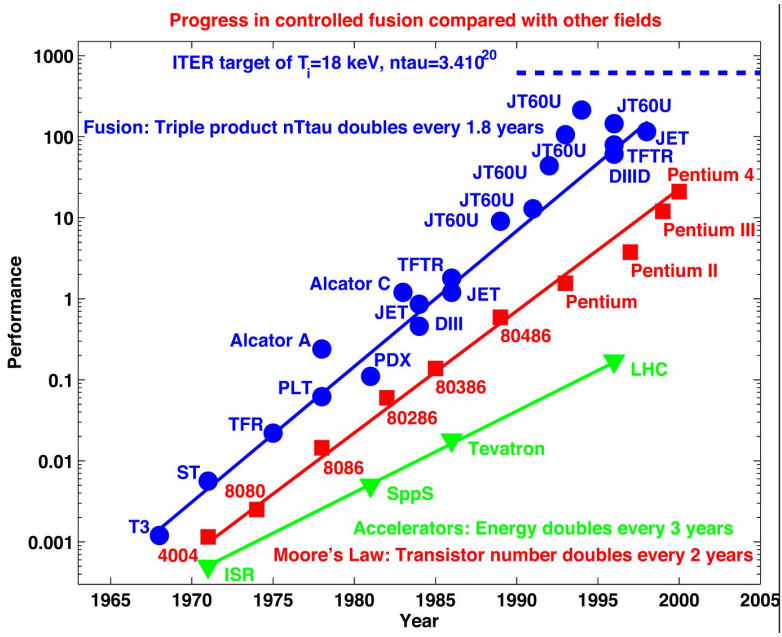

Figure 1.1: Progress in plasma confinement performance compared to that of other advanced technologies. The Figure is copied from Ref. [4].

collaboration due to the amount of money and manpower involved.

Furthermore, one could say: "if each new generation of tokamaks brought something new, usually leading to lower performance than expected - what ensures that this will not happen with ITER?" The honest answer is: "Nothing, as then it would not be a scientific research project." Nonetheless, the delay between building and operating ITER borrow some more time to scientists to check and question existing physics and scalings, making more reliable extrapolations towards ITER. Moreover, the ITER postponement gave time for reviewing and pushing the R&D of missing physics and technologies for ITER. In addition, ITER is a machine designed with the biggest care in the fusion history. The first ITER design from 1998 would probably under-perform, even though the necessary care was taken. Now with redesign of ITER in 2001, with constant reviews and experience gained due to the construction suspensions, the risk of ITER's failure is minimised but still there.

A long way has been taken regarding the plasma physics and auxiliary technologies development for fusion. The way started in the early '50s, with the first tokamaks being built at the end of the same decade in the former Soviet Union. Before the famous IAEA Conference in Novosibirsk held in 1968, Australia was the only country beside Soviet Union that had a toka-

mak - named LT-1. But after the conference almost all the worldwide largest fusion and plasma centers started to build their own tokamaks (see Fig. 1.2). The number of tokamaks in '70s raised fivefold in comparison to the number of tokamaks ever built before, the increase continued in the '80s where tokamak number was enlarged by 50% compared to the '70s. After these two decades, plasma control and stability, plasma diagnostics, plasma-wall interaction and impurity control, plasma heating and new plasma physics were advanced enough for the fusion community to start to think about the 'next step' - the fusion reactor. Unfortunately, the subsequent two and half decades have led to a more or less constant 30% drop of operating tokamaks per decade, where at the moment world has approximately two times less tokamaks in operation than in the '70s!

What could be the reason to this evident reduction of operating tokamaks? It is most probably ITER itself:

- larger (and more expensive) machines are more fusion-relevant;
- general public (with politicians in the front) started to doubt in fusion energy, as challenge taming the fusion showed drastically more difficult than expected half a century ago;
- ITER project is huge, thus it consumes most of the funds and manpower allocated to fusion;
- available funds coming from the governments are more and more focused towards ITER-relevant issues over-looking the other ones.

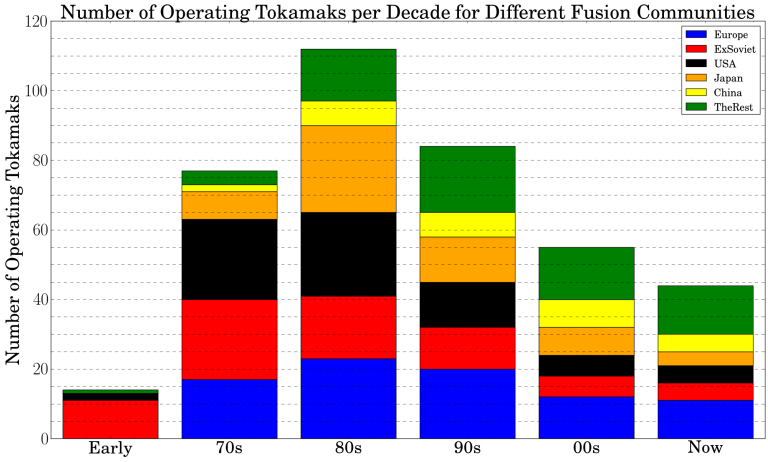

Figure 1.2: Number of operating tokamaks for 6 different fusion communities - Europe, the former Soviet Republics (FSR), the USA, Japan, China and the Rest of the World (RotW) - by decades. Main database used from Ref. [5], updated for this work.

Let's ask again - is ITER the **only** *way*? Every good gambler knows that putting all money on a single bet will not pay off, every business person knows that investing in one company will most probably bring to bankruptcy and every farmer knows that growing one kind of crops makes the future very dependent on the market prices. Actually, the focus of fusion community towards ITER in last two decades resembles to the aforementioned examples of gambler, businessman and farmer investing everything in one solution. Even though there are existing blueprints of different devices as the fusion power plant, the tokamaks are presently the only one seriously considered. This is simply because other fusion devices with high potential (e.g. stellarators, spherical tokamaks and reversed-field pinches) are one generation or more behind. Yet, none of those device types had a boost in the R&D as tokamak had during the '70s, first due to the high success of the tokamak and now due to the ITER project. Independently on the ITER success, new smaller machines are more than necessary. It does not matter if these machines would be tokamak or any other type of fusion device, as one should not only be focused on energy confinement and confinement principles, but with other more subtle reasons:

- *experience:* Scientists and engineers that made the basics of the fusion science for ITER are now either close to retirement, retired or even passed away. While the number of experienced scientists necessary for ITER will be enormous, the continuous experience cannot be maintained with having only large fusion devices with strict rules.

- *models:* Even though fusion science is well developed, there is still a lot of place for improvement in theories of H-mode, ELMs, runaway electrons, turbulent transport, heating, non-inductive current drive, etc. Waiting for a few plasma discharges in medium or large machines can take some time, while with local-smaller machines one could first benchmark a code much faster.

- *diagnostics:* Around fusion devices, diagnostic tools have to survive harsh environment under strong and intensive electromagnetic and neutron radiation in presence of strong magnetic field and (if inside the vacuum vessel) significant temperatures. It is always good to have smaller facilities for endurance testing of the diagnostics. The failure of diagnostics would cost more money and time on the larger machines. Moreover, the success of the experiment itself would also be jeopardised.

- *materials:* Probably the toughest challenge for fusion is to manufacture all kinds of necessary materials surrounding the plasma. Here special long-pulse devices with severe reactor-like environment is a must.

All of the above issues are very import for ITER success and having more small experiments could speed up fusion progress. Lack of experience could

lead to ITER failure due to human factor. Better models mean better extrapolation towards ITER and better exploitation of the experimental time. Better diagnostics give better control and analysis of the plasma. All the aforementioned three issues are hopeless without proper material in future fusion power plants, for which testing facilities are required, they often do not have all the features of the fusion environment at once, which could lead to incomplete or even wrong conclusions. In addition, medium/large fusion facilities with strict rules, large bureaucracy and tight schedules are making progress slow. The point here is not to say that large fusion devices are not important, but how smaller ones might make progress at least slightly (but notably on the longer run) faster, contributing and supporting larger ones.

Anyhow, a few positive examples can be found across Europe[5]. GOLEM at the Czech Technical University in Prague is a tokamak that serve mostly for educational and training purposes. The ISTTOK tokamak, located at the Instituto Superior Técnico in Lisbon, is also a small tokamak that makes contributions in fields such as data acquisition system, plasma diagnostics, plasma control and plasma physics. Furthermore, the WEGA stellarator served as a training facility for young scientists in IPP Greifswald. Next is the the TORPEX device, located at École Polytechnique Fédérale de Lausanne, that serves as a good test bed for various diagnostics, plasma physics and heating systems even without a central solenoid[6]. Finally, ToriX at the French École Polytechnique in Paris is a magnetized plasma toroidal device that provides various practical training to the students. The importance of medium size devices in EU is recognized through the set of MST (Medium Size Tokamak: AUG, TCV and MAST) Tasks newly established by the EUROfusion. However, the devices included in the MST Tasks were all built during the last century - should not be there something new? A good track is the newly build stellarator in IPP Greifswald, Wendelstein-7X, but it is again a large facility. Finally, beside all the aforementioned torodial fusion devices, what fusion scientific community also needs are specialized non-fusion experiments and facilities - e.g. testing materials, auxiliary heating, tritium breeding, etc.

As usual, the main obstacle for production of new things is money and political will. But is there any common sense in saying that the most promising abundant, carbon-free, base-load and low radiation energy source is asking for too much money? Saying that the ITER total construction cost is presently around 15 billion dollars sounds a lot, but one has to take into account that this cost is split between EU covering 45%, with the other parties (Russian Federation, USA, Japan, South Korea, China and India) sharing the residuum equally (approximately 9% each). The money that each ITER Party is contributing to the ITER project is denoted as ITER

[5]Notice that only toroidal devices are enlisted in this paragraph, while there are other plasma devices also useful for the fusion research. However, listing of all fusion-relevant devices in Europe is not the subject of this paragraph.

[6]It has the conductor inside the vessel to create the poloidal magnetic field.

ITER Party	GDP [trillions $]	IPC [%]
EU	18.0	<0.040
Russian Federation	1.8	<0.080
USA	17.5	<0.010
Japan	4.5	∼0.030
South Korea	1.4	<0.100
China	10.0	<0.015
India	2.0	<0.070
Total	**55.2**	**<0.030**

Table 1.1: Nominal Gross Domestic Product (GDP) is taken very roughly, the exact amount depends strongly on the source and annual fluctuations. Separated percentage of the GDP for each ITER Party is tabulated as IPC (ITER Party Contribution).

Party Contribution (IPC). These contributions are tabulated in Table 1.1 as percentage of the Parties nominal Gross Domestic Product[7]. The numbers are in the order of hundredth of percent, which doesn't seems so large when set like that. Additionally, the ITER expenditure is spread over its construction period (approximatelly 20 years), while solely Germany spends more than 15 million euros for subsidies in renewable energy per year[8] [6, Figure 33] in the period 2011-2015. Also notice that governments are paying for ITER, while private oil, car and telecommunication industries spend similar or even more money for their R&D. For example, in February 2014 Facebook bought WhatsApp for 22 billion dollars - a social network buying a social network application for 50% larger amount of money than required for ITER! The situation of fusion is similar with the famous ecological joke: "it is a pity that trees only give us oxygen, if they would give us WiFi they would be everywhere!" Finally, the most budget cuts on the fusion research comes from the USA that spends by far least of its GDP on ITER. The USA stopped financing many facilities to be able to finance the ITER project. The last example of USA government severity is the shut down of the Alcator C-Mod tokamak, a very significant facility located at the best technical university of the world, MIT.

To conclude, I shall answer the question of this Section - yes, ITER is the *way*, but it definitely should not be the **only** one and the national fusion funds and new ideas should not suffer due to the ITER project. ITER should be an additional investment and number of national fusion laboratories and devices should not decrease due to ITER, rather the opposite.

[7] Nominal GDP is the measure of the total economic output of the goods and services of a country without inflation adjustment.

[8] Note that those subsidies are significantly reduced from 2017.

1.3 Motivation for Runaway Electron Studies

As the tokamak concept has developed over the last 50 years and as it has advanced towards the ITER-like design, numerous challenges occurred and many have been solved. One of the remaining tasks is to control and/or to mitigate the runaway electrons (REs) that would likely appear in the ITER device after a disruption.

Even though the presence of the RE population was known from the bare beginning of the tokamak research, they were first not of great interest for the fusion community. The reason is simply because REs did not present any serious threat to the early tokamaks like in more recent small/medium tokamaks (e.g. FTU, COMPASS, TCV, AUG) for which the RE current is relatively low. On the contrary, in large and reactor-like tokamaks (e.g. in JET, and very probably in ITER) the REs arise mainly during disruptions in connection to a rapid decrease of the plasma current. They can drag a significant amount of the pre-disruptive plasma current. The present models predicting that up to 70% of the pre-disruptive plasma current [7, p. S178] could be carried by the REs, which would have several tens of MeV energy. The kinetic and magnetic energy carried by the high energy RE beam can severely damage plasma facing components (PFC) and blanket modules as a result of a highly localised RE deposition. Besides the high cost of the plasma facing components and blanket modules, the time to produce and replace those parts would delay ITER project by months or even years. Moreover, the worst case scenario (with very low possibility) of the RE damage to ITER predicts leakage of cooling liquids into the vacuum chamber that could stop completely the entire ITER project. Therefore, the REs have to be suppressed in ITER and in future commercial nuclear fusion reactors.

To do so, tokamak operators try to anticipate the RE production. Discharge scenarios with significant population of REs, necessary for detailed studies, can severely damage in-vessel components of a tokamak, which can ultimately lead to a permanent vacuum or water leak and a prolonged shutdown of the facility. Despite a high interest in understanding the RE physics, potential risk is a big limitation for the detailed experimental studies in the large tokamaks.

However, the COMPASS machine has relatively low plasma current in comparison to larger devices and there is not in-vessel cooling. Therefore, the RE cannot achieve very high energies and cannot cause a severe damage of the vessel, which makes COMPASS a suitable machine for this kind of studies.

1.4 Outline of the Thesis

The Introduction (Chapter 1) is followed by an overview of the current state-of-art in RE studies (Chapter 2). Besides reviewing the present RE knowledge, this Chapter introduces most of the terms used in the Thesis. Subsequently, the initialisation of COMPASS dedicated RE studies is presented (Chapter 3), as the author was heavily involved in all of its aspects (e.g. planning, preparing, conducting, analysing, etc.). Namely, this Chapter describes the experimental setups installed on the COMPASS tokamak relevant for RE studies and an overview of the first four RE campaigns - their goals and achievements.

The toroidal electric field E_{tor} is an important parameter for RE studies that is hard to estimate precisely experimentally. In Chapter 4, the discrepancy between the different way of estimating E_{tor} is investigated and its influence on RE parameters (especially for the maximum RE energy W_{max}) is shown. Chapter 5 reports a method on how to estimate the RE current I_{RE}, which is then used to show RE generation at the early stage of the COMPASS discharge. Limiting RE energy due orbit drift is also examined in this Chapter. Furthermore, an analysis of synchrotron radiation observation at COMPASS tokamak is performed in Chapter 6. Finally, investigation of Ar injection in the plasma and creation of post-disruptive RE beam is addressed in Chapter 7.

The main conclusions of the Thesis are drawn in Chapter 8.

Chapter 2

Overview of Runaway Electron Studies

An overview of the current runaway electron (RE) status will be presented here, noting that this does not give a comprehensive review. The Chapter will be split into three parts. The current theory about REs and its implementation into different codes are covered first. The second part contains experimental observations and achievements on RE studies in fusion plasma devices. The final part will be dedicated to RE diagnostic methods as an essential bridge between theory and experiment. Finally, note that the last proper review paper was written almost 4 decades ago by Knoepfel and Spong [8] in the late 70s.

Before the main three parts, a brief historical overview and a principal definition of the RE phenomenon are given here. REs do not present a tokamak-specific effect, in fact they are not even associated solely with the fusion plasma, as the REs can theoretically appear in any form of plasma. Probably the first description of runaway effect was done by Wilson, the founder of the cloud chamber detector, in his attempt to explain processes in thunderclouds [9]. Afterwords REs appeared across different physical fields, e.g. solar flares [10, Section 24], mesosphere [11], solar wind [12] and in the following thundercloud processes studies [13]. In addition, stable relativistic electron beams (a type of RE) were studied in betatrons [14], the first important machine for producing high energy electrons.

The electrons are said to run away when the (Coulomb) collisional drag force acting on them becomes smaller than the accelerating force due to the electric field $\vec{E}$. Note that acceleration from the electric field does not depend on the electron velocity $\vec{v}_e$, while the Coulomb drag force at high $v_e = |\vec{v}_e|$ decreases approximately as $\sim v_e^2$. The dependence of RE generation on their velocity v_e makes it a statistical process in the velocity-space.

2.1 RE Generation and Modelling

Even though the literature lacks an up-to-date overview on RE in fusion plasma, Boozer [15] recently wrote a summary of the theories and defined the parameters relevant for the ITER RE mitigation.

This Section will start with the theory on RE generation mechanisms. The subsequent part will outline the consequence of finite speed on the RE generation theory. Before switching to the RE related codes and models, imperfections in the previously described theory will be emphasised.

Note that the theory described here will be focused solely on the electrons, but it can be applied to any charged particles (e.g. ion [16] or positron [17]).

2.1.1 Dreicer Mechanism

Even though RE effect was known since the 1920s, the first detailed theoretical explanation came in the late 1960s by Dreicer [18, 19]. Dreicer assumed an infinite, homogeneous, cylindrical, non-relativistic, fully ionised, quasi-steady-state plasma in an electric field, with an electron distribution function close to a Maxwellian.

The interaction between the bulk plasma and one electron presents two regimes depending on the velocity of the electron, the threshold velocity being the electron thermal velocity $v_{th,e}$. In general, this interaction gives a resulting force that slows down the electrons and therefore the force is called *drag force* F_{drag}. In the first regime (for velocity $< v_{th,e}$), as in conventional gas, the F_{drag} increases linearly with the electron velocity. In the second regime, if the electron moves faster than the electron thermal velocity of the bulk plasma, the F_{drag} starts to drop as the electron velocity increases. Here the main interaction with other plasma charged particles is through the Coulomb force. For significantly higher velocities than the thermal one, the F_{drag} coming from Coulomb collisions can be approximated as a function of the electron velocity v_e [8]

$$F_{drag}(v_e) \approx \frac{(2 + Z_{eff}) n_e e^4 \ln \Lambda}{4\pi\varepsilon_0^2 m_e v_e^2} \propto \frac{1}{v_e^2} \tag{2.1}$$

where n_e is the electron density, $\ln \Lambda$ is the Coulomb logarithm (typically 15-20 for fusion plasmas), $Z_{eff} = \sum_i \frac{n_i Z_i^2}{n_e}$ is the effective ion charge, e is the electron elementary charge, m_e is the electron rest mass and ε_0 is the vacuum permittivity.

In opposition to the drag force F_{drag}, the electrons are accelerated by the electric field that is present in the plasma either created internally by the plasma itself or generated externally. This accelerating electric force F_E depends solely on the electron charge and on the strength of the electric field $F_E = eE$. As shown in Eq. 2.1, the F_{drag} decreases proportionally

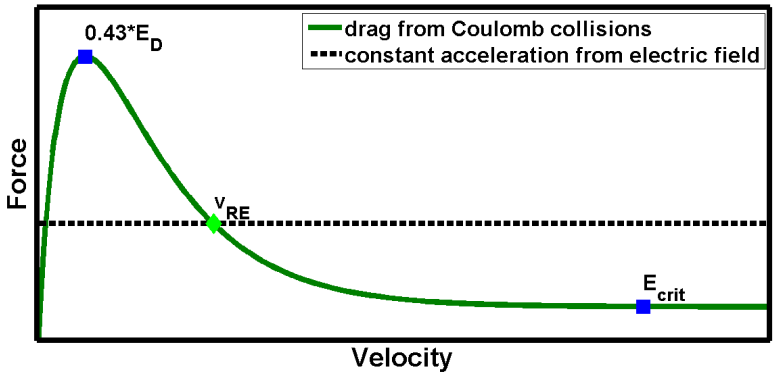

Figure 2.1: Schematic presentation of the forces acting on an electron in a plasma under an electric field - the drag force from the Coulomb collisions (green solid curve) and the accelerating force from the electic field (dashed black curve). The important quantities explained in the text are also labelled - E_D, v_{RE} and E_{crit} (see Section 2.1.4 for the later one).

quadratically with the velocity v_e. Thus, F_{drag} becomes lower than F_E at a threshold velocity v_{RE} (see Fig. 2.1)

$$F_E = F_{drag}(v_e = v_{RE}) \implies \frac{v_{RE}}{v_{th,e}} = \sqrt{(2 + Z_{eff})\frac{E_D}{E}} \tag{2.2}$$

and electrons are "continuously" accelerated, making them *run away* in the velocity space. In the above equation, $v_{th,e} = \sqrt{2eT_e[\text{eV}]/m_e}$ is the thermal velocity[1] of the electrons and E_D represents the so-called Dreicer field

$$E_D = \frac{n_e e^2 \ln\Lambda}{4\pi\varepsilon_0^2 T_e\,[\text{eV}]}, \tag{2.3}$$

also depending on the thermal velocity through the electron temperature T_e. E_D is the most crucial parameter of the Dreicer RE generation theory. Namely, if the electric field strength (internally or externally generated) in plasma would be equal to E_D then all electrons in plasma would run away.

Despite the fact that the electric field almost never reaches the E_D value in nature or in laboratories, REs can still be found in both of them. RE production comes as a result of the stochastic nature of the Coulomb collisions and plasma heating, creating a finite probability for electron to acquire higher velocity than v_{RE}. Notice here that lower v_{RE} corresponds to higher probability for an electron to run away. Also more energetic bulk electrons have larger probability to surpass the v_{RE} threshold. Moreover, in the terms

[1] Because of the 2 it is the most probable velocity.

of the plasma parameters, one can see from Eqs. 2.2, 2.3 and Fig. 2.1 that plasma with low n_e or/and high T_e (i.e. low E_D) or/and high electric field will have more REs. Furthermore, the RE generation process is continuous due to the constant recovery of the electron distribution function (EDF) through collisions. The rate of electron inflow into the runaway region was calculated in few papers after Dreicer[2], the latest expression given by Connor and Hastie Eqs. (66-67) [20] being:

$$\frac{\mathrm{d}n_{RE}}{\mathrm{d}t} \sim \frac{n_e^2 e^4 \ln\Lambda}{4\pi\varepsilon_0^2 m_e^2 v_{th,e}^3} \mathcal{E}_{\mathcal{D}}^{-3(1+Z_{eff})/16} \exp\left(-\frac{1}{4\mathcal{E}_{\mathcal{D}}} - \sqrt{\frac{1+Z_{eff}}{\mathcal{E}_{\mathcal{D}}}} \right) \quad (2.4)$$

where n_{RE} is the RE density and $\mathcal{E}_{\mathcal{D}} = E/E_D$ is the electric field normalised to the Dreicer one. Eq. 2.4 is known in the literature as the Kruskal-Bernstein growth rate.

2.1.2 Hot-tail Mechanism

The Dreicer mechanism described above in 2.1.1 explains the RE generation in small and medium size tokamaks, as those devices often have favorable conditions for RE generation (e.g. low n_e or/and high toroidal electric field E_{tor}). On the contrary, in large tokamaks (e.g. JET, TFTR, JT-60U, Tore Supra), plasmas with high n_e (for better fusion performance) and low E_{tor} (due to the machine size) are encountered, resulting in typical stable discharges without REs (explained in Section 2.1.4).

Nevertheless, if a sudden (and undesired) termination of the confined plasma (so-called disruption) occurs, RE can emerge in large devices and carry a significant amount of the pre-disruptive plasma current I_p. The generation of REs during disruptions could not be solely explained via Dreicer and *avalanche* mechanisms[3], i.e. an other RE generation process had to be found. The main idea behind this new mechanism is as follow: the abrupt cooling of the plasma during the first stage of the disruption - called thermal quench (TQ) - is too fast for the hottest electrons to get thermalised and, the collisionality being low, they become REs (breaking the steady-state assumption by Dreicer). As the hottest electrons usually represent the tail of the electron distribution function, the RE generation mechanism is named "hot-tail" mechanism.

Fleischmann and Zweben [21] first predicted theoretically the existence of this additional RE generation mechanism during the disruptions in large fusion devices. Some years later, the hot-tail mechanism was used to explain RE generation during the pellet injection in DIII-D by Harvey *et al.* [22]. Then, a simple model was proposed by Smith *et al.* [23] for spontaneous (i.e. natural and non-assisted) post-disruptive RE generation.

[2] See the review paper [8] for a list of the different RE growth rate calculations.
[3] The avalanche mechanism is described in Section 2.1.3

Equations describing the hot-tail mechanism are rather cumbersome and far from the scope of this Thesis, thus only an overview of the critical parameters involved is given[4]. The most crucial parameter is the time evolution of the temperature, i.e. the cooling rate. The faster the TQ is, the more RE seed will be produced due to the hot-tail mechanism. An approximate condition derived assuming a linear drop of T_e [23] states the time t_0 when the hot-tail mechanism dominates over the Dreicer one. The condition gives an upper limit for the T_e-decay time t_0 for the fixed pre-disruptive collisionality ν_0

$$\nu_0 t_0 < \frac{1}{3}\left(\frac{1}{2\mathcal{E}_\mathcal{D}}\right)^{3/2} \simeq \frac{1}{3}\left(\frac{\pi T_e}{8m_e}\right)^{3/4}\left(\frac{3\mu_0 e n_e q_0 R_0}{B_{tor}}\right)^{3/2} \tag{2.5}$$

with μ_0 being the vacuum permeability and where the toroidal electric field has been expressed as

$$E_{tor} = \eta_{res}\, j = \eta_{res}\frac{2B_{tor}}{\mu_0 q_0 R_0} \tag{2.6}$$

with η_{res} the plasma resistivity, B_{tor} the toroidal magnetic field, q_0 the safety factor on the plasma axis and R_0 the major radius of the tokamak. From this equation, the reason why large tokamaks have post-disruptive RE beam due to the hot-tail mechanism (unlike the small ones) is obvious - they feature larger T_e, n_e and R_0, while B_{tor} is not large enough to compensate.

H. Smith *et al.* [23] also found that high $\mathcal{E}_\mathcal{D}$ before disruption and low n_e after the disruption reinforce the initial RE population, so-called RE seed. As the hot-tail mechanism occurs before the Dreicer mechanism during disruption in large devices, it is essential for RE mitigation to suppress RE seed formation in this period as emphasised by Boozer [15].

2.1.3 Avalanche Mechanism

The above described mechanisms, both the Dreicer 2.1.1 and the hot-tail 2.1.2 mechanisms, are commonly named *primary mechanism*, because they drive thermal (bulk) electrons into the runaway velocity region due to plasma conditions, creating what is called RE *seed*. However, the thermal electrons can also become REs through collisions with the already existing REs (so-called *knock-on collisions*), while the existing REs also stay in the runaway region. This mechanism is called *secondary* RE generation mechanism, or *avalanche* RE generation mechanism due to its exponential growth nature.

The mechanism was first theoretically investigated by Sokolov [25], while it drew more attention from scientists after the devastating prediction for ITER done by Rosenbluth *et al.* [26]. Rosenbluth assumed that transfer of RE kinetic energy to bulk electron is small and that REs are relativistic,

[4]The interested reader can consult Ref. [24] for more details

moving perfectly along the magnetic lines. Such calculation led to prediction that the post-disruptive RE beam in ITER could carry almost the whole pre-disruptive I_p, having energies of few tens of MeV. Later predictions done in the ITER Physics Basis [7, Section 3.4] were not so severe, but still a possible production of 10 MA RE beam was estimated. Anyway, the anticipated amount of kinetic and electromagnetic energy that REs would carry, in particular due to the avalanche effect, could be devastating for the ITER plasma facing components (PFC) - see 2.2.7.

For proper calculation of the effect of knock-on collisions a numerical tool is necessary [27], thus only an approximate condition for avalanche multiplication effect derived by Rosenbluth and Putvinski [28] is given here

$$\left(\frac{\mathrm{d}n_{RE}}{\mathrm{d}t}\right)_{ava} = \frac{I_p}{I_A \ln \Lambda}. \tag{2.7}$$

Note the linear dependence of the avalanche rate on the plasma current I_p, as the Alfvén current $I_A = 4\pi\varepsilon_0 m_0 c^3/e \approx 17.1\,\mathrm{kA}$ is a constant and the Coulomb logarithm $\ln \Lambda$ can be taken as a constant.

2.1.4 Critical Field

As mentioned at the beginning of Section 2.1.1 in Dreicer calculation, the plasma is considered to be non-relativistic. This results in an asymptotic decrease of F_{drag} towards zero as $\propto v^{-2}$, when the velocity goes to infinity. Consequently, a RE would be infinitely accelerated and would reach infinite velocity. However, it is well known in relativistic theory that the maximum velocity is the speed of light in vacuum c. Taking into account relativistic effects, Connor and Hastie [20] found a finite value F_{drag} acting on the electrons when v_e is approaching c. This value of F_{drag} corresponds to a certain value of the electric field, so-called "critical" electric field

$$E_{crit} = \frac{n_e e^3 \ln \Lambda}{4\pi\varepsilon_0^2 m_e c^2}. \tag{2.8}$$

Notice that the only difference between the expression for E_D and E_{crit} is that the electron thermal energy T_e [eV] in Eq. 2.3 is replaced by the electron rest mass $m_e c^2$ in Eq. 2.8. No RE can be generated with the mechanisms described above if $F_E = eE_{crit} < F_{drag}$, i.e. if the electric field in plasma is lower than E_{crit}. This relativistic effect threshold explains why large devices lack REs during high power plasma discharges.

2.1.5 Room for Improvement

Dreicer did not take into account neither the relativistic effect nor the influence of magnetic field. The former effect which was taken into account by Connor and Hastie is described in previous Section 2.1.4. However, even

though the presence of magnetic field is very common in plasma, a rigorous approach towards the integration of its effect on the RE generation population has not been done yet. Moreover, Dreicer assumed cylindrical plasmas, while tokamaks (and other fusion relevant devices) have toroidal geometry. In other words, the effect of the curvature has not been considered either. The toroidicity effect on the Dreicer and avalanche mechanisms was investigated by Nilsson [27], while the same author also characterised the so-called *trapped-electron runaways* [29] as an additional feature of the toroidal magnetic geometry.

In the experiments, the threshold electric field E_{crit} is found to be larger than the theory predicts [5]. There could be several reasons, including wrong data interpretation and/or improvement in theory and modelling. Regarding the latter reason, synchrotron radiation is a good candidate for theory improvement as the additional drag force (as the radiation loss can be interpreted like the drag force) for the ultra-relativistic electrons ($>10\,\mathrm{MeV}$) increases the total friction on the particle, increasing the E_{crit}. Additionally, the synchrotron radiation induced drag force leads to aggregation of REs in the velocity space. If the RE piling up is significant, RE distribution function gets a so-called *bump-like* shape. Moreover, one could expect that the bulk electron temperature T_e has some effect on the RE generation threshold, an effect which was shown by Stahl [30]. In addition, Boozer [15] found that the kinetic energy threshold W_{crit} and E_{crit} increases when the influence of the pitch angle scattering on the RE generation is considered. Boozer also concluded that the REs could drift out in the early stage of thermal quench if the plasma is highly non-axisymmetric, i.e. preventing the RE seed creation and the upcoming avalanche multiplication.

Additionally, Zhang [31] is developing a new algorithm to take into account the RE gyro-motion, as a generally applied gyro-center approximation overestimates the outward drift predicted by theory [32]. The reason for that can be explained as follow. The overestimation is more significant if the RE has larger perpendicular velocity, i.e. a larger gyro-radius. Due to the large gyro-radius, the RE is affected by the considerable curvature change in the tokamak magnetic field. Therefore the trajectory does not close up on itself after one gyro-period in the plane perpendicular to the magnetic field. In other words, RE trajectory is very deformed in comparison to the trajectory of the thermal electron.

Notice that the electric field is the main source of electron acceleration in all the above described RE seed creation mechanisms. Besides this, RE could be created via β-decay, cosmic radiation, Compton scattering, plasma instabilities and waves [15, 26], magnetic reconnection [33], etc., effects not readily taken into account.

[5] See Section 2.2.1 for more details about this experiments

2.1.6 RE Related Codes

Plasma is in principle an extremely difficult system to describe theoretically, due to the excessive number of particles, long distance forces and various dynamic processes having the time- and space-scale difference going up to 10 orders of magnitude. Additionally, the particle motion is affected by the electromagnetic field, that is changing due to the particle movement itself, making plasma a nonlinear system. Therefore, numerical calculations (i.e. computer simulations, models, codes) are used for understanding better the plasma behaviour. Here, a brief note about codes used for the RE analysis will be presented.

LUKE (Lower Upper solver for Kinetic Equation) is a numerical solver of a 3D relativistic bounce averaged drift kinetic equation [34], where the momentum space is characterised in 2D and only one spatial dimension is considered. LUKE is used for RE generation studies in the quasi-quiescent plasma (due to the lack of the time evolution) for various plasma scenarios. As it lacks time evolution, it is being coupled with the simple, but efficient time evolution code **METIS** (Multi-Element Tokamak-oriented Integrated Simulator) [35]. Moreover, LUKE is not specifically used for the RE studies, it is mostly used for modelling heating and current drive via waves in plasma.

Similarly to LUKE, another kinetic code often used for RE generation analysis is **CQL3D** (Collisional Quasi-Linear 3D) [36], which has the same three dimensional features like LUKE (2 velocity and 1 spatial dimension) and correspondingly it is not specifically used for the RE studies.

The code named **CODE** (COllisional Distribution of Electrons) is a 2D-momentum kinetic equation model [37], which is a simplified (no spatial dimension) and faster version of LUKE, made solely for the RE studies.

Nowadays, one more 2D-momentum kinetic equation model called **NORSE** (NOn-linear Relativistic Solver for Electrons) [38] is being developed for the RE studies. Its main purpose is to study low density and high electric field discharges, when usually a significant part of the current is driven by the REs.

The non-linear MHD code **JOREK** [39] taking into account the toroidal geometry. There is now an initiative by CEA Cadarache to implement REs into JOREK, which could bring interesting results on the MHD activities in between the bulk plasma and the RE beam. Particularly, particle tracking for the electron center orbits is being implemented [40].

ANTS (plasmA simulatioN with drifT and collisionS) [41] is a full - f[6] 3D Monte Carlo code that simulates plasma processes including drift motion and particle collisions. It is used for RE loss behaviour studies under magnetic perturbation influence. As it was developed to estimate the thermal loads on the W7-X walls, it is far from being RE-specific. To get the time evolution of the output, ANTS is often used in DIII-D tokamak

[6] *Full-f* means that the code follows a full distribution function and not just the deviation from a Maxwellian.

with **DINA** [42], a two-dimensional toroidal geometry code.

GO model [43] is a one-dimensional fluid model in cylindrical plasma. It is explicitly designed for understanding the RE generation during disruptions.

A zero-dimensional model for the tokamak disruption has been developed by Bozhenkov [44] at TEXTOR tokamak facility. It can be used for the time evolution of the global plasma and RE parameters during disruption.

The **SYRUP** code (SYnchrotron spectra from RUnaway Particles) estimates the synchrotron radiation spectrum of REs depending on diverse plasma and tokamak parameters [45]. It can use CODE as an input for RE distribution function.

The code **IMAGINE** [46] was developed to simulate gas penetration into plasmas recently and could be an useful tool for RE mitigation studies.

The main drawback of all the models mentioned above is that plasma and RE effects are not interlinked, i.e. coupled. On the other hand, implementation of RE-specific codes into a more general plasma codes present a possible task, albeit difficult and lengthy. Because of that, EUROfusion has recognised the importance of the RE modelling and granted an Enabling Research project on "Kinetic Modelling of Runaway Electron Dynamics" [7]. Notably, G. Papp is trying to connect various codes to obtain self-consistent RE modelling: LUKE and CODE, ANTS, GO, SYRUP, etc. - the details can be seen in the Ref. [47].

2.2 RE Experimental Observations

The Section will start with the experimental results that question the previously reported theories, namely the theory around E_{crit} reported in Section 2.1.4. Then, RE observations in different typical stages of the fusion plasma discharge will be presented. Mechanisms explaining RE losses are listed afterwards. Subsequently, estimates of the potential damage that REs could make to the ITER tokamak are reviewed. In the last part, the present RE mitigation scenarios are reported.

Note that experimental observations and results described here are from the literature, not from the COMPASS tokamak. As the focus of the present work is the fusion plasma, the corresponding RE results are presented. However, reader should be aware that REs exist in various non-fusion plasmas - as already mentioned in the Introduction of this Chapter.

2.2.1 Questioning the E_{crit} criteria

As already mentioned earlier in Section 2.1.5, higher values of the critical electric field E_{crit} have been observed in tokamak experiments compared

[7] Project number ER15-CEA-09.

to what the theory predicts. As higher E_{crit} values would have a positive consequence for ITER and fusion power plants, the International Tokamak Physics Activity (ITPA) recognised this issue as highly relevant and investigated it on few different tokamaks in the world [48]. The estimated discrepancy factor found between theoretical and experimental E_{crit} for Alcator C-mod and KSTAR is 4.5-5, for FTU it is around 8.5, while in DIII-D and TEXTOR it was measured that E_{crit} is 10-12 times larger than the theoretical one.

The discrepancy between theory and experiment could be because unambiguous data are not available when REs are too slow and/or too few, as all the detectors have some finite lower threshold of sensitivity. Consequently, Stahl did a detailed calculation [30] on necessary RE population to be detected. Stahl went even further and included T_e dependence for the detection threshold. In the same article, Stahl also questions the methods used by the ITPA Team in [48] from the theoretical point of view. Namely, he shows that observations of the apparent "RE fading" could be explained in terms of the RE re-location in the velocity space rather than RE number declining.

A more detail investigation of the E_{crit} was done in DIII-D [49]. The authors used "on-set" of the RE generation with pre-defined n_e-drop for upper E_{crit} boundary, as the on-set gives the highest density when RE generation is observed. Contrary to the on-set, "off-set" of the RE generation via an additional gas puff into the quiescent phase of the discharge to estimate the lowest n_e when the RE losses start to be dominant over the RE generation was performed. The lowest n_e gives accordingly the lower E_{crit} boundary. The CODE code[8] was also used for estimating the RE density n_{RE} when the experimental detection and the RE generation occurred. Even though the discrepancy factor using CODE is lower than are reported in the ITPA paper [48], the experimental E_{crit} is still larger than the theory - it is found to be 3-5 times larger.

Furthermore, a similar technique as in DIII-D is applied to FTU data to correct the experimental estimation of E_{crit} by Popovic *et al.* [50]. After including synchrotron radiation into the equation it is found that the distinction factor between the theory and the experiment is not so large as before, as a factor of 1.1-1.5 is reported. On the other hand, if synchrotron radiation was not included, the factor would be 1.6-5 - showing the importance of the synchrotron radiation for the RE force balance calculations.

In conclusion, all experiments show larger E_{crit} than the theory predicts independently of the method improvement. However, as method improves, the experimental E_{crit} value approaches the theoretical one. Moreover, as reported by Stahl, those experiments have methodological flaws: the basic principle and the RE detection challenges. Therefore, the experimental E_{crit} value is still an ongoing research/topic.

[8] See Section 2.1.6 for more details about CODE.

2.2.2 RE during the I_p Ramp-Up Phase

To create a plasma, first a free electron has to be created either spontaneously (e.g. cosmic radiation) or intentionally (e.g. electrode) and then accelerated. After obtaining enough energy, the free electon starts to kick-out more electrons from the surrounding atoms. The free electron population grows exponentially, creating an electron avalanche. It is called *plasma breakdown*.

A sufficiently strong electric field E is usually applied in tokamaks to accelerate the initial free electrons and to reach the breakdown. Just after the breakdown, the tokamak plasma has a low density n_e and relatively high toroidal electric field E_{tor}, which are favourable conditions for the RE generation. In tokamak plasmas, the so-called *current ramp-up* phase follows the breakdown, where (as it name says) the plasma current I_p rises to the value requested by operators.

E_{tor} is usually not measured directly in tokamaks, but it is rather derived from the toroidal loop voltage V_{loop} measurement that is measured by a dedicated magnetic coil along the torus. Knowing that E_{tor} can be estimated from the measurement of the loop voltage V_{loop} by

$$E_{tor} = \frac{V_{loop}}{2\pi R_0}, \tag{2.9}$$

one sees that for constant V_{loop} the E_{tor} decreases as the machine gets larger, i.e. for larger major radius R_0. Fortunately, the V_{loop} is more or less the same for all modern tokamaks, independently on the size. This is the main reason why large devices such as JET or TFTR do not have REs during the current ramp-up or during high-power discharge itself, but is not the case for smaller devices.

Before Rosenbluth and Putvinski [28] drew attention to the REs, they were considered as "exotic" population by theoreticians and unwanted effect by the operators. Operators in smaller devices developed various techniques to avoid REs during the discharge. Common techniques are a smooth increase of the n_e during the current ramp-up phase or a short but intensive "killer" gas puff. An interesting solution was implemented in the stellarator TJ-II, where a mechanical paddle is installed that sweeps through the plasma during the current ramp-up phase [51]. Moreover, a detailed study was done on DIII-D using *low-voltage* and/or electron cyclotron resonance heating (ECRH) assisted start-up of the plasma [52], that have reduced RE generation as one of the consequences.

The ramp-up phase is also a difficult phase of plasma discharge to study and model, because all the plasma parameters are changing fast with time and measurements are often very scarce or non-existing. Therefore, the RE studies in smaller devices are more challenging due to the uncertainties of the RE origin.

2.2.3 RE during the I_p Flat-Top Phase

After the current ramp-up phase a quiescent period comes, where I_p is more or less constant - so-called *current flat-top* phase. In contrast to the ramp-up phase, the current flat-top is desirable for RE modelers as the parameters do not change considerably. However, extension of these theoretical studies is questionable as the nature of the RE behaviour could be different between the flat-top and the disruption RE generation. In addition, note that only the latter case is ITER-relevant.

Anyway, REs do exist during the flat-top phase in small tokamaks, if the suppression in the ramp-up phase failed and/or the flat-top n_e is low enough. In the case of medium machines, REs are less probably generated even for a relatively low flat-top n_e, as the E_{tor} during the flat-top phase is usually too low. On the other hand, avalanche effect could produce a considerable RE population in medium tokamak, if there was a significant amount of RE seed from the ramp-up phase and if I_p is in the order of 1 MA [28].

In addition, a particular type of plasma discharge due to a significant RE population was observed, called *slide-away* regime [53]. This plasma regime is characterised by a low n_e and a significant RE population that carries a noticeable amount of I_p and hence decreases V_{loop}. Slide-away regime is usually denoted separately from the runaway regime due to the difference in the amount of the I_p carried by the RE (higher in the slide-away regime). Compared to the runaway regime, in the slide-away regime REs have lower energies (typically hundreds of keV), but are more numerous - enough to carry few tens of percent of the total I_p ending in a significant drop of plasma resistivity η_{res}. As an example, V_{loop} drops only about 2 times in the runaway regime, while in the slide-away regime V_{loop} can drop by an order of magnitude [54]. The consequence of the V_{loop}-drop is that plasma discharge can last longer and anomalous ion heating provides better energy confinement τ_E [55]. The latter consequence is crucial from the point of view of the fusion power, see Eq. 1.2. The main parameter of the slide-away regime is the streaming parameter ξ, which is defined as the ratio of the electron drift v_{dr} to the thermal $v_{th,e}$ velocity. The slide-away regime can occur when ξ is larger than 1. Furthermore, since ξ is proportional to B_{tor}/R_0, the regime was mostly observed in small tokamaks with high magnetic fields [8]. More recently, the slide-away regime is used for dedicated RE studies, e.g. in studies of RE-wave interaction [56] in KSTAR or observation of RE trapping [57] in HT-7.

2.2.4 Disruption and RE

Disruption is a sudden (and undesired) termination of the confined plasma, that can be split in two consecutive phases:

- The thermal Quench (TQ) phase, corresponding to a fast ($\sim 10^{-4}$ –

10^{-3} s) loss of the thermal energy;

- The current Quench (CQ) phase, corresponding to a slow ($\sim 10^{-3} - 1$ s) loss of the magnetic energy.

The generation of the RE seed during the TQ is enhanced due to the hot-tail mechanism (see 2.1.2). During the TQ, the fast drop of T_e leads to a drastic increase of the plasma resistivity $\eta_{res} \propto T_e^{-3/2}$, while the plasma current density $\vec{j}$ stays more or less constant as the CQ has a much longer time scale. Consequently, E_{tor}, being proportional to $\eta_{res}\, j$ (omitting inductance in the formula), will rise tremendously during the CQ, as η_{res} increases faster than j drops due to the inductance. The increase of the field will accelerate RE seed generated during the TQ, which will then be multiplied enormously by the avalanche effect - the avalanche multiplication factor for ITER disruption could be as large as 10^{22} [7, Table 5]. These REs form a beam that is confined and accelerated. Eventually the beam can be lost to the first wall of the tokamak. This is the reason why REs are a major concern for the ITER community.

Only large tokamaks (e.g. JET, TFTR, JT-60U, Tore Supra) generate the RE beam spontaneously during disruption, since a high enough I_p is required to induce a sufficient E_{tor}. However, the toroidal magnetic field B_{tor} is observed to be an additional important parameter for the post-disruptive RE generation (remember that B-field is not included in the present theory - see 2.1.5). It was first noticed on Tore Supra that no REs are created during disruptions if $B_{tor} \leq 2$ T [58] and similar results have been observed later in JT-60U [59] and JET [60]. Also in DIII-D the RE beam was not observed, as its maximum $B_{tor} = 2.2$ T is around the observed limit. On the other hand, evidence of spontaneous RE beam generation for $B_{tor} = 1.3$ T is observed in KSTAR [61]. However, their examination of the B_{tor} limit explanation using whistler wave instability [62] lacks a post-disruptive T_e measurements. Additionally, no RE beam was observed for B_{tor} in between 1.4 and 1.9 T.

Nevertheless, the disruptions triggered with injection of noble elements in gaseous or solid state could lead to post-disruptive RE beam even if B_{tor} is lower than 2 T. The first corresponding experiments were performed in JT-60U by Yoshino *et al.* [59] where the initial goal was RE mitigation, but the experiments showed that Massive Gas Injection (MGI)[9] or pellet injection[10] system could create the RE beam. These techniques were then tested for producing RE beam with $B_{tor} < 2$ T in DIII-D [63] and Tore Supra [64] successfully. Recently, similar results were achieved in COMPASS (in the

[9] An injection of gas that has much more particles than the plasma (i.e. the injected gas is more massive than the plasma) is called Massive Gas Injection - MGI. The injected gas is usually a noble gas.

[10] Pellet injection represents a firing of frozen/solid material into the plasma with relatively high velocities - on the order of km/s. Beside noble gas, the hydrogen isotope can also be used.

framework of this Thesis)[11], AUG and TCV [65]. Moreover, a detailed study of the B_{tor}-limit for generation of REs as a function of the amount of Ar gas injected was performed recently in JET [66], where post-disruptive REs were observed even for $B_{tor} = 1.0\,\mathrm{T}$. One of the possible explanations for the RE generation after usage of MGI could be due to the suppression of Alfvén instabilities [67] that usually occur in the post-disruptive plasma with lower B_{tor}. Another possibility is that the high-Z environment is more prone to produce positron, as the cross-section for positron production increases with Z^2 [68, Eq.(1)]. As electron and positron from pair production have energies over the rest electron/positron mass, both of them are intrinsically in runaway velocity region from their creation. Therefore, high-Z background plasma could lead to enhanced runaway current.

2.2.5 RE Losses

So far, solely RE generation mechanisms and their occurrence during discharges have been discussed, while in this Section an overview of the RE losses is given. The RE confinement being not fully understood, there is a lack in understanding the RE losses and thus only wide accepted and experimentally confirmed loss mechanisms will be addressed here. The particle losses are reported first, and then RE radiation losses are explained.

Particle Losses

Due to the significant acceleration of the RE beam, the centrifugal force can be large enough to shift the RE beam axis more outwards with respect to the plasma axis [69]. Consequently, REs with enough energy will drift radially outwards, which limits the maximum RE kinetic energy [70, Eq.(2.19)]

$$W_{max} = ecB_{tor}\frac{a_p}{q_a}, \tag{2.10}$$

where a_p is the plasma minor radius and q_a the safety factor at the a_p position. As for many systems, diffusion transport of REs can also contribute to the losses [71, 72]. An other RE loss mechanism arises from the imperfections of the toroidal magnetic field, i.e. magnetic ripple, that can also de-confine REs [73, 74], leading to an additional limitation of the maximum RE kinetic energy [75]:

$$W_{max} = ecB_{tor}\frac{R_0}{n_{mr}N_{tc}} \tag{2.11}$$

where N_{coil} is the number of toroidal coils, while n_{mr} is the resonance harmonic of the magnetic ripple. Moreover, the stochasticity of the magnetic field can also enhance the RE losses [76].

[11] See Chapter 7 for more details

It has been suggested that some plasma instabilities can de-confine REs, e.g. magneto-sonic-whistler waves [77]. Furthermore, an anomalous Doppler resonance instability (also called *Parail-Pogutse instability*) is a specific feature of the REs [78]. It occurs when a RE tail of the electron distribution function has the positive gradient in the velocity space. Finally, observation of influence of the MHD modes on the REs was reported [79] recently in the DIII-D tokamak.

Radiation Losses

Beside particle loss from the plasma, REs can loose energy through radiation due to their acceleration [80]. Additionally, if the radiation power is comparable to the power gained from the accelerating electric field, it introduces an additional drag force on the RE (i.e. power loss).

The typical radiation of megaelectronvolt REs is the synchrotron radiation. As the magnetic field is an intrinsic feature of the tokamak, the RE gyrates around the magnetic field line and emits synchrotron radiation[12]. The power loss coming from the synchrotron radiation is expressed as [81]:

$$P_{synch} = \frac{2 r_e m_e c^3 \beta^4 \gamma^4}{3 R_c^2}, \tag{2.12}$$

where $r_e = e^2/(4\pi\varepsilon_0 m_e c^2)$ is the classical electron radius, $\gamma = (1-\beta^2)^{-1/2}$ is the relativistic Lorentz factor, $\beta = v_e/c$ is the electron velocity normalised to the speed of light in vacuum and R_c is the curvature radius of the RE trajectory. If the RE is found near a charged ion, it can also emit bremsstrahlung [82]

$$P_{brems} = \frac{4}{137} n_e (Z_{eff}+1) r_e^2 m_e c^3 \beta\gamma (\ln 2\gamma - 1/3). \tag{2.13}$$

In this reference, Bakhtiari *et al.* showed how the bremsstrahlung power loss could be highly relevant for the MGI experiments, especially in small/medium machines with lower B_{tor} (e.g. the COMPASS tokamak).

2.2.6 Potential Damage

Quantitative estimates of the potential damage of REs on ITER first wall are presented here. As an illustration, Fig. 2.2 shows the consequence of JET regular campaigns during which the PFC material was damaged.

REs did not make any substantial damage in early stage tokamaks due to low currents and moderate energies carried by the beam, as well as the usage of a relatively robust PFC material. However, as fusion devices become larger, with higher I_p and with more sophisticated PFC, RE damages can become nowadays more and more significant, as theory predicts (see

[12] See Sections 2.3.4 and 2.3.5 for more details about the synchrotron radiation.

Figure 2.2: Re-deposited molten beryllium at JET ITER-like first wall due to the RE impacts. The picture is copied from Ref. [83].

Section 2.1). The main challenge in predicting the potential RE damage is to correctly estimate the conversion of magnetic to kinetic energy [84].

REs are presently set as the second highest priority for the ITER disruption mitigation system [85], just after the slowing down of the CQ in order to prevent mechanical damage to the blanket modules. This high priority in RE mitigation follows from the nature of their impact - (1) a very localised wetting area, (2) a very short time (few milliseconds), and (3) a deeper penetration length than any other transient event.

For the same energy deposition, an estimated RE damage to the PFC will be lower than from plasma or observed transient event heat loads for C and Be. This higher PFC tolerance on RE damage is because plasma and transient events will be deposited on the surface, while RE could penetrate deeper in to material and RE energy would be deposited on larger volume. The depth of the RE penetration for C and Be is estimated to be 2.0 mm and 2.5 mm, respectively [86]. On the other hand, as already mention above, the main issue is how much energy of RE beam will deposited on the PFC. The deposited RE energy could be significantly higher than the transient heat loads. Furthermore, the deeper RE penetration in to materials like C and Be[13] with RE energies well above the melting limit could be a problem for the cooling structures.

2.2.7 On the Mitigation of REs

This Section is an overview of the different RE suppression/mitigation techniques. In general, it is estimated that ITER walls could sustain a RE beam up to $I_{RE} = 2\,\mathrm{MA}$ [84,85] or $I_{RE} = 3\,\mathrm{MA}$ [15] - thus suppression/mitigation systems should make sure that the RE beam has a lower current before it is

[13] N.B. not the case for W.

deposited on the ITER first wall. In the energy units, the RE beam should have less than 4 MJ so that no melting occurs even during the fast beam terminations [84]. Due to the highly limited accessibility to the plasma and vulnerability of the first-wall in ITER, the mitigation scheme choice has been narrowed down to two main options: 1) impurity injection and/or 2) magnetic coil ramps [85].

The first way to mitigate RE is to decrease the RE generation rate by increasing n_e and thus increasing E_{crit} and E_D, which is done either via MGI or pellet injection. However, as it was mentioned earlier in Section 2.2.4, both techniques can have the side effect of generating the RE beam following the disruption. Indeed, this happens with the injection as disruption mitigation system which is triggered before the TQ. Then additionally, one can introduce the second MGI or pellet for the RE mitigation purpose. Reux *et al.* [87] found that the timing of the second injection is decisive - if it is too close to the TQ, no effect will be observed (at large machines, e.g. JET). An additional issue with MGI is the amount of injected gas: if there is too little gas there is again no effect on the RE beam; while too much gas can be heated near the valve and result in Be melting. Moreover, most of the conducted experiments had localized injections, while there are speculations that more symmetric injections would be more beneficial.

Recent investigations also show how penetration of the gas towards the magnetic axis could be too slow to stop the RE generation, as majority of the REs is generated around the magnetic axis. Therefore, pellet injection seems to be a better solution for the RE mitigation, since they can reach the magnetic axis faster. On the other hand, the MGI allows a better toroidal expansion of the injected gas compared to pellet injection. Furthermore, the amount of gas needed for complete RE generation suppression in ITER is three order of magnitude larger than the ITER plasma number of particles[14]. The injection of 10^{26} particles [86] during a very short time (order of milliseconds) is a rather challenging technological task. This amount of injected gas could have a weighty effect on the ITER vacuum system and machine in-vessel conditions. Moreover, pure Ar or Ne are more prone to the RE beam formation. Correspondingly, experiments with mixtures of high-Z atoms with D_2 were performed [87, 88] with significant, but not perfect improvements. The mixture experiments are probably more efficient due to two effects: (1) deuterium has higher penetration speed than of Ar/Ne that increases core n_e fast enough and (2) it also has low radiation efficiency that outcomes in the slower CQ than with Ar/Ne injections.

The TQ should be slowed down or prolonged to suppress the hot-tail mechanism[15] creating critical RE seed. A way to slow down the TQ is to inject impurities in the proper mixture. Slowing down the TQ would also allow the injected gas to reach the magnetic axis and to expand toroidally,

[14]Number of particles in ITER plasma: $N_{ITER} \approx n_e V_{ITER} = 10^{20}\,\mathrm{m}^{-3} \times 800\,\mathrm{m}^3 \sim 10^{23}$ particles.

[15]See Section 2.1.2 for more details about the hot-tail mechanism.

thus increasing the efficiency of RE mitigation and suppression. Therefore, this technique has been proposed as a preventive tool for the RE seed mitigation. The plasma cooling time scale during the TQ for ITER should be larger than 80 ms according to Smith [23] or 40 ms according to Boozer [15] to prevent the RE seed formation. To illustrate difficulty of achieving such a long TQ phase, notice that times reported by Smith and Boozer are larger by approximately an order of magnitude than the ones reported in ITER Physics Basis [7, Table 5]. Moreover, in the same Table one can find that a minimum predicted CQ duration in ITER is around 35 ms. As the CQ is typically longer than the TQ and that too long CQ generates halo-currents[16] [7, Section 3.3.2.], an optimisation has to be done - a long enough TQ for RE suppression and a short enough CQ to avoid halo-currents.

De-confinement of REs due to a stochastic magnetic field induced by magnetic perturbations before they become accelerated present another RE mitigation method. Those perturbations are usually called Resonant Magnetic Perturbations (RMP) and they are induced by RMP coils. Three machines, DIII-D, JT-60 and TEXTOR [85], have shown effects of perturbations on RE confinement. DIII-D used perturbations with a toroidal mode number $n = 1$, while JT-60 and TEXTOR used 2 and 3, respectively. On the other hand, experiments in JET did not show any clear effect. However, JET results should be taken with care, as simulations showed that JET does not have adequate RMP coils for RE mitigation. Furthermore, codes - DINA and ANTS[17] - showed that the penetration of the magnetic perturbations towards the magnetic axis in ITER could be too slow, i.e. only the plasma edge would be affected. Simulations also predict that intentional field perturbations could enhance toroidal localisation of the RE heat loads on the first wall, increasing the risk of damaging PFC in ITER.

Additionally, as mentioned in Section 2.2.3, RE can be affected by electromagnetic waves and several devices have shown their RE mitigation potential. Besides the already mentioned KSTAR case [56] where ECRH is used for this purpose, the ENEA Fusion Division in Frascati (Italy) has long term experience regarding the RE mitigation by waves. They first demonstrated that the RE mitigation was possible using lower hybrid waves on the FT tokamak [89] and later using ECRH [90] on the FTU tokamak.

Moreover, controlling the vertical position of the RE beam will be a challenge in ITER. The coil system design should be able to control a beam that carries at least 10 MA [85, 91]. The Frascati team is now developing a direct control system of the RE beam location via real-time feedback as proposed by Boncagni [92] and the implementation was recently reported by Carnevale [93].

[16] The current occurring during the disruption with unstable plasma position that could go through the surrounding material and cause a deformation of the tokamak chamber.
[17] See Section 2.1.6 for more details about the codes.

2.3 RE Related Diagnostics

Diagnostics are essential tools for merging experiment and theory. In this Section an overview of applied and potential RE diagnostics is presented. The overview starts with passive photon detections, continues with active photon detections and finishes with magnetic diagnostics.

2.3.1 Soft X-Ray Diagnostics

X-ray is a common name for photons with energies lying between 100 eV and few MeV. In general, the X-ray photons origin from accelerated electrons, either free ones or bounded ones. Due to technical reasons and different applications, X-ray spectra is divided into two parts: Soft X-Ray (SXR) up to approximately 10 keV and Hard X-Ray (HXR) above 10 keV. SXR as RE diagnostics is the subject of this Section, while next Section 2.3.2 explains how HXR radiation is used for the RE analysis.

In tokamak plasma SXR radiation originates from bremsstrahlung, radiation coming from a free decelerated electron moving in the field of an ion. The SXR radiation is usually measured with the few set of detectors that allow for tomographic reconstruction. SXR tomography is routinely used for diagnosing fusion plasmas via observation of the core plasma activities. In JET, SXR were used to observe location of the RE beam generation [94] in the plasma core, which appears to agree with modelling [27]. Another source of bremsstrahlung in the SXR spectrum could occur if the lost REs hit the tokamak wall.

As the bremsstrahlung radiation power spectrum increases with the square of the ion atomic number $\propto Z^2$ [80], this diagnostic could have high potential for RE studies when high-Z gas is introduced during the disruption. However, decrease of temperature T_e and low collisionality reduce the radiated power under the sensitivity threshold. Moreover, various generated waves during the disruption often lead to detector saturation. Therefore, dedicated SXR detectors should be designed and installed for disruption and RE studies.

2.3.2 Hard X-Ray and γ-Ray Diagnostics

When a RE loses its confinement, it is stopped by the first wall of the fusion device. With RE energy higher than few tens of keV, the bremsstrahlung from material is usually in the HXR spectra. Moreover, if the RE hitting the wall delivers energy higher than MeV it can excite a nucleus from the wall atoms, which can then emit γ radiation. Differently from X-ray, γ-ray photon originates from the nuclei of an atom or an ion, which typically carries more than 1 MeV of energy. In practice, there is no strict transition line between HXR and γ radiation. In another words, photons can have the same energy, but different generation history. Therefore, detectors operating

in the overlapping region of spectra ($0.1-5\,\mathrm{MeV}$) could detect photons from both HXR and γ radiation, depending on their sensitivity.

Classical nuclear detectors, e.g. scintillators, have been used from the beginning of fusion research as HXR detectors for characterisation of the RE loss [8]. These initial measurements were made with detectors placed outside the facility. Further development led to more localised measurements with collimated detectors looking inside the vacuum vessel [95] or even with a potential for tomography reconstructions [96, 97]. Recently, a HXR tomography of fast electron bremsstrahlung (FEB) was developed at JET for the in-flight localisation of the REs, which also allows estimating the evolution of the RE energy spectra [98].

More sophisticated tools exist for γ-ray detection, such as the γ spectrometer developed on TFTR [99]. This gives important information about the RE tail energy spectrum [100].

2.3.3 Photoneutrons and γ-Ray Diagnostics

A γ-photon can undergo an interaction with an atom's nucleus in the wall leading to the emission of a neutron. As the neutron is emitted by a highly energetic photon it is named *photoneutron*. Consequently, common nuclear detectors for neutron detection can be used for the RE studies. However, neutrons coming from the fusion reactions also have to be considered (see Eq. 1.1), which can make both (fusion and RE) neutron production analysis more challenging.

In addition, detectors can be sensitive to both neutrons and γ radiations. In that case, it is important to distinguish them. For example, at FTU two ways of distinguishing neutrons and γ-rays are used. First, a BF_3 counter, sensitive solely to the neutrons is used, while liquid NE213 scintillator is used for both neutron and γ-ray detection [101]. Subtraction between those two signals corresponds to γ radiation due to REs. Second, a neutron camera that separates neutrons and γ-rays according to the shape of the detected pulse is used [95].

2.3.4 Electron Cyclotron Emission Diagnostics

Due to the magnetic part of the Lorentz force $-e\vec{v}\times\vec{B}$, electrons gyrate periodically around the magnetic field lines in such way that their trajectories close themselves in the plane perpendicular to $\vec{B}$. This kind of motion is called gyro-motion, gyration or cyclotron motion, as it was firstly observed in particle accelerators of the cyclotron type. Therefore, radiation coming from the gyrating particle is named *cyclotron emission*. In fusion plasmas, the Electron Cyclotron Emission (ECE) detection can be used to measure the electron temperature T_e at various plasma locations. Furthermore, ECE from tokamak plasmas lies in the microwave range, so the

modified industrial/off-the-shelf technology of microwave antennas can be used for ECE detection.

As the electron gyration is periodic, the emitted spectrum in homogeneous plasma is discrete with frequency ω_l depending on the fundamental frequency $\Omega = eB/m_e$ and the harmonic number l

$$\omega_l = \frac{l\Omega}{\gamma(1 - \beta_{\parallel} N_r \cos\alpha)} \tag{2.14}$$

where N_r is the refractive index of the plasma at the electron location and α is the angle between the magnetic field B and the observation line. The relativistic effects are negligible for thermal fusion plasmas and most of the irradiated power is contained in the first few harmonics. However, the first harmonic often cannot be used as most of the base frequency ($l = 1$) is reabsorbed in the fusion plasma.

RE detection via ECE diagnostic technique was reported in a few fusion devices, including the WEGA Stellarator [102], FT-1 and DIII-D tokamaks [103]. RE parameters such as threshold energy for RE creation, pitch angle $\theta = \angle(\vec{B}, \vec{v})$, number of REs, exponential decay of RE distribution function and RE population location were estimated. However, the estimates were done with limiting assumptions, because main cyclotron theory was developed for bulk (few keV), supra-thermal (few tens of keV) and relativistic (few MeV) electrons. The difficulty is the fact that relativistic downshift (contribution of γ in Eq. 2.14) of the observed frequency allows overlapping of several harmonics. Nonetheless, the ECE has a strong potential as one could (in theory) derive the shape of the RE distribution function for wide range of RE energies[18]. Therefore, ECE as RE diagnostic tool presents a good potential for a future research.

2.3.5 Synchrotron Radiation Diagnostics

As RE becomes very energetic, i.e. $W_{RE} \gtrsim m_e c^2$, the cyclotron power described above starts to be emitted from higher harmonics and the power spectrum tends to be continuous. In fact, the cyclotron radiation of ultra-relativistic particles at high harmonics is called *synchrotron radiation*, as it was firstly observed in accelerators of the synchrotron type. Note that the names are usually distinct in the literature due to historical reasons. Moreover, theoretical analysis of synchrotron radiation has to include relativistic effects making the calculation different from cyclotron emission. The synchrotron radiation is not isotropic, being emitted preferentially in the direction parallel to the RE velocity - the so-called *headlight effect*. Due to the headlight effect, synchrotron radiation has to be observed particularly with a counter-current tangential view.

[18] Section A.1 has more detailed elaboration on the potential of ECE as RE diagnostics.

Firstly observed in fusion plasma by Finken in the TEXTOR tokamak [104], the synchrotron radiation generated by REs in tokamaks has a continuous spectrum and usually its peak intensity lies from the near-infrared to the mid-infrared region ($0.75 - 10\,\mu m$) [105]:

$$\lambda_{peak} \approx \frac{8\pi}{15} \frac{R_0}{\gamma^3 \sqrt{1+\eta^2}} \tag{2.15}$$

where $\eta = \Omega R_0 v_\perp / \gamma v_\parallel^2$ and λ_{peak} represents the wavelength at which the synchrotron radiation is at the maximum power.

A detailed analysis of the first measurements in TEXTOR was performed by Jaspers in his Ph.D. Thesis [70], while a comprehensive theory and modelling development was recently done by Stahl [45]. Experimentally, a 2D camera in the infrared (IR) or in the visible spectrum can be used for measurements of the position, pitch angle, $v_\perp$ [81] of REs, while an IR or a visible spectrometer is more suitable for the energy, RE intensity, and transfer rate estimates [63, 81].

2.3.6 Incoherent Thomson Scattering

Incoherent Thomson scattering (ITS) denotes scattering of a photon on an electron at scale much smaller than the Debye length[19], where the photon energy is much smaller than the electron's one $h\nu < m_e c^2$. The ITS diagnostic technique is widely used in diverse plasma devices (i.e. not only for fusion plasma) for measurements of T_e and n_e profiles. Even though it is an active diagnostic probe, as high-power laser is injected in plasma, the technique itself is considered as non-perturbative and localised, making it attractive for diagnosing fusion plasmas.

However, even though there was no dedicated attempt to diagnose the high energy REs via ITS in practice, at MIT Pieroni and Segre [106] detected low energy REs using this technique. However, theoretically it should be possible to estimate a larger part of the RE distribution function with this diagnostic technique. The main complication to this purpose is that ITS already requires very high power lasers due to the low n_e in tokamaks and the low scattering cross-section. As the RE density n_{RE} is by orders of magnitude lower than the plasma density n_e, it would require even more powerful laser to observe REs with this diagnostics. Besides, as RE energy increases, the ITS cross-section decreases, requiring yet even more powerful laser. Furthermore, *final transit time effect* [107, Section 4.4] assumes the constant electron population in the observed volume during the measurement, and this assumption could be inapplicable for the measurements of the REs with ITS.

Nevertheless, if the proper choice of detector and observation geometry is made, RE could be observed in principle by ITS[20]. Namely, scattered

[19] The Debye length is usually approximated as $\lambda_D^2 = \varepsilon_0 k_B T_e / n_e e^2$.

[20] Section A.2 has more detailed elaboration on the potential of ITS as RE diagnostics.

photons in the tangential direction could have significant contribution from the RE population due to the head-light effect. Finally, RE measurements do not need to be done with sophisticated equipment usually used for ITS measurements, as the spectrum range and spectral resolution can be broad. Detector could be made of sensitive enough visible/UV light spectrometer - the background would be challenging, as the ITS is not the only source of light in this range.

2.3.7 Cherenkov Probe

The Cherenkov radiation occurs when a charged particle moves through a media with a higher velocity than the speed of light in that media. As the REs are reaching relativistic velocities, a novel active diagnostic technique is under development in NCBJ Otwock (Poland) [108] based on the Cherenkov effect. Cherenkov detector uses typically diamond or aluminum nitride as a sensitive layer, which is inside a light-protected measuring head (probe) localised close to the edge or scrape-off-layer (SOL) of the plasma. The time evolution of the Cherenkov radiation intensity related to the RE population can then be measured.

In practice, the Cherenkov radiation is integrated over a wide range of energies (above several tens of keV). Furthermore, tokamaks CASTOR [109], ISTTOK [110] and Tore Supra [111] used a similar setup. The measurements primarily provided information on the presence of REs, rather than their number and energy, which made it more a qualitative than a quantitative tool. However, it allowed for localised and prompt measurement of the RE losses in the SOL. When the detector is equipped with more channels with entrance windows of different thicknesses, different energy ranges can be inferred [112].

2.3.8 Magnetic Diagnostics

Magnetic detection coils are a fundamental diagnostic method in fusion research facilities. It is used for real-time control of plasma position and shape, as well as for various other measurements (e.g. plasma current, loop voltage, plasma diamagnetic energy, etc.) while it is typically not considered for RE observations. Anyhow, apart from the bulk plasma, the RE beam/population is an independent conductive media/fluid, so it influences the magnetic diagnostics independently.

The most important magnetic RE measurement consists in estimating the E_{tor}, as it is the main parameter for the RE generation. A proper estimation of the E_{tor} in the tokamak is far more complicated than Eq. 2.9 as explained in the Ref. [113]. A good knowledge of the E_{tor} is also necessary for estimation of the maximum kinetic energy W_{max} that RE can achieve during the discharge. If no losses and $v_{RE} \approx c$ are assumed, W_{max} is directly

proportional to the history of the E_{tor}:

$$W_{max} = ec \int_0^t E_{tor} \mathrm{d}t. \tag{2.16}$$

In addition, a Parail-Pogutse instability (see 2.2.5) is sometimes detected with negative V_{loop} spikes, like in TFTR [100]. The slide-away regime (see 2.2.3) is indicated by a level of V_{loop} significantly below a value expected for a thermal (Maxwellian) distribution of particle energies. If the RE beam carries enough current it produces a larger shift of the magnetic axis than predicted by the Shafranov shift [114]. Consequently, a set of poloidally distributed pick-up coils could detect the location of a RE beam in the presence of the plasma. Besides, magnetic diagnostics play a crucial role in studies of the MHD effects on the REs [79, 115].

Moreover, magnetic diagnostics combined with the position control poloidal field coils should in principle be able to stabilise and slow down de-confinement of the RE beam. The basic idea is to implement the betatron equilibrium condition equation [116, Chapter 11]

$$B(R_0) = \frac{\Delta\Phi}{2\pi R_0} \tag{2.17}$$

in the real-time control of the magnetic field B in the fusion device depending on the flux change $\Delta\Phi$. However, this task is far from trivial due to the fast changes in the plasma current and RE beam location during the disruption. Dedicated efforts have been focused to this subject on the FTU tokamak [92, 93].

2.4 Overview

REs are relativistic electrons accelerated to velocity v_{RE} close to the light speed c due to low plasma collisionality and electric field that can arise in fusion devices. Large amount of REs can drag tens percent of the plasma current forming a so-called RE beam. Importantly, after a disruption in ITER, a RE beam carrying a significant amount of pre-disruptive current could be formed. It could severely damage ITER first wall and the cooling pipes behind the first wall. Consequently, the RE damage could lead to unplanned shutdowns and high maintenance costs. Therefore, mitigation of RE beams is considered as the second highest priority for the ITER disruption mitigation.

Robust predictions of the RE beam generation are necessary for the development of a realistic and reliable RE mitigation scheme. Unfortunately, the predictions of RE beam generation with subsequent RE damage in ITER have large uncertainties as a consequence of the scarce experimental database and difficulties in describing theories or modelling the experiments. The predictive ability could be significantly improved with diagnostic tools

dedicated to disruption studies, as the majority of the common diagnostics is saturated and/or affected by the strong noise background from HXR radiation. The disruption dedicated diagnostics should have a substantial shielding, a lower sensitivity and better time resolution than the rest of the usually used diagnostics. Besides measuring important plasma parameters during the disruption, the RE parameters should also be measured/estimated. In addition, some phenomenon (e.g. the MGI RE mitigation) cannot be scaled from medium to large facilities.

Aforementioned solution for a proper development of the RE mitigation scheme requires a significant amount of resources and time. Nonetheless, the potential RE damage of ITER wall and ITER delays could cost much more than the proposed studies on smaller devices. For that reason, a larger effort should be made in diagnosing, understanding and controlling the REs.

Chapter 3

Review of Runaway Electron Studies in the COMPASS Tokamak

The present Chapter presents an overview of the dedicated RE studies in the COMPASS tokamak that started in spring 2014 under EUROfusion funding[1]. The project is strongly connected to the framework of this Thesis, as the author participated in the diagnostic installations, managing the experiments, analysing data and in actively participating in result presentations.

Moreover, four experimental RE campaigns as part of the MST2 RE project showed that COMPASS is suitable for runaway models validation and scaling towards ITER. The successful experiments and obtained results brought COMPASS RE studies in the framework of the EUROfusion MST1 RE project that represents broad European collaboration towards direct ITER-relevant studies. In addition, RE studies became one of the main focuses of the COMPASS facility. Note that the doctoral student also participated in the first MST1 RE campaign in COMPASS (fifth RE campaign in total). Although its detailed summary is not done here, the relevant results will be mentioned and highlighted in this Chapter.

The Chapter will start with a description of the COMPASS tokamak. Then, a brief overview of the first four RE campaigns (i.e. MST2 campaigns) is given. The Chapter continues with the diagnostic tools and additional experimental setup used during the RE campaigns. The following Sections will cover the influence of the plasma density n_e, loop voltage V_{loop}, plasma current I_p, MHD modes and instabilities, position and shaping, RMP and Ar/Ne gases on the RE population in COMPASS plasmas. The final part of the Chapter will outline the commonly used RE codes, where some of

[1]The project was part of the EUROfusion MST2 project WP14-MST2-9, as supported by the EUROfusion MST projects.

them are utilised for this Thesis.

3.1 The COMPASS Tokamak

The COMPASS tokamak [117] was first operating in the Culham UKAEA center from 1989 to 2002. Afterwards, it was transferred in 2004 to the IPP Prague and the first plasma was achieved in 2008. From 2012, the COMPASS tokamak is in full scientific operation contributing to ITER relevant scientific and engineering issues.

The COMPASS tokamak is a compact experimental fusion facility with a major radius $R_0 = 0.56\,\mathrm{m}$ and a minor radius $a_p = 0.2\,\mathrm{m}$. The toroidal magnetic field B_{tor} is in the $0.9 - 2.1\,\mathrm{T}$ range (typically set to $1.15\,\mathrm{T}$), coming from 16 toroidal field (TF) coils depicted in Fig. 3.1. The plasma current I_p can reach up to $400\,\mathrm{kA}$ using an air transformer. The range for the electron densities is flexible and is typically in the $10^{19} - 10^{20}\,\mathrm{m}^{-3}$ domain. Plasma shaping varies from circular and elliptical to single-null D-shaped ITER-like plasmas. When circular, the plasma is limited by a carbon HFS wall. The regular pulse length is $\sim 0.4\,\mathrm{s}$, although low current circular discharges with RE can last almost $1\,\mathrm{s}$ [118].

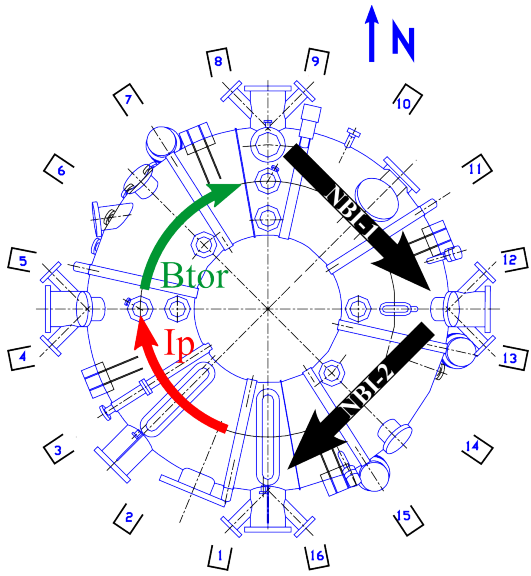

Figure 3.1: Top view of the COMPASS tokamak showing the typical orientations of the plasma current $\vec{I}_p$, the toroidal magnetic field $\vec{B}_{tor}$ and the neutral beam injections NBI-1 and NBI-2. The north direction is also marked for orientation purposes.

The tokamak vacuum vessel is split in 16 sectors, i.e. in between each pair of TF coils. For example, sector 2/3 means the sector between TF coils 2 and 3 (see Fig. 3.1). Another orientation nomenclature uses cardinal direction, where sector 8/9 represents the north direction, also labeled in Fig. 3.1.

The COMPASS tokamak is equipped with 55 radial and 9 tangential ports. Radial ports can be divided in five groups:

- 9 horizontal (H) or mid-plane ports with 4 large ports on each cardinal

direction (sectors 1/16, 4/5, 8/9 and 12/13),

- 10 vertical upper (VU) ports,
- 10 vertical lower (VL) ports,
- 8 angular upper (AU) ports and
- 18 angular lower (AL) ports.

8 horizontal tangential (HT) ports are located in pairs around each of the 4 large horizontal port. In addition, 1 angular upper tangential (AUT) port is located in sector 5/6.

The vacuum pressure in the tokamak vessel is usually about 10^{-6} Pa before the discharge. A glow discharge is done between the tokamak discharges for better reproducibility and wall conditioning. Usually glow discharge is typically done in helium, but the gas can be varied on request. In addition, boronisation can be done on request, for better wall conditioning and consequently better n_e control.

Due to the relatively short plasma discharge, the data acquisition (called DAQ) system should have appropriate time resolution. The majority of the main signals (magnetic diagnostics, interferometer, etc.) are sampled with 0.5 μs (2 MHz) time resolution, while feedback-relevant data is re-sampled to 50 μs (20 kHz) time resolution for faster calculation. Other diagnostics have specific time resolution, which will be mentioned when (and if) the data are presented. Additionally, the EFIT equilibrium reconstruction [119] is used for obtaining the magnetic topology of the COMPASS plasma after the discharge. The typical time step of EFIT calculation is 1 ms, but it can be recalculated with higher sampling rate. Time-zero for all data acquisition systems is taken as the start of the charging of the main power supplies. With such timing, typical discharge (i.e. beginning of the plasma formation) in COMPASS starts at around $955 - 960$ ms.

On COMPASS, auxiliary heating and current drive can be obtained with two neutral beam injectors (NBIs). Each NBI can inject a 40 keV neutral deuterium or hydrogen beam that carries up to 350 kW. Presently, both NBIs are directed in the same direction (see Fig. 3.1), with possibility of doing co- and counter-injection depending on I_p direction. Beside, future plans should allow NBIs to be operated in balanced injection mode.

The main scientific focus of COMPASS is oriented towards SOL and H-mode studies in ITER-shaping plasma discharges. SOL studies are realised by extensive variety of electrostatic probes and magnetic coils. The COMPASS tokamak can have Ohmic and NBI-assisted ELMy H-mode, which is foreseen as the reference ITER plasma discharge scenario for achieving $Q = 10$ for 400 ms [120]. However, those two studies are not the only fusion-oriented research conducted on COMPASS. For example, flexibility of various plasma parameters (e.g. shaping, densities, plasma current, etc.)

combined with significant, but still safe, runaway population make COMPASS suitable for runaway models validation and scaling towards ITER.

3.2 RE Campaigns Overview

The RE campaigns in COMPASS tokamak during 2014-2015 were conducted as part of the MST2 Project by EUROfusion as already mentioned in the introduction. There were four experimental campaigns, each being separated by about half year. The main summary is given in Table 3.1.

Campaign:	1st	2nd	3rd	4th	**TOTAL**
Dates	*May 2014*	*November 2014*	*April 2015*	*October 2015*	
Total Discharges	124	137	265	174	**700**
First Discharge	#7278	#8548	#9799	#10775	
Last Discharge	#7516	#8684	#10079	#10948	
Highly Relevant Discharges	69	105	189	124	**487**
Potentially Rel. Discharges	18	10	21	26	**75**

Table 3.1: Summary of MST2 RE campaigns in COMPASS tokamak.

As part of the MST2 project, COMPASS RE campaigns are not only focused towards RE physical studies, but also as a test bed for the novel RE diagnostics.

3.3 Diagnostics and Experimental Setup for RE Campaigns

A description of the experimental setup used during all four campaigns is described here. The Section starts with diagnostic tools that measure essential plasma parameters for RE studies. Then specific RE diagnostics used on COMPASS are presented. Additional installations necessary for RE campaigns are described in the last part.

3.3.1 General Plasma Diagnostics

The time evolution of **the line-averaged density** $\bar{n}_e$ was measured by a heterodyne interferometer [121]. In the 1^{st} RE campaign, the interferometer had a probing microwave beam with frequencies in the range of

131 − 133 GHz [122]. For the rest of the campaigns, the frequencies of the probing microwave beam are 139.3 and 140.0 GHz.

The loop voltage was measured by a flux loop (FL). There are 8 flux loops installed on the COMPASS vacuum vessel, where FL2 located on upper HFS is commonly used (see Fig. 3.2b) for V_{loop} measurement. **The plasma current** I_p is determined by a Rogowski coil localised in sector 1/2 inside the vacuum vessel. Poloidally distributed 16 pick-up coils with non-negligible length (5 cm) used for plasma position and shape observation are located in the sector 9/10, both internally and externally. Those pick-up coils are called Internal (**IPR**) and External Partial Rogowski (**EPR**) coils. Notice that IPR and EPR coils are arrays of poloidally distributed coils, while Rogowski coil is a single coil wound in the poloidal direction. Nevertheless, due to the non-negligible size of the IPR and EPR coils, they could be considered as one continuous coil and therefore are named 'Rogowski'. So-called **Mirnov coils**, are installed in 3 different toroidal positions - under TF coil 7 (set A), 13 (set C) and 15 (set B). To each toroidal position 24 poloidally distributed Mirnov coils (see Fig. 3.2c) are installed in the three torus directions, i.e. toroidal, poloidal and radial, i.e. there is 72

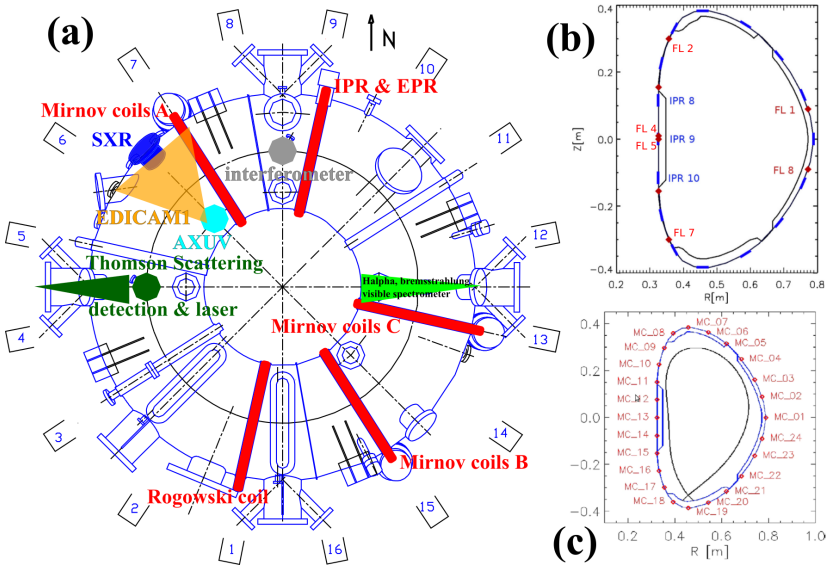

Figure 3.2: Common plasma diagnostics on COMPASS used for the RE studies: **(a)** toroidal position of the interferometer (gray), different magnetic coils (red), SXR (blue), AXUV (cyan), visible light (green triangle), EDICAM camera (orange) and Thomson scattering (dark green); **(b)** poloidal position of IPRs (blue) and Flux Loops (red); **(c)** poloidal distribution of Mirnov coils - identical for all three sets (A, B and C).

coils in total per toroidal location. However, not all of the Mirnov coils are operational at the moment.

Two arrays of 35 silicon photodiodes and one array of 20 photodiodes are used for **SXR** detection on the COMPASS tokamak. The spectral sensitivity of the system is mainly determined by the thickness of the beryllium foil (10 μm) filtering out the photons with energy below 1 keV and by the thickness of the diode active layer (about 200 μm) which limits the detector sensitivity to photon energies up to 13 keV. All SXR arrays (named A, B and F) are located in sector 6/7. Furthermore, five arrays of 20 silicon **AXUV** photodiodes, located at the sector 6/7 provide a measurement of the total radiation in the spectral range from 7 eV to 6 keV [123]. The temporal resolution of SXR and AXUV diagnostics is about 3 μs and the spacial resolution is $1-2$ cm. Both SXR and AXUV arrays use small pinhole to observe radiation along defined lines of sight. Moreover, an H_α or D_α detector (using $656-657$ nm filter) equipped with a photomultiplier tube (PMT) is located radially at the sector 12/13 of the tokamak vessel to measure the Balmer transition from the 3$^{\text{rd}}$ to the 2$^{\text{nd}}$ energy level of **the excited hydrogen**. In addition, a single-channel detector at (523.5±1.0) nm assembled with a PMT measures **bremsstrahlung** radiation from the plasma. The bremsstrahlung detector has the same toroidal location as the H_α detector. Furthermore, a visible light detector from 350 to 850 nm is connected at the same position as H_α and bremsstrahlung radiation.

A **visible camera** is used for monitoring the plasma discharge and the plasma-wall interaction of the COMPASS plasma. The camera is called EDICAM1 and is positioned in the sector 5/6. The time resolution of EDICAM1 is approximately 2.7 ms, i.e. 370 frames per second.

The **Thomson Scattering** (TS) diagnostic system [124] in COMPASS uses two Nd:YAG lasers of wavelength λ_i =1064 nm with an energy of W_{laser} =1.5 J for each laser. The whole system is set in sector 4/5, the lasers being oriented vertically and the scattered light being recorded in the radial direction. Each laser has 30 Hz repetition rate, which offers a $\sim$16.7 ms time resolution if the two lasers are operated equidistantly.

3.3.2 Specific RE Diagnostics

The technical detail about RE diagnostics in the COMPASS tokamak is reported here and their disposition is schematically presented in Fig. 3.3.

The main measurements of RE losses are done with a photoneutron detector located nearby the north wall and a set of scintillators sensitive to Hard X-Ray (HXR). *Photoneutrons* with energy above 0.5 MeV are observed with a ZnS(Ag) neutron detector embedded in a plastic matrix. The detector is located at approximately 4 m from the tokamak vessel. Beside the neutrons, the photoneutron detector is also sensitive to strong fluxes of HXR, although the detector is shielded by 10 cm of Pb[2]. Therefore,

[2]This is the reason why we had to purchase a new neutron detector. The justification

the detector will be named **Shielded HXR** detector. On the COMPASS tokamak, HXR detectors can be split in 3 groups:

- Standard HXR detector,
- CTU HXR detector(s),
- CsI(Tl) HXR detectors.

Standard HXR detectors are unshielded NaI(Tl) scintillation detectors, for which the signal is amplified by a PMT. Their energy range of detection lies approximately from 50 keV to few MeV. The Standard HXR position is in the north part of the tokamak hall, 4 m from the tokamak vessel. Additionally, note that the lower limit of HXR detector determines the lower limit of detected RE. Usually RE do not loose all their energy at once, and consequently the lower RE detection limit is typically at least few times larger then the detector limit.

Furthermore, few additional detectors were on loan from the Faculty of Nuclear Sciences and Physical Engineering (Czech Technical University - **CTU**) in Prague, with similar energy detection range to the Standard HXR. In the 1^{st} RE campaign, 3 HXR detectors were borrowed and were installed in the west, south and east part of the tokamak hall with a distance of about 5 m from the tokamak. During the 2^{nd} RE campaign two CTU HXR detectors were localised at the south-west and the south-east of the tokamak hall with an approximate distance of 6 m from the tokamak. Only one HXR detector was provided for the 3^{rd} and 4^{th} RE campaign positioned in the north-east side of the tokamak hall, also 6 m far from the vessel. In addition, 4 **CsI(Tl) scintillation** detectors with semiconductors were purchased for spatial analysis of the RE

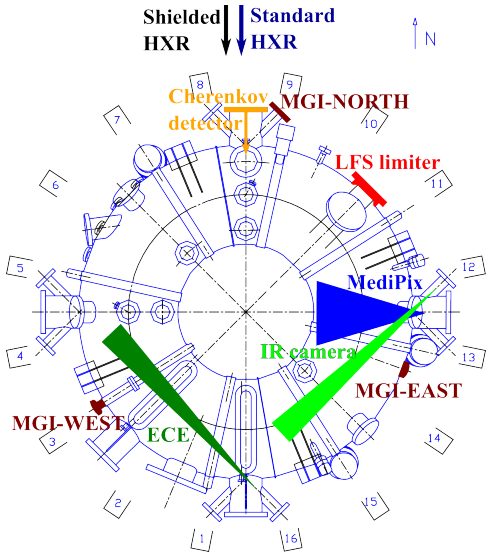

Figure 3.3: Toroidal location of RE diagnostics in the COMPASS tokamak: Standard HXR (dark blue), Shielded HXR (black), IR camera view during first three RE campaigns (light green), Cherenkov detector (orange), TimePix SXR camera (blue), ECE (dark green). The positions of LFS limiter (red) and MGI valves (maroon) are also shown.

behind the made decision is reported in Appendix B.

losses. However, the detectors showed to be inadequate for RE studies in the COMPASS tokamak due to the incompatibility of the electronic with the generated fluxes of HXR during the RE discharges [125].

Next, a bolometric **IR camera** with a wavelength range between $7.5 - 13\,\mu$m was used for RE studies, as the peak of synchrotron radiation falls in the mid-wavelength IR region for the REs generated in the COMPASS tokamak. The time resolution of the camera is 120 frames per second. During the first three RE campaigns, the IR camera was installed at the mid-plane tangential port located in the sector 11/12 and was observing the counter-current direction (i.e. electrons move towards the camera). The diameter of the observed area of the plasma cross-section varied between each RE campaign: 14.9, 16.9 and 15.5 cm for the 1^{st}, the 2^{nd} and the 3^{rd} RE campaign, respectively. As the NBI-2 was connected to the tokamak to this port during the 4^{th} RE campaigns, the IR camera was installed at the same location, but in the co-current direction to monitor heating of the Cherenkov probe. However, as the NBI-1 shutter next to the Cherenkov probe was closed, in some discharges reflection of synchrotron radiation from the shutter was observed, unexpectedly providing us an additional information on high energy RE.

Installation of the **Cherenkov detector** was foreseen for each RE campaign. Despite this plan, only the 3^{rd} and 4^{th} RE campaigns had measurements from the detector, as various technical challenges occurred during the first two campaigns. A single-channel Cherenkov detector with diamond radiator was installed for the 3^{rd} RE campaign, while a three-channel Cherenkov detector with diamond radiator was used in the 4^{th} RE campaign. However, the latter Cherenkov detector had strong parasitic signal coming from the HXR radiation and had to be modified for the subsequent use[3].

A 2D SXR camera, so-called **TimePix** [126], was used in the first three RE campaigns for spatial observation of RE losses. The detectors are sensitive to photons in the range $1 - 20$ keV. The time resolution of the TimePix is around 2.5 ms, i.e. 400 fps. The time resolution is not very well defined as it depends on the particle flux reaching the camera sensor. The camera was attached to the south-east part of the tokamak and observed radially the HFS of the tokamak through a pinhole.

During the 3^{rd} and 4^{th} campaigns electron cyclotron emission (**ECE**) was observed from oblique (i.e. tangential) view at sector 1/16 in counter-current direction. The ECE radiometer we used had 16 channels and it was possible to change the detection range between three different bandwidth sets: $26.5 - 40.0$ GHz (around the 1^{st} harmonic of ECE for $B_{tor} = 1.15$ T), $60 - 73.5$ GHz (around the 2^{nd} harmonic) and $76.5 - 90$ GHz (around the 2^{nd} and 3^{rd} harmonics).

[3]Note that the those issues have been resolved in succeeding campaigns, after Ix left.

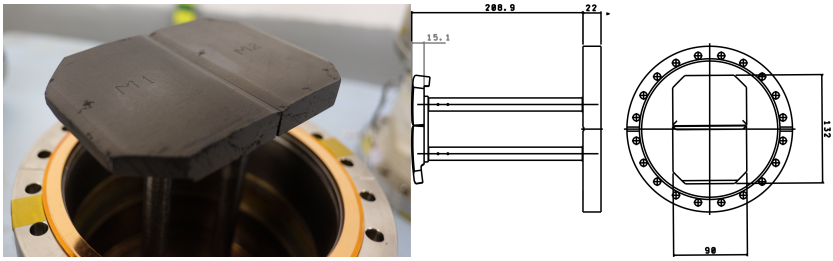

Figure 3.4: **Left:** Photo of the LFS limiter after exposition to RE beams; **Right:** right and front view on the LFS limiter with dimension.

3.3.3 Additional Setup for RE Campaigns

In all four RE campaigns, the first wall of the vacuum vessel was additionally protected by a graphite Low Field Side **(LFS) limiter** located in the sector 10/11 at the mid-plane position. The thickness of the LFS limiter was 15.1 mm, as shown in Fig. 3.4, that should be compared to about 2 mm, which is the penetration depth of JET REs into graphite [86]. Therefore, as COMPASS REs are typically less energetic than in JET, the COMPASS LFS vessel was well protected with this limiter.

On COMPASS, the separatrix of limited plasma intercepts the HFS limiter of the machine. The limiter is usually made of a ring of graphite tiles, protecting the central column. However, in the first two campaigns one tile was change for the purpose of another (i.e. non-RE) experimental sessions. Particularly, in the 1^{st} RE campaign, one tile was replaced with a recessed roof [127, Fig.1b] having 0 mm insertion. During the 2^{nd} RE campaign, a so-called double-roof tile was installed. The double-roof limiter was inserted around 40 mm towards the plasma compared to the other HFS graphite tiles, thus providing a smaller contact area between plasma and the main limiter. In the last two campaigns no special tile was used on the HFS wall.

In the 2^{nd} RE campaign, **MGI** was realised using a solenoid valve, located in the sector 13/14 (EAST valve). For the 3^{rd} and 4^{th} RE campaigns two additional solenoid valves were installed and tested in the sectors 4/5 (WEST) and 8/9 (NORTH). The solenoid gas valves are connected to the vessel through two stainless steel tubes about 1 m long.

3.4 Effect of Density on RE Generation

As described in Subsection 2.2.2, the main RE seed population is created during the current ramp-up phase if n_e is low and E_{tor} high enough. In the COMPASS ramp-up phase, n_e can be lower than $10^{19}\,\mathrm{m}^{-3}$ and E_{tor} can be over 1 V/m. These values lead to a ratio $\mathcal{E}_{crit} = E_{tor}/E_{crit}$ above 125,

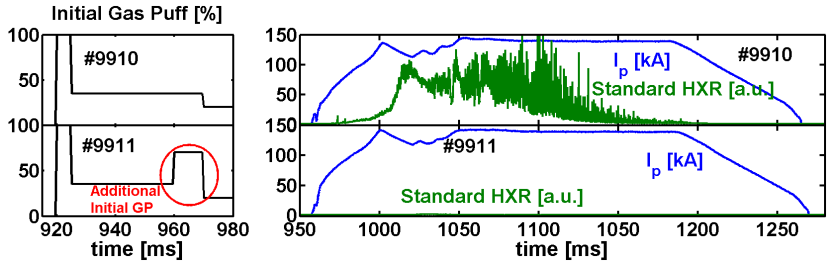

Figure 3.5: Impact of initial GP on RE population in the COMPASS tokamak for circular plasma. The Figure is reproduced from Ref. [118].

which indicates a very high probability for RE generation. Consequently, RE studies started by looking at the effect of gas puff injection (GP) during the current ramp-up phase, which will be named in the following as **initial GP**. In COMPASS, gas injection starts around 920 ms at full valve opening for few milliseconds. For the RE studies, gas injection continues at lower level for few tens of milliseconds. The plasma breakdown in COMPASS occurs around (955 ± 5) ms, when the current through the central solenoid coils start to change.

Increasing n_e by higher GP results in an increase of E_{crit} reducing the probability of RE generation. Therefore, additional initial GPs were conducted after the breakdown to experimentally investigate the suppression of RE generation or the enhancement of RE losses. The conclusion was that suppression usually occurred when the additional initial GP was earlier than 980 ms, while the enhanced RE losses followed for later puffs. An example of the discharge with lack of REs is shown in Fig. 3.5. One clearly sees that in discharge #9911 no HXR are measured compared to discharge #9910, while the plasma densities level and their evolution were very similar in both discharges during the flat-top phase. Meaning that the additional GP can be used for avoidance of RE generation.

Subsequently to the initial GP tests, scan over different initial electron densities $\bar{n}_e$ was also performed. The influence of the REs on the current ramp-up phase is reported by the author of this Thesis in Ref. [128] and update of this study can be found in Section 5.4. It was shown how the lower initial n_e results in higher I_p during the ramp-up phase that is driven by RE population.

Furthermore, care must be taken in order to have other plasma parameters constant as much as possible during such scans. However, some of the plasma parameters are dependent on each other. For example, I_p was kept constant (see Section 3.5), but then different plasma elongation κ and safety factor q_{95} at the edge followed due to the higher density demands. Therefore, experiments with constant elongation κ (but variable I_p) were also realised, as presented in Section 3.7.

3.4.1 Classification of RE Discharges

On COMPASS, different waveforms of GP injection provide different amount of generated REs during the discharges. We then decided to split the discharges of the 4 RE campaigns between 4 groups[4]:

- Standard discharges: either RE-free discharges or discharges when the Standard HXR detector measurements were barely visible (blue pluses in Fig. 3.6);
- Slide-away discharges: $V_{loop} < 0.5\,\mathrm{V}$ and relatively weak signal on the Shielded HXR signal (red dots in Fig. 3.6);
- RE dominated discharges: V_{loop} is of the same magnitude as for the standard discharge, but observation of high energy RE losses is shown by the high level of Shielded HXR signal (yellow diamonds in Fig. 3.6);
- Parail-Pogutse discharges: sub-group of RE dominated discharges with a very low density ($\lesssim 1.5 \times 10^{19}\,\mathrm{m}^{-3}$), but located in Fig. 3.6 at the transition region between the previous two regions (black crosses in Fig. 3.6).

Labeling of the last group, comes from the occurrence of the so-called *Parail-Pogutse instability* [78]. An example of Parail-Pogutse observation in the COMPASS tokamak is presented in Fig. 3.7. The instability is observed when the plasma frequency $\omega_{pe} = \sqrt{e^2 n_e / m_e \varepsilon_0}$ is lower than the fundamental electron cyclotron frequency Ω. The saturating bursts of HXR signals present RE losses due to the Parail-Pogutse instability.

[4]The classification is based on the explanation given in Section 2.2.3

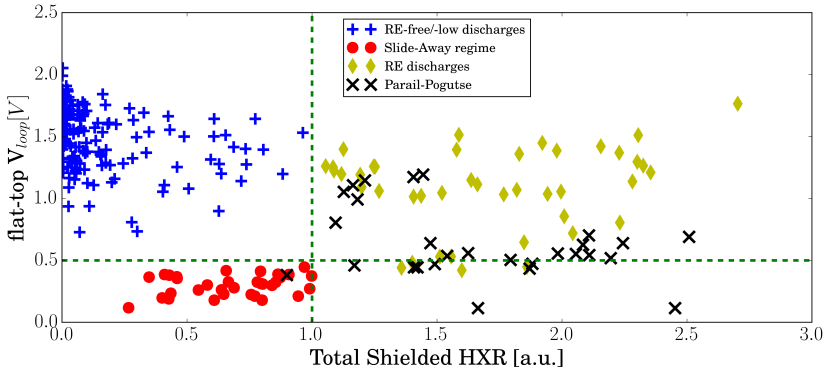

Figure 3.6: Distinction between different RE discharges using the mean value of V_{loop} estimated over the time window $1080 - 1150\,\mathrm{ms}$ versus the mean value of the Shielded HXR computed along the whole discharge.

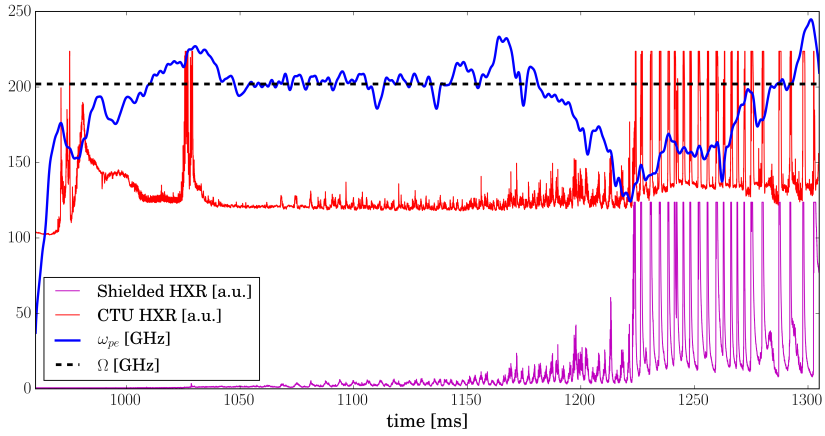

Figure 3.7: Regular periodic saturated bursts in Shielded (magenta) and CTU (red) HXR signals after 1200 ms show detection of a Parail-Pogutse instability in the COMPASS discharge #8559. As the theory predicts, Parail-Pogutse instability occurs when the plasma frequency ω_{pe} (blue) - line average $\bar{n}_e$ is used for the calculation - is lower than the electron cyclotron frequency Ω. Figure reproduced from Ref. [129].

Furthermore, note that discharges with non-constant I_p during flat-top, disruptions before 1200 ms and plasma existing after 1400 ms are omitted in Fig. 3.6. Particularly, the discharges with plasma existing after 1400 ms, named *long-discharges*, were purposely designed scenarios to reach plasma discharges with duration up to 1 s. The key point was to have less than usual GP injection during the current ramp-up phase. This lead to slide-away plasma regimes with significantly lower volt-second consumption of the primary winding. Additionally, as mentioned in Section 3.3.3, during the 2^{nd} RE campaign a double-roof limiter was installed on the HFS, making smaller contact region between the plasma and the limiter. This resulted in a different, new (i.e. fifth) class of discharges, with a duration much longer than typical COMPASS discharge. On the other side, when fully aligned C-tiles were limiting the plasma a lower initial GP than for double-roof limiter was required to obtain long discharge, probably due to the lower gas recycling from the wall.

A study of RE losses and discharge termination for these COMPASS long discharges has been recently reported by Ficker *et al.* [130]. The most notable result is the very high speed RE HFS termination, as the current drops with approximately 1 GA/s rate. This value is 1-2 orders of magnitude faster than the usual COMPASS disruptions. Due to higher termination speed, the RE energy deposition time is smaller and potential damage in larger machines is higher. Therefore, this RE termination type will be

one of the focuses for the future RE studies in the COMPASS tokamak. Finally, beside discharges in Fig. 3.6, Parail-Pogutse was observed in all the long-discharges, as GP was purposely not performed during the discharge. Therefore, long discharges resulted in a decreases of n_e over time and thus decrease of ω_{pe}/Ω.

3.4.2 E_{crit} Experiments

As already explained in Section 2.1.4, E_{crit} is the lower limit for the value of the electric field E_{tor} under which no RE generation is possible with the Dreicer mechanism. In the COMPASS tokamak, experimental measurements of E_{crit} were done within the 4^{th} RE campaign, following the work done on other machines[5]. Namely, RE generation during the I_p flat-top phase of the discharge was achieved by stopping the GP injection, which led to a n_e drop and thus reduced the Coulomb collision force. To obtain the required density drop, boronisation had to be done for better wall conditioning in order to reduce wall recycling. Moreover, it was necessary to inject more gas at the beginning of the I_p flat-top phase to de-confine all the REs created during the plasma breakdown and the current ramp-up phase. The analysis resulted in values $14 - 21$ times higher than the theoretical value, also higher than those of other tokamaks (see Fig. 3.8). However, the DIII-D and TEXTOR E_{crit} estimations are also over 10 times higher

[5]For mode details about the inter-machine study of E_{crit} see Section 2.2.1

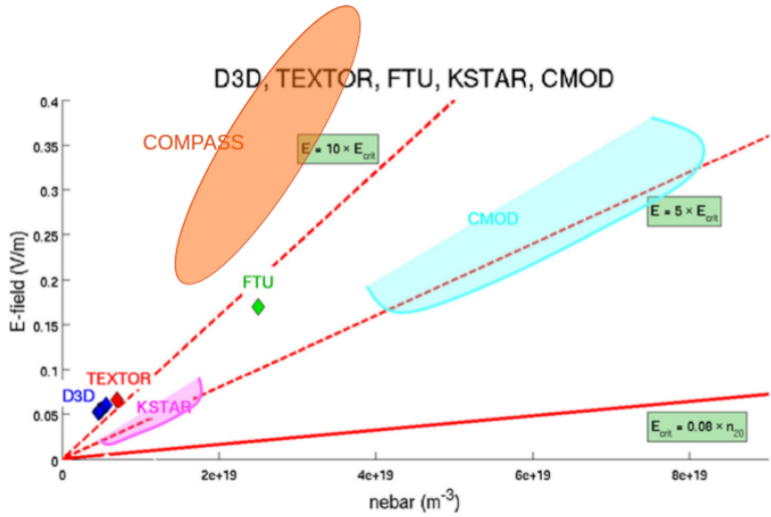

Figure 3.8: Comparison of COMPASS experimental E_{crit} estimations with the ones found in Ref. [48].

than the theoretical E_{crit} prediction, being comparable to the COMPASS observed values.

3.5 Effect of Electric and Magnetic Field on REs

During this Thesis, a scan over different I_p and consequently different q_{95} was performed with constant density $\bar{n}_e \sim 2.5 \times 10^{19}\,\mathrm{m}^{-3}$ [118]. Fig. 3.9 summarises the experimental results. One can see that for lower q_{95}, the REs are lost in a shorter time than for higher q_{95}. Therefore, the RE confinement decreases for lower q_{95}, i.e. higher I_p. Note that the constant absolute value of HXR signal does not correspond to the absolute number of lost REs due to detector saturation. Accordingly, the amount of REs generated during the I_p ramp-up phase (i.e. before 1000 ms) could be similar for all three analysed discharges. Moreover, at the moment of the final RE loss in discharges #9865 and #9867 an on-set of MHD activity was observed, which probably explains the sudden RE losses.

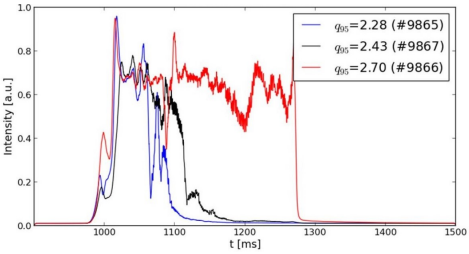

Figure 3.9: RE losses presented by CTU HXR as function of different q_{95} values. The RE confinement deteriorates with lower q_{95}, i.e. higher I_p. The Figure is reproduced from Ref. [118].

In addition to the I_p-scan, three sessions during the 2^{nd} RE campaign were devoted to a scan over the flat-top value V_{loop}. No unambiguous dependence was found in the first two sessions, owing to the difficulties of the density control. In the third session, the density was more reproducible and as V_{loop} decreased from shot #8655 to #8657 the Shielded HXR showed higher absolute signal. This observation would implicate that discharges with lower electric field have larger amount of high energetic REs on COMPASS. A similar observation has been done in the subsequent RE campaign for the set of discharges #9917-9920. Even though those findings could be in conflict with the Dreicer theory where high electric field means more REs, one should take into account that q_{95} increases by decreasing V_{loop} and (as seen in Fig. 3.9) the higher the q_{95} the lower the RE losses. Once again, one should take care of which parameters are changed by scanning over one parameter in tokamak plasma. Therefore, the result of the V_{loop} scans could be rather a consequence of the q_{95} increase than the V_{loop} decrease. As q is a very important fusion plasma MHD parameter, the aforementioned observation emphasises the importance of MHD activities in the RE losses, subject that will be briefly addressed in the next Section 3.6.

In addition, an attempt to study the influence of V_{loop} in the current ramp-up phase was conducted along with the current flat-top V_{loop} study. Despite that changing the ramp-up V_{loop} is relatively easily done on COMPASS, the reproducibility in n_e and I_p time-traces showed to be quite challenging and time-demanding. Therefore, there is no clear output from those experiments and more statistics is needed. Moreover, a scan over few different B_{tor} was performed, with no clear outcome.

3.6 Effect of MHD Modes and Instabilities on REs

It is widely accepted that magnetic reconnections are (among others) connected to sawtooth crashes [131]. Moreover, it is believed that REs could be generated during magnetic reconnection due to the extremely high electric fields that are created during these events. Consequently, one would expect REs to be generated during sawtooth crashes. This hypothesis was investigated experimentally [129, Chapter 4] on the COMPASS tokamak. The main results is shown in Fig. 3.10 where, two discharges with sawtooth activity are depicted. The HXR signal detects RE losses for discharge #8632 (Fig. 3.10b), while nothing is measured during discharge #8634 (Fig. 3.10c). The main difference between the two discharges is the ramp-up density $\bar{n}_e$ which is two times smaller in the first 25 ms of the discharge #8632 (Fig. 3.10a). Note that the subsequent plateau density is very similar in the

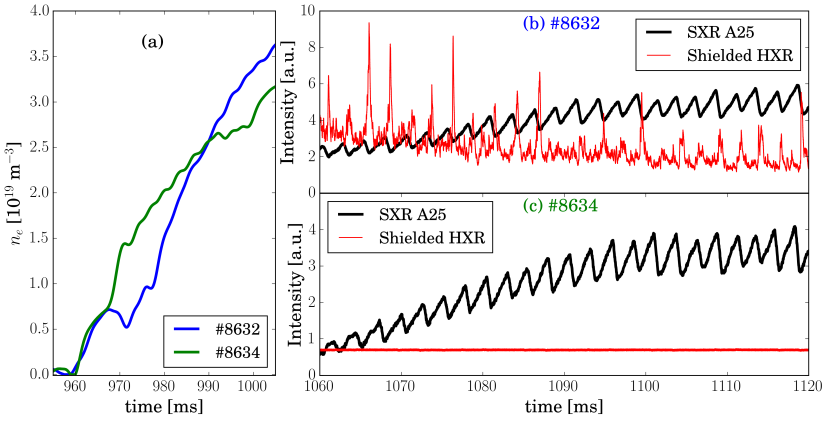

Figure 3.10: Experimental proof that RE are not generated during the sawtooth crashes in COMPASS tokamak: **(a)** line averaged density for both discharges, **(b)** SXR and HXR signals for #8632 showing sawtooth crashes and RE losses, respectivaly and **(c)** same as (b) but for discharge #8634. Figure reproduced from Ref. [129].

two discharges. Therefore, REs are generated during the ramp-up phase (when density is low enough) and sawtooth crash only de-confines them. The RE de-confinement probably occurs because magnetic field lines become stochastic during sawtooth crash deviating the RE trajectory. Successful repetitions of the experiment were routinely achieved.

RE losses also seem to be connected with the presence of tearing mode [132]. A measurement of CTU HXR and Mirnov coil A12 presented by spectrograms in Fig. 3.11a shows a clear link between the RE losses and the tearing mode [133]. Namely, a magnetic island with frequency around 8 kHz can be observed between 1050 and 1060 ms on Mirnov coils spectrogram and identical structure is found for the HXR signal. It means that RE losses are connected with the existance and behaviour of the magnetic island. Moreover, not only that plasma oscillations/instabilities (e.g. sawtooth, tearing mode) can de-confine RE, but also external technical oscillations coming from plasma movements (explained in the next Section) or flying wheel rotation for the power supplies [132]. For example, we observed a relation between the rotation frequency of the flying wheels and RE losses (see Fig. 3.11b) with the frequency of REs losses. Even though, the frequencies are not the same, the RE loss frequency increased between the discharges by the same factor as the flywheel frequency request. Additionally, we recognized experimentally [132] that the ratio between frequencies of CTU HXR peaks and the dominant poloidal field oscillations (measured by the flux loop FL2) drops linearly as the edge safety factor q_{95} increases.

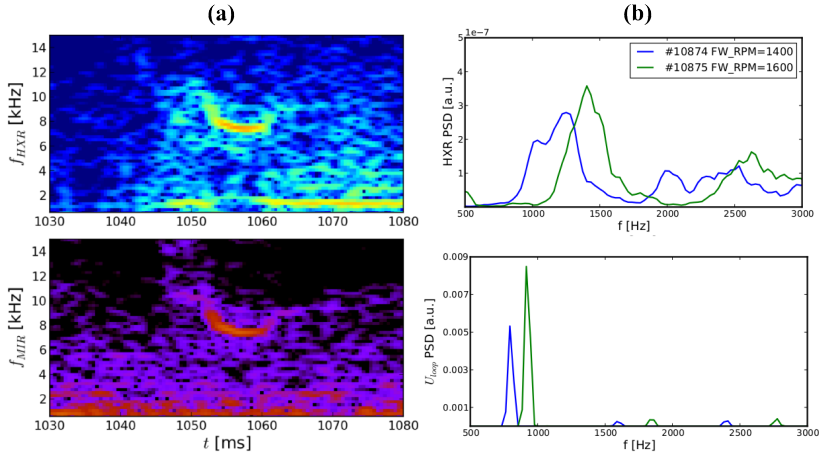

Figure 3.11: **(a)** Spectrograms of CTU HXR detector (top) and of the Mirnov coil A12 (bottom) for discharge #10945. **(b)** Frequency power spectra of HXR (top) and fly-wheel (bottom) signals for discharges #10874 and #10875 that have fly wheels rotating with 1400 and 1600 revolutions per minute (rpm), respecticely. Figures are reproduced from Ref. [133]

A passive observation of the Alfvén-wave oscillations associated with the REs losses at COMPASS is reported in Ref. [134]. Both, continuous and chirping-like Alfvén modes are found to be linked with the RE losses. Particularly, it is observed that RE losses trigger the modes. In the 4^{th} RE campaign there was an attempt to reproduce some of those experiments, but with limited success. The connection of RE with Alfvén-like MHD modes still presents ongoing research.

3.7 Position and Shaping Effects on REs

In the first two RE campaigns, the influence of radial and vertical movements of the plasma on the REs was investigated. At the same time an attempt to measure the heat load of REs on the HFS limiter by the radial inward movement with the IR camera was also performed. Additionally, different speeds of radial inward plasma movement were investigated. During the 1^{st} RE campaign, besides the vertical plasma movements, three discharges with very fast ($\sim$2 ms) vertical displacements of the plasma, so-called vertical kick, were done to examine their effect on RE losses. However, no obvious difference or dependence were detected in any of the aforementioned experiments. On the other hand, discharges with plasma movement showed to be useful for the verification of the RE diagnostic observations. Namely the IR and the TimePix cameras[6] observed the upward and downward motion of RE beam with the plasma. Moreover, oscillations of the plasma radial position induced by electrical noise coming from the power

[6]See Subsection 3.3.2 for the technical details on the cameras.

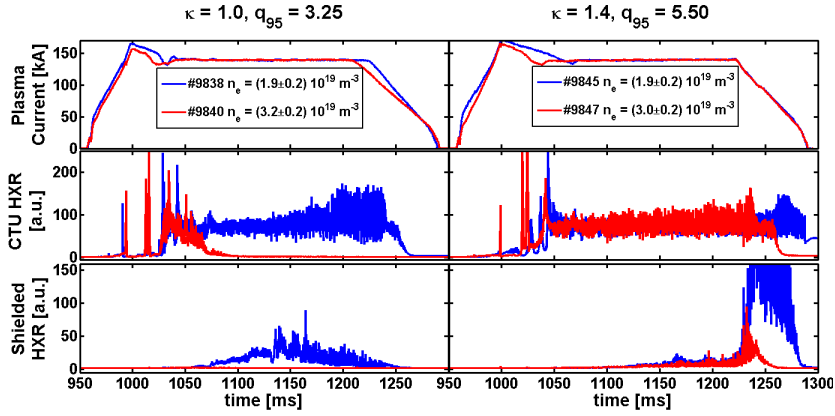

Figure 3.12: Effect of plasma shaping on the RE confinement in the COMPASS tokamak. **Left** panel: circular plasma ($\kappa = 1.0$); **right** panel: elongated plasma ($\kappa = 1.4$). The Figure is reproduced from Ref. [118].

supplies were suspected to cause RE losses [132]. This assumption was confirmed with the CTU HXR and fast IR camera used during the MTS1 RE campaign.

Regarding the plasma shape, it was observed that the more elongated the plasma was, the better REs were confined, and that higher elongation requires higher n_e for a RE-free plasma discharge [118]. Fig. 3.12 illustrates these conclusions for a circular plasma with $\kappa = 1$ and a limited D-shaped plasma with $\kappa = 1.4$, while the initial GP until 970 ms was the same for all 4 discharges. One can see from HXR signals that a density of $\bar{n}_e = 3.2 \times 10^{19}\,\mathrm{m}^{-3}$ for the circular plasma discharge #9840 was enough to suppress the confinement of REs at the beginning of the flat-top, while this is not the case for the D-shaped discharge #9847 even though the density had similar values during the whole discharge. Moreover, the Shielded HXR signal shows that high energy REs are better confined in D-shaped #9847 even with higher n_e than during the circular #9838 with lower n_e.

Beside limited plasma, the shaping experiments also included diverted and H-mode plasmas. The trend of better RE confinement with higher elongation ($\kappa = 1.8$) and diverted plasma continued. On the other hand, discharges with the early H-mode showed to be difficult to achieve and it has been left for future studies.

3.8 RMP Influence on RE

The COMPASS tokamak is equipped with a system of poloidal and toroidal coils that can introduce resonant magnetic perturbations (RMPs) in the toroidal direction with the n-mode number equal either to 1 or 2 [135]. As the RMP system was at a time one of the two main schemes for the ITER RE mitigation, COMPASS RE campaigns examined RMP's influence on the RE population. During the 1^{st} RE campaign modification of RE loss frequency with RMPs was observed, i.e. RE loss frequency was correlated with RMP frequency. In this experiment the configuration was set to $n = 2$ using all (bottom, mid-plane and top) coils with equal parity. In later campaigns, the mid-plane coils were switched off, while the rest of configuration was kept the same. With such configuration of coils, three discharges were performed during the 2^{nd} RE campaign and more than 10 during the 4^{th} one. No significant influence on the RE population has been observed showing the importance of the mid-plane RMP coils in RE mitigation. This is probably because REs are predominantly located at the plasma core and the mid-plane coils are the closest ones. Nevertheless, the effect of RMP coil closeness to the RE beam is still to be investigated in details.

3.9 MGI Influence on RE

As mentioned previously (Subsection 2.2.4), MGI triggered disruptions are more prone to the RE beam occurrence. Therefore, Ar injection was used to trigger the first post-disruptive RE beam in COMPASS. First tests have shown [136] that the easiest way to produce a RE plateau was to massively inject Ar during the ramp-up phase of the plasma current. The analysis of those first Ar tests showed that typical COMPASS disruptions without Ar injection can satisfy almost all parameters important for runaway plateau creation (e.g. n_e, V_{loop}, I_γ, q_{eff}, I_p), but that high-Z MGI is necessary for activation of thermal quench to enhance/trigger RE generation during the disruption.

Post-disruptive RE beams carrying more than 10% of the pre-disruptive current I_p (more then 10 kA usually) were obtained in 23% of analysed discharges, additional 30% of discharges had a RE current I_{RE} equal to few 100 A after the Ar-triggered disruption. Fig. 3.13 gives an example of an achieved RE beam in COMPASS using Ar puff that caries about 30% (i.e. 30 kA) of the pre-disruptive I_p. A comparison of COMPASS scenarios for post-disruptive RE beam generation with the ones from TCV, AUG and JET tokamaks was presented in the IAEA Fusion Energy Conference by Plyusnin *et al.* [137], showing the relevance of the COMPASS tokamak to the ITER-relevant studies.

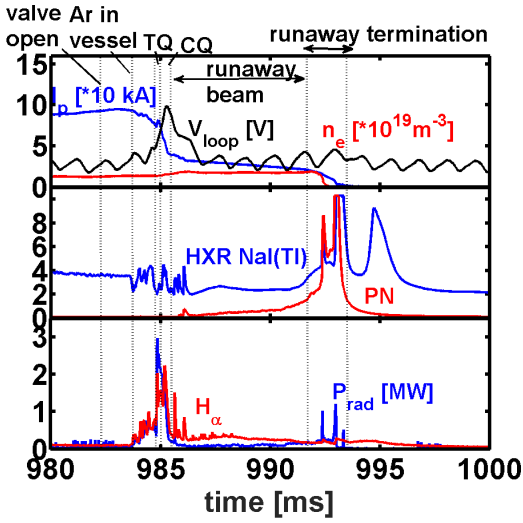

Figure 3.13: An example of the post-disruptive RE beam in the COMPASS tokamak [136]. **Top:** RE beam carried around 30 kA; **middle:** RE beam termination characterised with HXR losses during the final current drop; **bottom:** relatively weak plasma radiation after disruption shows lack of hot plasma after disruption.

Beside using MGI during the I_p ramp-up phase, Ar gas was also puffed during the current flat-top phase but without any RE beam generation. Furthermore, Ar was puffed somewhere after 1400 ms into the long discharges that have already beam-like RE population. No clear RE current plateau was realized in from the long discharges, probably because the RE beam practically already exists. However, a connection between RE losses and MHD activity was observed during those discharges and they show poten-

tial for studies of interaction between MGI and RE beam. Detailed analysis of the MGI discharges is done in Chapter 7.

Alongside Ar MGI, Ne gas was also used as MGI gas during the 4^{th} RE campaign. However, no clear sign of RE beam creation was observed. The probable reason is a too low Ne back pressure P_{back}[7], in argument with observations on AUG[8], P_{back} being limited by the reduction valve at the entrance of the MGI injection system.

3.10 RE Modelling in COMPASS

LUKE and METIS (see Section 2.1.6) are installed at COMPASS and coupled to simulate the time evolution of the main RE discharge parameters. These two coupled codes were used to verify the existence of the avalanche mechanism[9] in the COMPASS tokamak. According to Ref. [28] the avalanche mechanism significantly contributes to the total RE population in tokamaks that have $I_p \gtrsim 1\,\mathrm{MA}$, so it should not contribute significantly in the COMPASS case. To verify this presumption, parameters of discharge #8555 are taken as the starting point. Taking the plasma parameters at the beginning of the current flat-top phase, modelling with LUKE-METIS showed that avalanche could contribute up to 30% of the RE current after 100 ms. Dedicated experiments realised during the 3$^{\mathrm{rd}}$ RE campaign for modelling purpose provided valuable input. Additionally to LUKE-METIS simulation, COMPASS facility has been equipped with the so-called NORSE code and its first use is reported later in this Thesis.

3.11 Conclusion and Future Perspective

Around 500 relevant discharges were performed during the 2-year MST2 project on the COMPASS tokamak. As already mentioned, those were the first dedicated experiments at the COMPASS tokamak. Henceforth, the conclusions have been chronologically classified to show what we have learned from campaign to campaign.

As dedicated RE studies started with this project, plasma parameters crucial for the RE generation were investigated in the 1$^{\mathrm{st}}$ RE campaign, such as gas injection rate at the beginning of the discharge and influence of the density during the flat-top phase. For densities lower than $2 \times 10^{19}\,\mathrm{m}^{-3}$ we have explained that a significant RE population can be generated. Furthermore, effect of plasma position R_p, elongation κ and plasma current I_p were tested. At this moment only plasmas with relatively high currents showed

[7]The back pressure is the set pressure of injected gas before the valve from MGI system is opened.

[8]AUG required about 4 times larger back pressures for Ne than for Ar to achieve similar results.

[9]See Section 2.1.3 for the explanation of avalanche mechanism.

to confine RE better. Position tests did not show any clear dependence and elongation experiments were not conclusive after the 1st campaign. From the diagnostic point of view, the first synchrotron and Parail-Pogutse instability observations were recorded.

In the 2nd RE campaign, studies of shaping and designing fuelling scenarios continued, bringing us to the conclusion that RE are better confined during D-shaped limited plasmas than for circular ones. Link between sawtooth crashes and RE generation/losses was investigated. As it was reported here, we showed that REs are not produced during sawtooth crashes, but only lost due to the sawtooth induced magnetic field stochasticity. Additionally, the first long COMPASS discharges were successfully conducted. The main result of the 2^{nd} RE campaign was the achievement of post-disruptive RE beams. Even though the COMPASS tokamak itself is an intrinsically ITER-relevant machine, this achievement proved COMPASS to be even more ITER-relevant.

In the 3rd RE campaign, experiments with Ar puffing and systematic shaping scans continued. Even though RE beams were again achieved, their reproducibility did not increase. Diverted plasma experiments showed even better RE confinement than the D-shaped limited plasma. Studies of the MHD effect on RE confinement were intensified, showing promising results for the future. First Cherenkov detector measurements were obtained during this campaign and provided information on prompt RE losses.

Boronisation was realised before the last MST2 RE campaign for better wall conditioning. This resulted in a better $\bar{n}_e$-control and allowed estimation of the experimental E_{crit} on COMPASS. It resulted in $14 - 21$ times larger values than the theory predicts, but this is still to be investigated. Besides advancement of the previous studies, influence of continuous and chirping-like MHD modes on RE was also investigated.

The focus of present COMPASS RE studies are MHD influence on RE, novel diagnostics and Ar-puff injection with RE beam stabilisation.

Chapter 4

Importance of Electric Field Estimation for Runaway Electron Energy Calculation

The present Chapter examines the influence of the electric field E_{tor} on the maximum RE kinetic energy W_{max} calculation. The reported results show the importance of the E_{tor} definition used as well as the knowledge of the corresponding errors for the extrapolation towards ITER. However, the Chapter does not solve the issue of the E_{tor} definition. It is rather made to challenge the E_{tor} definitions often used in the literature and in the COMPASS tokamak and propose an acceptable guideline. Finally, the Chapter presents errors introduced on W_{max} by the different E_{tor} definitions.

As E_{tor} is usually estimated either from the measured loop voltage V_{loop} or from simulations using magnetic diagnostics, it is recommended to read Section 2.3.8 before reading this Chapter, where general information of the magnetic diagnostics for the plasma and RE studies is briefly reported. Information on the COMPASS magnetic diagnostics relevant for RE studies is described in Section 3.3.1. Nevertheless, be aware that a proper estimation of the E_{tor} in tokamaks is far more complicated than the first approach given by Eq. 2.9. The complexity of E_{tor} estimation can be seen for instance in Ref. [113].

This Chapter starts with the derivation of a theoretical model for the W_{max} calculation. The next Section focuses on one particular discharge with a constant V_{loop} where different E_{tor} and consequently different W_{max} values obtained from measurements, simulations and theory are compared. A selected set of mathematical tools from the previous Section are then

used for different types of discharges that are typical for the RE campaigns in the COMPASS tokamak. Finally, a summary is given for all reported estimates with an outline in which direction to improve the E_{tor} estimate is described.

4.1 Theoretical Expression for W_{max}

Before analysing the effects of different E_{tor} estimates, it is important to define the parameter W_{max}. Beside E_{tor} there are other potentially limiting factors for the RE energy estimate in tokamaks and they are firstly reported in this Section. Furthermore, the model for W_{max} estimate is also defined in this Section and it will be used throughout the whole Thesis.

4.1.1 General RE Energy Limits

If we assume that there are no RE losses and that all REs move with the speed of light, W_{max} is directly proportional to the history of the toroidal electric field E_{tor}:

$$W_{max} = ec \int E_{tor} \mathrm{d}t. \tag{4.1}$$

Taking typical electric field values ($0.3 - 0.5\,\mathrm{V/m}$) and discharge duration (around 0.3 s) for the COMPASS tokamak, it is estimated that RE can reach energies of about 30 to 50 MeV in COMPASS. However, there are various RE losses in tokamak and some of the most common ones are reported in Section 2.2.5. These losses can reduce the value of W_{max} as described by Jaspers in Ref. [70, Section 2.4].

Using equations from Section 2.2.5, one obtains theoretical W_{max} limits. Taking $B_{tor} = 1.15\,\mathrm{T}$ and $a_p = 0.2\,\mathrm{m}$ with q_a ranging from 2.2 to 3.5 for drift losses Eq. 2.10 gives W_{max} equal to 20-30 MeV. Furthermore, ripple losses[1] for the first harmonic $n_{mr} = 1$ should limit RE energy to about 12 MeV with machine major radius $R_0 = 0.56\,\mathrm{m}$ and number of toroidal coils $N_{tc} = 16$. Synchrotron[2] and bremsstrahlung[3] ($Z_{eff} = 1.5$) radiation are preventing RE to gain energies greater than 50 MeV and few GeV, respectively. Therefore, one could conclude that the REs in COMPASS could not reach more than $\sim 12\,\mathrm{MeV}$ due to the ripple losses (the most limiting factor). On the other hand, experiments prove the opposite, synchrotron radiation from REs with energies over 20 and even 30 are observed with the IR camera. The possible reason for discrepancy between experiment and theoretical prediction is in the simple nature of theory behind Eq. 2.11. Anyhow, investigation of this issue is out of the scope of the Thesis. Furthermore, bremsstrahlung is clearly not the limiting factor during the standard

[1] Defined in Eq. 2.11.
[2] Defined in Eq. 2.12.
[3] Defined in Eq. 2.13.

discharges, but it could significantly affect the MGI experiments, especially in small/medium machines with relatively low B_{tor} (e.g. the COMPASS tokamak).

Finally, RE drift losses should not be ignored as the potential reason of RE losses in COMPASS, but it is difficult to check this experimentally. Possibility for the experimental study could be the analysis of discharges with different q_a, same or similar to the ones mentioned in Section 3.5. Nonetheless, Eq. 2.10 is an approximation and one should use more sophisticated tools - e.g. analytic [69] or numerical [138].

In summary, synchrotron radiation does not really limit the RE energy in COMPASS, as observed energies are about 2 times smaller than the theoretically expected limit. Nevertheless, synchrotron radiation will be taken as the main RE loss in COMPASS, as it is directly proportional to the power of Lorentz factor γ and experiments have shown its existence and importance. The drift losses could be relevant, however their consideration is out of the scope for this Chapter and it will be implemented in the upcoming Chapter (see Section 5.5). Bremsstrahlung losses are also proportional to the γ and could be relevant for the MGI experiments where Z_{eff} can be larger than in standard discharge by an order of magnitude, but they are otherwise negligible. Ripple losses will be omitted throughout the whole Thesis, as the simplified theoretical estimation above is not supported by the experimental observations in the COMPASS plasma.

4.1.2 Model for W_{max} Estimation

The W_{max} parameter is one of the most crucial parameter along this whole Thesis. Therefore, precisely defining the E_{tor} calculation for estimating W_{max} is very important. However, Eq. 4.1 above is oversimplified. As explained previously, the synchrotron radiation loss is considered to be the most relevant RE losses in the COMPASS tokamak. In addition, the bremsstrahlung radiation is also taken into account, as it could be relevant for the MGI injection experiments due to the high Z_{eff} that arises from the injected gas. The introduction of radiation losses makes the whole system of non-linear equations, so that iterative solution must be searched as radiation power losses depend on the RE kinetic energy $\gamma(W_{RE})$[4].

The model is taken from Ref. [81], where radiation losses are subtracted from the acceleration. It is a 0D model, as there is no dimensional dependency, but only time evolution. Particularly, the lost power by synchrotron radiation P_{synch} and bremsstrahlung radiation P_{brems} are subtracted from the power gained by the RE thanks to the electric field P_E

$$\frac{\mathrm{d}W_{max}}{\mathrm{d}t} = P_E - P_{synch} - P_{brems} \tag{4.2}$$

[4]For more detail about synchrotron and bremsstrahlung radiation see Section 2.2.5

to obtain the time dependence of W_{max}. Note that taking into account the bremsstrahlung radiation is a refinement of this Thesis as Yu *et al.* [81] did not include it in their calculation. The power gain by E_{tor} is simply calculated as

$$P_E = ecE_{tor} = \frac{ecV_{plasma}}{2\pi R_p}, \tag{4.3}$$

with R_p standing for the plasma major radius. The synchrotron power loss

$$P_{synch} = \frac{2r_e m_e c^3 \beta^4 \gamma^4}{3R_C^2}, \tag{4.4}$$

and the bremsstrahlung power loss

$$P_{brems} = \frac{4}{137} n_e (Z_{eff} + 1) r_e^2 m_e c^3 \beta\gamma (\ln 2\gamma - 1/3). \tag{4.5}$$

were already defined in Section 2.2.5. The curvature radius R_c is calculated using Eq. (9) from Ref. [139]:

$$R_c = \frac{R_p}{1 + \eta^2 + 2\eta \times 2/\pi} \tag{4.6}$$

where $2/\pi$ at the end of the denominator comes from the average taken over the gyro-motion angle, and where $\eta = \langle v_\perp \rangle / v_{dr}$ and v_{dr} is the drift velocity

$$v_{dr} = \frac{\langle \gamma \rangle \left\langle v_\parallel^2 \right\rangle}{\Omega R_p} \tag{4.7}$$

where $v_\parallel$ and $v_\perp$ are the electron velocity components parallel and perpendicular to the magnetic field, respectively. Furthermore, the angle brackets in the definitions of η and v_{dr} denote the average of spatial and momentum average, therefore making the whole calculation dependent on the RE distribution function. For simplicity, a mono-chromatic RE beam with a small enough minor radius will be assumed to simplify the averaging and thus the bracket can be omitted. The mono-chromatic RE energy distribution is a legitimate assumption, as only fastest RE are interesting here, since they are the ones that contribute the most to the kinetic energy limit W_{max}.

4.2 Uncertanties in W_{max} for the Discharge

In this part, how a different E_{tor} effects the W_{max} will be examined. For this purpose, the COMPASS discharge #9814 will be used for the analysis, as the current carried by RE was negligible comparing to the I_p (so there was no disturbance to the magnetic measurement), a constant V_{loop} was requested during the I_p flat-top phase and, most importantly, the discharge is of the highest relevance for the synchrotron radiation studies (see Section 6.4).

The plasma in discharge #9814 was circularly shaped, with $B_{tor} = 1.15\,\mathrm{T}$ and a linearly rising current due to the constant V_{loop}. Even though the plasma current is rising, this phase will be addressed as the *flat-top phase* due to the common nomenclature and for convenience.

In order to compare the effect of different E_{tor} on W_{max}, the difference δ^W between two W_{max} calculations coming from different E_{tor} estimate will be used in the rest of the Chapter. It is defined as the ratio between the difference and the mean value of the two examined W_{max}:

$$\delta^W_{xy} = \frac{|W_{max,x} - W_{max,y}|}{(W_{max,x} + W_{max,y})/2}\,100\%, \tag{4.8}$$

where x and y stand for the two different E_{tor} (or V_{loop} used for E_{tor}) time-traces coming from either measurements or simulations. The mean value in the denominator normalises the absolute difference, instead of the common practice that requires one value as the "reference" one, simply because none of them is the "reference" value. The error defined as in Eq. 4.8 is know in the literature under the name "symmetric mean absolute percentage error" and it has values in the 0 - 200 % range. Moreover, in tokamak plasmas a relative error of 50% is often considered as tolerable limit. We can see from Eq. 4.8 that if one value is 50% larger than the other, it corresponds to $\delta^W = 40\%$. Henceforth, $\delta^W = 40\%$ will be taken as the allowable limit for discrepancy between two signals.

The Section starts with usage of differently located V_{loop} measurements for the E_{tor} estimate. It continues with estimate of E_{tor} from simulations. Next part is a comparison between measurements and simulations. At the end, a method for estimating E_{tor} that corrects the experimental measurements using simple expression is compared with the E_{tor} estimates from the simulations.

4.2.1 $\mathbf{V_{plasma}}$ from Measurements

In tokamak, E_{tor} is usually not measured directly and is rather derived from the toroidal loop voltage V_{loop} measurement. In electrostatics the electric field E is defined as the opposite of the gradient of the potential V. Therefore, E_{tor} can be approximated from the measurement of the voltage inside plasma V_{plasma} by

$$E_{tor} = \frac{V_{plasma}}{2\pi R_p}, \tag{4.9}$$

omitting the negative sign as the amplitude is of consideration here. However, the plasma voltage V_{plasma} is not measured directly and is often approximated to be equal to the loop voltage V_{loop} (see Eq. 2.9). This assumption is not always correct, especially when the plasma current is ramped up or down due to the differently energised inductance that depends on the

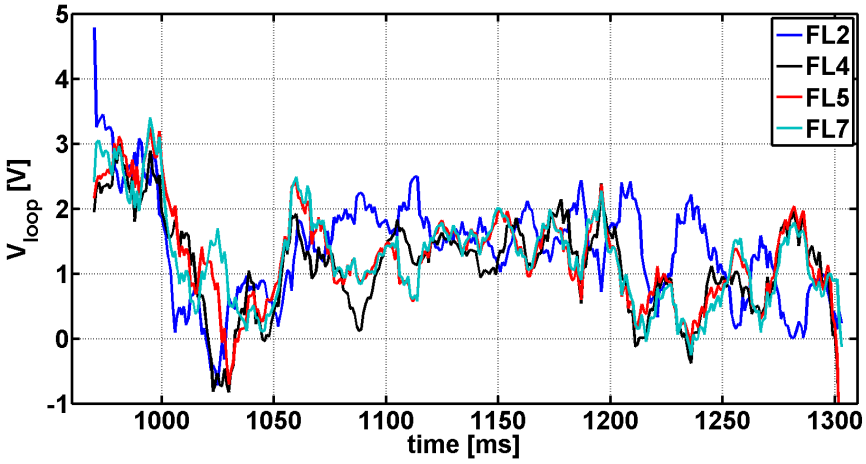

Figure 4.1: Time traces of all four available V_{loop} signals for discharge #9814. The signals are smoothed over 10 ms time window for better visualisation.

plasma, its location, the vacuum vessel material and the tokamak magnetic coil systems. In short, the system is not electrostatic, but electrodynamic. Moreover, even when plasma current is quiescent, corrections should be done depending on the loop location and the plasma region of interest, due to the plasma induction, making the whole problem non-linear.

As reported in Section 3.3.1, V_{loop} is usually measured by wire loops wound in the toroidal direction, so-called flux loops (FLs). There are 8 flux loops physically installed on the COMPASS vacuum vessel, where FL2 located on the upper HFS is commonly used (see Fig. 3.2b) for V_{loop} measurement. Besides FL2 there are only 3 more functional flux loops - FL4 (mid-plane HFS), FL5 (mid-plane HFS) and FL7 (lower HFS). An analysis of which flux loop is to be used for RE studies is performed next.

As an illustration, Fig. 4.1 shows all four available V_{loop} signals for the discharge #9814. Discrepancies between the different signals can be observed due to their different location on the COMPASS tokamak.

The time traces of the difference δ^W between the flux loop FL2 and the flux loops FL4, FL5 and FL7 are shown in Fig. 4.2. Two things can be observed from this Figure: **(1)** δ^W is significantly different during the flat-top phase of discharge (> 1050 ms) for FL4 in comparison to the other two **(2)** and the signals from FL5 and FL7 are quite similar during the whole discharge.

Nevertheless, the "correct" or "proper" flux loop is not yet chosen - so the flux loop FL2 should not be the only one compared to the other ones. On the other hand, it would be cumbersome and redundant to make the graphs for each flux loop as in Fig. 4.2. Therefore, the mean values μ^W_{xy} and

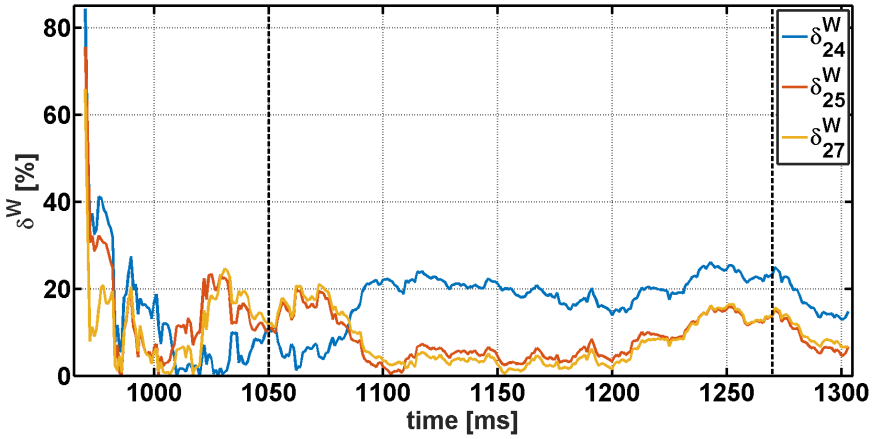

Figure 4.2: Time traces of the relative error δ^W of the W_{max} calculated using flux loops FL4 (δ^W_{24}), FL5 (δ^W_{25}) and FL7 (δ^W_{27}) with respect to the flux loop FL2. Two vertical black dashed lines at 1050 and 1270 ms show the approximate start and end times of the "flat-top phase".

the standard deviations σ^W_{xy} for the whole δ^W_{xy} time traces are systematically collected in Table 4.1. Beside the two aforementioned observations made from Fig. 4.2, a surprising observation from the Table is the relatively large difference between the flux loops FL4 and FL5 signals even though their location is relatively symmetric. The large similarity between the signals coming from the flux loops FL5 and FL7 was also unexpected.

The Table 4.1 shows how the flux loops are compared among themselves, while there is no information on which one is the best to use to estimate E_{tor}. Intuitively, the best flux loop to use should be the one closest to the plasma itself - which are FL4 and FL5 in the case of limited plasmas and FL2 in the case of diverted plasmas. Therefore, the choice of the best flux

μ^W_{xy}	FL2	FL4	FL5	FL7
FL2	-	17	10	9
FL4	17	-	14	15
FL5	10	14	-	2
FL7	9	15	2	-

σ^W_{xy}	FL2	FL4	FL5	FL7
FL2	-	9	8	7
FL4	9	-	5	6
FL5	8	5	-	3
FL7	7	6	3	-

Table 4.1: **Left:** The mean values μ^W_{xy} of δ^W_{xy} for each combination of the flux loops over the whole discharge period. For example, the FL2 row or column summarises the Fig. 4.2. **Right:** Same as the left Table, but for the standard deviation σ^W_{xy} calculated from δ^W_{xy} signal. The quantities are in percent [%].

loop for E_{tor} estimation will be left for the following Sections.

4.2.2 V_{plasma} from Simulations

Unfortunately, the flux loops measure the voltage from outside the plasma, while REs are generated in (the core of) the plasma, as mentioned in Section 2.3.1. When the flux loops are close enough to the plasma (e.g. FL4 and FL5 for limited plasma), measurements could be approximated at best as the voltage at the plasma boundary. However, theory and/or simulation can help to recover the V_{plasma} at a given location based on the knowledge of V_{loop}.

In this Section, two simulations - from EFIT and METIS[5] - are used here to get V_{plasma} (i.e. E_{tor}). The **EFIT** reconstruction creates data in a 2D mesh cross-section of the poloidal plasma plane solving the Grand-Shafranov equation for plasma MHD-equilibrium, using only magnetic measurements in the current setup of the COMPASS tokamak. In the analysis addressed here, V_{plasma} is calculated on the plasma axis [6]. **METIS** simulates a plasma discharge taking additional measurements (e.g. electron temperature and density, radiated power from the plasma, auxiliary heating power) on top of the magnetic ones. Its output provides directly a radial profile of the toroidal electric field E_{tor} and the value computed on the plasma axis makes again the output. As the Z_{eff} is required for METIS calculation, has to

[5] See Sections 3.1 and 2.1.6 for more details about EFIT and METIS, respectively.
[6] N.B. not on the vacuum vessel axis.

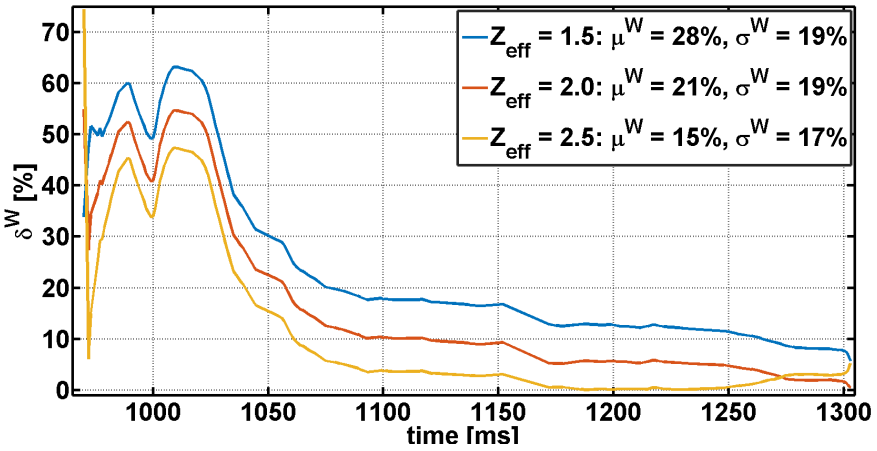

Figure 4.3: The time trace of the error δ^W calculated mutually between the W_{max} from EFIT V_{plasma} and the W_{max} from METIS E_{tor}, which is calculated for $Z_{eff} = 1.5, 2.0$ and 2.5. The mean value μ^W and the standard deviation σ^W are reported in the legend.

be estimated as it was not measured during RE campaigns. Consequently, the effect of different Z_{eff} on METIS simulation will also be investigated in this Section.

The time evolution of the difference between the two simulations is presented in Fig. 4.3. As it can be seen, the difference δ^W between the simulations is in the 0 - 20 % range after 1050 ms, while during the ramp-up phase there is a larger discrepancy between EFIT and METIS. Moreover, METIS with $Z_{eff} = 2.5$ seems to match EFIT pretty well during the flat-top phase, while for $Z_{eff} = 1.5$ the difference is over 10%.

The above results lead to the preliminary conclusion that METIS with $Z_{eff} = 2.5$ should be more appropriate to use. This is in agreement with the experimental observations that indicate Z_{eff} values up to 2.5 [140]. On the other hand, recent estimates using Thomson scattering data [141] reported even lower values of Z_{eff} than 1.5. Moreover, with regular preconditioning of the wall with boron before campaigns and with the glow discharge in between plasma discharges, Z_{eff} should not go as high as 2.5. The final recommendation on which Z_{eff} to use for METIS will be addressed afterwards.

4.2.3 Comparison between Measurements and Simulations

Measurements and simulations are compared in this Section. On one side - the V_{loop} measurements are taken outside the vacuum vessel, but they are still affected by the significant RE population. On the other side - both EFIT and METIS simulations do not handle REs in the rigorous manner. Although, METIS has an option to include the Dreicer generation, the output clearly does not correspond to the experiments.

The results are organised in Tables 4.2 and 4.3, in a similar manner as earlier. The first and the most important thing to notice is that FL4 is the flux loop with the lowest error δ^W with respect to both simulations. One can also notice that the δ^W between simulations and measurements are larger than the δ^W among the measurements themselves, reported in Table 4.1. This is probably due to the nature of signals - simulations provide estimate of E_{tor} inside plasma, while measurements are giving E_{tor} around

EFIT	FL2	**FL4**	FL5	FL7
μ^W_{Ey}	20	**15**	19	20
σ^W_{Ey}	25	**19**	22	22

Table 4.2: Comparison of the difference δ^W between the experimental flux loops V_{loop} (y) and the EFIT V_{plasma}. The second row are the mean values μ^W_{Ey} and the third one are the standard deviations σ^W_{Ey}. The quantities are in percent [%].

$Z_{eff} = 1.5$	μ^W_{My}	σ^W_{My}
FL2	50	40
FL4	**38**	**40**
FL5	49	40
FL7	50	41

$Z_{eff} = 2.5$	μ^W_{My}	σ^W_{My}
FL2	37	40
FL4	**31**	**35**
FL5	38	37
FL7	39	37

Table 4.3: Same as the Table 4.2, but the reference W_{max} is calculated from the METIS E_{tor} value with $Z_{eff} = 1.5$ (left) and 2.5 (right). The quantities are in percent [%].

the vacuum vessel. On the other hand, EFIT simulations systematically show to have W_{max} estimate closer to the measurements than the METIS ones, while METIS with $Z_{eff} = 2.5$ is closer to the measurements than when $Z_{eff} = 1.5$ is used. Additionally, a reason for the standard deviation σ^W to be so large is the fact that δ^W has values over fifty percent before 1050 ms (see Fig. 4.3, for example). As the RE kinetic energy W can go up to 10 MeV during the COMPASS ramp-up phase and W_{max} time-trace is relevant for the calculation in Chapter 5, the error coming from that time range is highly relevant.

Finally, it can be concluded that the flux loop FL4 introduces the lowest error for estimating the W_{max} value in the case of the discharge #9814, if EFIT or METIS reconstructions are to be trustworthy. In other words, the flux loop FL4 is the best to use for circularly shaped plasma discharge without significant RE current. Therefore, it will be the only flux loop used for V_{loop} measurement in the following Section.

4.2.4 Fujita's Correction to the Measurements

A theory developed by Fujita [142] and collaborators that allows a recovery of V_{plasma} from V_{loop} measurements will be presented here. They estimated the voltage in the plasma (denoted as *resistive part*) from V_{loop} measurements by using a theoretical expression. This expression is given by Eq. (15) from Ref. [142]

$$V_{plasma} = V_{loop} - \mu_0 R_p \left[\frac{l_i}{2} + \ln\left(\frac{b}{a_p}\right)\right] \frac{\mathrm{d}I_p}{\mathrm{d}t}, \tag{4.10}$$

where l_i is the internal inductance of the plasma and b is the minor radius at the position of the flux loop.

As already stated at the end of the previous Section, the flux loop FL4 will be used for the V_{loop} measurement. In the case of the COMPASS tokamak, $b \approx 0.235$ m for the flux loop FL4 [143, Table 3-4]. The l_i will be taken from EFIT or METIS[7] according to the code to which the Fujita's

[7] Note that both EFIT and METIS codes also use the measured V_{loop} as an input.

	μ^W	σ^W
EFIT	33	101
METIS($Z_{eff} = 1.5$)	28	37
METIS($Z_{eff} = 2.5$)	39	50

Table 4.4: The difference δ^W between the Fujita's theory and simulations - EFIT (second row) and METIS with $Z_{eff} = 1.5$ (third row) and $Z_{eff} = 2.5$ (forth row). The quantities are in percent [%].

correction is compared.

The results are given in Table 4.4. The difference mean value μ^W for Fujita's correction is larger from EFIT and METIS with $Z_{eff} = 2.5$ and smaller from METIS with $Z_{eff} = 1.5$ when compared to the Table 4.4. Therefore, we conclude that Fujita's correction is closest to the most distant simulation from the measurements, i.e. METIS with $Z_{eff} = 1.5$. Again, the huge standard deviation (especially in the EFIT case) is most likely due to the V_{plasma} difference in the beginning of the discharge.

The large difference between V_{plasma} obtained from Eq. 4.10 and the EFIT and METIS simulations shows one of the main points of the analysis addressed here. The most probable reason for discrepancy is the relatively large uncertainty for the l_i estimate, coming from EFIT and METIS. However, those are the best tools for its estimation in the COMPASS tokamak. A simple analytic approximations, such as Fujita's (and many others), could introduce non-negligible errors throughout the literature without examining the consequences. Note that it is in the responsibility of every researcher (and not of an author of a formula) to know of the possible errors. Moreover, those errors could further produce predictions inaccurate in the orders of magnitudes, as W_{max} is only the intermediate (but very important) parameter in most of RE studies.

To **summarise** the Section, we can say that (1) FL4 seems to be the most appropriate flux loop for studying REs in circular discharge, as it gives the closest W_{max} to the ones coming from simulations, (2) EFIT is the has closest W_{max} from simulations to the measurements, (3) and METIS gives the closest W_{max} to the ones from EFIT and measurements with $Z_{eff} = 2.5$. Additionally, I would recommend FL4 instead of FL2 to the COMPASS operators.

Consequently V_{loop} measurement possibly affects the estimation of the inductance l_i from simulations and thus introduces a non-linearity in Eq. 4.10. This effect is neglected here.

4.3 Uncertainties in W_{max} for Different Discharges

It was shown previously that the flux loop FL4 is closest to the simulations, namely the differences δ^W are 15% and 31% using COMPASS discharge #9814 for the EFIT and the METIS, respectively. On the other side, EFIT seems to have closest W_{max} with respect to the one from measurements. Even though, the errors are relatively high, those values lie in an "acceptable" level for thermonuclear science, as explained in the introduction of the previous Section.

Nevertheless, the final conclusion should not be drawn from only one discharge. Especially since the loop voltage in the flat-top phase for some special RE discharges[8] is much lower than for typical RE-free discharge, as it can be seen in Fig. 3.6. Therefore, different types of discharges are now considered to investigate the differences in the W_{max} estimation.

The discharge #7337 is taken as representative of the RE-free discharges (the same type as the discharge #9814 analysed above), the RE discharge sample is #8555, while the discharges #8556 and #10806 are examples for the Parail-Pogutse and the slide-away regimes, respectively. The criteria for the discharges is to have as extreme discharges as possible with high versatility between the campaigns and taking discharges with high relevance for the Thesis.

The relative errors δ^W are presented in Tables 4.5, 4.6 and 4.7 where EFIT and METIS (with $Z_{eff} = 1.5$ and $Z_{eff} = 2.5$) are taken as the

[8] See RE discharge classification in Section 3.4.1.

μ^W	FL2	FL4	FL5	FL7	METIS: $Z_{eff} = 1.5$	$Z_{eff} = 2.5$
#7337	22	24	26	26	32	19
#8555	50	27	23	26	16	30
#8556	57	38	34	43	62	79
#10806	59	56	60	65	106	145

σ^W	FL2	FL4	FL5	FL7	METIS: $Z_{eff} = 1.5$	$Z_{eff} = 2.5$
#7337	88	27	31	31	14	15
#8555	32	24	31	33	11	15
#8556	25	29	30	32	32	28
#10806	81	49	48	47	46	22

Table 4.5: **Above:** The mean values μ^W of δ^W of all four flux loops and METIS ($Z_{eff} = 1.5$ and 2.5) with respect to the EFIT W_{max} values calculated for different discharges. **Bottom:** Same as the upper Table, but for the standard devition σ^W of δ^W. The quantities are in percent [%].

μ^W	FL2	FL4	FL5	FL7	EFIT	METIS: $Z_{eff} = 2.5$
#7337	48	56	57	58	32	11
#8555	40	35	31	32	16	14
#8556	56	65	69	68	62	20
#10806	112	71	72	73	106	75
σ^W	FL2	FL4	FL5	FL7	EFIT	METIS: $Z_{eff} = 2.5$
#7337	78	45	50	49	14	7
#8555	36	19	26	29	11	7
#8556	29	36	37	36	32	4
#10806	39	36	35	34	46	46

Table 4.6: Same as Table 4.5 but W_{max} calculated from the METIS E_{tor} values with $Z_{eff} = 1.5$ is taken as reference.

reference, respectively.

First, it is observed that FL4 does not have the closest value to the simulations for all the examples, as sometimes it is FL2 or FL5. Moreover, the discrepancies can be quite different, as for the discharge #8556. Next, in comparison to both METIS options, the EFIT has systematically smaller δ^W values. Again, METIS with $Z_{eff} = 2.5$ is closer to measurements as in the above, except for the slide-away discharge #10806. The discharge #7337 has similar μ^W values as discharge #9814 reported above, which could be expected as they are of the same type, i.e. discharge with a negligible amount of RE. Furthermore, μ^W for the RE discharge #8555 are not much different from #7337. Finally, the δ^W for the other 2 discharges is

μ^W	FL2	FL4	FL5	FL7	EFIT	METIS: $Z_{eff} = 1.5$
#7337	42	38	37	38	19	11
#8555	31	37	33	32	30	14
#8556	57	69	74	69	79	20
#10806	159	88	84	79	145	75
σ^W	FL2	FL4	FL5	FL7	EFIT	METIS: $Z_{eff} = 1.5$
#7337	45	39	43	42	15	7
#8555	29	14	17	19	15	7
#8556	30	37	37	40	28	4
#10806	8	38	39	39	22	46

Table 4.7: Same as Table 4.6 but $Z_{eff} = 2.5$ is taken for METIS.

larger than before, especially in the case of the slide-away discharge #10806. This is important to notice, as magnetic diagnostics could be influenced by RE, if RE are large in their population or their net kinetic energy. Moreover, V_{loop} measurement is one of the key parameters to detect slide-away and/or Parail-Pogutse regimes as in #8556 and #10806. Consequently, large discrepancy between experiment and models in the RE-relevant types of discharges is critical for RE studies.

4.4 Conclusions and Outlook

To summarise, the knowledge of W_{max} should be as precise as possible for more reliable the RE studies, as W_{max} is a contributor for the further RE-related calculations - e.g. RE distribution function, RE current (see Chapter 5) and synchrotron radiation (see Chapter 6). It can be seen from Section 4.1.2 that W_{max} is a non-linear function of E_{tor} or V_{plasma}. Therefore, analysis of how the different E_{tor} estimates available at COMPASS are influencing W_{max} was performed here.

A detailed analysis was done for the discharge #9814, where V_{plasma} was taken from the four operational flux loops in the COMPASS tokamak, EFIT and METIS code and Fujita's correction. It was shown that the V_{plasma} from flux loop FL4 gives closer values of W_{max} compared to the ones obtained using V_{plasma} from simulations, that the V_{plasma} from EFIT has the closer W_{max} compared to the ones obtained from measurements than METIS and that METIS gives closer W_{max} compared to the ones from measurements using $Z_{eff} = 2.5$. Moreover, Fujita's correction has acceptable difference in W_{max} estimate, but still too large for making it of any importance. This is important to notice, as there are few simple analytic corrections on V_{plasma} in the literature that are taken without considering or at least mentioning the introduced error. Finally, the error into W_{max} estimate introduced mutually between the codes was around 25%, which is practically a tolerable discrepancy for tokamak plasmas.

Noticeable difference between W_{max} estimates for the RE-relevant discharges in respect to the RE-free discharges are visible by both codes for RE and Parail-Pogutse discharges, while the error is high for the slide-away discharge. In all cases analysed, EFIT showed to be closer to the measured changes. Especially in the case of slide-away discharge #10806, where the mean value μ^W of δ^W for METIS is over 70% for $Z_{eff} = 1.5$, i.e. over 80% for $Z_{eff} = 2.5$.

Furthermore, we recovered that both simulations give a profile of toroidal electric field E_{tor}. However, the EFIT takes only MHD equilibrium, while the METIS has more physical constraints.

Finally, important to mention is that the METIS is coupled with the LUKE code (see Section 2.1.6) for simulation of the RE distribution function evolution. Therefore, even though EFIT seems to estimate the W_{max} closer

to the measured estimates, for the sake of consistency with LUKE, W_{max} from METIS E_{tor} will be used for the purposes of this Thesis. Notice again that the error between EFIT and METIS is still in the acceptable range. The Z_{eff} used in this Thesis will be 2.5, as it has lower difference δ^W with EFIT for almost all the analysed cases.

OUTLOOK. As mentioned above, E_{tor} from METIS code will be used in the further Chapters. Nonetheless, one should be aware that neither METIS nor any tool used here for estimating E_{tor} is the perfect one, especially inside the tokamak plasma with a significant RE current. Indeed, for proper knowledge of E_{tor} a self-consistent modelling that includes interaction between plasma and RE beam using all possible magnetic diagnostics would be the best approach, but this is out of scope of this Thesis. Anyhow, the goal of this Chapter was not to solve the issue of defining E_{tor}, but rather to examine the different accessible tools for the E_{tor} estimation at COMPASS and present their consequences on the W_{max} calculation.

Maybe the first logical step could be application of equations (4.59) and (4.60) from Ref. [143]. Application of a model reported in Ref. [113,144, 145] or a model used at DIII-D by Yu [81] would present a more advanced approach. All proposed solutions should have proper knowledge of self-inductances L and mutual inductances M from plasma and RE beam to the diagnostics and between themselves. Notice that Yu [81] probably used the RE beam in the V_{plasma} model only (as described above) when he analysed the post-disruptive RE beam. However, if one has only the RE beam, METIS and EFIT should also give reliable results with some changes in the coding. The problematic point is when the plasma and the RE beam are combined.

In this Chapter only limited plasma has been considered, as all analysed discharges in the Thesis will have limited plasma. A diverted plasma has different distances to the flux loops, therefore it is to be seen whether a different flux loop than FL4 should be used for the fast E_{tor} estimation.

Furthermore, the analytic approximation for the Dreicer growth rate (see Eq. 2.4) is highly dependent on the strength of the electric field E_{tor}. Therefore, one should take care when estimating the E_{crit} experimentally, as in Ref. [48], because proper generation rate and theoretical calculation of the E_{crit} are directly dependent on the experimental values of the E_{tor}.

Finally, the loop voltage is not the only RE-relevant magnetic diagnostics, as it can be seen from Section 3.3.1. For example, the pick-up coils in the COMPASS tokamak could be used to localise the RE beam, when RE carry an observable amount of the total current.

Chapter 5

Discharges with Significant Runaway Electron Current

The discharges with high RE current I_{RE} reported in Section 3.4.1 will be analysed in this Chapter, i.e. the discharge where plasma and RE beam coexist. The Chapter will start with an experimental observation of the RE beam coming from the very first RE dedicated campaign. Theoretical models and detailed description of the setting used in the models for comparison with the experiments are reported then. The first experimental analysis will be an estimation of the RE current I_{RE}. Subsequently, influence of the REs on the current ramp-up phase of the discharge is evaluated. Following, a principle on how to localise RE beam is done in the next Section, using the knowledge of the RE beam current and its maximum energy. Finally, the conclusion is given in the last Section with discussion on expected future works.

Note that the Section 7.6 could also be part of this Chapter, as it uses the analysis reported herein. However, due to the importance of the long discharges for MGI experiments, the Section is part of Chapter 7.

5.1 Experimental Observations

The first magnetic observations of high RE current in the COMPASS tokamak were reported in Ref. [146]. The discharge #7298 was used in the reference, which had circular-shaped limited plasma, with toroidal magnetic field $B_{tor} = 1.15\,\mathrm{T}$ and plasma current $I_p = 120\,\mathrm{kA}$. The plasma density feedback was not working due to an interferometer failure, which resulted in $n_e < 1.5 \times 10^{19}\,\mathrm{m}^{-3}$ in the plasma core as measured by the

Thomson Scattering system. We will now show the RE observations made for that discharge in more elaborate details than in Ref. [146]. The main measurements are shown in Fig. 5.1.

The loop voltage V_{loop} is presented in Fig. 5.1a. It is clearly seen that the V_{loop} during the current flat-top phase (between 1050 and 1220 ms) is lower than 1 V. Typical values in the COMPASS tokamak are between 1 and 2 V. The low V_{loop} values compared to the "standard ones" are a trace of the non-inductive current driver, i.e. the RE beam in the case of the presented discharge.

Furthermore, a constant plasma current I_p during the current flat-top

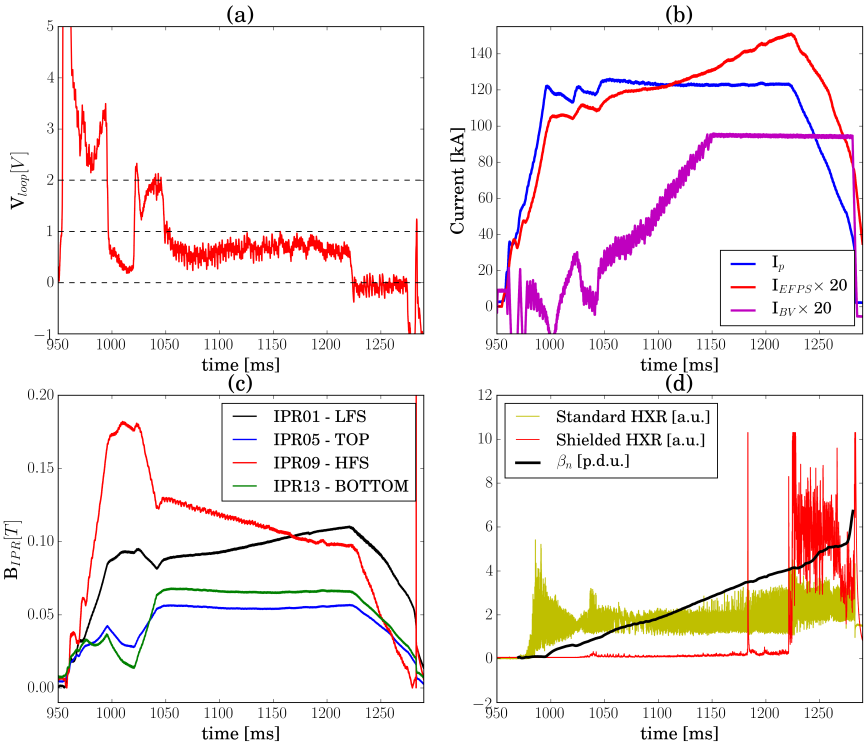

Figure 5.1: **The time traces from the discharge #7298: (a)** the loop voltage V_{loop} with highlighted V_{loop} values at 0 V, 1 V and 2 V; **(b)** the plasma current I_p (blue) and the currents going through two radial stabilisation poloidal field coil systems multiplied by 20 for rescaling purpose - I_{EFPS} (red) and I_{BV} (magenta); **(c)** pick up coils, i.e. IPRs, located at LFS (black), top (blue), HFS (red) and bottom (green); **(d)** the normalised pressure β_n (black) in the procedure defined units (p.d.u.) and the HXRs signals showing the RE losses.

phase can be observed in Fig. 5.1b. In addition, it is obvious from Fig. 5.1c that the signal of the IPR coils[1] at the low field side (LFS) increases, while the signal from IPR at HFS decreases during the current flat-top phase. The other two IPRs located at the bottom and the top of the vessel and they measure constant signal during the current flat-top phase. This is due to the outward movement of the RE beam. As a result, an external vertical field for radial stabilisation[2] I_{EFPS} and I_{BV} increase (see Fig. 5.1b), creating an inward force to keep the plasma and the RE beam confined and stable. Note that the I_{BV} saturates around 1150 ms.

The proof of a significant RE presence can be seen from Standard HXR and Shielded HXR[3] signals, shown in Fig. 5.1d. Unfortunately, dynamics of the RE losses with low energies cannot be seen due to a saturation of the Standard HXR electronics. Nonetheless, constant losses are observed from the Standard HXR signal. Interestingly, Shielded HXR shows that almost all REs with energies over 1 MeV are lost at the very end of the discharge, i.e. during the current ramp-down phase. The late loss of high energy REs means their good confinement during the discharge. This is a typical observation in COMPASS if the Parail-Pogutse instability does not occur or if the plasma density is not increased.

In the end, the EFIT reconstruction[4] also demonstrates a certain behaviour when the RE beam is present in the plasma. Particularly, an overestimate of the plasma pressure β_n is the best indicator. The β_n is the normalised *plasma beta* β_p

$$\beta_p = \frac{\langle p_{pl} \rangle_V}{B^2/2\mu_0} \tag{5.1}$$

normalised to two machine parameters (the minor radius a_p and the toroidal magnetic field B_{tor}) and one plasma parameter (the plasma current I_p):

$$\beta_n = \frac{\beta_p}{I_p/a_p B_{tor}}. \tag{5.2}$$

The typical value of β_n for a limited plasma is less than 1. Knowing this, the overestimate of β_n is obvious from Fig. 5.1d, where β_n goes up to 6 at the end of the discharge. Looking at Eq. 5.2, it is clear that EFIT also predicts an additional pressure to which the vertical field EFPS is reacting. Note that the additional pressure due to the RE beam comes from the inertia, i.e. it is not of thermal origin as for the bulk plasma $\langle p \rangle_V$. Furthermore, β_n

[1] For more details about the IPR coils in the COMPASS tokamak see Section 3.3.1.

[2] There are two such systems in the COMPASS tokamak. Slower but strong system is denoted as EFPS (Equilibrium Field Power Supply), while faster but weaker one is denoted as BV (magnetic field B Vertical).

[3] For more details about the HXR diagnostics in the COMPASS tokamak see Section 3.3.2.

[4] For more details about the EFIT reconstruction at the COMPASS facility see Section 3.1.

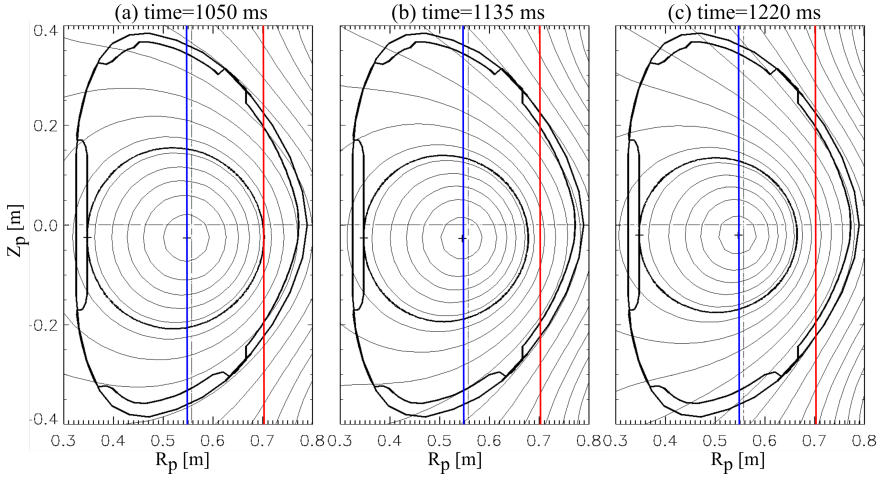

Figure 5.2: Poloidal cross-sections of the plasma reconstructed by the EFIT simulation. The major axis of the COMPASS tokamak is located on the left of the pictures. The bolded magnetic field line represents the plasma separatrix or the last closed field surface. Three different times are presented: **(a)** 1050 ms as the beginning of the flat-top phase, **(b)** 1135 ms as the middle of the flat-top phase and **(c)** 1220 ms as the end of the flat-top phase. Blue and red vertical lines map the I_p baricenter and the LFS border point at the 1050 ms, respectively.

increases by about 5 times, while I_{EFPS} is increased by approximately 25% during the current flat-top phase. This can be explained by the average decrease of the net vertical field imposed on plasma due to the RE beam itself, as reported in Ref. [147]. The cause of the vertical field decrease is the RE beam influence on the poloidal magnetic field profile, which is increased outside and decreased inside the RE orbits. In other words, RE beam changes the magnetic topology in such manner that it helps its own confinement.

Moreover, the plasma shrinkage can be seen from the EFIT 2D reconstruction of the magnetic fields in Fig. 5.2. At the beginning of the current flat-top phase at 1050 ms the difference between the plasma geometrical and plasma current centers follows the famous Shafranov shift[5] [114]. However, after 85 ms the plasma size is decreased, while the I_p barycenter is practically unchanged. The difference is even more pronounced at the end of the current flat-top phase at 1220 ms. The apparent relative outward shift of the plasma baricenter cannot be explained via the Shafranov shift anymore but through the existence of the RE beam in the outer (low field side) plasma region. The equilibrium deformation due to the RE beam was studied by

[5] Rearrangement of the flux surfaces center outwards due to the plasma pressure.

Yoshida [147], where the aforementioned shift is plotted in Fig. 8. Also note that the stronger radial force generated by the vertical stabilising field EFPS leads to the lower plasma volume, which is also seen from Fig. 5.2.

5.2 Theories and Data Used

The previous Section presents a qualitative interpretation of the experimental data. The quantitative evaluation for the RE beam discharges will be done in the upcoming Sections. Namely, a concise synopsis of RE generation theory and model used in the Thesis are presented in this Section. Theories can be used for comparison of either the RE density n_{RE} or RE current I_{RE}. However, to estimate I_{RE} one usually needs n_{RE} [142, Eq. 7]:

$$I_{RE} = ec \langle n_{RE} \rangle \langle \beta \rangle A_{RE}, \tag{5.3}$$

where A_{RE} is the area of the RE beam cross-section and the angle brackets $\langle \ \rangle$ denote the average in spatial and velocity space. Therefore, to avoid assumption on A_{RE} and knowing that n_{RE} is a direct output of the theories and calculation from the experiment - comparison of only n_{RE} is conducted here.

The Kruskal-Bernstein formula (defined in Eq. 2.4):

$$\frac{\mathrm{d}n_{RE}}{\mathrm{d}t} \sim \frac{n_e^2 e^4 \ln\Lambda}{4\pi\varepsilon_0^2 m_e^2 v_{th,e}^3} \mathcal{E}_{\mathcal{D}}^{-3(1+Z_{eff})/16} \exp\left(-\frac{1}{4\mathcal{E}_{\mathcal{D}}} - \sqrt{\frac{1+Z_{eff}}{\mathcal{E}_{\mathcal{D}}}} \right) \tag{5.4}$$

is taken here as an analytic solution for the RE growth rate, since it is most commonly used in the literature in the past decades. In addition to the Dreicer mechanism, avalanche RE generation will also be added to the existing seed using an analytic estimate derived by Rosenbluth and Putvinski [28]

$$\frac{1}{n_{RE}} \frac{\mathrm{d}n_{RE}}{\mathrm{d}t} = \frac{e(E_{tor} - E_{crit})}{2mc \ln\Lambda}. \tag{5.5}$$

It is clear from both Eqs. 5.4 and 5.5 that they are most sensitive to the toroidal electric field (incorporated in $\mathcal{E}_{\mathcal{D}} = E_{tor}/E_D$ for Eq. 5.5).

The E_{tor} will be taken from METIS due to the reasons described in Chapter 4, where we also justify why $Z_{eff} = 2.5$ should be used. The next important parameter beside Z_{eff} is the electron density n_e. The density can be taken from the interferometer[6] measurement as the line-average measurement $\bar{n}_e$, which can also be estimated from the Thomson Scattering data $\bar{n}_{e,ts}$. Additionally, Thomson Scattering gives the density in the plasma core $n_{e,c}$, where the RE generation has largest probability to occur. The last necessary parameter from measurements in the Eq. 5.4 is the

[6] See Section 3.3.1 for details about interferometer and Thomson Scattering set-up in the COMPASS tokamak.

electron temperature T_e, appearing through the definition of the thermal velocity $v_{th,e} = \sqrt{2T_e[\mathrm{eV}]/m_e}$. T_e in COMPASS tokamak is only measured by the Thomson Scattering, thus estimates of the line-averaged $T_{e,ts}$ or core $T_{e,c}$ are available from the measured T_e-profile. Therefore, for consistency purpose, between n_e and T_e and knowing that most of REs are generated at the plasma core - $n_{e,c}$ and $T_{e,c}$ will be taken.

The NORSE code [38] has intrinsically implemented time-evolution of E_{tor}, n_e, T_e, B_{tor} and Z_{eff}. Advantageous usage of the NORSE code for this Chapter is its design requirement to work in slide-away regime (i.e. very low n_e)[7]. The key point of NORSE is its non-linearity with respect to the bulk electron temperature T_e. On the other hand, NORSE lacks spatial distribution and toroidal effects. Presently, NORSE takes into account only the Dreicer mechanism[8] and the implementation of the avalanche mechanism[9] is underway. Furthermore, the input data for NORSE are also taken from METIS in the same manner as for Kruskal-Bernstein theory above. The electron density n_e, temperature T_e and E_{tor} are taken as time-varying parameters, while Z_{eff} and B_{tor} are constant. Finally, the n_{RE} is computed by multiplying the total electron density from measurements $n_{e,c}$ with the RE fraction calculated by NORSE.

5.3 RE Current

The β_n overestimate for the discharge #7298 reported in Section 5.1 will be exploited here for the estimate of the RE current I_{RE}. The analysis will be based on work done by Fujita *et al.* [142]. Even though the basic principle done here is the same as Fujita's, the calculation is different as he theoretically estimated all the parameters, while we have measurements from EFIT and Thomson scattering. Therefore, the estimation of I_{RE} using poloidal beta β_{pol} (defined in Eq. 5.6), the influence of different RE distribution functions and pitch angles θ will be addressed first. The result for different β_{pol} estimates, RE distribution functions and pitch angles θ will follow. Finally, a comparison of the experimental results with the theory and code is shown.

5.3.1 Methodology

The normalised beta β_n parameter is typically used to illustrate the existence of a RE beam. The β_n is directly connected to the plasma beta β_p through Eq. 5.2, which furthermore can be split into two parts - toroidal and poloidal:

$$\frac{1}{\beta_p} = \frac{1}{\beta_{tor}} + \frac{1}{\beta_{pol}}. \tag{5.6}$$

[7] Note that the NORSE code can be used for any plasma regime.
[8] See Section 2.1.1 for more details about the Dreicer mechanism.
[9] See Section 2.1.3 for more details about the avalanche mechanism.

The toroidal beta β_{tor} is the main contributor to the β_p in tokamaks, as the toroidal magnetic field B_{tor} is typically larger by an order of magnitude than the poloidal magnetic field B_{pol} (see Eq. 5.1). However, β_{pol} is still an important parameter as the vertical stabilising magnetic field B_{EFPS} is affected by its value [148]

$$B_{EFPS} = \frac{\mu_0 I_p}{4\pi R_p}\left[\ln\left(\frac{8R_p}{a_p}\right) + \Lambda - \frac{1}{2}\right] \tag{5.7}$$

through the so-called Shafranov lambda $\Lambda = \beta_{pol} + l_i/2 - 1$ parameter.

Moreover, knowing the total overestimated plasma pressure

$$\langle p_{tot}\rangle_V = \frac{2\mu_0\beta_{pol}}{B_{pol}^2} \approx 5\times 10^{-6}\frac{\beta_{pol}}{\pi}\left(\frac{I_p}{a_p}\right)^2 \tag{5.8}$$

from the EFIT and pure contribution of the Maxwellian bulk plasma pressure $\langle p_{pl}\rangle_V$ from the Thomson scattering measurements, one can deduce the RE pressure

$$P_{RE} \equiv \langle p_{RE}\rangle_V = \langle p_{tot}\rangle_V - \langle p_{pl}\rangle_V . \tag{5.9}$$

Furthermore, RE pressure can be connected to the RE energy W_{max} (through γ) and the RE density n_{RE} [149]:

$$\langle p_{RE}\rangle_V = \frac{1}{2}m_e\langle n_{RE}\rangle\left\langle\gamma v_\parallel^2\right\rangle + \frac{1}{4}m_e\langle n_{RE}\rangle\left\langle\gamma v_\perp^2\right\rangle, \tag{5.10}$$

where $v_\parallel$ and $v_\perp$ denote the RE velocity in the parallel and perpendicular direction to the magnetic field $\vec{B}$, respectively. By estimating the RE energy as in Section 4.1.2 one can estimate the RE density $\langle n_{RE}\rangle$ from Eq. 5.10.

RE Pressure Calculation

Practically, METIS has all the outputs that EFIT has, hence betas and the pressures can also be taken from the METIS code. Moreover, Fujita *et al.* [142] estimated the average plasma pressure $\langle p_{pl}\rangle_V$ theoretically, while on COMPASS tokamak one can obtain the $p_{pl}(r)$ profile using Thomson scattering measurements of the T_e and n_e profiles. Then, one obtains $\langle p_{pl}\rangle_V$ experimentally through (Eq.1.3 in Ref. [150]):

$$\langle p_{pl}\rangle_V = \frac{2}{a_p^2}\int_0^a {}_p p_{pl}(r) r\mathrm{d}r. \tag{5.11}$$

Additionally, β_{pol} can be estimated from Eq. 5.7 knowing B_v and l_i. The vertical field B_v varies with the machine radius, which could complicate the calculations. Due to simplicity the B_v will be estimated at the vacuum vessel center

$$B_v[\mathrm{mT}] \approx 10.7[\mathrm{mT/kA}]I_{EFPS}[\mathrm{kA}] + 2.0[\mathrm{mT/kA}]I_{BV}[\mathrm{kA}], \tag{5.12}$$

where coefficients in front of I_{EFPS} and I_{BV} can be found in Ref. [143] on pages 44 and 51, respectively. The internal inductance l_i can be either estimated assuming $j_p(r)$ profile peaking or be taken from EFIT and METIS. Here, only the latter case is considered, i.e. the l_i is taken from the reconstruction codes.

Five different β_{pol} estimates for discharges #8553 and #7298 are plotted in Fig. 5.3. The discharge #8553 presents the reference discharge with a negligible amount of REs and it is chosen due to its relevance in the upcoming Sections. From Fig. 5.3a, one can see that during the flat-top phase ($1050-1180$ ms) EFIT gives around 35% and 60% larger β_{pol} estimate than Thomson scattering and METIS, respectively, while the difference between Thomson scattering and METIS themselves is less than 20%. Furthermore, the poloidal beta estimates from the vertical field B_v have calculation artefacts at the beginning and the end of the discharge. Those artefacts are probably coming from the over-simplified nature of Eqs. 5.7 and 5.12 used here. The β_{pol} using l_i from EFIT has about 30% larger values from EFIT, while estimate with l_i from METIS has good matching with EFIT β_{pol} during the flat-top phase. However, the comparison of the β_{pol} directly from EFIT and β_{pol} from B_v using l_i from METIS has a debatable consistency. For now, looking at all five β_{pol} estimates for discharge without REs we note that the discrepancy factor is larger than 2, which will bring the need to choose the proper calculation.

Let us now see what the β_{pol} estimates are for the RE beam discharge #7298. As for β_n from Fig. 5.1d, EFIT also overestimates β_{pol}. The overestimate is also seen using the B_v calculation. As expected, β_{pol} from Thomson scattering is very low since it observes only bulk plasma electrons ignoring the RE population[10]. Interestingly, β_{pol} from METIS simulation is similar to EFIT β_{pol} and the β_{value} value from the B_v at the beginning of the discharge, but during the flat-top phase METIS can not estimate the β_{pol} rise and follows the trend of the β_{pol} from the Thomson scattering, i.e. of the bulk plasma only.

Finally, both β_{pol} from B_v estimation will be omitted due to the artefacts at the end of the discharges. Moreover, METIS β_{pol} will also be omitted as it does not predict the β_{pol} rise measured by the magnetic diagnostics. Therefore, β_{pol} from EFIT will be used to estimate the total pressure $\langle p_{tot} \rangle_V$ of the bulk plasma and the RE beam together, while the pressure estimate from the Thomson Scattering measurements will be taken for the bulk plasma pressure $\langle p_{pl} \rangle_V$. As discrepancy between the EFIT and the Thomson Scattering β_{pol} measurement is around 40% (see explanation for Fig. 5.3a) - it will be taken as the threshold value for the I_{RE} calculation. The upper limit will be set to 100%. In other words, the I_{RE} will be calculated when conditions $\langle p_{tot} \rangle_V > 1.4 \langle p_{pl} \rangle_V$ and $\langle p_{tot} \rangle_V > 2.0 \langle p_{pl} \rangle_V$ are satisfied and the average between them will be taken as the final I_{RE}

[10]The reason why COMPASS Thomson scattering system does not observe RE population is elaborated in more details in Section A.2.

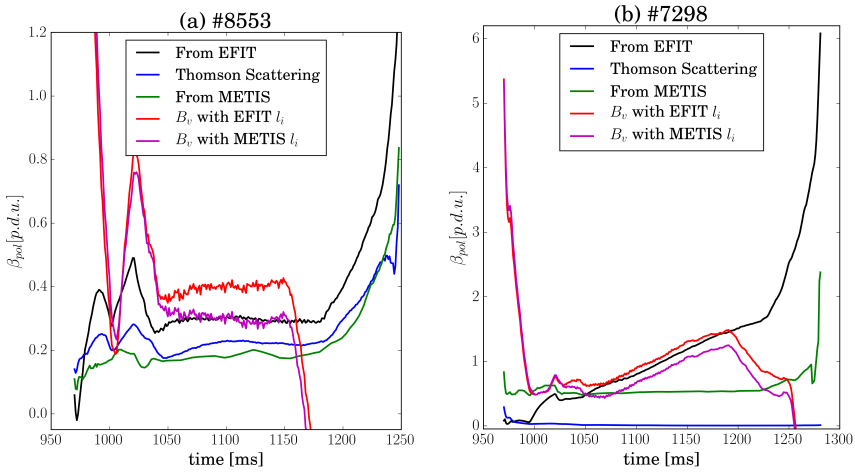

Figure 5.3: The time traces of the poloidal beta β_{pol} signals for discharges **(a)** #8553 and **(b)** #7298. The β_{pol} is taken from EFIT (black) and METIS (green), calculated from Thomson scattering (blue) using Eq. 5.11 and from B_v (red and magenta for l_i from EFIT and METIS, respectively) using Eqs. 5.7 and 5.12. Note the difference in the scale of y-axis in the two graphs.

value.

Different RE Distribution Functions

Fujita also investigated the influence of different RE distribution functions (REDF) on the I_{RE} calculation. The REDF he used were monoenergetic f_{mono}, uniform f_{uni}, linear f_{lin} and quadratic f_{quad} that could seem quite simplistic from a perspective of the present knowledge of a RE generation dynamics. Namely, most of the codes predict the existence of an RE accumulation at higher energies. This part of the REDF is often addressed as a *bump* in the REDF. The most recent study regarding the bump formation was done by Decker *et al.* in Ref. [151] using the LUKE and CODE codes[11]. The drag force by synchrotron radiation was investigated as the limiting factor and the source of bump formation.

More importantly, the location of the bump in the perpendicular normalised momentum $\bar{p}_{\|} = p_{re}\cos\theta/m_e c$ space is

$$\bar{p}_{\|,b} \approx \frac{1}{1+Z_{eff}} \frac{(\mathcal{E}_{crit}+\sigma_r)(\mathcal{E}_{crit}-1)}{\sigma_r}, \tag{5.13}$$

[11] See Section 2.1.6 for more details about LUKE and CODE.

where σ_r is defined

$$\sigma_r = \frac{2}{3\ln\Lambda}\left(\frac{\Omega}{\omega_{pe}}\right)^2 \approx 0.097\frac{B_{tor}^2}{n_e[10^{20}\,\mathrm{m}^{-3}]} \tag{5.14}$$

through the fundamental electron cyclotron frequency Ω and the plasma frequency ω_{pe}. The extreme values (but realistic for COMPASS) are used here to examine a possible bump occurrence in the COMPASS tokamak. To examine the bump occurrence, one needs first to see what the lowest $\bar{p}_{\parallel,b}$ or the corresponding $W_{bump} = mc\sqrt{1+\bar{p}_{\parallel,b}}$ is (assuming a pitch angle $\theta = 0$) and compare it to the expected W_{max}. To minimise the bump energy W_{bump}, one needs to maximise Z_{eff}, n_e, B_{tor} and to minimise E_{tor}. Using $\ln\Lambda = 15$, $Z_{eff} = 2.5$, $n_e = 10^{20}$ m^{-3}, $B_{tor} = 1.15$ T and $E_{tor} \sim 0.14$ V/m (corresponding to $V_{loop} = 0.5$ V) a $W_{bump} \approx 70$ MeV is obtained. Knowing that for a typical length of COMPASS discharges the RE do not obtain more than $40 - 50$ MeV, it is highly probable that REDF in the COMPASS plasma does not have the bump-like tail. Moreover, the electron density of $n_e = 10^{20}$ m^{-3} is not relevant at all for the RE studies and more realistic values would be under 2×10^{19} m^{-3}. For comparison, this 5 times lower density rises W_{bump} 10 times, i.e. to over 700 MeV. Henceforth, the bump-like tail will not be assumed in the simulated REDF used in this Thesis and so REDFs investigated by Fujita seem realistic enough for COMPASS after all. However, out of four REDF used by Fujita, the quadratic one f_{quad} will not be used in this work. Instead, a more realistic exponential REDF will be assumed.

The definitions of the other three distributions as functions of RE energy w are as follows:

$$\begin{aligned} f_{mono}(w) &= \delta(W_{max}), \\ f_{uni}(w) &= \frac{1}{W_{max}}, \\ f_{lin}(w) &= \frac{2}{W_{max}}\left(1 - \frac{w}{W_{max}}\right). \end{aligned} \tag{5.15}$$

The coefficients come from setting the REDF maximum value to 0 at W_{max} and then normalising the REDF to 1. Furthermore, three additional REDF will be introduced here: exponential f_{exp}, skewed Gaussian f_{sG} and Maxwell-Jüttner f_{MJ} distribution. As all the three functions have asymptotic behaviour towards zero, the detailed calculation of the corresponding parameters will be given next. As an illustration, all the five non-monoenergetic REDF are plotted in Fig. 5.4 for $W_{max} = 10$ MeV.

As already mentioned, the exponential REDF f_{exp} is introduced instead of f_{quad} to present a distribution with a steep decrease that could be important if the avalanche mechanism were to dominate. The exponential REDF is defined as

$$f_{exp}(w;\epsilon) = \epsilon e^{-\epsilon w}, \tag{5.16}$$

where it is obvious that $f_{exp}(+\infty) \to 0$. To determine the arbitrary parameter ϵ, the condition is $f_{exp}(W_{max}) \leq 10^{-5}$, from where ϵ coefficient is calculated through iterations with a precision of 10^{-5}. Note that larger ϵ corresponds to lower W_{max}.

The (negatively) skewed Gaussian represents a more realistic case than f_{mono}, as it not a delta-function. In other words, the negatively skewed Gaussian represents REDF where almost all RE tend towards W_{max} but they never reach it. It also has an exponential rise with the RE energy w, hence it could also be presented as contrary to the exponential one. Even though simpler linear or exponential rise could behave similarly, the skewed Gaussian is chosen due to its smooth drop towards W_{max}. This is more realistic than Heaviside-step-like ends in the case of linear or exponential rises. The skewed Gaussian definition

$$f_{sG}(w; l_{sG}, \zeta, \alpha_{sG}) = \frac{2}{\zeta} f_{Gpdf}(s) f_{Gcdf}(\alpha_{sG} s) \tag{5.17}$$

uses the Gaussian probability distribution function

$$f_{Gpdf}(s) = \frac{1}{\sqrt{2\pi}} e^{-s^2/2} \tag{5.18}$$

and Gaussian cumulative distribution function

$$f_{Gcdf}(\alpha_{sG} s) = \frac{1}{2}\left[1 + \mathrm{erf}\left(\frac{\alpha_{sG} s}{\sqrt{2}}\right)\right] \tag{5.19}$$

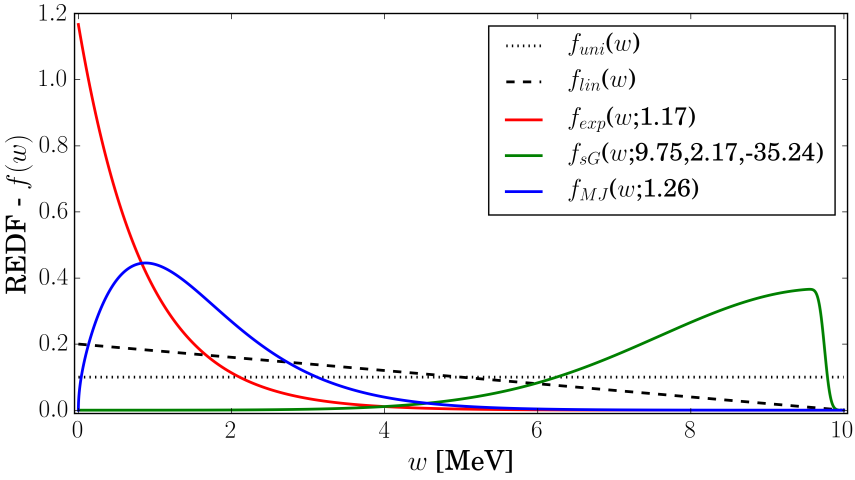

Figure 5.4: The non-monoenergetic RE distribution functions as function of the energy w: uniform f_{uni} (black dotted), linear f_{lin} (black dashed), exponential f_{exp} (red), skewed Gaussian f_{sG} (green) and Maxwell-Jüttner f_{MJ} (blue).

where

$$\mathrm{erf}(x) = \frac{1}{\sqrt{\pi}} \int_{-x}^{x} e^{-t^2} \mathrm{d}t \tag{5.20}$$

is the error function, $s = (w - l_{sG})/\zeta$, l_{sG} is the location parameter of f_{sG}, ζ is the scale parameter of f_{sG} and α_{sG} is the skewness of f_{sG}. To have hard limit on the positive end of the REDF, a negative skewness α_{sG} is used. f_{sG} is found numerically in such way that its maximum is located over $w = 0.95 W_{max}$ and $f_{sG}(W_{max}) < 10^{-5}$. The location parameter l_{sG} estimate accompanies the α_{sG} one. The f_{sG} tends to 0 towards infinity with the same sign as α_{sG}, so it is negative in our case. As there is no negative energy, the scale parameter ζ is chosen so that satisfies $f_{sG}(0) < 10^{-5}$. One could say from Fig. 5.4 that f_{sG} has a bump-like shape, but it is not connected to the bump formation of REDF discussed earlier in the Section.

The Maxwell-Jüttner distribution function f_{MJ} is also selected, as it is one of the most common relativistic distribution function. f_{MJ} is defined through the normalised particle energy $\mathcal{W} = w/m_e c^2$ as

$$f_{MJ}(w; \mathcal{W}) = \frac{\beta \gamma^2}{\mathcal{W} K_2(1/\mathcal{W})} e^{-\gamma/\mathcal{W}} \tag{5.21}$$

where K_2 is the modified Bessel function of the second order. $\mathcal{W}$ is chosen so that inequality $f_{MJ}(W_{max}) < 10^{-5}$ stands. It could be the most important REDF for the slide-away regime as it gives a relativistic Maxwellian with a maximum much lower than W_{max}.

Effect of the Pitch Angle

Eq. 5.10 indicated that the pressure separation through the velocities $v_\parallel$ and $v_\perp$ implies knowing the pitch angle θ. Fujita *et al.* omitted the $\langle \gamma v_\perp^2 \rangle$ term and approximated the other one $\left\langle \gamma v_\parallel^2 \right\rangle$ by $c \langle \gamma \beta^2 \rangle$. However, we will consider the θ influence to be consistent with the estimation of W_{max} reported in Section 4.1.2, where θ plays a role through the parameter $\eta \propto \langle \beta_\perp \rangle / \left(\langle \gamma \rangle \left\langle \beta_\parallel^2 \right\rangle \right)$.

Table 5.1 shows the influence of different REDFs on essential parameters for I_{RE} calculation. Firstly, it is important to state that averages done in Table 5.1 are done for energy span from 0 to W_{max} using the mean of any function/variable U:

$$\langle U \rangle = \int_0^{W_{max}} U * f_{REDF} \mathrm{d}U, \tag{5.22}$$

i.e. neglecting the RE limit at lower energies. The error is negligible due to the high W_{max} reached in the COMPASS discharges in a matter of milliseconds. Typically $W_{max} > 10\,\mathrm{MeV}$ before the ramp-up phase ends.

Table 5.1: Comparison of parameters (RE energy w, relativistic β, the term from Eq. 5.10 $\langle\beta\rangle = \left\langle\beta_{\parallel}^2\gamma\right\rangle + 0.5\left\langle\beta_{\perp}^2\gamma\right\rangle$ and drift term η for W_{max} estimation) averaged over w for different REDFs.

			$\langle\beta^2\gamma\rangle$		$\langle\eta\rangle$	
REDF	$\langle w\rangle$ [MeV]	$\langle\beta\rangle$	$\theta = 0.0$	$\theta = 0.3$	$\theta = 0.1$	$\theta = 0.3$
f_{mono}	10.00	0.9988	20.5	19.6	4.91	15.8
f_{uni}	5.00	0.9721	10.6	10.2	9.55	30.7
f_{lin}	3.33	0.9497	7.30	6.98	13.9	44.7
f_{exp}	0.86	0.8141	2.18	2.09	43.8	140
f_{sG}	8.02	0.9980	16.6	15.9	6.05	19.4
f_{MJ}	1.58	0.9301	3.78	3.62	26.21	84.2

The average energy $\langle w\rangle$ is calculated for illustration, while $\langle\beta\rangle$ can be seen in Eq. 5.3. From the same equation one would expect that the exponential REDF has the smallest I_{RE} for the same P_{RE}, as it has the far smallest $\langle\beta\rangle$. However, due to the term $\left\langle\beta_{\parallel}^2\gamma\right\rangle + 0.5\left\langle\beta_{\perp}^2\gamma\right\rangle$ in Eq. 5.10 used for the $\langle n_{RE}\rangle$ estimation (by knowing P_{RE} in Eq. 5.10), the result is opposite. Namely, difference in $\beta^2\gamma$ from Table 5.1 of an order of magnitude creates much larger difference in estimated n_{RE} between REDFs than $\langle\beta\rangle$ does in Eq. 5.3. Therefore, even though the exponential has by far the smallest $\langle\beta\rangle$, it has the largest I_{RE}. Furthermore, even though two extreme values are taken for θ to investigate maximum possible effect from the corresponding variations, the difference is smaller than a few percent for every REDF. Furthermore, the aforementioned η is calculated for $\theta = \{0.1, 0.3\}$ rad, as it is zero at $\theta = 0$ rad. Here, a significant influence of the pitch angle is observed and it will be implemented in η for W_{max} calculation. Therefore, even though θ does not affect the I_{RE} estimate directly, it is important for more precise W_{max} estimation used as the REDF input that indirectly affects the I_{RE} estimation. Another expected thing that can be noted from Table 5.1 is that the most similar REDF to the monoenergetic one is the skewed Gaussian f_{sG} REDF as their parameters are close to each other.

5.3.2 Resulting I_{RE} for Discharge #7298

As already reported in Chapter 4, E_{tor} at the plasma center from METIS (with $Z_{eff} = 2.5$) is used here for W_{max} estimation where the pitch angle θ is taken to be 0.2 rad as a mean value found in Chapter 6. The RE minor radius a_{RE} for the RE area calculation A_{RE} is assumed to be constant and equal to 5 cm, as an approximate value of what is observed in discharge #9814 (analysed in Section 6.4). The METIS data and plasma pressure $\langle p_{pl}\rangle_V$ from Thomson scattering are interpolated and extrapolated to the EFIT time scale. As EFIT measures before the first and after the last Thomson

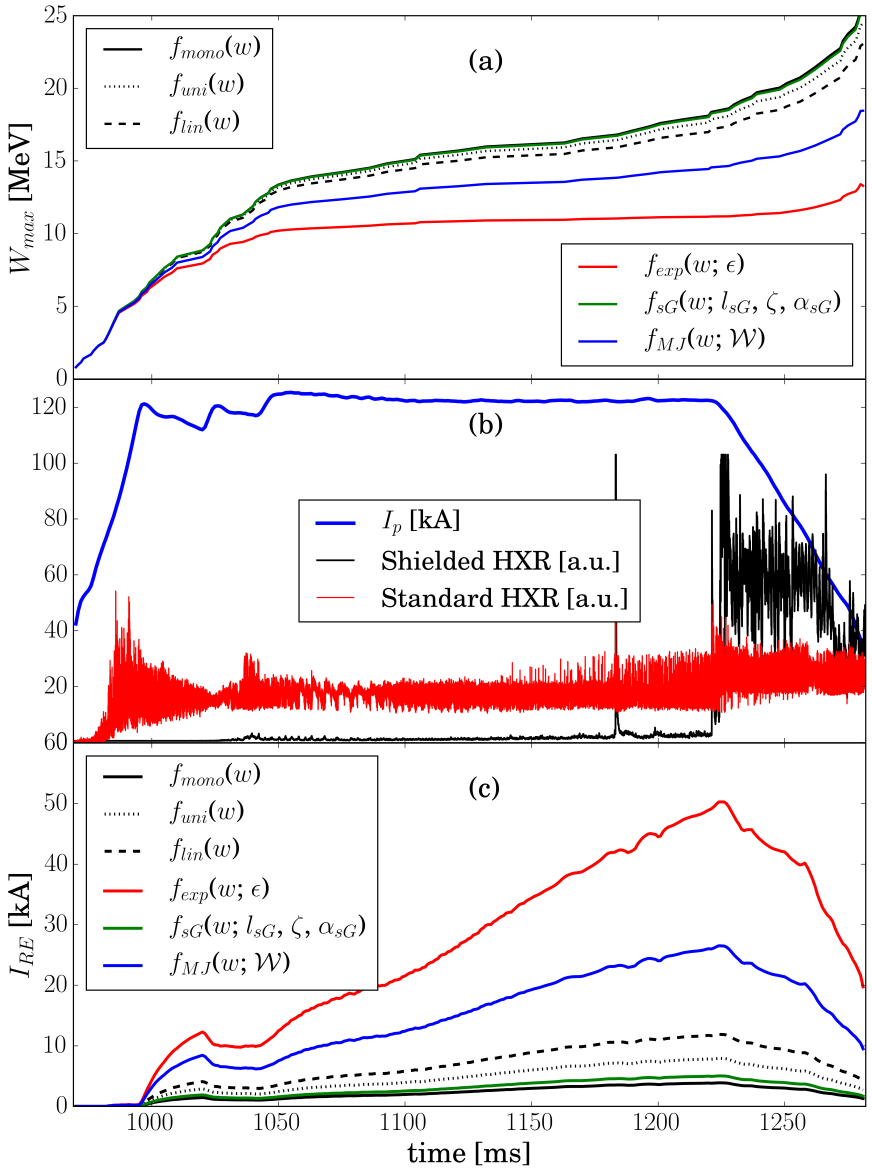

Figure 5.5: **(a)** The maximum kinetic energy W_{max} of discharge #7298 obtained for the different RE distribution functions: mono-chromatic f_{mono} (black solid), uniform f_{uni} (black dotted), linear f_{lin} (black dashed), exponential f_{exp} (red), skewed Gaussian f_{sG} (green) and Maxwell-Jüttner f_{MJ} (blue). **(b)** Time traces of the plasma current I_p (blue), Shielded HXR (black) and Standard HXR (red). **(c)** Estimated RE current I_{RE} corresponding to each RE distribution function with the same labeling as on (a).

Table 5.2: The calculated maxima of W_{max} and I_{RE} time traces, plotted in Fig. 5.5.

REDF	max (W_{max}) [MeV]	max (I_{RE}) [kA]
f_{mono}	25.61	3.9
f_{uni}	24.49	7.9
f_{lin}	23.05	11.9
f_{exp}	13.39	50.3
f_{sG}	25.37	5.0
f_{MJ}	18.54	26.5

scattering measurement, the first and the last point of the extrapolated $\langle p_{pl} \rangle_V$ are approximated to be 95% (arbitrarily taken)[12] of the first and the last Thomson scattering measurement, respectively. The main result is presented in Fig. 5.5.

The comparison between the W_{max} estimate coming from different RE distribution functions described in Section 5.3.1 is shown in Fig. 5.5a and their maximum values are tabulated in Table 5.2. Only W_{max} from the exponential f_{exp} and the Maxwell-Jüttner f_{MJ} distribution function are significantly different, as could be expected from the $\langle \eta \rangle$ values in Table 5.1.

The estimate of the RE current I_{RE} for different RE distribution functions are presented in Fig. 5.5c and their maximum values are listed in Table 5.2. The plasma current I_p is plotted in Fig. 5.5b for comparison purposes. In the same Figure, Shielded HXR and Standard HXR are also plotted. Even though β_{pol} from EFIT increases significantly during the ramp-down phase of the discharge (see Fig. 5.3), a relatively strong decrease in RE current I_{RE} can be seen in Fig. 5.5. This is a consequence of the current drop in the total plasma pressure $\langle p_{tot} \rangle_V$ calculation from EFIT in Eq. 5.8. It is interesting that the I_{RE} drop coincides with the RE losses seen from Shielded HXR signal, even though RE losses are not implemented in the calculation. Numerically, the I_{RE} drop is a calculation artefact as $\langle p \rangle_V$ depends on I_p^2 through B_{pol} if Eq. 5.1 is taken for solely poloidal part of the plasma beta. Physically, this can be connected to the additional RE energy limit due to the RE beam drift, which will be reported in Section 5.5. Next, notice that I_{RE} values span over 2 orders of magnitude - from a few kA to tens of kA. Moreover, even that f_{mono} is the most unrealistic of all the used RE distribution functions, it gives minimum I_{RE} as β, γ and η have extreme values. Therefore, we conclude that at least a few kA of current should definitely be driven by the REs in COMPASS discharge #7298. However, it is not possible to determine which REDF gives the most accurate RE current I_{RE} estimate from Fig. 5.5.

[12] The value is chosen in such manner to have the stable calculation and to not have a constant value as it is unrealistic in the ramp-up and the ramp-down phases.

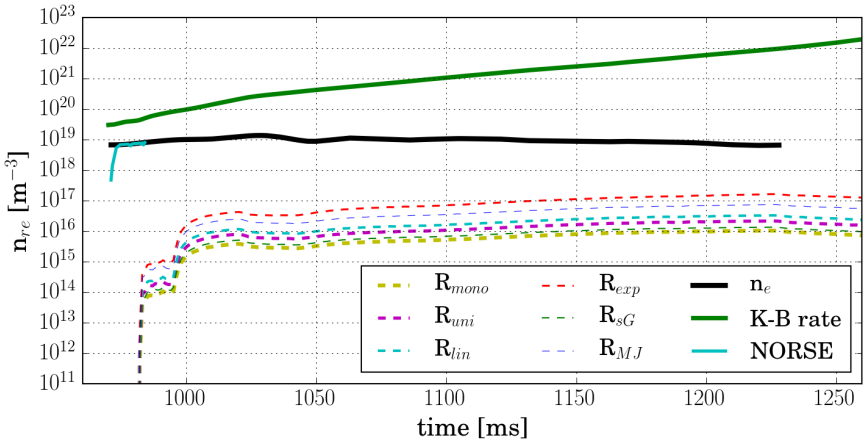

Figure 5.6: Time traces of total electron density (black), RE density from Kruskal-Bernstein theory (green), RE density from NORSE simulation (cyan) and RE densities corresponding to RE currents from Fig. 5.5c. (dashed lines)

5.3.3 Comparison with Codes

The above experimental results are compared here with the Kruskal-Bernstein theory and NORSE simulation in Fig. 5.6. The Kruskal-Bernstein theory predicts RE density n_{RE} larger from 1 to 3 orders of magnitude than the total one n_e. This is a non-physical result of course and we shall consider this theory not relevant for this particular case. Furthermore, NORSE reaches slide-away regime (when all electrons runaway) at the very beginning of the discharge. Such early slide-away regime is not supported by the experimental results.

The possible reasons for the overestimating results from Kruskal-Bernstein theory and NORSE simulation could result from overestimating the electric field E_{tor} by METIS or from too high sensitivity of the theories on the E_{tor} parameter.

5.4 RE Influence on Ramp-Up Phase

As reported in Sections 2.2.2 and 3.4, RE are frequently generated during the current ramp-up phase in the COMPASS tokamak. Here, the influence of the RE generation on the plasma current I_p at the end of the ramp-up phase is investigated using the estimation for the RE current I_{RE} described in the previous Section.

The density scan in the range $1 - 5 \times 10^{19}$ m^{-3} was done during the 2^{nd} RE campaign. The scan consisted of 10 COMPASS discharges from #8552

to #8561. Plasma current I_p was feedback controlled to 130 kA during the flat-top phase and the toroidal magnetic field B_{tor} was 1.15 T for all the discharges.

5.4.1 Experimental Observations

The time traces of the relevant measurements for three COMPASS discharges from the analysed density scan are plotted in Fig. 5.7. The three discharges are chosen to cover the standard tokamak discharge (#8553), the slide-away regime (#8559) and the transient between the previous two (#8555). Fig. 5.7b shows the realized line-average density $\bar{n}_e$ from the interferometer and core density $n_{e,c}$ measured by the Thomson scattering diagnostics. One can see from Fig. 5.7a that the plasma current peaks at the end of the current ramp-up phase I_p^{max} increases as the density decreases.

An initial guess for higher I_p^{max} from the perspective of plasma physics would be a significant drop of plasma resistivity $\eta_{res} \propto T_e^{-3/2}$, which obviously can only come from higher electron temperature T_e. However, the electron temperature measurements from Thomson scattering diagnostics shown in Fig. 5.7c are showing the opposite. The electron temperature is highest for discharge #8553, which has the lowest I_p^{max}. Moreover, the higher I_p^{max} the higher RE losses are, as seen from the HXR signals in Figs. 5.7d and 5.7e, implying existence of higher RE population for higher I_p^{max}. Finally, the normalised plasma pressure β_n has also higher value when the I_p^{max} is higher, suggesting that a measurable part of I_p is driven by REs.

Furthermore, HXR signals and β_n give the best arguments for defining the discharge #8555 as the transient between the two regimes. Namely, the standard discharge #8553 has no activities detected on Shielded HXR, and from CTU HXR one can observe that the RE population slowly diminishes at the end of the discharge. Regarding slide-away discharge #8559, relatively low RE losses are detected until the end at 1220 ms on both detectors, while after this moment the Parail-Pogutse instability occurs. The late RE losses on the Shielded HXR show good confinement of the high energetic REs. In the case of the transient discharge #8555, the losses are in the order of magnitude of discharge #8559, showing the existence of a significant RE population. On the other hand, RE losses start at 1050 ms reflecting the worse confinement of RE and no Parail-Pogutse instability can be seen on any of the HXR signals. Notice that for discharge #8555, β_n starts to drop at about the time when RE losses start to be significant, confirming the RE loss interpretation.

Note that other standard discharges in the analysed set (#8552, #8554 and #8560) have practically the same β_n time trace as the one from the discharge #8553. In addition, clear β_n rise as in discharge #8599 is seen in other slide-away discharges from the analysed set (#8556, #8557, #8558 and #8561).

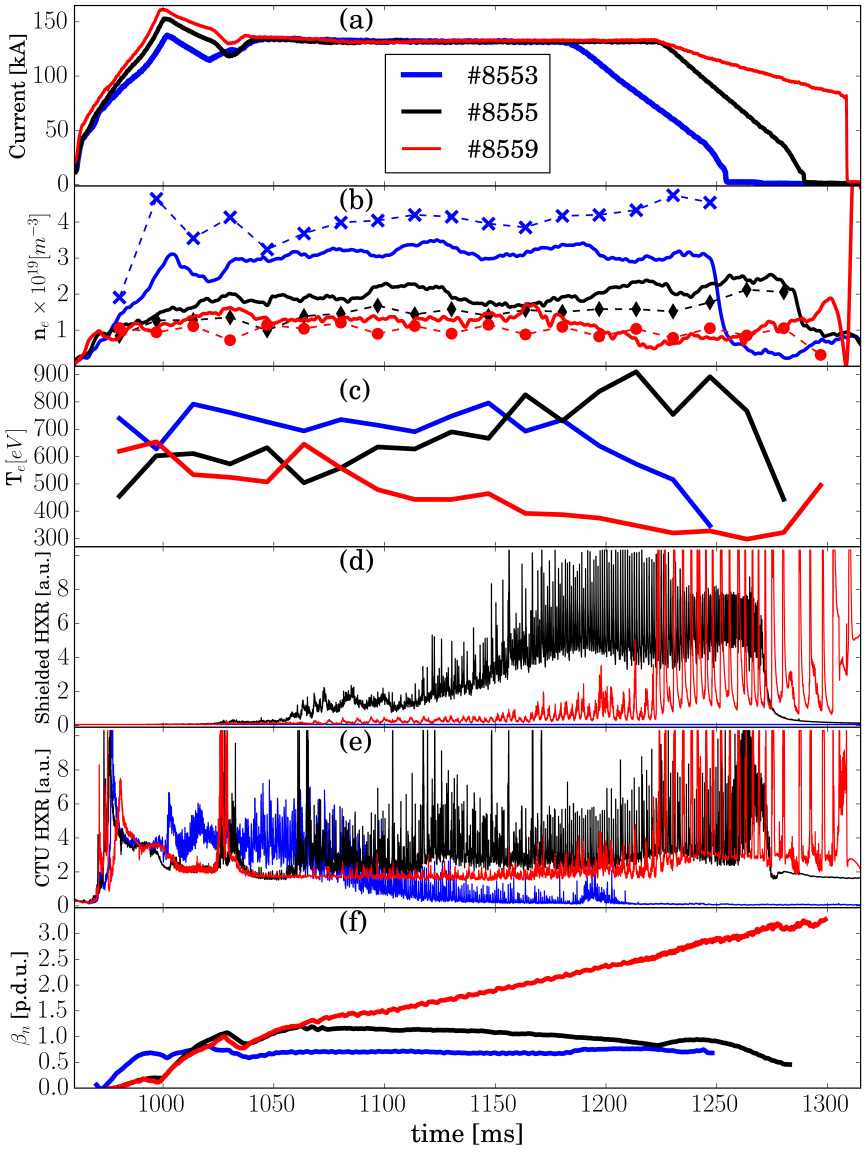

Figure 5.7: The density scan illustrated by three discharges: #8553 (blue), #8555 (black) and #8559 (red). The signals are from:**(a)** the plasma current I_p; **(b)** electron densities - line-averaged $\bar{n}_e$ (solid) and core $n_{e,c}$ (dashed with markers); **(c)** core electron temperature $T_{e,c}$; **(d)** Shielded HXR; **(e)** CTU HXR and **(f)** β_n from EFIT.

Next to be presented is the dependence of the HXR signals and the plasma current peak I_p^{max} as a function of the number of particles N_{GP}^{ru} injected during the ramp-up phase via gas puff. The number of particle injected N_{GP} is used instead of the density measurement due to two reasons: (1) the dependence is clearer, as the interferometer signal has significant fluctuations, i.e. low signal-to-noise ratio; (2) as the COMPASS tokamak lacks a Z_{eff} measurement important for the RE generation, taking N_{GP} gives (besides n_e) information about the neutrals inside the tokamak chamber (assuming that recycling from the wall was comparable in all discharges). The result is depicted in Fig. 5.8. The direct correlation between the peak current I_p^{max} and Shielded HXR can be observed in Fig. 5.8a. Hence, discharges starting with the higher I_p end up having larger losses of high-energetic RE electrons. Moreover, one can see from Fig. 5.8b that RE losses recorded by the CTU HXR are practically the same during the ramp-up phase (i.e. before the plasma current maximum I_p^{max}) for all the discharges. This shows that the RE losses are not influenced by the plasma density change. On the other hand, the CTU HXR measures increase of the RE losses for the rest of the discharge as N_{GP}^{ru} decreases.

Before making the final conclusion about the experimental observations above, let's take a look at one more possibility why I_p^{max} could increase by decreasing n_e. Namely, higher volt-second consumption from the primary winding could induce a higher plasma current. To verify that point, integration of the flux during the ramp-up phase was performed. The flux is

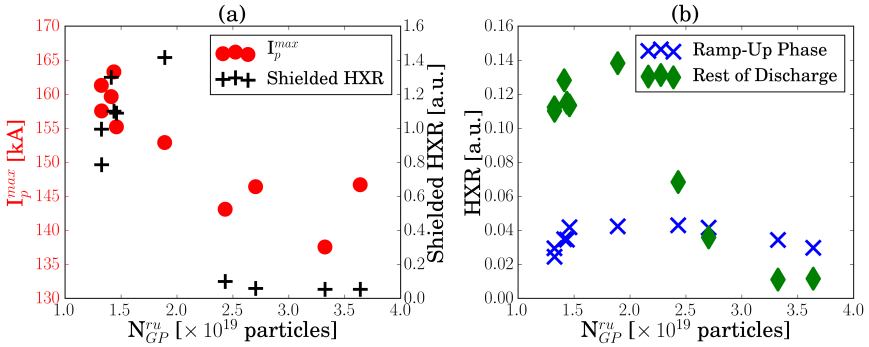

Figure 5.8: The data analysis for the whole set of analysed (10) discharges. **(a)** The peak plasma current at the end of the ramp-up phase I_p^{max} (red circles) and mean value of Shielded HXR signal from whole discharge (black pluses) as function of the number of particles injected N_{GP}^{ru} during the ramp-up phase. **(b)** The mean of CTU HXR signal before the plasma current peak (blue crosses) and after the peak (green diamonds) plotted versus N_{GP}^{ru}.

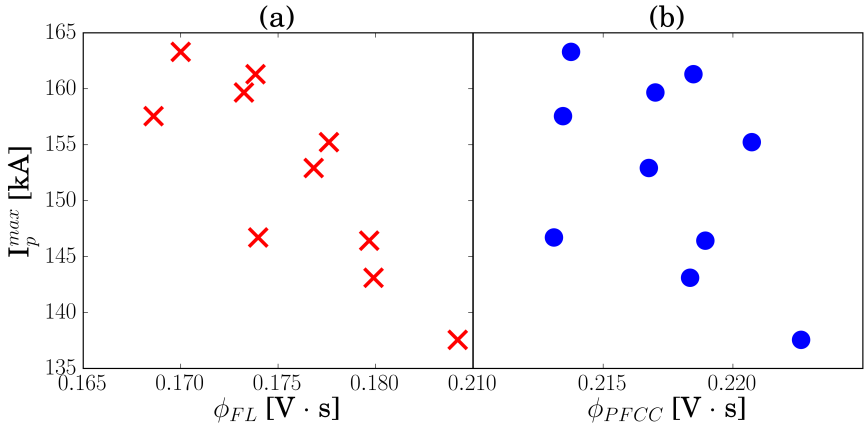

Figure 5.9: The peak plasma current at the end of ramp-up phase I_p^{max} as a function of **(a)** the flux calculated from the loop voltage measurement ϕ_{FL} and **(b)** the induced flux from the total poloidal field coil circuts ϕ_{PFCC}.

calculated in two ways: from the V_{loop} measurement as

$$\phi_{FL} = \int_0^{t_{ru}} V_{loop}(t)\mathrm{d}t \tag{5.23}$$

and from the current going through all poloidal field coil circuits (PFCCs) on the COMPASS tokamak:

$$\phi_{PFCC} = \sum_{PFCC} L_{PFCC} * I_{PFCC} \tag{5.24}$$

where I_{PFCC} is the current and L_{PFCC} is the inductance through the corresponding poloidal field coil circuit. The PFCC currents are measured, while PFCC inductances for the vacuum vessel axis were calculated and can be found in Table 3-6 of the Ref. [143]. The I_p^{max} is plotted as a function of both fluxes in Fig. 5.9 for both discharges. It is obvious that the plasma current peak I_p^{max} increases when the flux is lower, which is opposite to the assumption we made of a higher I_p^{max} due to a higher volt-second consumption.

In conclusion, taking into account all the aforementioned observations, we can only conclude that higher plasma current at the end of the current ramp-up phase I_p^{max} is due to the REs or slide-away influence. HXR signals and β_n estimate show a significant presence of RE when I_p^{max} is higher. The drop in the electron temperate T_e measurement confirms the slide-away regime. Surprisingly, the lower the loop voltage V_{loop} (i.e. electric field E_{tor}) the more REs are generated. Henceforth, this set of experiments could present a different insight in the relevance of the bulk electron density on the RE generation theory.

5.4.2 Results and Discussion

To confirm the above claims, an estimate of RE density n_{RE} from experiments and from codes is presented here.

Fig 5.10 presents a comparison of n_{RE} calculated from the measurements using the method described in Section 5.3 with Kruskal-Bernstein and NORSE theories. To avoid redundant lines, n_{RE} is calculated only for the two most extreme REDF - the monoenergetic f_{mono} and the exponential f_{exp} ones. The expected trend can be easily observed. The discharge #8553 has n_{RE} lower by an order of magnitude than the other two discharges during the ramp-up phase. Surprisingly, the discharges #8555 and #8559 have a similar n_{RE} at the beginning of the discharge. However, n_{RE} drops for the former discharge as expected from the missing β_p rise from EFIT (see Fig. 5.7f) and drop from the Thomson Scattering system (see Fig. 5.7 c). Finally, the corresponding RE current I_{RE} at the end of the ramp-up phase for the discharges #8553, #8555 and #8559 are $0.3-2.0\,\mathrm{kA}$, $2.3-17.8\,\mathrm{kA}$ and $2.4-19.6\,\mathrm{kA}$, respectively. Note that the non-continuous line for discharge #8553 comes from the defined thresholds of the method.

To complete the analyses, Kruskal-Bernstein theory and NORSE code are used to theoretically estimate n_{RE}. The results are presented in Fig. 5.11. Notice first that both methods have the expected trend in density of RE rising from #8553 to #8559. Differently from discharge #7298 in Section 5.3.3, the Kruskal-Bernstein theory does not give n_{RE} over n_e, while n_{RE} do rises towards n_e at the end of discharge for #8555 and #8559. For

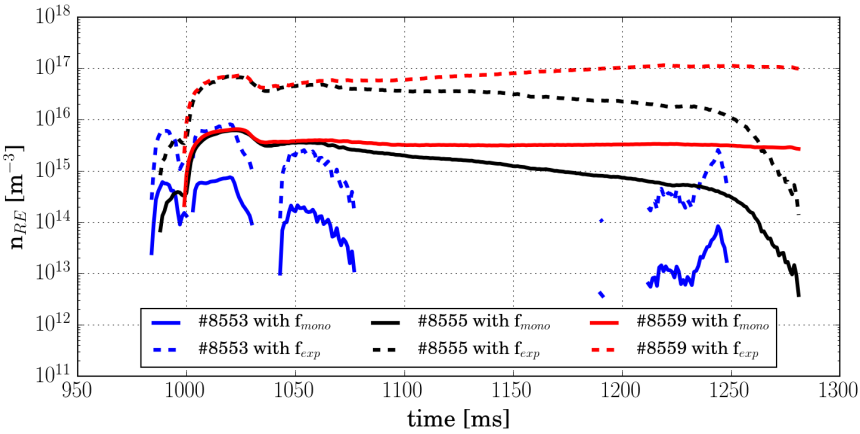

Figure 5.10: Time traces of the estimated n_{RE} from measurements for the three typical discharges: #8553 (blue - standard discharge), #8555 (black - intermediate case) and #8559 (red - slide-away regime). For each discharge n_{RE} is estimated using the two most extreme REDF - the monoenergetic f_{mono} (full line) and the exponential f_{exp} (dashed line).

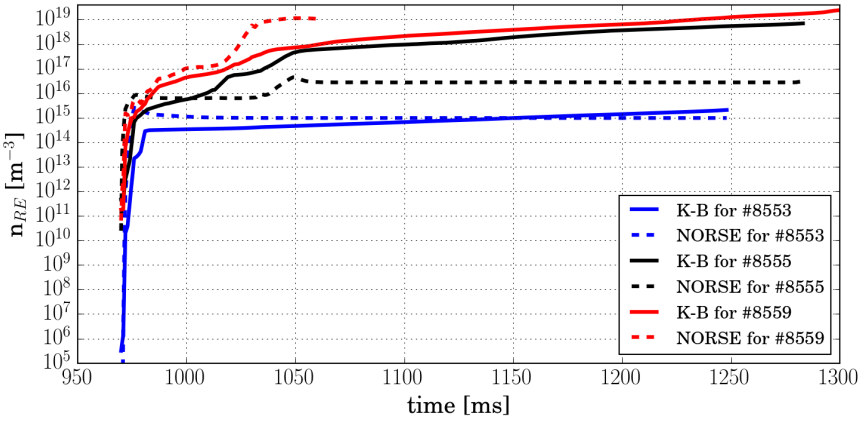

Figure 5.11: Time traces of estimated n_{RE} using Kruskal-Bernstein theory (solid line) and NORSE simulation (dashed line) for the three typical discharges: #8553 (blue - standard case), #8555 (black - intermediate case) and #8559 (red - slide-away regime).

these two discharges, the Kruskal-Bernstein theory does not show a significant difference in n_{RE}. On the other hand, NORSE estimates that those two discharges are quite different - according to this code #8559 reaches slide-away regime already around 1060 ms, which is probably too early.

Interestingly, in the case of the standard discharge #8553, both codes seem to approximately agree in the order of magnitude with the experimental n_{RE} (between 10^{14} and 10^{15} m^{-3}). The same is valid when the NORSE simulation is compared with experimental n_{RE} using f_{exp} for the discharge #8555. However, the NORSE code does not predict the drop of n_{RE}, clearly observed in Fig. 5.10 and from the measurements in Fig. 5.7f.

5.5 Drift of Runaway Electrons

Up to now, only the radiation process was considered as the possibility for the RE energy limitation, which is discussed in Section 4.1.1. In this Section, we will finally introduce the RE energy limit from the RE outward drift through the analytically derived calculation reported by Zehrfeld [69].

Zehrfeld's analysis is more advanced than the simple Eq. 2.10, which gives a single solution for the whole plasma, while Zehrfeld's calculation provide the W_{drift} as a function of the normalized minor radius $\rho = r/a_p$. One of the main messages from this analysis is that W_{drift} profile can have (depending on machine and plasma parameters) maximum value inside plasma (i.e. $\rho < 1$), which indicates that REs of certain energy can be lost before they reach the plasma edge (i.e. the last closed flux surface). Therefore, we

will first illustrate how the W_{drift} profile looks for the typical COMPASS discharges and the COMPASS high I_{RE} discharges. Next we look for location where RE beams with parameters previously obtained in this Chapter can exist in the plasma.

Zehrfeld's theory [69] states that the RE energy limit for RE coming from the plasma core ($\rho = 0$) is

$$W_{drift} = \left\{ \left[1 + \left(\frac{2R_p \Delta_S(\rho) I_p}{a_p I_A} \right)^2 \right]^{1/2} - 1 \right\} m_e c^2, \tag{5.25}$$

where

$$\Delta_S(\rho) = \frac{1 - (1-\rho^2)^{e_I+1}}{\rho(1 + \Delta'_{sh}(\rho))}, \tag{5.26}$$

with e_I being a positive integer exponent in the definition of the plasma current profile

$$I(\rho) = I_p \left(1 - (1-\rho^2)^{e_I+1}\right) \tag{5.27}$$

and derivative of Shafranov shift

$$\Delta'_{sh}(\rho) = -\rho \frac{a_p}{R_p} F[x(\rho)] \tag{5.28}$$

is defined through

$$F(x) = \beta_{pol} \frac{1 + e_p x^{e_p+1} - (e_p+1)x^{e_p}}{(1 - x^{e_I+1})^2} + \frac{F_{e_I+1}(x) - 0.5 F_{2(e_I+1)}(x)}{(1 - x^{e_I+1})^2} \tag{5.29}$$

where

$$x = 1 - \rho^2, \tag{5.30}$$

$$F_{e_I+1} = \sum_{k=1}^{e_I+1} (1 - x^k)/k \tag{5.31}$$

and e_p is a positive integer exponent in the definition of the plasma pressure profile

$$p_{pl}(\rho) = p_{pl,c}(1 - \rho^2)^{e_p} \tag{5.32}$$

with $p_{pl,c}$ being the plasma pressure on the magnetic axis. i.e. in the plasma core.

Some typical shapes of the W_{drift} profile are presented in Fig. 5.12, where $e_p = 3$ is taken in agreement to the measured pressure profile from Thomson Scattering for the discharge #7298. Moreover, we choose e_I to be 1 or 2, because typical l_i for COMPASS indicates $e_I = 1.5$. Concerning β_{pol}, it has typical COMPASS values during the ramp-up phase around 0.3 and during the flat-top phase does not exceed 1.0, while $\beta_{pol} = 0.03$ corresponds to the values gained from the Thomson scattering system during

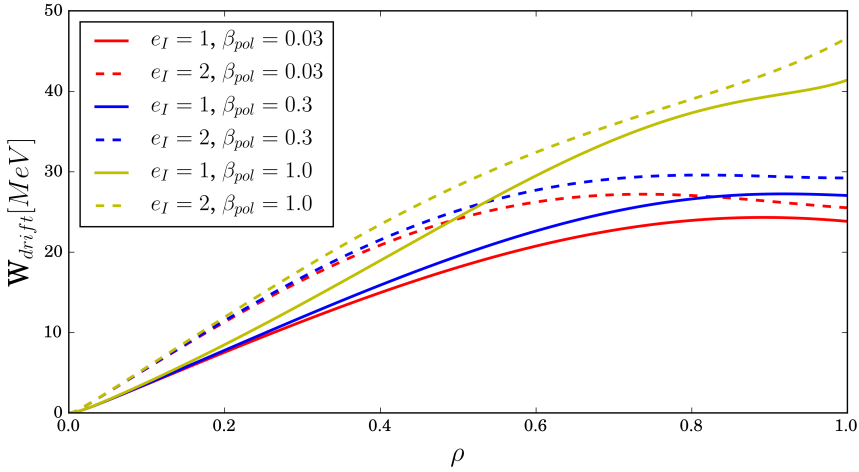

Figure 5.12: Poloidal profiles of the RE drift limiting energies W_{drift} for three different β_{pol} - 0.03 (red), 0.3 (blue) and 1.0 (yellow) and for two different e_I - 1 (solid line) and 2 (dashed line).

the high I_{RE}, such as #7298. One can see from the Figure that there is no maximum of W_{drift} inside plasma for β_{pol} as high as 1.0, while there are weak maxima for lower β_{pol}. The only clear maximum is seen for the lowest β_{pol} and $e_I = 2$, the parameters that are the most important for the high I_{RE} discharge. Moreover, the maximum of W_{drift} for lower β_{pol} is in the range of $25 - 30$ MeV, which is just above the reported W_{max} from Fig. 5.5a. It means that W_{drift} is not the main reason of the RE losses during the flat-top phase of COMPASS discharges with high I_{RE}, as W_{max} did not reach the W_{drift} value.

Nonetheless, knowledge of the $W_{drift}(\rho)$ profile can be used for localization of the RE beam. Knowing W_{max} at a given time of the discharge, one can find the minimum minor radius ρ_{min} where $W_{drift}(\rho_{min}) = W_{drift}$, corresponding to the minor radius below which REs with energy W_{max} cannot be confined. On the other hand, upper minor radius limit ρ_{max} does not depend on the RE beam parameters (provided that $W_{max} > \max[W_{drift}(\rho)]$ holds). Actually, ρ_{max} depends on the shape of the W_{drift} profile (i.e. plasma parameters β_{pol} and m) and on the position where this profile reaches the maximum. The corresponding major radii of ρ_{min} and ρ_{max}, defined as $R_{min} = R_{sh} + a_p * \rho_{min}$ and $R_{max} = R_{sh} + a_p * \rho_{max}$, for discharge #7298 are calculated and presented in Fig. 5.13 for all six previously analysed REDFs and two different exponents m. Here, R_{sh} is the theoretical bulk plasma barycenter from the Shafranov shift

$$R_{sh} = R_{geom} + a_p * \Delta_{sh} \tag{5.33}$$

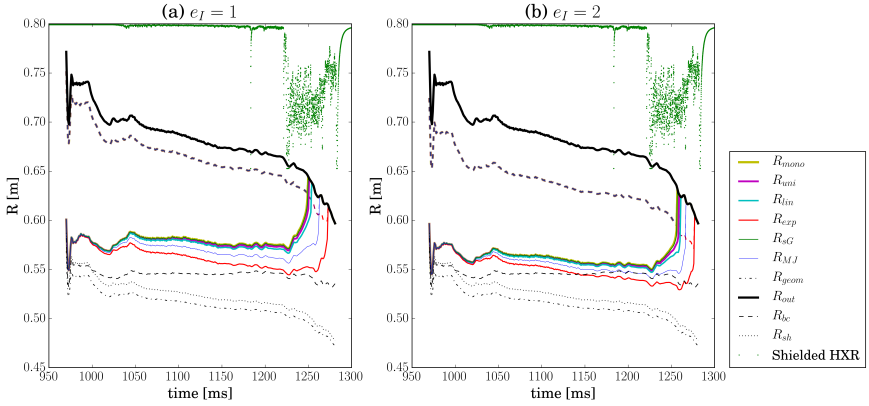

Figure 5.13: Time traces for lower (solid colored lines) and upper (dashed coinciding colored lines) limits of RE major radiuses for all six REDFs are presented for discharge #7298. For orientation, major radius of plasma geometrical center R_{geom} (black dash-dotted line), outer plasma major radius R_{out} (black solid line), plasma current barycenter R_{bc} (black dashed line) and theoretical bulk plasma barycenter from Shafranov shift R_{sh} (black dotted line) are added. Beside all major radiuses, the Shielded HXR signal (green points) is presented. Figure is plotted for two of current profile factor e_I values: **(a)** $e_I = 1$ and **(b)** $m = e_I$.

where the Shafranov shift is calculated using Eq.(26) from [69]:

$$\Delta_{sh}(\rho = 0) = \frac{a_p}{2R_{geom}} \int_0^x F(x')\mathrm{d}x'. \tag{5.34}$$

Beside the major radius of plasma geometrical center R_{geom} and bulk plasma barycenter R_{sh}, the outer plasma major radius R_{out} and plasma current barycenter R_{bc} from EFIT are shown in the same Figure for orientation purposes. One can notice from the Figure that RE orbits can exist in $10 - 15\,\mathrm{cm}$, which is not very limiting knowing that the COMPASS minor plasma radius is around $20\,\mathrm{cm}$. RE orbits are localised more inside the plasma for higher e_I, as could be expected from higher peaking of W_{drift} profile seen in Fig. 5.12. For the same reason, later significant losses of high energy RE are expected for higher e_I, which can be seen by slightly delayed equalisation of the RE radius with R_{out} (for $5 - 15\,\mathrm{ms}$) for factor of current profile $e_I = 2$ than in the $m = 1$ case. However, both timings for significant high energy RE losses are a few tens of milliseconds after the Shielded HXR observes those losses. On the other hand, this Section shows that these losses are probably due to the RE outward drift as I_p is decreasing (W_{drift} decreases with I_p, see Eq. 5.25) and connection of strong Shielded HXR signal and I_p ramp-down phase is indeed observed in Fig. 5.5b.

5.6 Conclusions and Outlook

The COMPASS discharges where RE beams drive a measurable amount of the total current and co-exists with the plasma were analysed in this Chapter. The analysis of those discharges can also be used for a long RE discharges, which can be used for simulation of RE mitigation with MGI. Therefore, knowledge of the RE beam position, the RE current and the density of REs are of high importance for the RE mitigation studies in the COMPASS tokamak.

The experimental observation of high RE current discharge was exemplified with the discharge #7298, the very first discharge of this kind during the COMPASS RE campaigns. A relatively low V_{loop} during the flat-top phase of the COMPASS discharge indicated a current component not induced via the central solenoid. IPR coils clearly observe a total outward current redistribution, while both - fast and slow - radial position systems detect a significant outward force, causing the system to increase an inward balancing force. On the other side, I_p and its barycenter remained constant as was pre-requested by the operator. Furthermore, the EFIT reconstruction also overestimates β_p and shrinkage of the plasma volume. All of the above are evidences of the RE population that drives a significant amount of the I_p.

The same discharge was used to demonstrate how to estimate I_{RE}. The method is an adaptation of Fuijta's approach [142] to COMPASS tokamak. Originally Fuijta estimated all the needed parameters, while COMPASS has direct measurements of one of them - the plasma pressure measured by the Thomson scattering diagnostics. Furthermore, extraction of the RE pressure from the measurements and use of the RE distribution functions for W_{max} estimation were explained. The influence of the pitch angle on the I_{RE} estimation was also investigated - following Fujita's example - concluding that it mainly influences the W_{max} calculation. The resulting I_{RE} computation gave an evidence that REs do carry at least 4 kA for the discharge #7298 ($I_p = 120$ kA). On the other hand, the upper limit is difficult to deduce and it results in the order of a few tens of kA.

The RE influence on the ramp-up I_p was noticed on a set of discharges for which n_e varies from 1×10^{19} to 5×10^{19} m^{-3}. Three distinct discharges were taken - a standard discharge, a slide-away, and an intermediate case. Firstly, a thorough description of the measurement observations was presented. It was clearly shown that a drop in the plasma resistivity and the volt-second consumption from the central solenoid can not be the reason for the I_p rise at the end of the ramp-up phase. Moreover, the higher the I_p was, the higher the HXR signals and β_n were - indicating a correlation between the I_p peak and the REs. Therefore, the aforementioned I_{RE} estimation was used to estimate the RE density for those three discharges. A clear trend between n_{RE} and the I_p peak was then shown, demonstrating that RE are responsible for this peak.

For both the above analyses - discharge #7298 and the three n_e-scan discharges - the final result is compared with theoretical expectations. Kruskal-Bernstein formula for Dreicer growth rate with Rosenbluth-Putvinski avalanche growth rate is used as an analytic approach, while the NORSE code is used as a more complex tool. Even though the exact amount of REs is unknown and the accuracy of the experimental RE estimation is not validated, we are sure that both computations overestimate the exact amount of the REs. For example - the Kruskal-Bernstein theory predicts higher n_{RE} than n_e to 1 to 3 order of magnitude. Furthermore, for the high E_{tor}, NORSE often forecasts that all electrons run away too early, while this is not confirmed by experimental observations. On the other hand, both theories do predict the observed trend for the three discharges from the n_e-scan.

The final part of the Chapter addressed the issue of the RE drift energy limit in the COMPASS tokamak. It was shown that this limit is probably not fully relevant for the RE losses during the flat-top phase, as it limits the RE energy to around 30 MeV. However, this limit is probably the main cause of the often observed significant RE losses during the ramp-down phase due to the I_p decrease. Moreover, knowledge of I_{RE} for the discharge #7298 is used in combination with the Zehrfeld's RE beam drift theory to localise the RE beam. It has been seen that - from this perspective - the RE beam can exist for all of the analysed RE distribution functions.

OUTLOOK. Fujita also showed that l_i (the internal plasma inductance) has an impact on the I_{RE} estimate [142, Fig. 7]. Unfortunately, the accuracy of l_i estimate from EFIT is very poorly known during the RE discharges and thus it has not been investigated here. For this purpose, one would need to implement the RE current into EFIT. Something similar has been done by Yoshida [147] more than 25 years ago and implemented on the ORMAK tokamak. Nonetheless, the implementation of the RE current into the equilibrium is left for future work on the COMPASS tokamak.

Finally, theories used here are also the most commonly used model basis in the RE research community. However, they obviously overestimate the number of REs. Yet, their further development is far beyond the scope of this Thesis. The results obtained from theories are here to show the issue being oversimplified and the need for a better modelling of the RE generation.

Chapter 6

Synchrotron Radiation in COMPASS

The current Chapter will describe synchrotron radiation (SR) coming from RE in the COMPASS tokamak. A brief physical introduction about SR in tokamaks is given in Section 2.3.5 and the COMPASS experimental setup for SR diagnostics is concisely reported in Section 3.3.2.

Measured with IR cameras, SR can give the location of REs and the average value of their pitch angle θ. Moreover, SR is one of the few ways to observe directly confined, in-flight, MeV REs due to the so-called *headlight effect*. In fact, direct observation of the REs in COMPASS is presently possible only with measurements of SR.

The Chapter starts with a simple analysis for explaining what was expected in the experiment. The description of a more complex model used in the Thesis is then presented. After a theory, the experimental setup for COMPASS is described in more details than in Section 3.3.2. The observations of SR and their classification are presented afterwards. Furthermore, data analysis from numerous discharges is given. Then, a correlation between Shielded HXR and IR camera signals is reported. The next Section addresses a detailed analysis of the SR direct observation for the particular COMPASS discharge #9814. Finally, a summary of the work and conclusions are given in the very end of the Chapter.

6.1 Theoretical Expectations

Observations of SR in the COMPASS tokamak had never been performed before the dedicated RE experiments (neither in Culham nor in Prague). Therefore, in order to show that the first observations reported in Ref. [146] by the doctoral candidate were not coincidental, preceding theoretical calculations are presented in this Section. Furthermore, the qualitative con-

Table 6.1: The estimated wavelength λ_{peak} for which the SR has maximum power radiated according to Eq. 2.15 for different RE energies W and pitch angles θ. Wavelength values near the IR camera range are bolded. The units are in the μm.

W[MeV] =	10	15	20	30
$\theta = 1/\gamma$	80.4	31.0	**14.1**	4.38
$\theta = 0.2$ rad	27.5	**12.2**	**6.64**	2.68

temporary theoretical knowledge is also reported. The end of the Section is devoted to the SYRUP code.

6.1.1 Wavelength of SR Maximum

Firstly, on estimation of the wavelength λ_{peak} or frequency ν_{peak} at which the radiated power of SR should have maximum was performed. Eq. 2.15 gives an approximate formula for the λ_{peak} and its values are tabulated in Table 6.1 for typical COMPASS parameters. Four different RE energies W are taken: 10, 15, 20 and 30 MeV, as typical values at the COMPASS tokamak are a few tens of MeV - see Chapter 4. Furthermore, the pitch angle θ is estimated in two different ways. Firstly, the common astrophysical approximation $\theta = 1/\gamma$ is taken, where γ is the relativistic Lorentz factor. Secondly, θ is set to 0.2 rad as this is a common maximum value measured in other tokamaks [81, 105], and it was also measured afterwards in the COMPASS tokamak as a typical value[1] [152]. It is clear from the Table that the λ_{peak} has values in the infrared range for analysed RE energies. As already reported in Section 3.3.2, the IR camera available on COMPASS has a detection range from 7.5 to 13.0 μm. Therefore, we can conclude that our IR camera is able to detect SR from RE with energies over $15-20$ MeV.

6.1.2 Background Radiation

Even though RE seems to radiate SR in the detectable range of the available IR camera, we still need to check what is the detectable amount of power from radiation with respect to the background coming from the wall and the plasma itself. This kind of analysis for ITER disruption was reported by Jaspers *et al.* in Section V of Ref. [105] and a similar analysis will be conducted here. Jaspers *et al.* investigated two background radiation sources - thermal radiation from the wall and plasma bremsstrahlung. In the case of the COMPASS discharge, the density is lower, temperature a bit higher and the effective charge is lower than what is expected during ITER disruptions, making bremsstrahlung radiation 3-5 orders of magnitude weaker than the thermal wall radiation. Therefore, bremsstrahlung

[1] For more details about the pitch angle measurement in COMPASS see Section 6.4.

will be neglected in the analysis conducted here. Planck's law of black body radiation can be applied for the thermal wall radiation and yields

$$B_{bb}(T_{wall}, \lambda) = \frac{2hc^2}{\lambda^5 \left[\exp(hc/\lambda k T_{wall}) - 1\right]} \tag{6.1}$$

where λ is the radiation wavelength and T_{wall} the wall temperature. The SR radiance is

$$B_{SR} = \frac{2\pi R_p I_{RE}}{ecA_{RE}} \frac{\mathcal{P}(\lambda)}{\Omega_{SR}} \tag{6.2}$$

where $\Omega_{SR} = \pi/\gamma$ is the solid angle at which the SR is emitted and $\mathcal{P}(\lambda)$ is the spectral density of emitted power, which is estimated with the single electron approximation

$$\mathcal{P}(\lambda) \approx \pi m_e c^3 r_e \sqrt{\frac{2\sqrt{1+\eta^2}}{\lambda^5 R_p \gamma}} \left(I_0(\eta_a) + \frac{4\eta}{1+\eta^2} I_1(\eta_a) \right) \mathrm{e}^{-\xi_{SR}} \tag{6.3}$$

where $I_\nu(x)$ are the modified Bessel function of the first kind of the ν^{th} order, $\eta_a = \xi_{SR}\eta/(1+\eta^2)$ and $\xi_{SR} = (4\pi R_p)/(3\lambda\gamma^3\sqrt{1+\eta^2})$, while $\eta = \langle v_\perp \rangle / v_{dr}$ already reported in Section 4.1.2. However, if $\lambda = \lambda_{peak}$, i.e. when $\mathcal{P}(\lambda)$ is maximum, then the above equation can be simplified into

$$\mathcal{P}_{peak}(\lambda) \approx 0.1 m_e c^3 r_e (1+\eta^2)^{3/2} \gamma^7 / R_p^3. \tag{6.4}$$

Before going to the result of the calculation, it is important to note that only rough approximations are made and that more precise equation could be considered for the SR power spectrum. However, for the present purpose the aforementioned approximations are good enough and a more advanced power spectrum characterisation and their limitations will be discussed later in Section 6.1.4.

The results of the above-elaborated analysis are shown in Fig. 6.1. To obtain this Figure, the parameters used are $R_p = 0.56\,\mathrm{m}$, $B_{tor} = 1.15\,\mathrm{T}$, $\theta = 0.2$, $a_{RE} = 0.1\,\mathrm{m}$ for A_{RE} calculation and $T_{wall} = 350\,\mathrm{K}$ is taken as as upper estimate for the LFS wall temperature of the COMPASS tokamak without disruption or the RE impact. As earlier, the RE energy is varied from 10 to 30 MeV, while two different RE currents are taken to study the detection threshold: 0.1 kA and 1 kA. Finally, three different wavelengths are considered - the minimum and the maximum of the IR camera range, i.e. $\lambda = 7.5$ and $13\,\mu\mathrm{m}$, and the calculated λ_{peak} for each corresponding RE energy. Finally, from Fig. 6.1 it is obvious that REs over 15 MeV carrying 0.1 kA would be well visible with the IR camera available on COMPASS (well above the black lines that correspond to the thermal noise). Moreover, having 1 kA RE current would be detectable even if the RE energies would be just above 10 MeV. Therefore, we conclude that the background radiation in the COMPASS tokamak is not a constraint for the SR observation compared to the wavelength range of the IR camera, which is connected to the RE energy through the spectrum maximum λ_{peak}.

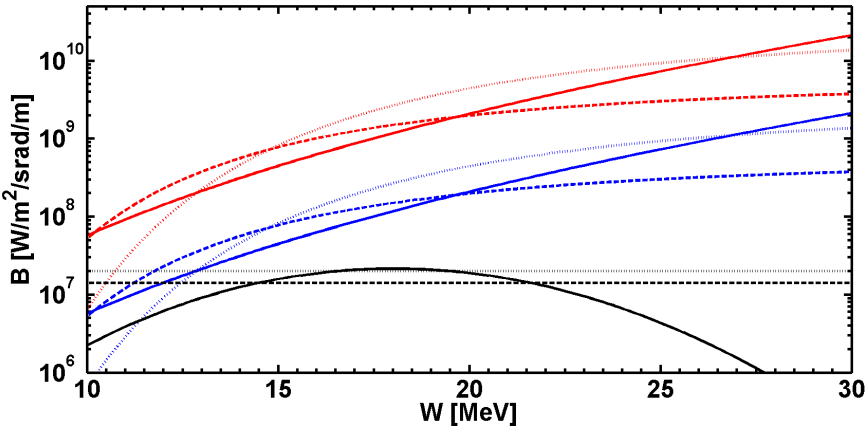

Figure 6.1: Thermal wall radiation B_{bb} (black lines) and synchrotron radiance B_{SR} for RE current $I_{RE} = 0.1\,\mathrm{kA}$ (blue lines) and $I_{RE} = 1\,\mathrm{kA}$ (red lines) versus the RE energy W. The wavelenght was set to the IR camera minimum $\lambda = 7.5\,\mu\mathrm{m}$ (dotted lines), to the IR camera maximum $\lambda = 13\,\mu\mathrm{m}$ (dashed lines), or to the wavelength corresponding to the power spectrum maximum $\lambda = \lambda_{peak}$ (solid lines).

6.1.3 Brief Overview of the SR Theory

The approximated approach presented above concerning the SR comes from the work of Schwinger [153] on radiation from accelerated electrons. Trubnikov was the first to adopt this theory for high temperature (i.e. fusion) plasmas [154]. A good overview of the cyclotron and synchrotron theory development can be found in Bekefi's book [155] and Landau-Lifshitz series [156]. However, most of the theory development in fusion research concentrated on the electrons of a few tens of keV, while no-one investigated the effects specific to fusion plasmas for MeV energy range until Finken [104] and Jaspers [70] published their experimental works. Finken and Jaspers assumed that the SR power spectrum is dominated by the highest energies and large pitch angle. The detailed theoretical work was finally accomplished analytically by Pankratov [139] and numerically by Stahl *et al.* [45]. They showed how toroidal effects and bulk plasma parameters (e.g. toroidal magnetic B_{tor} and electric E_{tor} fields, electron density n_e and temperature T_e) are important in estimating the RE density and energy from measurements of SR in fusion devices. Namely, SR emitted power would increase with higher B_{tor}, T_e, n_e, Z_{eff} and lower E_{tor}. Moreover, Stahl *et al.* [45] numerically investigated Pankratov full analytical expression for SR. The main conclusion was that the SR diagnostic based on single particle emission model [81, 105] can be misleading and, usually, overestimating the SR per particle, and then underestimating the RE density. The most recent

work by Hirvijoki *et al.* [157] and Decker *et al.* [151] concentrated on the Abraham-Lorentz-Dirac force, the reaction force to the SR, that can form a non-monotonic feature in the RE distribution. This non-monotonic feature of the RE distribution function is often called 'bump' as already mentioned in Section 5.3.1 (where it was shown that the bump cannot occur under COMPASS plasma conditions). This is probably because the reaction force is proportional to the B_{tor}^2, which is relatively low in the COMPASS tokamak. Finally, the importance of SR and its dependence on the RE distribution dynamics is reported by Stahl *et al.* [30] where he examines the experimental estimation of E_{crit}[2].

To **summarise** - typically COMPASS tokamak has relatively high E_{tor}, low B_{tor}, n_e and Z_{eff}, which leads to weak SR. On the other hand, high E_{tor} and low n_e produce more REs and high E_{tor} and low B_{tor} allow REs to reach higher energies that both lead to stronger SR. Moreover, the available IR camera in COMPASS seemed to observe the proper spectral range for SR and already about 100 A of RE current could be distinguished from background radiation. In conclusion, the attempt to measure SR in the COMPASS tokamak was supported by the theoretical expectations.

6.1.4 SYRUP Code

Analytical expressions for the SR power spectrum presented in Ref. [45] were implemented by Stahl in a code named SYRUP (SYnchrotron spectra from RUnaway Particles). SYRUP is written in MatLab and can be run as graphical user interface.

Beside choosing the SR spectrum formula for a given wavelength range, it allows to choose the RE distribution function - single electron, analytical avalanche, or provided from the code CODE[3]. The single electron case requests the RE pitch angle θ and the RE maximum energy W_{max} knowledge, while analytical distribution function only needs the maximum energy. Additionally, analytical distribution function needs plasma parameters (E_{tor}, n_e, T_e and Z_{eff}) as an input. Beside RE and plasma parameters, tokamak parameters (R_0 and B_{tor}) should be specified for all the SR spectra and RE distribution functions.

The full analytical expression for SR from RE in toroidal fusion plasma [139] is

$$\mathcal{P}_f(\lambda) = \frac{4\pi m_e c^3 r_e}{\lambda^3 \gamma^2} \left\{ \int_0^\infty \frac{\mathrm{d}y}{y} (1+2y^2) J_0(ay^3) \sin\left[\frac{3}{2}\xi_{SR}\left(y+\frac{y^3}{3}\right)\right] - \frac{4\eta}{1+\eta^2} \int_0^\infty \mathrm{d}y y J_0'(ay^3) \cos\left[\frac{3}{2}\xi_{SR}\left(y+\frac{y^3}{3}\right)\right] - \frac{\pi}{2} \right\} \quad (6.5)$$

[2]For more details on the experimental estimation of E_{crit} see Section 2.2.1.
[3]See Section 2.1.6 for more details on CODE.

where $J_\nu(x)$ is the Bessel function of order ν and $J'_\nu(x)$ its derivative. Numerically solving the above equation costs a lot of computational time and therefore one needs to find an approximate solution to speed up the analysis. One such approximation was already reported in Eq. 6.4 as $\mathcal{P}(\lambda)$, which we will take to be the first approximation $\mathcal{P}(\lambda) \equiv \mathcal{P}_1(\lambda)$. This approximation is valid for the wavelength range [139]

$$\lambda_{1l} \equiv \frac{4\pi R_p \eta}{3\gamma^3 \sqrt{1+\eta^2}^{3/2}} \lesssim \lambda \ll \frac{4\pi R_p}{3\gamma^3 \sqrt{1+\eta^2}} \equiv \lambda_{1u}. \tag{6.6}$$

The second approximated expression named $\mathcal{P}_2(\lambda)$ for the SR power spectrum [139] is

$$\mathcal{P}_2(\lambda) = \frac{\sqrt{3} m_e c^3 r_e \gamma}{2\lambda^2 R_p} \frac{(1+\eta)^2}{\sqrt{\eta}} \exp\left(-\frac{4\pi R_p}{3\lambda\gamma^3(1+\eta)}\right) \tag{6.7}$$

that only has an upper limit on the validity range of the wavelength:

$$\lambda \ll \frac{4\pi R_p \eta}{3\gamma^3(1+\eta)^3} \equiv \lambda_{2u}. \tag{6.8}$$

Beside the above three equations for SR power spectrum in toroidal plasma, SYRUP can calculate the SR power spectrum for the cylindrical plasma [153] (i.e. straight magnetic field lines):

$$\mathcal{P}_c(\lambda) = \frac{4\pi m_e c^3 r_e}{\sqrt{3}\lambda^3\gamma^2} \int_{\lambda_c/\lambda}^{\infty} K_{5/3}(l)\mathrm{d}l \tag{6.9}$$

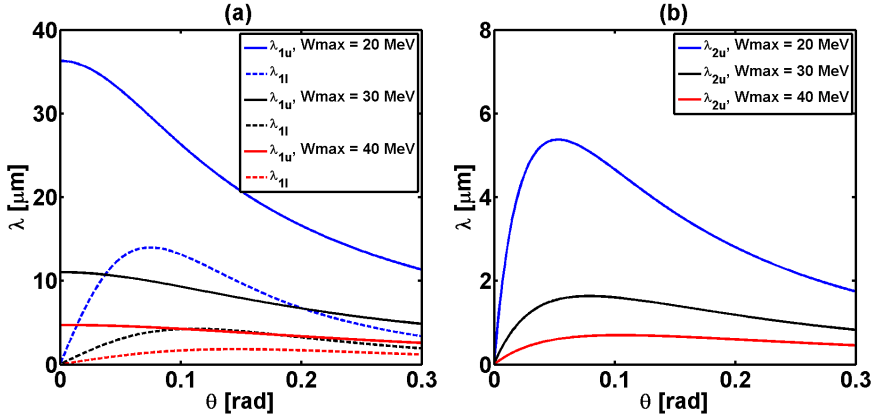

Figure 6.2: **(a)** Theoretical upper λ_{1u} (solid lines) and lower λ_{1l} (dashed lines) wavelength limits versus the pitch angle θ for the $\mathcal{P}_1$ validity. **(b)** Theoretical upper λ_{2u} wavelength limits versus the pitch angle θ the for the $\mathcal{P}_2$ expression to be valid. Each limit is calculated for three different RE energies: 20, 30 and 40 MeV. Notice the different y-axis scale between (a) and (b).

where $\lambda_c = (4\pi m_e c\gamma_{\|})/(3eB_{tor}\gamma)$ and $K_\nu(x)$ is the modified Bessel function of the second kind of the ν^{th} order.

The question to address here is which approximation should be used for the COMPASS plasma to avoid lengthy calculation of the full expression $\mathcal{P}_f$. Stahl *et al.* showed that $\mathcal{P}_c$ can be used for ITER due to its large size and that $\mathcal{P}_2$ suits the DIII-D tokamak the best, while Jaspers [105] used the other toroidal approximation $\mathcal{P}_1$.

The wavelength ranges defined in Eqs. 6.6 and 6.8 should answer this issue, theoretically. This is plotted in Fig. 6.2 for three different RE energies - 20, 30 and 40 MeV. For the wavelength range of importance for the Thesis ($7.5-13\,\mu$m) only $\mathcal{P}_1$ seems to be suitable for energies between $20-30$ MeV, as seen from Fig. 6.2a. On the other hand, from Fig. 6.2b it seems that $\mathcal{P}_2$ is not appropriate for the COMPASS IR camera.

However, COMPASS is equipped with an IR spectrometer that has an upper wavelength limit at 1084.64 nm, where $\mathcal{P}_2$ should be valid. Unfortunately, SR was not detected then. On the other hand, the lack of observation with the IR spectrometer can be used to estimate the W_{max} for the detectable RE population. The theoretical maximum energy that RE can obtain from the electric field in COMPASS is around 40 MeV. Therefore, we will again use three different RE energies - 20, 30 and 40 MeV - with the single electron and analytical distribution function. The result is presented in Fig. 6.3, where the plasma parameters are $T_e = 800$ eV, $n_e = 2 \times 10^{19}$ m^{-3}, $E_{tor} = 0.15$ V/m and $Z_{eff} = 2.5$. For both distributions SR from RE with 40 MeV shows relatively high radiation levels, while the SR power for 20 MeV seems to be quite low. The SR from RE that has a 30 MeV energy using the analytical distribution has a similar order of magnitude as the single electron SR from 20 MeV RE. Knowing that SR should be at least a few W/nm to be detected over the background measured by the IR spectrometer, the lower limit for the number of RE N_{RE} can be estimated. Lack of SR on IR spectrom-

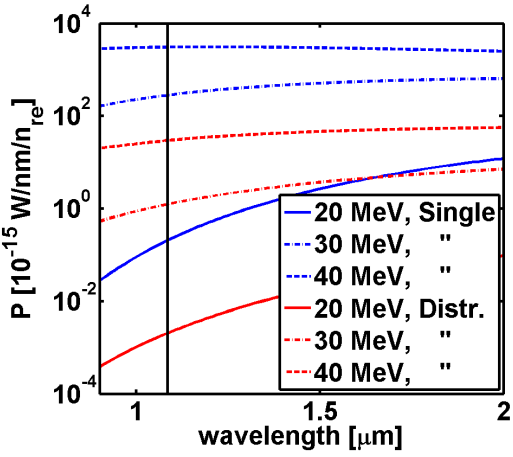

Figure 6.3: SR power spectra per RE for the single electron (blue) and the analytical (red) distribution functions using the $\mathcal{P}_2$ expression. Spectra are plotted for three different RE energies - 20 (solid), 30 (dot-dashed) and 40 MeV (dashed). The black vertical solid line is the upper limit of COMPASS IR spectrometer at 1084.64 nm.

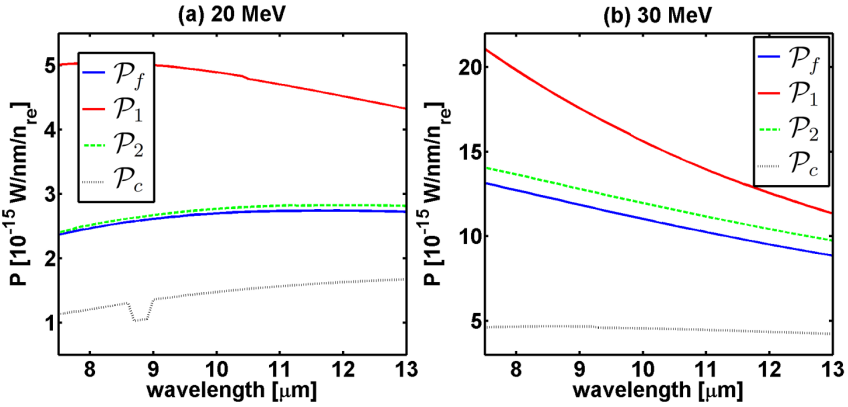

Figure 6.4: The SR power spectra for all four different equations - 6.5, 6.4, 6.7 and 6.9 - for RE with two different energies: **(a)** 20 and **(b)** 30 MeV.

eter suggests that there is no significant population (approximately over $10^{12}\,\mathrm{m}^{-3}$) of REs in COMPASS with energies higher than 30 MeV.

An additional thing to observed from Fig. 6.3 is the significant difference between the power spectrum from the single electron and the analytical distribution function, already reported by Stahl [45], meaning that the distribution function is of great importance when looking at SR. Moreover, the aforementioned validity conditions for both approximations are derived for a single RE radiation. However, the validity tests cannot be performed as simply as in Fig. 6.2 in the case of any distribution function. Therefore, Fig. 6.4 is plotted to visualise the direct comparison of $\mathcal{P}_1$, $\mathcal{P}_2$ and $\mathcal{P}_c$ with $\mathcal{P}_f$ in the IR camera wavelength range. The plasma parameters for analytic distribution function are identical to the ones in the previous paragraph. For both energies - 20 and 30 MeV - the approximation $\mathcal{P}_2$ is the closest to $\mathcal{P}_f$. This is expected for the lower energies as seen from the theoretical conditions. However, the discrepancy between $\mathcal{P}_f$ and $\mathcal{P}_1$ is quite surprising in comparison with results presented in Fig. 6.2a. This is probably due to the collective effect, which show to be important. Finally it is concluded that for the COMPASS tokamak IR camera approximation $\mathcal{P}_2$ can be used for the RE energy range between 20 and 30 MeV.

6.2 Details on Experimental Setup

The outline of the IR camera and its location on the device were already briefly reported in Section 3.3.2. As shown in the previous Section, this camera is suitable for the SR coming from the REs with energies over approximately 15 MeV. In addition, the absence of SR in the IR spectrometer implies that no detectable RE population exists over 30 MeV in the COM-

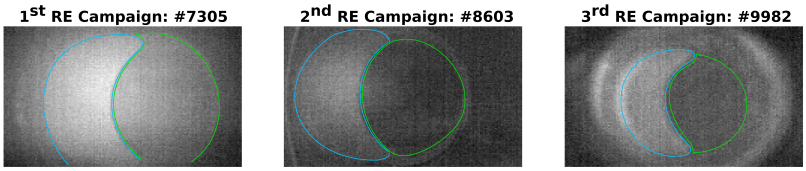

Figure 6.5: Three different views of the IR camera to the LFS wall for the first three RE campaigns. Light blue depicts NBI dump and light green indicates mid-plane port.

PASS tokamak.

In this Section we will focus mainly on the different IR camera views due to the slightly different locations from campaign to campaign. These views can be seen in Fig. 6.5, where discharges without plasma are chosen. The observed structures will be important in the upcoming Sections, thus their nomenclature has to be addressed and explained here. The moon-like structure on the left is the carbon NBI dump[4], which is closer to the plasma than the LFS wall (that is the reason why it shines). The ellipse in the middle of the photos is the south mid-plane port, therefore it is vacant with respect to the surface of the LFS wall.

Additionally to the Fig. 6.5, Table 6.2 is provided. The Table contains details on the window installed on the mid-plane tangential 11/12 port - the material of which it is made, the size, and the characteristic transparency corresponding to the spectral range of the IR camera. As the IR camera position and orientation were not identical in the three campaigns, the observed region with respect to the core d_{IR} and the IR camera distance from the most tangential location with respect to the core l_{IR} were different for each campaign (see Table 6.2).

6.3 Observation and Classification of IR Measurements

The raw signal from the IR camera is digital and not calibrated. As the IR camera measurement was first intended for wall temperature measurements, the signal output in temperature is automatic. However, to use the IR camera as a SR diagnostic requires radiation intensity or/and brightness calibration. This proved to be far from trivial and needs a case-by-case approach. Moreover, the IR camera can be run at 4 different sensitivities that correspond to its 4 different temperature ranges. The raw signal for all sensitivities goes from the negative values (depending on the sensitivity) to the measured maximum or instrumental maximum (i.e. saturation at

[4]The protection from NBI particles that pass through the plasma.

Table 6.2: Detailed information on the IR camera setup during the first three RE campaigns (corresponding discharge numbers from Fig. 6.5 are also depicted). l_{IR} is the distance from the camera lens to the plasma core, while d_{IR} is an approximate diameter of the observed region at the plasma core.

RE Campaign	Window: material	Window: diameter [cm]	Window: transparency [%]	l_{IR} [cm]	d_{IR} [cm]
1st: #7305	ZnSe	3.7	∼70	111.6	14.9
2nd: #8603	Ge	8.5	80-90	139.5	16.9
3rd: #9982	Ge	8.5	80-90	153.5	15.5

10500 counts), which is exemplified in Fig. 6.6b. Henceforth, to unify all the sensitivities without tedious calibration, we define a ratio between the measured maximum and the absolute minimum value which we shall denote as the *relative intensity* $\mathcal{R}$.

Beside categorising the SR observations into those with and without the appearance of SR on the IR camera, there are a few less obvious or expected measurements. The **disconnection** is one such measurement, which occurs when SR is so strong that the IR camera simply switches off. Sometimes the IR camera can measure **wall heating** that can radiate the level of weak SR, but it can be clearly distinguished from the SR due to the slower decay time, location and shape. Also, the SR intensity strongly depends on **the discharge length** and presence of massive gas injection (MGI).

Moreover, SR in COMPASS is usually observed as a reflection from the

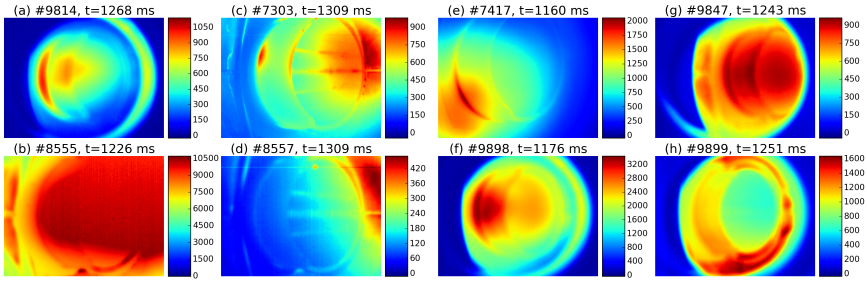

Figure 6.6: Examples of different observed SR shapes/patterns in COMPASS tokamak: **(a)** direct SR observation, **(b)** IR camera saturation, **(c-d)** SE reflection from the wall on the RHS, **(e-f)** SE reflection from the wall on the LHS, and **(g-h)** SR reflection all around the port. Note the different scale of the color map for each graph.

stainless steel wall, as almost all direct observations ended in what we call the disconnection event. The SR reflections were not always the same and some typical patterns are plotted in Fig. 6.6. Figures 6.6c-h show different kinds of SR reflection from the wall, which can come from the right-hand side of the wall (Fig. 6.6c-d), the beam dump on the left-hand side (Fig. 6.6e-f) or all around the Li-port (Fig. 6.6g-h). Wall structures in Fig. 6.6c, 6.6d, and 6.6h prove that radiation is reflected. However, more intensive radiation from the left beam-dump edge is probably due to its heating, as it is a few centimeters closer to the plasma. Finally, an infrequent measurement of the direct SR is depicted in Fig. 6.6a, which will be analysed in details in Section 6.4.

6.3.1 Data Analysis Integrating Different Campaigns

The aforementioned relative intensity $\mathcal{R}_{max}$ will be the parameter used to characterize SR in different campaigns and IR camera sensitivities. In previous study, it was found that $\mathcal{R}_{max}$ is inversely proportional to the RE critical energy [152]

$$W_{crit} = \frac{e^3 \ln \Lambda}{4\pi\varepsilon_0^2} \frac{n_e}{E_{tor}} \sqrt{2 + Z_{eff}}, \tag{6.10}$$

as we will show in the remainder of this Section. For simplicity and as we lack clear measurements, the effective charge Z_{eff} is considered constant for COMPASS and equal to 2.5 (as described in Section 4.4). Importantly, W_{crit} is inversely proportional to the normalised electrical critical field

$$\mathcal{E}_{crit} = \frac{m_e c^2}{W_{crit}} \sqrt{2 + Z_{eff}}. \tag{6.11}$$

The electron density is taken from the Thomson scattering measurements at the core and the toroidal electric field is estimated from the METIS code. Both values are time-averaged during the first 240 ms of the discharge independently of the discharge length.

The dependence of $\mathcal{R}_{max}$ as a function of W_{crit} and $\mathcal{E}_{crit}$ is plotted in Fig. 6.7 for the first three RE campaigns. First, one can observe is that there is no high IR camera $\mathcal{R}$ for W_{crit} over 41 keV or under $\mathcal{E}_{crit} \sim 26.5$ and that the same stands for the disconnection events. However, one should be careful with those numbers as they are averaged over time and therefore do not represent a direct number of the RE generation energy threshold or electric field in COMPASS. On the other hand, it gives a good idea of the order of magnitude to obtain significant high energy RE population in the COMPASS plasma. Moreover, the high $\mathcal{R}_{max}$ can be divided into three groups: (1) normal discharges with plasma length up to 350 ms; (2) long-discharges, which are longer than 350 ms and (3) long-discharges with Ar-induced disruption. A lower threshold for the SR observation is depicted in

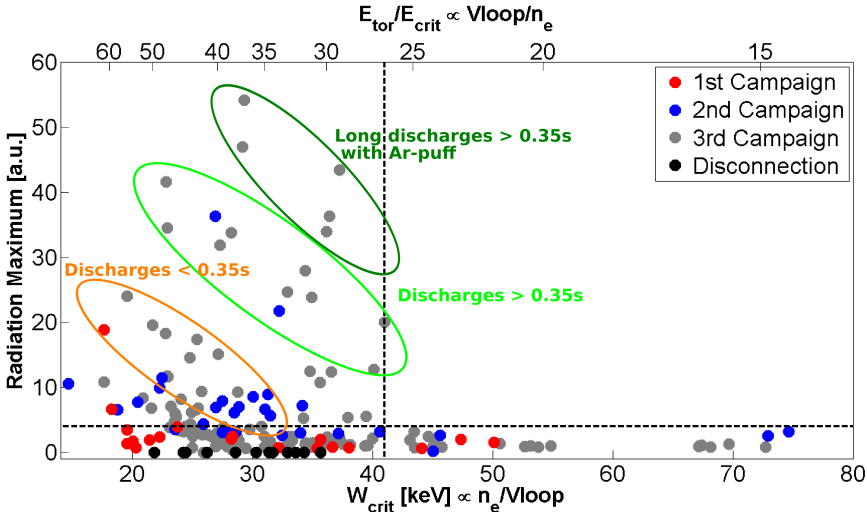

Figure 6.7: The maximum of relative intensity from IR camera during discharge $\mathcal{R}_{max}$ as function of critical energy W_{crit} (bottom axis) and critical electric field E_{crit} (top axis).

the Figure at $\mathcal{R}_{max} = 4$. Although SR can be observed under this threshold, it is difficult to analyse as the radiation level is of similar intensity as the thermal radiation from the wall.

6.3.2 Correlation with the Shielded HXR

In this Section, we briefly report on the correlation of the time-trace signals between the IR camera and the Shielded HXR. Fig. 6.8 shows the mean value of the IR camera measurement for each frame and the smoothed signal of Shielded HXR over 8 ms (as 8 ms is the approximate time resolution of the IR camera) for the COMPASS discharge #9992. Similar behaviour observed in the Figure is expected as both, IR camera and Shielded HXR, observe the high-energy REs. Also, one can notice that the IR signal increases and has maximum before the Shielded HXR signal increase and maximum, respectively. The delay between the two is due to the fact that the IR camera observes in-flight/confined REs, while the Shielded HXR observes their losses on the wall. Moreover, these kinds of correlation are mostly observed just before or during the I_p ramp-down phase. Henceforth, the observed losses probably come due to the decrease of the W_{drift} limit that decreases with the I_p, as described in Section 5.5. On the other hand, there is a second kind of correlation where maximum of the Shielded HXR signal occurs before the signal of the IR camera. This can appear for two different reasons, and both of them are observed in Fig. 6.9. Either the SR signal

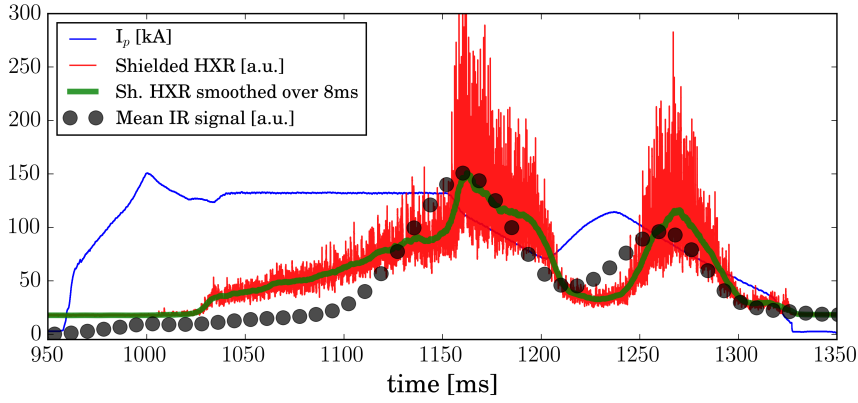

Figure 6.8: Time traces of the plasma current (blue line), Shielded HXR (red line), smoothed Shielded HXR over 8 ms (green line) and mean value of the IR camera frames (black dots) for the COMPASS discharge #9992.

is strong but the RE confinement is weak and their losses are observed with the Shielded HXR diagnostic before the IR camera measures SR[5] (see Fig. 6.9a), or the SR signal is weak and/or wall heating is detected by the IR camera (see Fig. 6.9b). These two cases differ in intensity (SR usually

[5]This is due to the lower RE energy threshold for the Shielded HXR than for the IR camera - see Section 3.3.2 for more details.

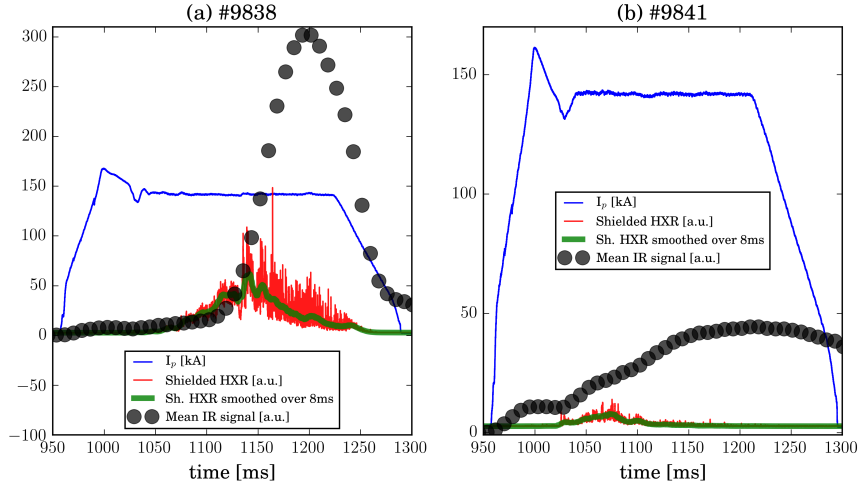

Figure 6.9: Same time traces in Fig. 6.8 but for different discharges.

has higher values than the wall heating) and decay time of the IR signal (SR usually has shorter values than the wall heating). Data analysis was performed in an attempt of setting an automatic tool based on physical reasons to distinguish between these two cases, but it showed to be far from trivial and the only way to do unambiguous classification at the moment is looking at the raw IR camera signal.

6.4 Direct Observation

As already mentioned in Section 6.3, direct measurements of SR in COMPASS tokamak were quite infrequent, mostly due to the fact that the IR camera disconnected during intensive SR. Explicitly said - direct observation is claimed only for 13 discharges out of 363 highly relevant ones in the first 3 RE campaigns (statistics taken from the Table 3.1). Moreover, some of the 13 discharges could have too strong reflected and/or background radiation, as all the recorded direct SR observations were relatively weak. Therefore, extraction of the SR information only from these measurements was rather challenging task.

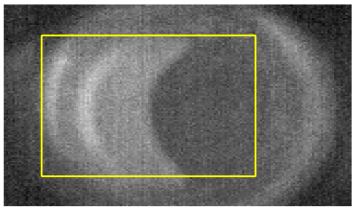

Figure 6.10: View of the IR camera towards the LFS wall for the 3rd RE campaign (same as in Fig. 6.5). The yellow rectangle depicts the area taken in the reported analyses (Fig. 6.11).

Eventually, the discharge #9814[6] showed to have the best direct SR measurement. The analysis was firstly reported in Ref. [152]. We recall that the plasma in the discharge #9814 was circularly shaped, with $B_{tor} = 1.15\,\mathrm{T}$ and a linearly rising current due to a constant V_{loop}. Even though the plasma current is rising, this phase will be addressed as the *flat-top phase* due to the common nomenclature and for convenience. Direct SR is observed during the ramp-down phase at the end of the discharge, approximately after 1220 ms.

We will first describe how the raw IR camera data is processed, i.e. in particular background subtraction. This signal is then used for the pitch angle estimation. The Section continues by showing how the pitch angle can be used for the estimation of the current driven by the high energetic REs. Finally, a comparison of this estimate with codes is presented.

6.4.1 Background Subtraction

As already mentioned above, the 13 discharges with the direct SR observation had rather weak signals, i.e. SR was usually comparable with the

[6]Note that this discharge was used in the Section 4.2 as well.

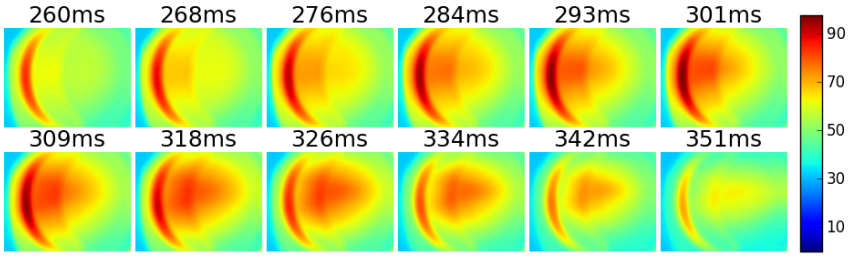

Figure 6.11: Raw IR camera data for the discharge #9814. The analysed IR camera region is marked with a yellow rectangle in Fig. 6.10. The colorbar is in W/sr/m^2. The Figure is reproduced from Ref. [152].

thermal radiation from the vacuum vessel wall. Therefore, a subtraction of the thermal IR background radiation had to be realized to extract pure SR measurement.

An example of IR raw signal is presented in Fig. 6.11 for #9814. Note that only part of the IR camera view is shown corresponding to the part depicted in yellow in Fig. 6.10. This is done to avoid radiation from significant heating of C-tile and to reduce reflection artifacts of SR coming from the side of the IR camera view.

The frame taken at 227 ms[7] has been taken as the background frame, because in the following frames one could observe some SR from the RE beam. However, frames presented in both Figures 6.11 and 6.12 do not start from this particular moment. Namely the first plotted frame (at 260 ms) is when the SR intensity at one pixel reaches around 50% of the pixel IR signal maximum during the whole discharge. Note that this 50% intensity

[7]This time corresponds to the 1177 ms of the COMPASS time, as 950 ms was taken for the starting time.

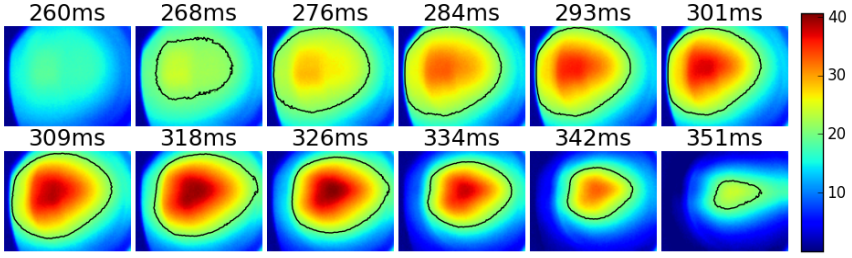

Figure 6.12: Same frames as in Fig. 6.11 but with subtracted frame at 227 ms. Black line in the different frames corresponds to 50% of the maximum intensity. The Figure is reproduced from Ref. [152].

of whole discharge maximum is also taken to be the edge of the RE beam, the condition based on Ref. [81].

6.4.2 Pitch Angle Estimation

The pitch angle θ can be estimated after inferring the RE beam shape from IR camera pictures. A simplified geometry view of a single RE trajectory is given in Fig. 6.13, from where θ can be expressed through the curvature radius R_c and the difference between the width and the height Δr of the observed SR contour:

$$\theta = \arccos\left(1 - \frac{\Delta r}{R_c}\right). \tag{6.12}$$

In the above calculation of the pitch angle, we assumed that the IR camera observes the whole RE beam in the vertical direction. However, in Section 3.6 of Ref. [70] the author explains that this does not have to be the case. Another possibility is that the observed RE beam vertical length (with half-height h_{RE}) is limited by the pitch angle itself. Furthermore, those two possibilities cannot be distinguished by looking only at the IR camera measurements if it is located at the tokamak mid-plane, which is the case for the COMPASS tokamak IR camera. For further analysis, note that there is no port on the COMPASS tokamak that would be able to measure SR off-mid-plane.

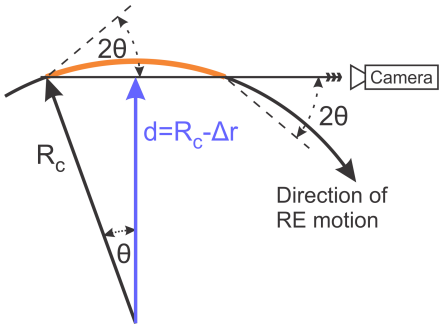

Figure 6.13: Geometry of the SR observation from REs in tokamak.

Anyhow, we will show that our initial assumption was correct by considering the opposite and showing that it does not lead to a physical result. When the pitch angle limits the vertical measurement of the IR camera, the RE beam minor radius a_{RE} is larger than the observed vertical half-length h

$$a_{RE} > h_{RE} = l_{IR} \sin\theta, \tag{6.13}$$

where l_{IR} is the distance between the IR camera and the RE beam[8]. Knowing that h_{RE} is not larger than 5 cm, as estimated by black line from Fig. 6.12, one calculates from Eq. 6.13 that $\theta < 0.0326$ rad. In addition to the aforementioned geometrical condition Eq. 6.13, Pankratov [158] adds one more condition for which the RE beam is not seen completely in the

[8] Values for l_{IR} are listed in Table 6.2

vertical direction:

$$\tan\theta < \frac{a_{RE}}{q(r)R_c}, \tag{6.14}$$

where $q(r)$ is the safety factor at the corresponding minor radius $r = R_c - R_p$. For the discharge #9814, R_c is around 65 cm and $q(r)$ does not go over 2.6, which limits θ under 0.03 rad. Such low θ is about an order of magnitude lower than what is measured in other machines. Moreover, a low pitch angle means that REs in COMPASS practically move along the magnetic field lines. It would be physically surprising to expect such a scenario for such high RE energies and relatively low magnetic field as it is the case for the COMPASS discharge #9814. Henceforth, we are confident that our initial assumption of observing the whole RE beam in the vertical direction is acceptable.

6.4.3 High RE Density Estimation

The SR radiance B_{SR} from Eq. 6.2 can be defined through the density of RE population observed by the IR camera n_{RE}^{synch} [81] through

$$B_{SR}(\lambda, \theta, W_{max}) = \mathcal{P}(\lambda)\frac{2R_c}{\pi\theta}n_{RE}^{synch}. \tag{6.15}$$

To compare SYRUP output with experiment it is necessary to integrate the SR radiance B_{SR} over the observed wavelength range measured by the IR camera [81], obtaining the brightness

$$S(\theta, W_{max}) = \int B_{SR}(\lambda, \theta, W_{max})T(\lambda)\mathrm{d}\lambda, \tag{6.16}$$

where λ is the wavelength and $T(\lambda)$ the transparency of the optical path between the RE beam and the IR camera. In our case, transparency of the Ge window[9] is the only factor to take into account.

The iterative procedure for estimating the high-energy RE density is the following:

1. calculate $\mathcal{P}(\lambda)$ from the SYRUP code using $\mathcal{P}_2$[10] (defined in Eq. 6.7) with the plasma parameters - $\bar{n}_e = (1.6 \pm 0.2) \times 10^{19}\,\mathrm{m}^{-3}$, $T_e = 530 \pm 60\,\mathrm{eV}$, $E_{tor} = 0.33 \pm 0.04\,\mathrm{V/m}$ and $Z_{eff} = 2$;

2. take "a priori" n_{RE}^{synch} and obtain the corresponding theoretical brightness;

3. compare this theoretical brightness (from point 2.) with the experimental one measured with the IR camera;

[9] Values for window transparency are listed in Table 6.2

[10] Reason why $\mathcal{P}_2$ is used is elaborated in Section 6.1.4.

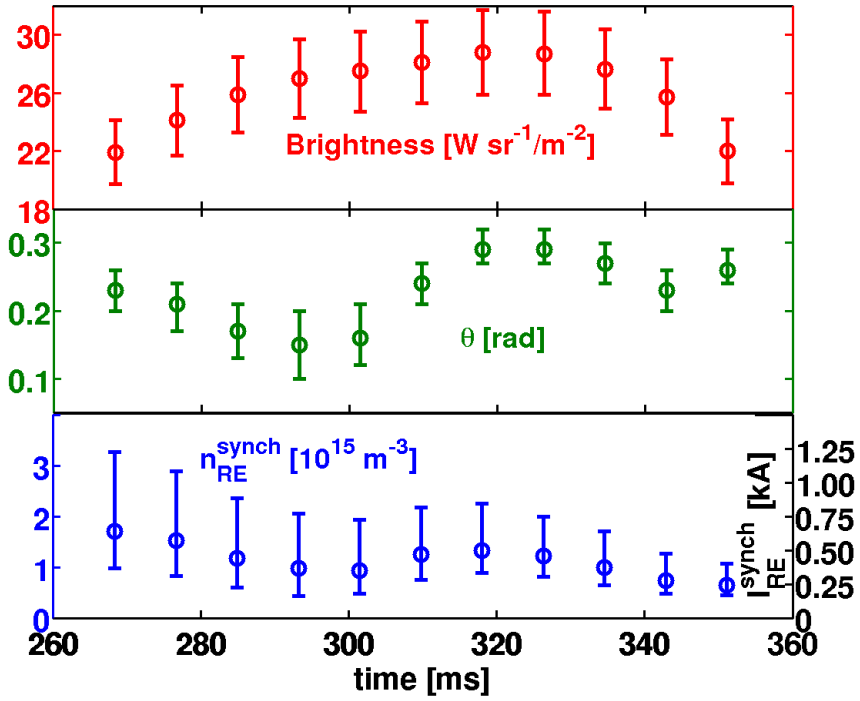

Figure 6.14: Time traces of the theoretical brightness for the contours, pitch angle and the density of the high-energy REs with their corresponding RE current for beam radius of 5cm for discharge #9814. The Figure is reproduced from Ref. [152].

4. IF difference is visible to the third significant digit go to step 2, OTHERWISE save n_{RE}^{synch} value.

The results for the theoretical brightness, the estimated θ and the high-energy REs with the corresponding RE current are depicted in Fig. 6.14 for discharge #9814. The estimated current driven by high-energy REs is of order of a few 100 A, which is in agreement with the analysis done for Fig. 6.1.

Furthermore, the above results from the experiment are compared with the NORSE code. The simulation is done in the same manner as described in Section 5.2. In Fig. 6.15 the estimate of n_{RE} from the NORSE code is shown for the whole RE population and the parts that have energies over 15 and 20 MeV. Additionally, $n_{e,c}$ from measurements and n_{RE} from Kruskal-Bernstein theory are added for illustration purposes. One can see that Kruskal-Bernstein gives an order of magnitude higher n_{RE} than NORSE slowly approaching the total electron density at the end of the discharge.

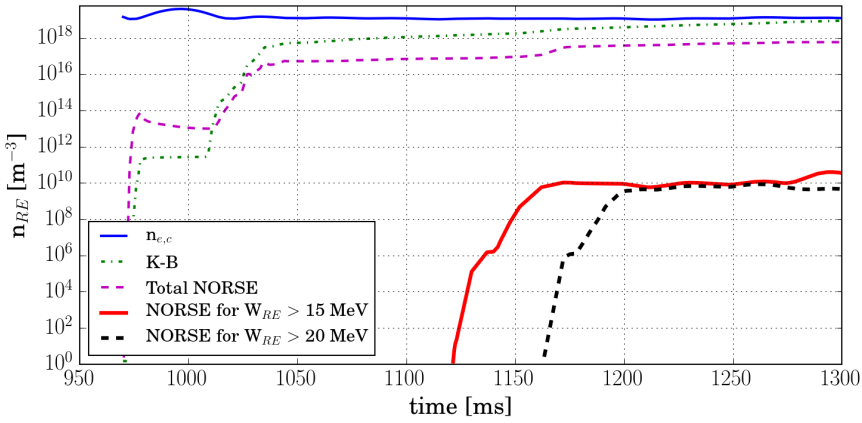

Figure 6.15: Time traces of measured $n_{e,c}$ (solid blue), total RE density from Kruskal-Bernstein (dash-dotted green) and NORSE (dashed magenta) models, and RE density for population over 15 (solid red) and 20 MeV (dashed black).

Anyhow, the main point to focus on from Figure 6.15 is that NORSE estimates a number of high-energy REs about 5 orders of magnitude lower than it was obtained in Fig. 6.14. Furthermore, the time when the RE population over 20 MeV from NORSE reaches its highest values coincides with the detection of the SR signal. This shows a good agreement of RE population dynamics between the NORSE code and the experiment, with a large discrepancy in RE absolute numbers.

6.5 Summary and Conclusions

SR is one of the most direct ways to detect REs. Therefore, due to its importance, the first measurements and analysis on the COMPASS tokamak are reported here.

First, it was shown that those measurements are not accidental, but that they were supported by theoretical calculations. The fortunate fact was that the available IR camera (not designed for the SR observation) had wavelength in the necessary range for the SR observation from the COMPASS plasma. Furthermore in this Chapter, the handling and the purpose of the SYRUP code was explained. In combination with the IR spectrometer, SYRUP is also used to estimate the upper RE energy limit at around 40 MeV in the COMPASS tokamak.

Next, experimental observations are analysed in details. Namely, the most common shapes of SR reflection on the COMPASS wall are described. The correlation is found between the relative SR intensity $\mathcal{R}$ and RE pa-

rameters W_{crit} and $\mathcal{E}_{crit}$. The deduced threshold for SR observation are $W_{crit} < 41\,\mathrm{keV}$ and $\mathcal{E}_{crit} > 26.5$. Also correspondence between time evolution of SR and the Shielded HXR is illustrated and discussed.

Direct observation of SR for discharge #9814 is exploited here in the details. It gave us an estimate of the pitch angle in the range $0.15 - 0.30\,\mathrm{rad}$ and we estimated that the RE density for energies above $15 - 20\,\mathrm{MeV}$ is of the order of a few $10^{15}\,\mathrm{m}^{-3}$. However, NORSE gave 5 orders of magnitude lower RE density for energy above $15-20\,\mathrm{MeV}$. On the other hand, timing of the experimentally observed SR and the rise of the high-energy RE density from NORSE are in excellent agreement.

Unfortunately, correlation between IR camera and the Shielded HXR signals did not produce any quantitative results. Therefore, some more work has to be done on this topic, specifically on the dynamics of the signal, i.e. temporal correlation. Moreover, reconstruction of the observed shapes in Fig. 6.6 based on method from Ref. [159] could be done and provide localisation of RE beam. Beside SR-related topics, an interesting point using the IR camera data could be to investigate the IR-camera-observed hot-spots origin, as they could be the a result from the lost REs.

Chapter 7

Post-Disruptive Runaway Electron Beam

A detailed analysis of the post-disruptive RE beam in the COMPASS tokamak will be presented in this Chapter. As previously reported in Section 3.9, Ar injection was used to trigger post-disruptive RE beams in COMPASS. This method was used in many other machines as MGI triggered disruptions are more prone to the RE beam occurrence, as stated in Section 2.2.4, even though MGI is one of the two main RE mitigation options (described in Section 2.2.7).

The Chapter starts with a motivation and details on achieving RE beam in the COMPASS tokamak. They are followed by the detailed parameter analysis on the RE beams occurrence in the COMPASS tokamak. The Chapter continues with a thorough study of the runaway current plateau phase. The termination of the RE beam is then investigated briefly. Then measurements from a IR camera and the lack of synchrotron radiation are described. Furthermore, MGI in long discharges is reported separately. Finally, the summary of all topics and main conclusions are given.

7.1 Achieving RE Beam

As already noted in Section 2.2.6, REs are presently set as the second highest priority for the ITER disruption mitigation system [85]. Therefore, obtaining post-disruptive RE beam was of the paramount importance for COMPASS, as it would lead towards more ITER-relevant RE studies. Notwithstanding that the COMPASS tokamak would became even more ITER-relevant fusion device.

However, achieving RE beam was not expected to happen spontaneously due to the B-limit. The B-limit is described in Section 2.2.4 and it predicts no RE beam generation for plasma with $B_{tor} \leq 2\,\mathrm{T}$, while the COMPASS

tokamak usually operates with $B_{tor} = 1.15\,\mathrm{T}$. Accordingly, the Ar injection was used to trigger the first RE beam in COMPASS. The first tests have shown [136] that the easiest way to produce a RE plateau was to massively inject Ar during the ramp-up phase of the plasma current. Henceforth, all following Section are addressing the Ar injection during the ramp-up phase.

The occurrence of the RE beam is already described in Section 2.2.4, where two initial phases - thermal quench (TQ) and current quench (CQ) - are described in details. The exact theory behind RE beam occurrence/formation is not yet clear, but most of the theories agree that REs are generated as a result of the Dreicer and hot-tail mechanisms[1]. After RE beam is formed, a relatively quiescent phase occurs where RE current is either flat or slowly decreasing - the so-called RE current plateau. The final phase is the termination of the RE beam.

MGI was achieved using the solenoid valves. Their location is depicted in Fig. 3.3 and their installation during RE campaigns is detailed in Section 3.3.3. Anyhow, the solenoid gas valves are connected to the vessel through a system of stainless steel tubes with a length of about 50 cm having an inner diameter in the $4-6\,\mathrm{mm}$ range. This non-negligible tube length implies a delay between the time of valve opening and the time at which the argon puff starts to interact with the plasma, i.e. roughly the time at which the gas enters the vacuum vessel. The delay is estimated to be $1-1.5\,\mathrm{ms}$ approximately, taking into account a mean velocity of approximately $400\,\mathrm{m/s}$ for argon gas in vacuum at 300 K. Based on the observations, all discharges with the MGI in the COMPASS tokamak can be classified as follows:

1. Strong (RE plateau): RE beam carries more than 10% of the pre-disruptive current I_p;
2. Weak (RE plateau): REs typically carry current equal to a few 100 A;
3. Slow (radiative current decay): the plasma current slowly decreases in a similar way to a ramp-down phase;
4. Zero (RE plateau): a 'typical' disruption, with no RE remaining or generated after the disruption.

An example of each class is shown in Fig. 7.1, where the right plot in the Figure is a close-up view of the left part to emphasise the difference between the weak and the zero plateau measurements. Although the weak and the zero cases might seem identical at first sight, the Shielded HXR signal confirms the release of the RE after the disruption in the weak case (2) and their loss during the disruption in the zero case (4). This classification is very important, as it will be used from now on throughout the Chapter.

There were 186 discharge attempts from the 2$^{\mathrm{nd}}$ to the 5$^{\mathrm{th}}$ RE campaign in the COMPASS tokamak, out of which 129 discharges ended successfully,

[1] For more details on Dreicer and hot-tail mechanism see Sections 2.1.1 and 2.1.2, respectively.

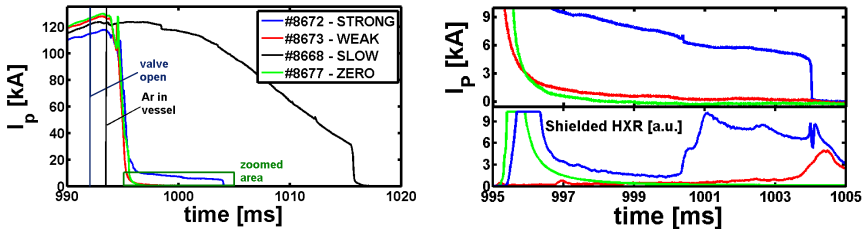

Figure 7.1: Classification examples. **Left:** discharge #8672 with a strong plateau, #8673 with a weak plateau, #8668 with a slow plasma current decay and #8677 as an example of disruption without RE surviving or produced. **Upper right:** Close-up of (a) for a better observation of the difference between the weak and the zero plateaus. **Lower right:** the Shielded HXR signal for comparison of the strong, weak and zero cases. The Figure is reproduced from Ref. [136].

i.e. are marked as highly relevant using the nomenclature from the Table 3.1. Furthermore, MGI was carried out during the ramp-up phase for 96 times out of the 129 highly relevant discharges. For this scenario, strong RE beams were obtained in 24 discharges, and 21 had a weak RE beam after the 88 Ar-triggered disruptions. Furthermore, Ne was used in the remaining 8 discharges that resulted in 2 weak RE beams. In addition, MGI into long discharges was performed 10 times with Ar and only ones with Ne. Finally, the secondary Ar puff into the RE beam was tested for the 2 last discharges of the 5$^{\text{th}}$ RE campaign, but more experiments are necessary for a detailed investigation.

7.2 Generation

A parametrisation of the post-disruptive RE beam generation will be conducted in this Section. Particularly, an update of the analysis performed in Ref. [136] will be presented. Additionally, new parameters were found to be important - e.g. a negative V_{loop} jump and magnetic fluctuations. On the other hand, there are parameters and data that are completely inconclusive and still awaits analyses and interpretation. The most prominent of such investigations is the dependence of the RE beam generation level with the Ar back pressure P_{back}. Even though the tests were executed in the wide range of P_{back} - from 0.6 to 4.0 bars - most of the Strong RE beams were created for $P_{back} = 2.4$ bars[2].

The Section starts with an example of the reproducibility of MGI experiments and explains why it is necessary to perform the data analysis

[2]For details on the injection system calibration and corresponding number of injected particles see the Appendix C.

between the shots. The data analysis reported on the RE beam formation are done for the I_p decay rate during the CQ, pre-disruptive E_{tor} and I_p, and magnetic fluctuations.

7.2.1 Repetition Attempts

In the 5th RE campaign we have tried to create a reproducible scenario for obtaining the post-disruptive RE beam. Unfortunately, this showed to be quite an onerous task. According to some authors (e.g. Abdullaev in Ref. [138,160]), this goal could even be impossible due to the stochastic and chaotic nature of the problem.

Anyhow, the best set of consecutive 3 discharges with identical tokamak and MGI setups are presented here. The set consists of two discharges with Strong RE beams - #10925 and #10926 - and one discharge ending in a Slow decay - #10927. For all the 3 discharges the solenoid valve was opened around 973 ms, implying that the gas was reaching the vacuum vessel around $974 - 975$ ms. The relevant measurements are plotted in Fig. 7.2.

Fig. 7.2a shows the I_p time evolution for complete discharges for the 3 aforementioned discharges. The zoomed I_p signal around the TQ and until the RE plateau end is plotted in Fig. 7.2b. Interestingly, even though the setups were identical - disruption of the discharge #10925 had a delay of 1.5 ms with respect to the disruption of the discharge #10926. The reason is unknown, as Ar seems to enter the vessel at the same time according to the EDICAM1 camera[3]. Therefore, we will first compare these 2 Strong RE beams between themselves. From Fig. 7.2c we can also see that densities before the TQ were rather identical - making no distinction between the RE generation. Negative voltage spikes can be observed in Fig. 7.2d and more clearly in Fig. 7.2e. At more or less the same moment when the voltage spikes occur, Mirnov coils also detect a jump (see Fig. 7.2f) and the plasma starts to move radially inwards (see Fig. 7.2g). Furthermore, CTU HXR from Fig. 7.2h measures RE losses a few tenths of a millisecond after the TQ. The Shielded HXR measures RE losses at the end of the RE plateau, as seen from Fig. 7.2i. Those REs are probably from the ones that survived the losses at the beginning of the plateau measured by CTU HXR. Interestingly, a large amount of RE has been generated also during the Slow radiative decay - making us to suspect that this regime is a mixture of REs and a warm plasma. Finally, ECE signals shown in Fig. 7.2j-m reveal that plasma got cooled around 1 ms before the TQ current spike for both Strong RE beams. Moreover, one can see that the Slow decay was influenced at almost the same time as #10926. Unfortunately, ECE does not seem to be useful during the RE plateau phase, as it seems to be influenced by the

[3]The visible camera EDICAM1 (see Sectin 3.3.1 for the camera setup details) is able to distinguish when the Ar puff interacts with the plasma, i.e. penetrates into the vessel, as a lot of visible light is emitted when this happens.

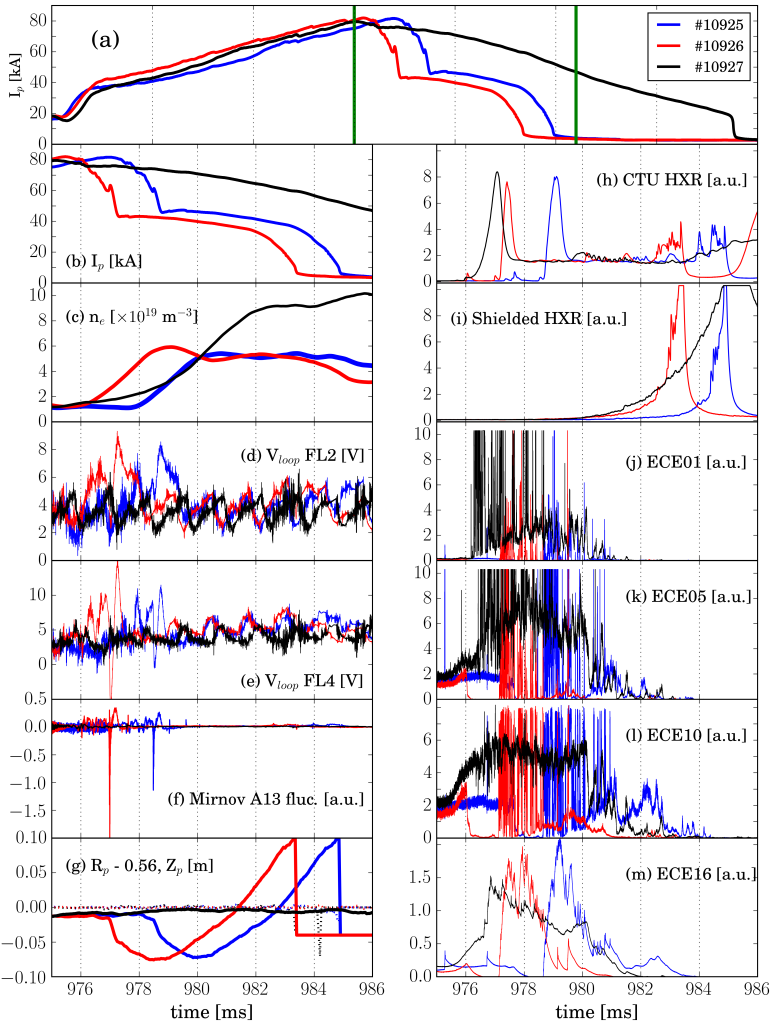

Figure 7.2: The RE beam reproducibility attempt presented with three discharges: #19025 (blue), #10926 (red) and #10927 (black). The signals are from:**(a)** the plasma current I_p for the whole discharge with green lines at 975 and 986 ms denoting zoomed time frame in the other parts of this Figure; **(b)** the plasma current I_p **(c)**; the electron density n_e from the interferometer; **(d)** the loop voltage V_{looop} from FL2; **(e)** the loop voltage V_{looop} from FL4; **(f)** magnetic fluctuations from Mirnov coil A13; **(g)** the radial $R_p - 0.56\,\mathrm{m}$ (solid) and vertical Z_p plasma position (dotted); **(h)** CTU HXR; **(i)** Shielded HXR; and **(j-m)** ECE signals from chord 1,5,10 and 16.

HXR signal. The difference of ECE16 with respect to the other ECE signals is probably due to the shielded observation region, being the outermost one.

Even though the tokamak and MGI setups were exactly the same and tokamak wall conditions very similar (as those are three consecutive discharges), no 3 close enough results were obtained. Discharges #10925 and #10926 have a delay in between their TQ spikes, while #10927 did not result in a RE beam. Moreover, from any relevant data presented in Fig. 7.2, no obvious reason can be seen why #10927 did not have a Strong beam. Therefore, lead by this experience and suspected chaotic nature of the problem, we will now turn to the data analysis among all available Ar discharges at the COMPASS tokamak.

7.2.2 Current Quench Speed

It is speculated that MGI improves RE generation due to the triggering of the fast CQ [161]. The plasma current quench rate

$$I_\gamma = \frac{1}{I_p}\frac{\mathrm{d}I_p}{\mathrm{d}t} \tag{7.1}$$

is one way to quantify the CQ speed. Yoshino *et al.* [59] did the first detailed parametrisation of disruptions with runaway occurrence in JT-60U tokamak. According to his article, the study of I_γ versus q_{eff} is important for the RE plateau occurrence, where the effective edge safety factor q_{eff} for circular plasma is defined as:

$$q_{eff} = \frac{5a_p^2 B_{tor}}{R_p I_p}\left[1+\left(\frac{a_p}{R_p}\right)^2\left(1+\frac{(\beta_p+l_i/2)^2}{2}\right)\right]. \tag{7.2}$$

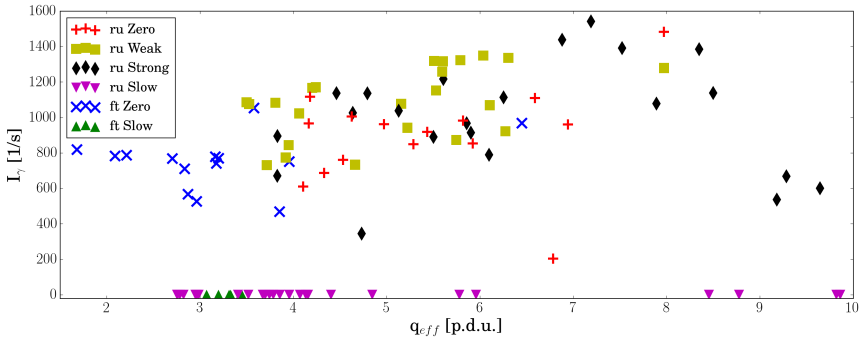

Figure 7.3: The plasma current quench rate I_γ plotted versus the effective edge safety factor q_{eff} in the procedure defined units (p.d.u.). The classification from Section 7.1 is used, with the ramp-up (ru) and flat-top (ft) discharges split for clearer interpretation.

All parameters are taken from the EFIT reconstruction at the closest moment from the disruption. Fig. 7.3 shows I_γ versus q_{eff} for the case of COMPASS. For all plateaus (except the Slow ones), I_γ is between 300 and $1600\,\mathrm{s}^{-1}$ and q_{eff} is between 2 and 10. It is interesting to observe that the majority of the disruptions above $q_{eff} = 7$ correspond to the Strong ones. Moreover, practically all the Weak and the Zero cases are confined in the $q_{eff} = 3.5 - 6.5$ region. Furthermore, there is 'an isolated island' of Strong disruptions in the right-bottom part of the Figure. Obviously, slow disruptions have significantly slower current decay than the rest of the discharges, therefore I_γ was simply set to 0.

Finally, no particular differences were observed between the discharges, as the majority of the I_γ values are in the range $300 - 1600\,\mathrm{s}^{-1}$ in all the cases. The values suggest that the whole pre-disruptive I_p is lost in $0.6 - 3.3\,\mathrm{ms}$ time range. Notice that all the values are slightly larger than the electromagnetic field penetration time of the COMPASS vacuum vessel ($\sim 0.5\,\mathrm{ms}$), which is labeled as the 'slow current termination' in Ref. [59].

7.2.3 Pre-Disruption Electric Field

According to the theory, as elaborated in Chapter 2, the production of RE is more intense for higher E_{tor}. Additionally, the value of the plasma current just before the disruption I_{disr} showed to be important experimentally. Thus, I_{disr} is plotted in Fig. 7.4 as a function of the toroidal electric field E_{disr} at the same moment estimated from the flux loop measurement[4].

[4]In this Chapter E_{tor} will be estimated from the flux loop FL4 (unlike the previous Chapters where E_{tor} was taken from the METIS) because for some discharges the necessary data should be available before 970 ms when both - METIS and EFIT - start their calculation.

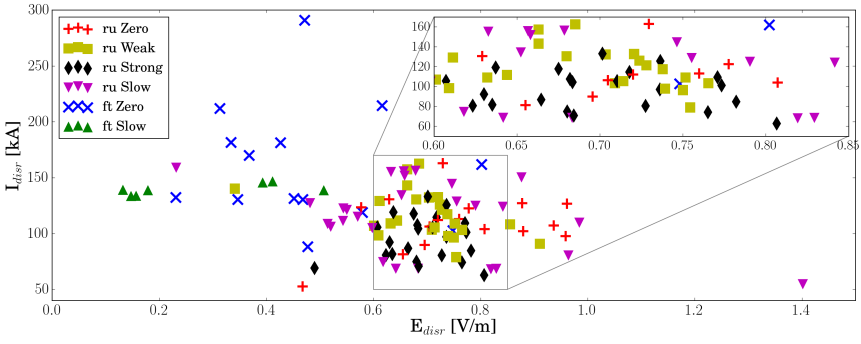

Figure 7.4: The plasma current before disruption I_{disr} plotted versus the toroidal electric field before disruption E_{disr}. The classification from Section 7.1 is used, with the ramp-up (ru) and flat-top (ft) discharges split for a clearer interpretation.

It is interesting to observe in Fig. 7.4 that the least scattered discharges are the Strong ones, while a bit more scattered are the Weak ones. The "Strong discharge region" is zoomed in the Figure. This possible E_{tor}-window for RE beam formation could be due to the too fast RE drift [160] (upper limit) and low RE generation (lower limit).

7.2.4 Magnetic Fluctuations

Magnetic perturbations were reported as one way to mitigate REs in Section 2.2.7. Moreover, it was observed experimentally in the TEXTOR tokamak [162] that REs do not occur above a certain level of magnetic fluctuations in the plasma. Some attempts were performed to explain the phenomenon theoretically [74, 163] or even to connect it with the B_{tor}-threshold [164] mentioned in Section 2.2.4. Therefore, we investigated magnetic perturbations as one of the possible parameters for the RE generation.

The signal from the Mirnov coil A13[5] during disruption with frequencies over 40 kHz (high-pass filter) is used to quantify the magnetic fluctuations. Furthermore, the magnetic fluctuations were always[6] preceded by negative spikes in the V_{loop} signal, which then jumped back to the positive values. The value from the negative spike peak to maximum reached after the jump is taken as an amplitude of the V_{loop}-jump. The amplitude of the magnetic fluctuations is plotted as a function of the V_{loop}-jump in Fig. 7.5 for illus-

[5] For details about Mirnov coils setup see Section 3.3.1 and Fig. 3.2.

[6] 'Always' refers to the disruptions with TQ and CQ phases, i.e. for all MGI triggered disruptions expect the Slow ones.

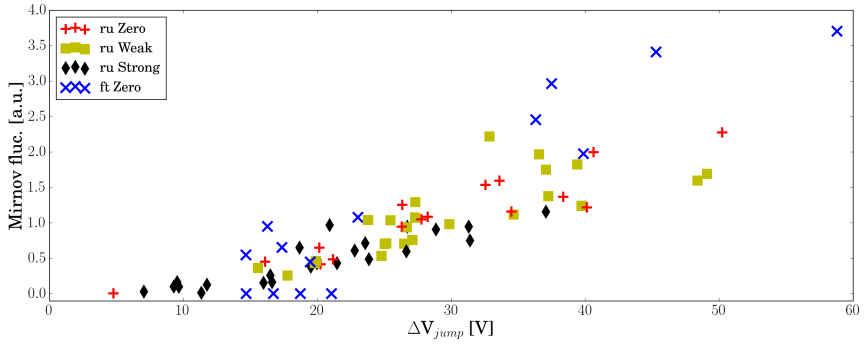

Figure 7.5: The magnetic fluctuation amplitude for frequencies higher than 40 kHz from the Mirnov A13 coil plotted versus the amplitude of the V_{loop} jump after the negative spike ΔV. The classification from Section 7.1 is used, with the ramp-up (ru) and flat-top (ft) discharges split for clearer interpretation and omission of Slow disruptions, as they did not have any negative spike in V_{loop}.

tration purposes.

One can see the linear relation between the fluctuation level and the voltage jump amplitudes. Moreover, majority of the Strong RE beams occurred only under $\Delta V < 30\,\mathrm{V}$, making ΔV a very important factor for the RE beam occurrence. Notice that an even more important influence of the voltage jump on the RE occurrence will be addressed afterward in Fig. 7.8. An interesting point is also how some flat-top Zero disruptions have low ΔV amplitude - same as in the Strong cases. They show that the lack of fluctuations does not have to end up in the RE beam, making the final conclusion uncertain. In fact, without the Zero disruptions during the current flat-top, we could be confident in the fact that the voltage jump and the magnetic fluctuations present the main cause of the RE beam appearance (or absence). However, the flat-top Zero cases leave us some space for further investigations.

The cause of the voltage spike and the magnetic fluctuations is still unknown, but it is probably connected to the plasma current spike during the TQ phase. Fig. 7.6 is put together in an attempt to find out what both parameters do depend on. It seems that both parameters are determined by the amount of the pre-disruptive plasma current. However, this conclusion might be misleading, as the Zero flat-top cases do not follow the same dependence as all the ramp-up ones. Furthermore, note a rather clear linear dependence of ΔV on I_{disr} in Fig. 7.6b.

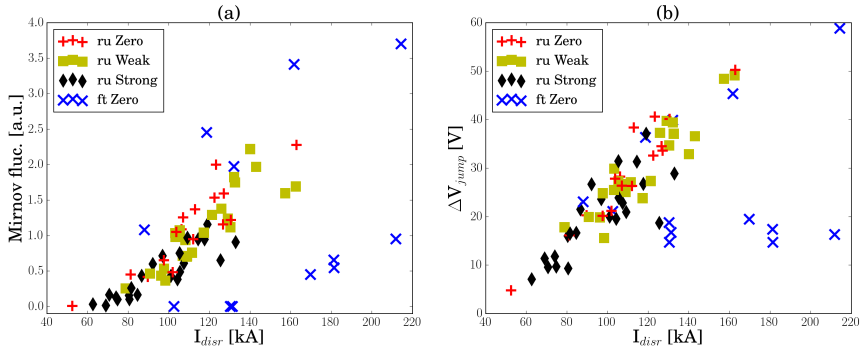

Figure 7.6: **(a)** The magnetic fluctuation amplitude for frequencies higher than 40 kHz from the Mirnov A13 coil and **(b)** the amplitude of the V_{loop} jump after the negative spike ΔV versus the plasma current just before the TQ. The classification from the Section 7.1 is used, with the ramp-up (ru) and flat-top (ft) discharges split for clearer interpretation and omission of Slow disruptions, as they did not have any negative spike in V_{loop}.

7.3 Plateau

The previous Section considered parameters before and during the disruption itself, as some of those parameters are governing the RE generation. After this initial stage, a RE beam is formed that is often addressed as the *RE plateau*, due to the constant RE current in the large fusion devices. However, the RE current during this phase in COMPASS is usually not constant but rather constantly decreasing. Anyhow, the phase will be labeled as the "RE plateau" for convenience. The RE plateau phase will be investigated in this Section.

The Section starts with the classification of the discharges looking at the induced E_{tor} after the disruption. It continues with two RE current investigations, ending with the RE current decay analysis.

7.3.1 The Induced Post-Disruptive Electric Field

As explained in Section 2.2.4, the plasma current I_p drop during the current quench (CQ) induces an increase of the toroidal electric field E_{tor} that enhances RE generation through the avalanche effect. In ITER the E_{tor} factor increase (and following the RE multiplication factor) will be tremendously high (by a few orders of magnitude higher compared to the values before the disruption). However, in COMPASS this is not the case, as it can be seen from the Fig. 7.7, knowing that typical value for E_{tor} during the ramp-up phase is in the $5 - 10\,\mathrm{V/m}$ range.

The trends observed in Fig. 7.7 are quite expected. The linear increase for both Zero sets of discharges is predicted by the well-known inductance formula $V = L_p I_p'$. If the plasma inductance L_p and the plasma current

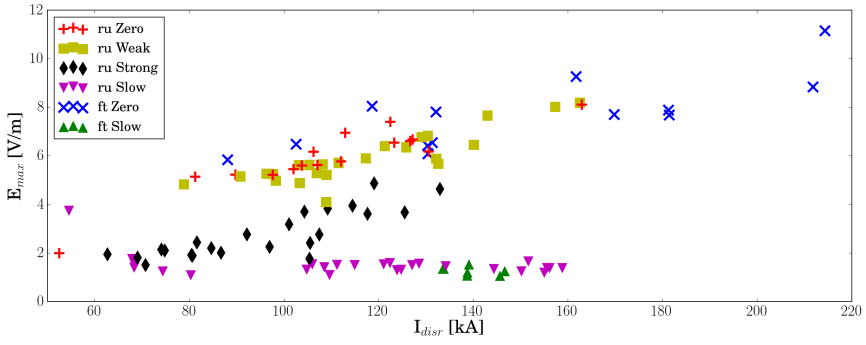

Figure 7.7: The maximum estimated electric field after the disruption E_{max} plotted versus the plasma current just before the TQ I_{disr}. The classification from Section 7.1 is used, with the ramp-up (ru) and flat-top (ft) discharges split for clearer interpretation.

derivative I'_p are assumed to be constant, the linear dependence comes from the longer CQ duration for the larger I_{disr}. The same stands for the Weak discharges, since the amount of the RE current is relatively low and the CQ phase looks the same as for the Zero case. On the other hand, Slow discharges practically do not have TQ and CQ phases of disruption, but only a slow radiation decay. In other words, no additional electric field is induced due to the lack of the rapid I_p drop. Hence, they have the lowest E_{max} on the Figure for both sets.

Finally, the Strong discharges have linearly increasing E_{max}, but the slope does not match those from the Zero and the Weak sets. This is because the CQ phase is shorter for the Strong discharges than for the Zero and the Weak discharges, as it lasts only until the RE beam is formed. Furthermore, it is interesting to notice from Fig. 7.7 that the RE beam was never obtained for $I_{disr} > 140\,\text{kA}$, even though there were attempts to do that. Unfortunately, most of those discharges ended in the Slow or the Weak cases. The existence of the upper current limit could be due to two reasons - either magnetic fluctuations are too high [59] or the REs drift is too fast due to the higher electric fields [160]. Those two potential reasons will be examined in Section 7.3.2 and 7.3.3, respectively. In Ref. [59], it is also claimed that too low I_{disr} generates too low electric field disabling the RE generation. However, this is not observed in Fig. 7.7. On the contrary, the Strong cases are the most common ones for the lowest experimentally achievable I_{disr} in the COMPASS tokamak ramp-up phase.

7.3.2 RE Beam Current during Plateau

As shown in Section 7.2.4, the voltage jump after the negative spike ΔV showed to be a relevant parameter for the RE generation. Therefore, a percentage of the disruption current I_{disr} driven by REs is presented in Fig. 7.8 as a function of ΔV. The percentage is obtained by division of mean I_{RE} during the plateau phase and I_{disr}. A clear decrease in the mean I_{RE} value can be seen from the Figure as ΔV increases. Now, let us take a look at the aforementioned reasons for the upper I_{disr} limit. As ΔV is directly connected to the magnetic fluctuations as shown in Fig. 7.5 and as Yoshino claims that the fluctuations are stronger for higher disruption current I_{disr} [59], in Fig. 7.9a I_{RE}/I_{disr} is plotted as function of I_{disr}. Moreover, Abdullaev reported that a too high E_{tor} creating RE drift is the reason for the lack of the RE beam. Therefore, Fig. 7.9b shows the I_{RE} as a function of E_{max}. The decreasing trend of the overtaken pre-disruptive plasma current by REs is seen in both cases. However, I_{disr} is taken 2 ms before TQ while E_{max} is always determined just after CQ. Having this in mind, we can deduce that the Yoshino's scheme is more realistic, as a higher E_{max} is rather a consequence of higher I_{disr}, not a cause of RE beam absence.

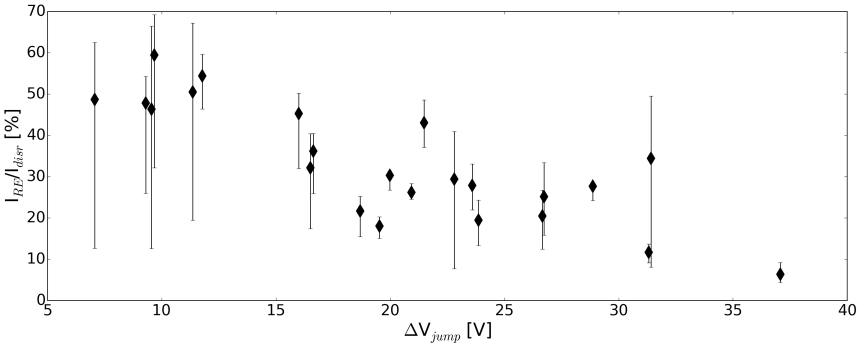

Figure 7.8: The percentage of the disruption current I_{disr} driven by REs I_{RE} plotted versus the amplitude of the V_{loop} jump after the negative spike ΔV. Obviously, only Strong disruptions are considered. The error bar represents the RE current at the beginning and the end of the RE plateau, while the marker represents the mean value of the I_{RE} during the plateau.

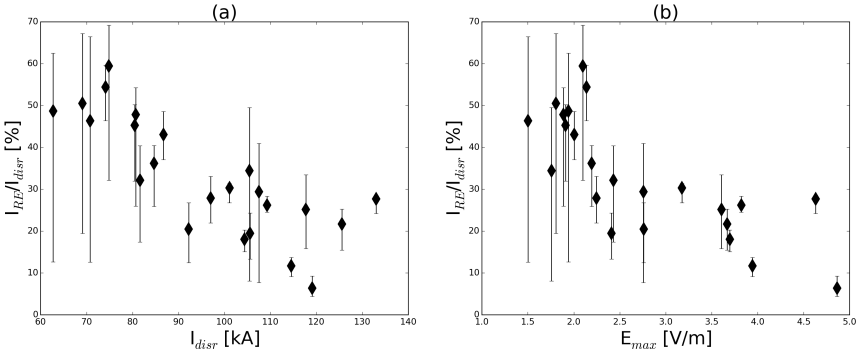

Figure 7.9: The percentage of the disruption current I_{disr} driven by REs I_{RE} plotted versus **(a)** the plasma current before disrption I_{disr} and **(b)** the maximum estimated electric field after the disruption E_{tor}. The y-axis data is presented in the same manner as in Fig. 7.8.

7.3.3 RE Beam Current Using Abdullaev's Hypothesis

A mechanism for unpredictable experimental results in obtaining the RE beam after disruption is reported in Ref. [160] and elaborated in details in Ref. [138] by Abdullaev *et al.* The basic schemes of the mechanism includes the existence of a magnetic island on some low rational magnetic surface number[7], the island's survival during disruption initiated stochasticity of

[7]Safety factor $q = m/n = 1/1, 2/1, 3/2, 5/2$, etc - where m and n stand for the number of particle trajectory turns along the toroidal and poloidal directions, respectively.

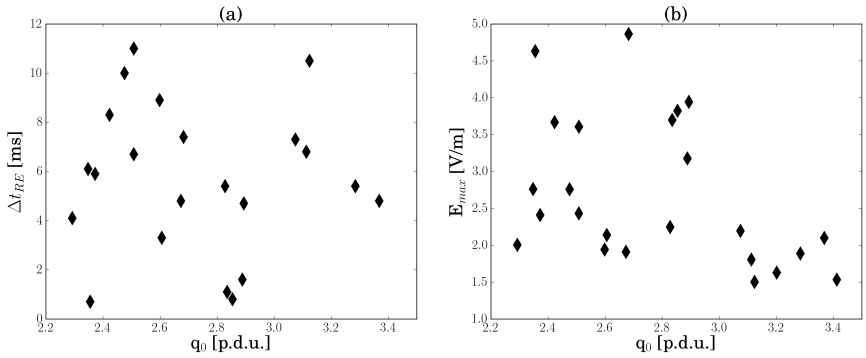

Figure 7.10: **(a)** The duration of the RE plateau Δt and **(b)** the maximum estimated electric field after the disruption E_{max} plotted versus the safety factor at the plasma core q_0 taken from the EFIT reconstruction.

the magnetic field under certain conditions (e.g. low magnetic fluctuations), and the creation of the RE beam inside the rational surface region.

Abdullaev stated that disruptions with plasma having lower core safety factor q_0 will have a larger electric field, resulting in shorter RE beam due to the faster drift coming from the stronger electric field (elaborated more in Section 7.3.4). Accordingly, Fig. 7.10 shows the dependence of the RE plateau duration and the peak E_{tor} value after the disruption as a function of q_0, taken from the EFIT reconstruction. Curiously, there is no peculiar tendency at all in validating the Abduallaev explanation for COMPASS.

Moreover, in his example, Abdullaev emphasize the importance of having $q_0 < 1$ - making q_0 as low as possible. For that reason, we conducted some experiments with Ar puffs into the flat-top phase of several discharges with sawtooth crashes[8]. Unfortunately, this attempt to obtain the RE beam during the flat-top phase was not successful. An interesting point here is also that those MGI experiments into sawtooth discharges represent points that have relatively low ΔV_{jump} in Fig. 7.5 and points that do not follow the main trend in Fig. 7.6 in the right-bottom part.

Nonetheless, EFIT does not see $q_0 < 1$ even for those sawtooth discharges. The reason could be twofold - either the sawtooth theory is not correct or the EFIT moderately fixed current density $j(r)$ profile does not predict properly the q-profile. Henceforth, the q_0 from EFIT a large error due to the practically unknown $j(r)$-profile. Even though the sawtooth issue is extremely interesting from the perspective of fusion plasmas, it is far beyond the topic of this work. On the other hand, the $j(r)$-profile issue could be solved with some modelling done by Yoshida [147] briefly described at the end of Section 5.1. However, as mentioned in Section 5.6, this topic

[8] As by theory those discharges should always have $q_0 < 1$.

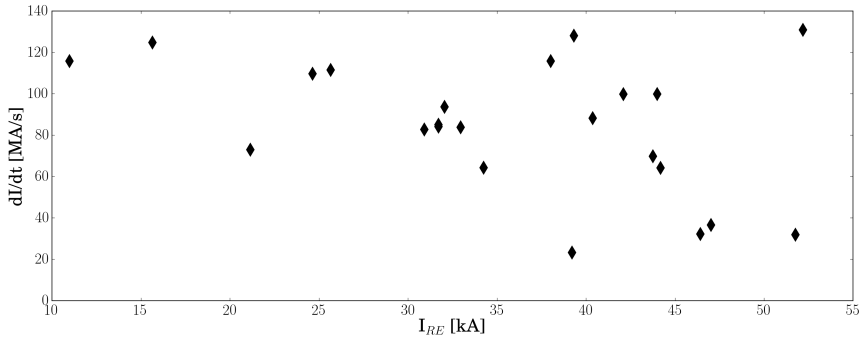

Figure 7.11: The slope of the I_p during the CQ plotted versus the RE current at the beginning of the plateau phase.

is left for the future work.

One more interesting observation reported by Abdullaev is that the plasma current decay during the CQ has a linear relation with the initial RE beam current, which is plotted in Fig. 7.11 for the COMPASS case. Obviously, no clear dependence can be distinguished, but one could see tentatively a linearly decreasing trend. Anyway, this issue will be more elaborated and investigated in the next Section.

Finally, Abdullaev also showed that the initial I_{RE} value is directly connected linearly with the q-value of the rational magnetic surface. Namely, the amount of the initial I_{RE} corresponds to the plasma current enclosed into the minor radius a_{RE} of the corresponding rational surface q_{RE}. Hence, we used EFIT to calculate the corresponding q_{RE} for the measured initial I_{RE} for COMPASS Strong RE beam cases. The result is presented in

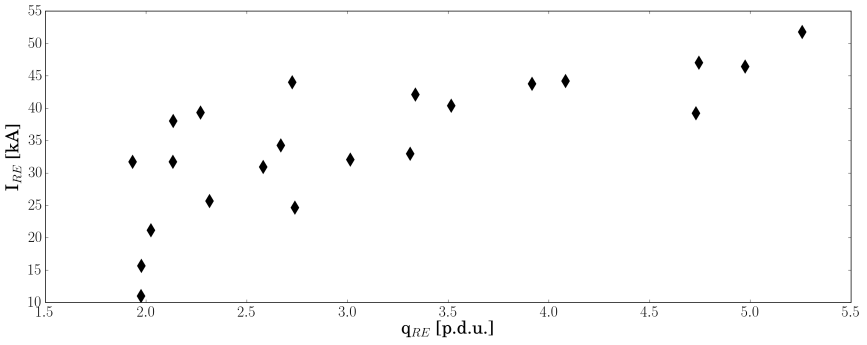

Figure 7.12: The RE current at the beginning of the plateau phase plotted versus the EFIT q-value located at the surface that has current equal to I_{RE} with timing just before the disruption.

Fig. 7.12. Even though COMPASS EFIT does not see $q_0 < 1$ as for Abdullaev's dedicated calculation for TEXTOR - there are some interesting features in the Figure. Firstly, one can notice the increase of I_{RE} with q_{RE}, which does go along with the Yoshino's results of obtaining RE beam for larger q_{eff}. Next to notice is a deployment of a few points around $q = 5/1$ and $4/1$, while there is a continuous set of data in the $q = 2 - 3.5$ range. Importantly, this range is quite rich in the number rational surfaces, as expected by the Abdullaev theory. Finally, it seems that the rational surface $2/1$ is the lower limit for obtaining the RE beam in the COMPASS tokamak. However, as already explained above, the q-profile from the EFIT should be treated with large error margins.

7.3.4 RE Beam Current Decay

One more important examination of Abdullaev [138, Section 6.2] is the connection between the RE beam drift with the RE current decreasing slope and the strength of the electric field. Namely, assuming that I_{RE} decreases due to the beam shrinkage and considering that the plasma current is proportional to its surface (i.e. $I_{RE} \propto a_{RE}^2$ as in Eq. 5.3), one obtains

$$\frac{\mathrm{d}I_{RE}}{\mathrm{d}t} = \frac{\mathrm{d}I_{RE}}{\mathrm{d}a_{RE}} \frac{\mathrm{d}a_{RE}}{\mathrm{d}t} \frac{2I_{RE}}{a_{RE}} v_{dr} \propto \frac{E_{tor}}{a_{RE}}, \tag{7.3}$$

so that the I_{RE} slope is proportional to the average drift velocity v_{dr} of the RE beam. Setting the common values for the RE beam in COMPASS for the above equation to $I_p = 20-40\,\mathrm{kA}$, $a_{RE} = 5-10\,\mathrm{cm}$[9] and $v_{dr} = 20-40\,\mathrm{m/s}$[10] the RE current decay is in the order of $4 - 32\,\mathrm{MA/s}$, while experiments give values in the $0.7 - 5.7\,\mathrm{MA/s}$ range. Unfortunately, no exact estimate of the

[9] Estimate of an order of magnitude by looking at the EDICAM camera.
[10] Taken from magnetic measurement of the radial position.

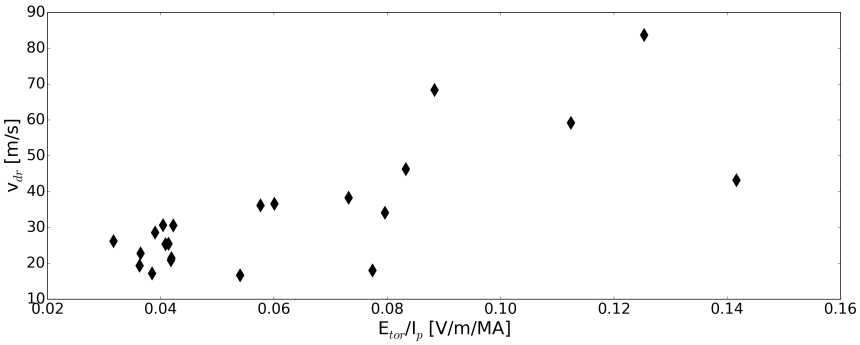

Figure 7.13: The median drift RE beam velocity v_{dr} values plotted versus the median values of the E_{tor}/I_p ratio during the RE plateau.

a_{RE} is available at the moment, therefore assuming $v_{dr} \propto E_{tor}/I_p$ is used to investigate the hypothesis accuracy and the result is plotted in Fig. 7.13. Note that the plotted values are the median values during the whole RE beam[11]. Even though the rate of increasing v_{dr} with E_{tor}/I_p is not clear, the general tendency seems to be there.

7.4 Termination

The termination phase of the RE plateau (always) has faster current decay than the plateau phase that is accompanied with a fast increase and saturation of the Shielded HXR signal (see Fig. 7.2i). However, there is no convincing interpretation for such a fast lost. The most probable reason is the RE beam drift[12] that cause the RE beam outwards movement due to the increase in the RE energy W_{RE}.

A detail numerical analysis of the RE drift was also performed by the TEXTOR team, the main result being published by Wongrach [165]. They found that REs are not confined when W_{RE} surpasses a critical value proportional to $\sqrt{I_{RE}}$. Practically, this was a confirmation of the Zehrfeld's analytic expression (Eq. 5.25). We made an attempt to confirm this theory for COMPASS experimentally, unfortunately without success. This could be either because the W_{RE} estimation from Section 4.1.2 is not suitable for the post-disruptive plasma or more probably because of a weak knowledge of the plasma parameters in the post-disruptive plasma. Hence, this is one more topic to investigate in future, especially because artificial drifting of RE in the early disruption stage could be a new and an effective RE mitigation technique, as explained by Abdullaev. Moreover, he emphasized the importance of the drift for the ITER and probably a reason why small aspect ratio tokamak (such as spherical tokamaks) do lack disruption created REs.

Furthermore, Abdullaev speculates that sudden RE beam terminations could result from a beam resonant interaction with the magnetic perturbations. Moreover, such behaviour is experimentally recognized in JET [87]. However, no evidence of any magnetic activity can be observed in the COMPASS tokamak RE beams, as it can be seen in Fig. 7.2f.

7.5 Absence of Synchrotron Radiation

In various tokamaks - e.g. DIII-D [81] and TEXTOR [165] - synchrotron radiation (SR) were observed during the post-disruptive RE beam. Nonetheless, this is not the case for the COMPASS tokamak RE beam. On the contrary, the SR is observed during the Zero, the Slow disruptions, and the long discharges.

[11] Median is chosen to avoid the outliers in the radial position
[12] See Section 5.5 for more details on the RE drift.

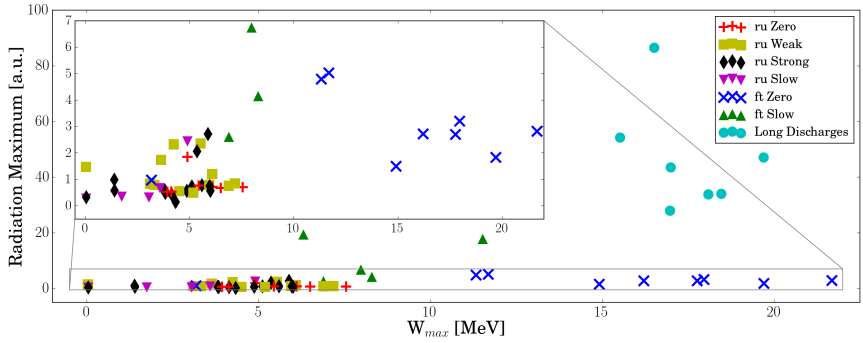

Figure 7.14: The relative maximum measured by IR camera $\mathcal{R}_{max}$ plotted versus the calculated RE energy W_{max} until the moment when Ar reaches the plasma. The classification from Section 7.1 is used, with the ramp-up (ru) and flat-top (ft) discharges split for clearer interpretation.

Accordingly to the aforementioned observations, we plot in Fig. 7.14 the measured $\mathcal{R}_{max}$[13] value against the W_{RE} estimated until the time when Ar affects the plasma. The latter parameter is practically the maximum W_{RE} before the disruption. Even though the apparent linear correlation is missing in the Figure, the tendency is there. Obviously, the IR signal is strongest for the long discharges, which is expected due to the sufficient time for REs to accelerate. Next ones are Zero and Slow discharges with MGI during the flat-top phase, where former have higher IR signal measurement and latter have higher estimated W_{max}. Note that SR appears in the one or two frames after the disruption in the case of the flat-top puffs. Interestingly, the set of discharges with the lowest value for both parameters in the discharge are the Strong RE beams.

Now we will discuss the Ar injection effects on the SR. Namely, the observation of SR seen after the Ar puff is expected by the model presented by Aleynikov [166], where he modules the Ar injection interaction with the RE plateau. The main result was that the RE beam looses half of the current, but individual RE gain energy if SR is omitted from the model. On the other hand, the inclusion of SR leads to an enhanced RE current and energy losses. Guided by this analysis and Fig. 7.14, we could suspect that the absence of REs in the pre-disruptive plasma is a favorable condition for post-disruptive RE beam creation in the COMPASS tokamak. This also coincides with the fact that no clear RE beam was created during the MGI into the long discharges. Anyway, the amount of the RE current to explain high SR during those puffs is calculated in the following Section.

Furthermore, the SR is clearly distinguishable for all discharges with MGI during the flat-top, while theoretically the maximum obtainable RE

[13]The parameter is explained in details in Section 6.3.

energy W_{max} goes as low as 7 MeV in some cases. However, the calculation from Section 6.1.2 and the experimental experiences are indicating that SR would be difficult to detect with the present IR camera under $15 - 20$ MeV. Therefore, we suspect that the measured IR signal after the disruption is a consequence of the RE additional generation due to the MGI itself.

Finally - with what was said above and having in mind that W_{max} during the RE beam existence does not exceed 7 MeV only for Strong cases - we deduce that REs existing in the post-disruptive COMPASS RE beam phase are created during the disruption, i.e. do not originate from the pre-disruptive plasma.

7.6 Long Discharges

Fig. 7.14 shows extraordinary high SR radiation for the long discharges. This is suspected to be due to the numerous RE population which drive a majority of the measured total current. To check how much current is driven, we use the method for I_{RE} estimation reported in Section 5.3.1 for discharge #10072, the most right-hand side point on the Fig. 7.14. The result is plotted in Fig. 7.15a, accompanied by the IR camera and the Shielded HXR measurements in Fig. 7.15b. The I_{RE} is estimated for monoenergetic and exponential REDFs, as the two limiting cases studied in Chapter 5. The obtained results give a large span of I_{RE} at the end of the discharge - between 3 and 100 kA. As both REDF used are probably extremes - we could assume that for sure at least a few tens of kA are driven by the REs.

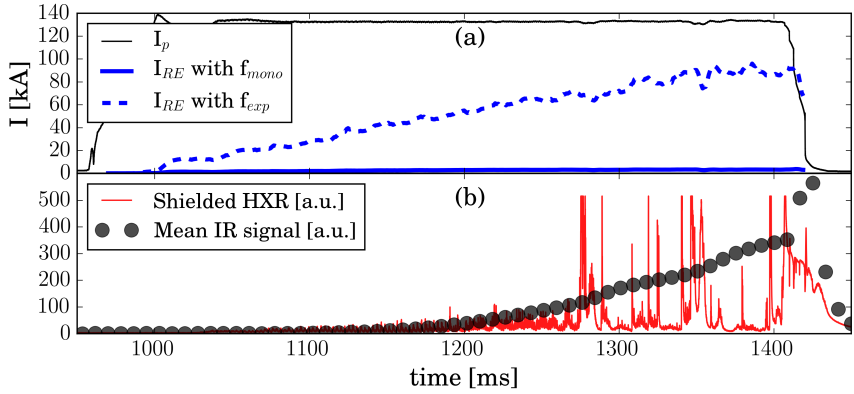

Figure 7.15: **(a)** The time traces of the measured plasma current I_p (black solid line) and estimated RE current I_{RE} from experiment using monoenergetic (solid blue line) and exponential (dashed blue line) RE distribution function. **(b)** The time traces of the mean value of the IR camera frames (black dots) and Shielded HXR (red solid line).

As it can be seen from Fig. 7.11, this amount of current is similar to the current driven by the post-disruptive RE beam. Henceforth, studying MGI with this discharge could contribute to the understanding of RE beam with injected gas, making such experiments very ITER-relevant. Those studies were already presented in Ref. [130] and will be part of other publications in future work.

7.7 Conclusions and Outlook

In ITER, the REs will appear only after the disruption. Moreover, the behaviour of REs during the quiescent plasma phases is probably not the same as RE beam behave in the post-disruption phase. Therefore, achieving the RE beam after the disruption was one of the paramount goals for the COMPASS RE studies. The importance is twofold - understanding of RE beam generation and its mitigation. Due to the complexity of the post-disruptive RE phenomenon only understanding of RE generation is reported in this Thesis.

Post-disruptive RE beams in COMPASS were obtained injecting Ar with typically 2.4 bars of P_{back}. Two types of post-disruptive REs exist in COMPASS: **Strong** RE beam carrying more than 10 kA and **Weak** RE beam having maybe a few hundreds of amperes. We attempted to create a reliable repeatable scenario of RE beam creation, but without a clear success, due to the stochastic nature of the RE beam generation. A series of data analysis is conducted for the relevant discharges.

Three groups of parameters were analysed for a better understanding of the RE generation. The analysis realised by Yoshino [59] was performed first. Here we found that practically all disruptions had a current quench rate I_γ between 300 and 1600 s^{-1} and that the Strong RE beams occur usually for an effective safety factor q_{eff} over 7. The next parameter considered was the electric field before the disruption E_{disr}. It was observed that both RE beam types, Strong and Weak, appeared for E_{disr} in the $0.6 - 0.8$ V/m range. Fig. 7.7 also shows how the Strong RE beam was mostly created for lower values of the plasma current before the disruption I_{disr}. The last and probably the most attractive analysis considered magnetic fluctuations and negative spike on the voltage loop V_{loop}. The dependence among those two parameters was obviously linear and lower values correspond to a higher possibility of Strong RE beam generation. We also found that both parameters were strongly connected to the I_{disr}, but the definite origin of voltage spike is still unknown. Attempting to induce V_{loop} spikes might be beneficial for the RE mitigation. However, thanks to MGI in the flat-top phases of the sawtooth discharges, we could see that the V_{loop} spike is a necessary but not sufficient condition for the RE suppression. Finally, none of the presented results lead to a clear conclusions, leaving space for the future research.

To inspect further the reason for creation of the Strong RE beam we

looked at the CQ-induced E_{max} and I_{RE}. For example, the E_{max} data allows the conclusion that there is nothing like a low-value limit, while some experts claim that E_{max} will be too low in COMPASS for the RE beam creation. On the contrary, the RE beam in COMPASS had higher RE current for lower E_{max}. Regarding I_{RE}, we found that it is higher for lower V_{loop}-spike, I_{disr}, and aforementioned E_{max}.

Moreover, Abduallaev [138,160] published some very interesting hypothesis on the RE behaviour. We investigated some parts of this in this Chapter, and most of them did not seem to match the COMPASS observations. Namely, only the connection of the RE current at the beginning of the plateau phase and the safety factor q_{RE} at the radial location where RE current is the same as the pre-disruptive plasma current showed the expected behaviour. We found that q_{RE} does not go under 2 and a possible aggregation around $q_{RE} = 4$ and 5, but those results should be taken with caution due to the scarce number of data points and large errors from EFIT in the plasma center.

Abdullaev's theory connects the decay of RE current in the plateau phase with the E_{tor}/I_p ratio, but the trend we could see in Fig. 7.13 is not very satisfactory. Moreover, he also connected RE drift to the termination phase of the post-disruptive RE beam. However, we could not find any distinctive tendency using W_{max} calculation from Section 4.1.2. Finally, no magnetic fluctuations were detected at the termination phase via Mirnov coils in COMPASS, contrary to the results of TEXTOR and JET.

Furthermore, IR camera observations during the MGI experiments obtained that SR is weakest for the Strong RE cases and strongest for the radiation decays (Slow decay and Long Discharges). This leads us to suspect that the lack of REs in the pre-disruptive plasma is prone to the Strong RE beam creation. We also demonstrated that due to the sufficient time, Long Discharges have high SR and a few tens of kA RE driven current, which makes them a good model of the post-disruptive RE beam in larger tokamaks. Henceforth, studies of MGI in these discharges is at least as relevant as MGI into the ramp-up phase reported in this Thesis.

OUTLOOK. As many of the parameters considered in this Chapter were derived from EFIT, it would be desirable to check their validity by implementing the Yoshida's calculation [147]. Moreover, a model for RE generation during the disruption (e.g. GO [43]) should be implemented on the COMPASS tokamak.

Chapter 8

General Conclusions

Mitigation of runaway electrons (REs) is one of the essential physics topics for safe ITER operation. In this Thesis, an experimental RE study at the COMPASS tokamak was reported together with some technical details connected to the RE studies. The main goal of the Thesis was getting the recipe for the post-disruptive RE beam generation and perform necessary analysis. In addition, the author investigated the very first synchrotron radiation, the importance of the experimental definition for the toroidal electric field, and implemented the method for the RE current estimation using Thomson scattering and EFIT. Besides scientific work, the author participated in the RE campaign preparations and realisations.

Chapter 2 of the Thesis provides a brief overview of the RE state-of-the-art, as the last one was written almost 40 years ago. Note that this overview is far from being comprehensive, and rather serves as an introduction to the RE topic and a reference tool for the rest of the Thesis. Of course, a large emphasis was made on the ITER-relevant topics, e.g. the RE mitigation.

Chapter 3 provides a description of the COMPASS RE experimental campaigns that were carried out during the author's stay at IPP Prague. The Chapter includes general and RE diagnostic setup used further in the Thesis and a brief review of the main scientific achievements. The initial gas injection and electron density influence on RE generation in COMPASS was studied and determined in detail as the basis for all the types of RE experiments. These tests included obtaining the slide-away discharges, eventually creating long discharges (typically longer than 1 s), observing the Parail-Pogutse instability in RE discharge. The threshold critical field E_{crit} for RE observation/generation in COMPASS was estimated to be $14-21$ larger than the theory expects. Furthermore, scans over plasma location R_p, elongation κ and current I_p were performed. Even though no clear dependence was observed with respect to R_p, we observed that more REs were confined for larger κ and I_p. The latter one is probably connected to the safety factor q (the existence of magnetic islands). In addition, we experimentally

demonstrated that REs were not generated during sawtooth crashes in the COMPASS tokamak. On the other hand, sawtooth as well as other MHD instabilities (e.g. fly-wheel rotation, R_p oscillations, chirping modes) are still being investigated as possible sources of RE losses. Finally, maybe the most prominent result was the achievement of post-disruptive RE beams, analysis being carried out in Chapter 7.

Chapter 4 addresses the issue of the toroidal electric field E_{tor} estimation and its use for maximum RE energy W_{max} calculation. We found here that the flux loop FL4 is the most suitable one for RE studies in circular plasma on COMPASS. It was shown that the EFIT code has systematically closer W_{max} values to the measured ones than the METIS code. However, both codes had significantly different values compared to the experimental ones for the slide-away discharges. Moreover, the METIS code provided closer results to the experiment when Z_{eff} was taken to be 2.5 instead of 1.5. To estimate E_{tor} we decided to use METIS with $Z_{eff} = 2.5$ instead of EFIT due to consistency, as the METIS code is coupled with LUKE. Of course, it would be clearly noted if E_{tor} was calculated in different manner. Finally, this Chapter showed how large errors could be introduced in estimating W_{max} by using different E_{tor}. Moreover, one should be aware that W_{max} is usually used further to estimate another RE parameter, hence error propagation could be significant. We therefore emphasise the fact that any author should at least give a brief explanation on how E_{tor} is being estimated for the RE studies.

Chapter 5 deals with the discharges for which REs carried measurable amount of current in comparison to the plasma one. The adapted method for RE current I_{RE} estimation by Fujita [142] applied to COMPASS showed that for such discharges at least few percent of I_p was driven by the RE. The upper limit showed more difficult to prove and it could be as high as 50%. Furthermore, this method was also used to quantify the influence of REs on I_p during the ramp-up phase as reported in Ref. [128]. Finally, using the aforementioned method we also showed that the most probable reason for common RE losses during the ramp-down phase was the RE drift.

Chapter 6 reports the analysis of the very first observations of synchrotron radiation from the COMPASS discharges. The fact that the IR spectrometer did not observe any synchrotron radiation was examined using the code SYRUP which estimated that REs in COMPASS do not reach energies over 40 MeV. Data analysis among discharges provided the threshold of the critical energy W_{crit} below 41 keV and the critical field E_{crit} above 26.5 V/m for synchrotron radiation to be detected with the IR camera available. The discharge #9814 had the strongest and the clearest direct synchrotron radiation among all available discharges and it was analysed in details. The main outcomes were an estimation of the pitch angle in the range $0.15-0.30$ rad and the experimentally derived RE density of the order of a few 10^{15} m^{-3} for REs that have energy above $15-20$ MeV.

As achieving post-disruptive RE beam was the paramount goal of the

Thesis, this topic was kept to the end - Chapter 7. We report two types of RE beam in COMPASS: Strong ($I_{RE} > 10\,\mathrm{kA}$) and Weak (a few 100 A). The RE beam generation was characterised with respect to several parameters. For example, all Strong beams were created when the effective safety factor was over 4 and almost all Ar injection experiments with $q_{eff} > 7$ ended in the Strong beam. Next, both types of RE beam were generated in the relatively narrow range of electric field before disruption $E_{disr} = [0.6-0.8]\,\mathrm{V/m}$. Also, the lower the plasma current before the disruption I_{disr} the more probable it was for the Strong beam to be generated. Furthermore, magnetic fluctuation and negative voltage spike in the loop voltage V_{loop} signal proven to be very important in RE beam generation, namely the weaker they were the higher the resulting I_{RE}. Next, the new Abdullaev's hypothesis from Ref. [138,160] on RE beam generation was investigated as it seemed to be quite realistic. Unfortunately, except connection of I_{RE} with the pre-disruptive current inside certain rational surface, none of the other parameters and dependencies were sufficiently clear in the COMPASS tokamak case. Finally, we deduced from the lack of synchrotron radiation for the Strong cases that REs in the beam were not generated before the disruption. The analysis done in this Chapter represents an update of Ref. [136].

Besides all the aforementioned experimental results, the Kruskal-Bernstein theory and the NORSE code were used in the Thesis for comparison between theory and experiments. In general, both methods do recover trends observed in the experiments, but often both codes overestimate RE density by a few orders of magnitude, especially the Kruskal-Bernstein theory. However, when the estimation was performed for the high-energy REs (over $15 - 20\,\mathrm{MeV}$) NORSE showed about 5 orders of magnitude lower density than the experiments predicted.

Since a Ph.D. Thesis does not put a stop to the scientific investigations initiated, we also identified a series of key points that could benefit from further studies:

- Beside the NORSE code, comparison of the LUKE code with experimental results;
- More advanced calculation of equilibrium that includes RE beam - e.g. work done by Yoshida [147];
- IR camera observations - RE beam shapes, correlation with Shielded HXR signal and origin of hot-spots;
- Implementation of GO model for better MGI studies;
- Development of a novel RE diagnostics - some ideas are given in Appendix A.

Appendix A

Basis for Novel Runaway Electron Diagnostics Proposals

Even though there were no funds for such venture during his Thesis, the author examined the theoretical possibility of novel RE diagnostics. Therefore, a brief overview of proposal basis and simple calculations for Electron Cyclotron Emission (ECE) and Incoherent Thomson Scattering (ITS) as RE diagnostics are given in this Appendix. However, the conclusions are far from final, as both ideas proved to be more complicated than initially expected. For that reason, the Appendix represents an initial work that could be revised and improved towards a more definite shape.

A.1 Electron Cyclotron Emission

An introduction to ECE was already given in Section 2.3.4. An insight into its potential for RE studies and a brief revision of experimental achievements are enlisted here. The Section starts with motivation and theoretical overview of relativistic effects on ECE. It is followed by an explanation of what frequency shifts due to the Doppler and relativistic effects can be expected. Next part illustrates which spectral region of the REDF could be measured by the COMPASS ECE setup. The Section before the summary outlines the already achieved measurements of RE with ECE in different machines. At the end, a summary is provided.

A.1.1 Motivation

One of the experimental challenges for both, RE studies and mitigation, is the detection of REs in the early stage of their generation. Therefore,

the potential of the ECE diagnostics for the RE studies is huge as it could estimate the shape of the REDF in the approximately $50 - 500\,\mathrm{keV}$ range[1] experimentally. This part of the distribution function is often denoted as 'supra-thermal' electrons, as they could also originate from the heated up electrons by auxiliary heating systems. Concerning RE mitigation, one could (in theory) measure the early RE generation during the disruption using a carefully designed diagnostic. Henceforth, ECE could be adapted as a trigger signal for the RE mitigation.

A.1.2 Introduction

The general theory of ECE is well developed but rather cumbersome and difficult to handle in its elemental form. Consequently, the ECE from electrons with low energies ($\ll m_e c^2$) where low harmonics dominate and from high energies ($\gg m_e c^2$) where high harmonics dominate (i.e. synchrotron radiation) have practical approximations. Unfortunately, the aforementioned energy range ($50-500\,\mathrm{keV}$) is the intermediate case. This makes calculation more complex and slower and devoted work should be spent on its calculation speed enhancement. Anyhow, an appropriate calculation of ECE for non-Maxwellian, i.e. more RE relevant, distribution function should be investigated.

To illustrate the complexity of the problem, we will shortly focus on the electron emissivity $j_l(\omega)$ for a given harmonic l propagating perpendicularly to the magnetic field [167, Eq.(2.7)]:

$$j_l(\omega) = \frac{e^2\omega^2}{8\pi^2\epsilon_0 c}\frac{N_{ray}^2}{N_{r\pm}}\int \left\{ {}^{p_\parallel J_l}_{N_{r-}KJ_l\gamma + p_\perp J_l'} \right\} \frac{1}{\gamma^2}\delta\left(\omega - \frac{l\Omega}{\gamma}\right) f(\vec{p})\mathrm{d}^3p, \quad \text{(A.1)}$$

where ω is the angular frequency, Ω is the fundamental cyclotron frequency, $\vec{p}$ is the momentum, γ is the Lorentz factor, $\delta(\quad)$ is the delta-function, N_{ray} is the ray refractive index, N_{r+} and N_{r-} are refractive indices of ordinary and extraordinary waves, respectively, J_l is the Bessel function of the first kind with argument $lN_{r\pm}p_\perp/\gamma$ and K is given by

$$K = \frac{\omega_p\Omega\omega}{(\omega^2 - \omega_p^2)^2 - \Omega^2\omega^2}. \quad \text{(A.2)}$$

Looking at Eq. A.1, beside non-Maxwellian distribution function, emissivity depends on refractive indices of the media. Refractive indices are often assumed to be around 1 for the ECE measurements of thermal electrons, but this is not the case for plasma with significant RE population. In short, for tokamak plasma with REs the "black body" assumption is not valid anymore and emissivity becomes a function of the direction.

[1] As REs usually reach tens of MeV, observation of REDF in the $50 - 500\,\mathrm{keV}$ range would give information on the early stage of REs.

The calculations in the radial or tangential views are even more demanding for ECE because radiation reaching detectors is not propagating in a constant magnetic field. The task is huge and very time demanding and as it is far out of the scope of this Thesis, it is left for the future. Hence, here we demonstrate the potential of ECE as a RE diagnostic using simple calculations.

A.1.3 Frequency Shift

From Eq. 2.14 one can see that the cyclotron frequency can change twofold - increase due to the Doppler effect ($1-\beta_{\parallel} N_r \cos\alpha$ in the denominator[2]) or decrease due to the relativistic RE speeds (γ in the denominator). This is presented in Fig. A.1 for the first ECE harmonic located at the plasma core where $B_{tor} = 1.15\,\mathrm{T}$. For tangential propagation ($\alpha = 0°$) Doppler effects dominates until 1 MeV, while with increasing α it becomes inferior effect for lower energies until $\alpha = 90°$ where $\cos\alpha = 0$.

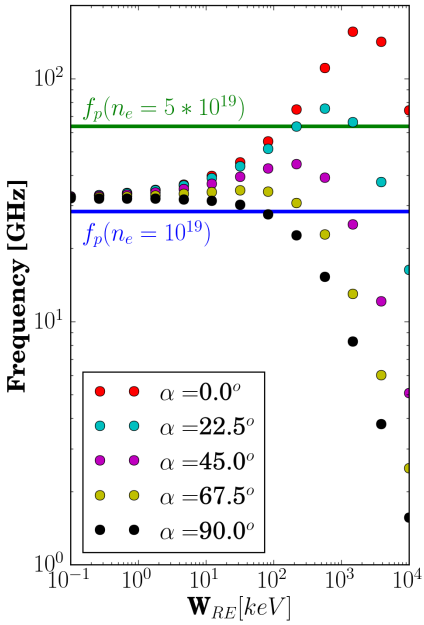

Figure A.1: Dependence of the first ECE harmonic from the COMPASS plasma core ($B_{tor} = 1.15\,\mathrm{T}$) on RE energies W_{RE} for different observation angles. The horizontal lines represent plasma frequencies as cut-offs for denoted n_e.

Moreover, vertical ECE observation has two advantages in comparison with the tangential one, besides the attractive reason of having a constant magnetic field along the inspected area, which results in less complex calculation (as explained in the previous Section). The first advantage is connected with the fact that ECE does not propagate if n_e is too high, as the plasma frequency f_p acts as a hard limit on the ECE. It is evident from Figure A.1 that the Doppler effect increases the cyclotron frequency even over $f_p(n_e = 5 \times 10^{19}\,\mathrm{m}^{-3})$, corresponding to density that is under the plasma core density for many present and practically all future tokamaks. This is not the case with vertical observation (i.e. propagation) as the frequency is decreasing. The second advantage of vertical observation is a lack of overlapping frequencies. For example, RE with $200 - 300\,\mathrm{keV}$ have the same resonant frequency as RE with 10 MeV as

[2]Where α is the observation angle with respect to $\vec{B}$.

seen from the Figure for $\alpha = 0°$. Note that radial observation has the same two advantages as it is also perpendicular to the magnetic field. However, in general, the wave propagates through different values of the magnetic field, making the calculation more difficult than for the vertical geometry.

A.1.4 Resonant Surfaces

To model resonant surfaces, the bulk plasma is mocked by a bi-Maxwellian distribution function [168, Eq.11.121-11.123], splitting it between the direction parallel ($\parallel$) and perpendicular ($\perp$) to the magnetic field

$$f_{bulk}(p_\perp, p_\parallel) = n_{bulk} F_\perp(p_\perp) F_\parallel(p_\parallel), \tag{A.3}$$

where n_{bulk} is the electron density without RE, and $F_\perp(p_\perp)$ and $F_\parallel(p_\parallel)$

$$F_\perp(p_\perp) = \frac{m}{2\pi T_\perp} \exp\left(- \frac{mc^2 p_\perp^2}{2T_\perp} \right) \tag{A.4}$$

and

$$F_\parallel(p_\parallel) = \left(\frac{m}{2\pi T_\parallel} \right)^{1/2} \exp\left(- \frac{mc^2 (p_\parallel - P_{th})^2}{2T_\parallel} \right). \tag{A.5}$$

In the equations above, the temperature T and the momentum p are split into the perpendicular and parallel direction, and $P_{th} = \sqrt{2 m_e T_\parallel}$ is the momentum of the thermal electron.

To simulate REDF, an analytic avalanche distribution function (that assumes constant avalanche growth, which dominates over the Dreicer one), from Ref. [45]

$$f_{RE}(p_\perp, p_\parallel) = \frac{n_{RE} \hat{\mathrm{E}}}{2\pi c_z p_\parallel \ln\Lambda} \exp\left(- \frac{p_\parallel}{c_z \ln\Lambda} - \frac{\hat{\mathrm{E}}\, p_\perp^2}{2 p_\parallel} \right) \tag{A.6}$$

is taken. Here $\ln\Lambda$ is the Coulomb logarithm, Z_{eff} is the effective ion charge, $\hat{\mathrm{E}} = (\mathcal{E}_{crit} - 1)/(1 + Z_{eff})$ and $c_z = \sqrt{3(Z_{eff} + 5)/\pi}$.

$n_e = 10^{19}\,\mathrm{m}^{-3}$	$E_{tor} = 0.3\,\mathrm{V/m}$	$I_{RE} = 150\,\mathrm{A}$
$T_\parallel = 1000\,\mathrm{eV}$	$\mathcal{E}_{crit} \sim 18.5$	$a_{RE} = 5\,\mathrm{cm}$
$T_\perp = 500\,\mathrm{eV}$	$p_{min}/mc = 0.24$	$n_{RE} \sim 4 \times 10^{14}\,\mathrm{m}^{-3}$
$I_p = 159\,\mathrm{A}$	$B_{tor}(R = 0.56\,\mathrm{m}) = 1.15\,\mathrm{T}$	$Z_{eff} = 2.5$

Table A.1: The data used to model ECE in COMPASS. p_{min} is the the lowest threshold for an electron to be considered a RE and here p_{min}/mc corresponds to $W_{crit} \sim 14.5\,\mathrm{keV}$.

The typical data used to numerically solve the Eqs. A.3 and A.6 for COMPASS discharge are depicted in Table A.1. A low E-band[3] for vertical observation at COMPASS will be used here to manifest which part of the distribution function is measured by each ECE detector chord. The frequencies of the low E-band detector chord in COMPASS are $f_{E-low} \in \{60.325, 61.175, 62.025, 62.875, 63.725, 64.575, 65.425, 66.275, 67.125, 67.975, 68.825, 69.675, 70.525, 71.375, 72.225, 73.075\}$ GHz.

The result is plotted in Fig. A.2 in the normalized momentum space. The thermal (bulk) electron population is clearly seen at the bottom as red and yellow lines, while ellipsoid lines towards higher $p_{\|}$ represent the RE tail. The resonant ECE lines (black lines) are calculated for the COMPASS plasma core ($R = 0.56$). Only the first 5 low E-band chords are depicted because they are the only ones under the cut-off for the given n_e. The outermost resonant circle is the chord with the lowest frequency (i.e. 60.325 GHz). It is important to notice here how all chords (black lines) with the lower frequency than the most inner one do resonate with the RE tail (blue elongated lines in $p_{\|}$-direction) at the given location. Meaning that each chord measures ECE from thermal electrons at a certain location (defined by chord's frequency and local magnetic field) with a possible influence of the RE tail from locations that correspond to the chords with higher frequency. Therefore, one chord measures ECE from different locations in the plasma and from different parts of the EDF. Estimating distribution function from such measurement could lead to ambiguous solutions, without any possibility to certify which one is correct. However, having precise enough measurement of T_e and n_e profiles with Thomson scattering could be used to theoretically calculate solely ECE from the thermal electrons. The difference between ECE measurement and calculation could then give information on the RE part of the distribution function.

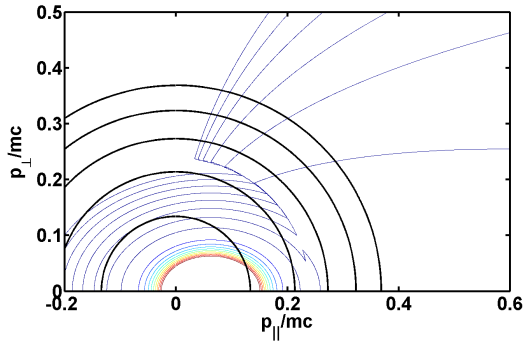

Figure A.2: The distribution function with both, bulk plasma and RE population. $f_{bulk} + f_{RE}$ is represented with the color map, starting from the red lines and decreasing across the yellow lines to the blue lines. The distorted blue lines on the RHS present the RE tail. Black lines represent the resonant surfaces for a vertical low E-band waveguide in COMPASS at $B_{tor} = 1.15$ T.

[3]The range of radio frequencies from 60 to 90 GHz.

A.1.5 Overview of the Earlier Observations

An overview of the experimental results from other devices already reported in Section 2.3.4 is done here, to lay out the above calculations. The presented measurements correspond to the most realistic cases from the point of view of the foreseen COMPASS scenarios.

Radial LFS observation of the 2nd and the 3rd extraordinary mode harmonics were used in the WEGA stellarator [102]. The measurements with $B_{tor} = 1.44\,\mathrm{T}$ had too high noise, which was reduced by increasing B_{tor} to 2.5 T. In Fig. A.3a, two clearly distinguishable electron populations can be observed. Using the theory developed by Celata and Boyd [169] they estimated the threshold energy W_{crit}, the pitch angle θ, the RE number N_{RE} and the exponential decay of the RE distribution function, as they assumed that REDF decays exponentially.

The radial HFS measurement of the 2nd extraordinary mode was performed in the FT-1 tokamak [103]. After unfolding raw measurements of the T_e profile, they obtained non-physical off-axis temperature peak (see Fig. A.3b). The reason is linked to what was said in the previous Section, i.e. that one chord measures ECE from different plasma locations in the presence of REs. In that case, the peak is the result of ECE from RE at the plasma core. The chords that observe RE have frequencies lower than the ones observing thermal electrons at plasma core, resulting in non-physical off-axis high T_e if REs are not taken into account. Analysis of the data was realised with a combination of Fokker-Planck code with ray-tracing coupled with reflection and emissivity codes. The maximum RE energy (addressed as "cut-off" energy in the reference) is estimated in this paper. They further used knowledge of this energy to deduce dominant RE loss mechanism.

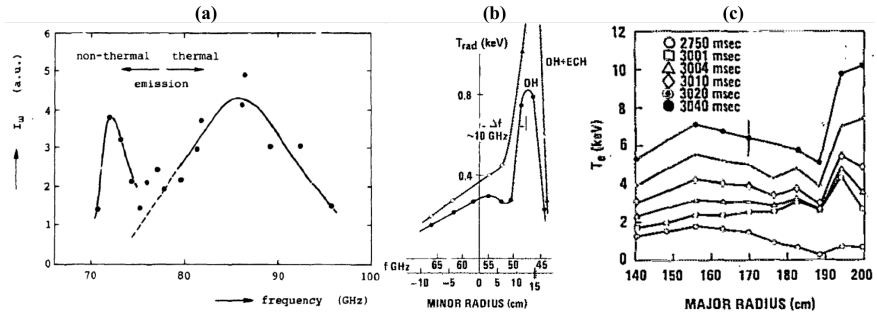

Figure A.3: **(a)** Measured ECE emissivity (dots) with the fit (lines) as a function of the frequency for the WEGA stellarator. Figure reproduced from Ref. [102]. **(b)** T_e profile from ECE at FT-1 as a function of minor radius, with corresponding frequencies to the minor radius. Figure reproduced from Ref. [103]. **(c)** T_e profile from ECE at DIII-D as a function of major radius. Figure reproduced from Ref. [103].

A measurement from the DIII-D tokamak is reported in the same reference as for FT-1, where a radial LFS observation of the 2nd extraordinary mode harmonic was conducted. One can observe in Fig. A.3 a non-physical scrape-off layer temperature rise. Using the same code as for FT-1, but assuming the maximum RE energy they managed to localise the RE beam.

A.1.6 Summary for ECE

An ECE diagnostic tool could be of great significance for the RE studies and mitigation. However, proper investigation of the topic would require dedicated task, which is beyond the scope of this work. Therefore, only the basic principles behind the idea are reported here.

To simplify the data interpretation, it would be probably best to use the vertical observation. For this case using COMPASS plasma parameters, we schematically showed which part of the distribution function would be measured by the COMPASS ECE setup. The predicted behaviour is seen in the reviewed past experimental observations in other machines, even though the observations were radial. However, the calculations they made are quite outdated and better calculations are possible with the present computation power. Besides larger computation power, one would need a very precise T_e and n_e profile measurements (for thermal plasma parameters) and ECE (for thermal and RE combined) to distinguish and estimate the RE distribution in spatial and velocity space with minimal assumptions or simplifications of the theory.

A.2 Incoherent Thomson Scattering

The introduction to the ITS was already presented in Section 2.3.6. The basis behind the statements on the tangential view and no need for sophisticated equipment, reported in the last paragraph of this Section, will be addressed here. The Section starts with motivation and some theoretical introduction to relativistic effects on ITS. The consequences of the RE relativistic motion are then examined with regards to tangential view, spectral range and photon collection. At the end, the summary of the Section is given.

A.2.1 Motivation

Most of the codes and simulations in Section 2.1.6 either need or estimate the RE distribution function (REDF). More precisely, scientists often assume a theoretical REDF, or REDF practical for the calculation or they even take an output of the simulations that estimates REDF.

Anyhow, none of the used or obtained REDFs was ever directly compared with an experiment, simply because REDF were never directly estimated

from measurements, which intrinsically leads to the unreliability of the simulations. Henceforth, a huge effort has been done for indirect estimation of the REs energy distribution in the DIII-D tokamak [170]. However, five different diagnostics were used, which makes the whole analysis very complex and more prone to large errors. Additionally, as already mentioned in Section 2.3.2, HXR tomography in JET gives REDF [98], but only for RE with energies over $1 - 2\,\mathrm{MeV}$.

Here we investigate if the ITS diagnostics can be a tool for a more direct, localized, wide energy range and single instrument measurement of the REDF.

A.2.2 Introduction

The possibility of ITS usage as RE diagnostic tool was first reported in Ref. [8]. As explained in the reference, this can be realised with a tangential measurement of the TS signal due to the "headlight" effect (examined in the next Section) of the relativistic particles, effect for which the light is preferentially directed in the propagating direction of the particles.

The first non-Maxwellian electron distribution measurements with the TS diagnostic related to the REs were published by Pieroni and Segre [106] from MIT. A non-Maxwellian distribution was also measured with ITS in the TORTUR tokamak [171], but it was not related to the REs. Also, in the same report it was mentioned that the non-Maxwellian ITS signals associated to the REs are observed in the Frascati tokamak and the Thor tokamak. Unfortunately, nowadays there are no reports on such measurements in the large tokamaks. The reason is twofold - presently the experimental setup of ITS diagnostics are designed only for bulk plasma and RE energies are higher in today's experiments than in the aforementioned tokamaks. The later reason leads to photons scattered in an undetectable range of the spectra due to a too large Doppler shift, which will be demonstrated in Section A.2.4.

Regarding the relativistic effects, theoretical calculations reveal that relativistic effects should be taken into account when $T_e > 1\,\mathrm{keV}$, which is the case for most of modern fusion plasmas. Moreover, the REs are easily reaching ultra-relativistic energies ($>511\,\mathrm{keV}$). The first steps toward the relativistic corrections of TS theory were done in 60's and 70's, and the most important results were reported by Sheffield [172] (the first order in β) and Matoba [173] (the second order in β) valid until $5\,\mathrm{keV}$ and $30\,\mathrm{keV}$, respectively. Further relevant improvement was developed by Naito [174] up to $100\,\mathrm{keV}$. Finally, Palastro [175] derived a fully relativistic scattered power model for the TS in unmagnetized plasmas[4].

However, three things should be pointed out about Palastro's paper. First, as already mentioned, note that the calculation is derived for the un-

[4]The detailed history and the development of the relativistic TS can be found in Appendix E.8 of Ref. [107]. In the same reference, comparison to other theories is presented.

magnetised plasma as already said. Second and perhaps the most important point, Palastro uses the Maxwell-Jüttner (MJ) distribution function (or relativistic Maxwellian velocity distribution, reported in Section 5.3.1) for the electrons. In other words, the derivation is done with a relativistic bulk plasma. Unfortunately, this is not valid for tokamak plasmas as REs are in minority compared to the bulk non-relativistic plasma electron[5]. However, revising Palastro's calculation with a more relevant (or more realistic) REDF is cumbersome and is out of the scope of this work.

Third point, the straight line assumption of Palastro's model is fulfilled in the relativistic case when $8\gamma^2 v_{osc} \ll c$ holds, where $v_{osc} = (eE_{i,0}/\gamma m_e c) \times \lambda_i/2\pi$ is the relativistic oscillation velocity with $E_{i,0}$ and λ_i being the electric field and the wavelength of the incidence photon, respectively. From here, a condition for the maximum allowed amplitude of the laser electric field $E_{i,0}$ as a function of γ and λ_i can be found:

$$E_{i,0} \ll \frac{\pi m_e c^2}{4e} \frac{1}{\gamma \lambda_i} \approx \frac{4 \times 10^5}{\gamma\, \lambda_i[\mathrm{m}]} [\mathrm{V/m}] \tag{A.7}$$

Therefore, knowing the wavelength λ_i, the energy of the laser (which are always known in practice) and the maximum RE energy, one can easily validate the suitability of the Palastro's derivation.

For the purpose of calculation for this Appendix, we will take the COMPASS Thomson scattering setup. Necessary details (wavelength and energy of the laser) of the Thomson scattering diagnostic system in COMPASS can be found in Section 3.3.1. Using the wavelength λ_i =1064 nm from the COMPASS laser and $\gamma = 40$, corresponding to approximately 20 MeV RE, the laser electric field limit is $E_{i,0} \ll 10^{10}$ V/m. To verify if the COMPASS Thomson scattering system matches this condition, the general expression for light energy in vacuum is recalled [176]:

$$E_{i,0} = \sqrt{\frac{2W_{laser}}{\epsilon_0}}. \tag{A.8}$$

Hereby, the laser electric field amplitude is estimated to be $E_{i,0} \sim 10^5$ which is 5 orders of magnitude smaller than the estimated limit. Thus, Palastro's "strait-line" assumption is valid for the Thomson scattering system used in COMPASS and the REs generated in its plasma.

A.2.3 Tangential Geometry

The aforementioned "headlight" effect will be addressed here. It can be calculated from the general theory of the radiation emitted by moving charges [177], where the scattered power per solid angle $\mathrm{d}P\mathrm{d}\Omega$ assuming

[5] An exception could be when a runaway beam is kept after or created during a disruption (runaway plateau).

that the particle velocity $\vec{\beta}$ is perpendicular to its acceleration $\dot{\vec{\beta}}$ (which is a rough assumption, but a valid simplification for a tokamak) is expressed as:

$$\frac{\mathrm{d}P}{\mathrm{d}\Omega} = \frac{e^2\dot{\beta}}{4\pi c}\frac{1}{(1-\beta\cos\theta_{ts})^2}\left(1-\frac{\sin^2\theta_{ts}\cos^2\phi_{ts}}{\gamma^2(1-\beta\cos\theta_{ts})^2}\right) \tag{A.9}$$

where θ_{ts} is the polar and ϕ_{ts} the azimuthal angles, respectively. For ITS diagnostics, θ_{ts} is the angle between the electron velocity and the scattered photon (θ_s). If the scattered photon is observed tangentially then its direction almost coincides with the magnetic field direction in tokamak, making θ_{ts} equal to the pitch angle θ. After averaging the Eq. A.9 over ϕ, the geometrical factor (now depending just on the scattered angle θ_s) is:

$$dP_{geom}(\theta_s) = \frac{1}{(1-\beta\cos\theta_s)^2}\left(1-\frac{\sin^2\theta_s}{\gamma^2(1-\beta\cos\theta_s)^2}\right). \tag{A.10}$$

For calculation purposes, the scattered angle θ_s is taken to be $1.8° = \pi/100\,\mathrm{rad} \approx 0.03\,\mathrm{rad}$ (as the "perfect" case, where RE almost moves toward the detector), $9° = \pi/20\,\mathrm{rad} \approx 0.16\,\mathrm{rad}$ (as the common lower measured θ) and $18° = \pi/10\,\mathrm{rad} \approx 0.31\,\mathrm{rad}$ (as the common upper measured θ). The normalised velocity β and the Lorentz factor γ are calculated from the predefined RE energy W. The calculation of Eq. A.10 for the given pitch angles θ and RE energies W is presented in Table A.2. From the Table one can notice a rapid increase of power for tangential view with higher RE energies and smaller pitch angles (i.e. scattering angles). Additionally, there is a gap in the geometrical factor for larger angles around 100 keV that significantly reduces detection of REs with those parameters. Therefore, we conclude from Table A.2 that REs should be easier to observe with ITS system if θ_s is small and the RE energy is high.

θ_s \ W:	10 keV	100 keV	1 MeV	10 MeV	30 MeV
1.8°	1.54	4.88	274	60300	774000
9°	1.48	4.37	87.9	3750	6170
18°	1.30	3.09	0.820	363	411

Table A.2: The geometrical factor of the "headlight" effect, defined in Eq. A.10.

A.2.4 The Spectral Range

It is possible to calculate the wavelength of a scattered photon by a fast RE using Doppler-shift for electromagnetic wave

$$\omega_s = \omega_i\frac{1-\hat{i}\cdot\vec{\beta}}{1-\hat{s}\cdot\vec{\beta}} = \omega_i\frac{1-\beta\cos\theta_i}{1-\beta\cos\theta_s}, \tag{A.11}$$

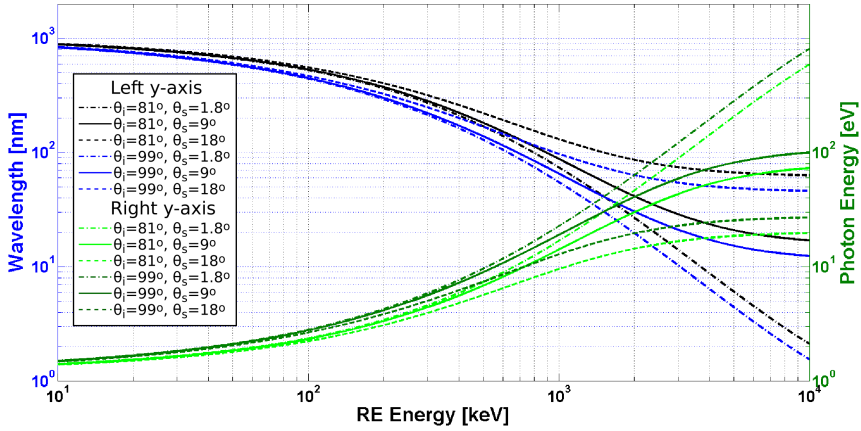

Figure A.4: The wavelength and the energy of the scattered photon as a function of the RE energy W. Two different values are taken for the θ_i: 81° (black and light green lines) and 99° (blue and dark green lines). While three different values are taken for the θ_s: 1.8° (dash-dotted lines), 9° (full lines) and 18° (dashed lines).

where ω_i and ω_s are the angular frequencies of the incident and the scattered photons, respectively and θ_i (θ_s) is the angle between the RE velocity and the incident (scattered) photon. From this expression, the scattered light frequency depends only on angles between the incident light and the electron trajectory θ_i and between the electron trajectory and the scattered light θ_s.

The values for the angles are taken near the perfect tangential particle trajectory ($\theta_i = 90°$ and $\theta_s = 0°$). Two different values are taken for $\theta_i \in \{81°, 99°\}$ and three different values for $\theta_s \in \{1.8°, 9°, 18°\}$. In Fig. A.4 it can be seen that the scattered light is in the IR spectra region for the RE energies up to $30 - 40$ keV. Furthermore, visible light is coming from the electrons with energies until 150 keV. Finally, only the "perfect" case reaches the soft X-ray region at energies of 3-4 MeV, while for the other two ("more realistic") cases, the scattered light stays in the UV region. Anyhow, the wide spectral range of the potential RE signal from ITS is more than obvious in Fig. A.4.

A.2.5 Photon Collection

As it was pointed out in Section 2.3.6, the drawback of the ITS diagnostics is the number of detected photons N_p. To represent the issue, the fraction of the detected scattered photons in the total number of incident photons in the observation region is taken.

The fraction of scattered photons is equal to $\sigma_{ts} n_e L_{ts}$, where σ_{ts} is the

Thomson scattering cross section and L_{ts} is the observed length of the incident light passing through the plasma of the electron density n_e. The TS cross section is fundamentally constant [178], as it depends only on the classical electron radius r_e: $\sigma_{ts} = 8\pi r_e^2/3 = 6.65 \times 10^{-29}\,\mathrm{m}^2 = 0.665\,\mathrm{barn}$. The small σ_{ts} value is the reason why the ITS technique is non-perturbative, but technically demanding.

As an example, RE dominant plasma from COMPASS is taken here for further calculation. Typically for this plasma $n_e \sim 1 \times 10^{19}\,\mathrm{m}^{-3}$ and the resolution of the ITS diagnostics in the plasma core is $L_{ts} \approx 1\,\mathrm{cm}$ [124]. Using these given data, the fraction of the scattered photons is estimated to be $\sigma_{ts} n_e L_{ts} = 6.65 \times 10^{-12}$. Moreover, not all the scattered photons will be collected, but just a fraction of them depending on the detector size, detector sensitivity, its distance from the laser beam, mirrors installed, window type, etc. The size parameters are usually represented by a solid angle in steradians, which in the core of COMPASS plasma is 2×10^{-2}. Finally, the fraction of the scattered photons detected with respect to the incident photons from the plasma core of COMPASS RE discharge is 1.33×10^{-13}. Therefore, it is now obvious why high intensity (energy) incident light is required for the ITS diagnostics.

Moreover, the number of detected photons N_p is proportional to a differential cross-section $\frac{d\sigma}{d\Omega}$ [124]. Unfortunately, the differential cross section is directly connected to the power spectrum, whose calculation is beyond the scope of this Thesis. On the other hand, we can estimate the ratio ω_i/ω_s, because $\frac{d\sigma}{d\Omega} \propto \omega_i/\omega_s$ [178]. In theory, if this ratio is not included, then the $\frac{d\sigma}{d\Omega}$ represents the energy scattered, while the main interest here is in the photon scattering. In practice, this ratio is usually omitted as it is approximately equal to 1 for small enough frequency shifts. In the case of the REs, from Fig. A.4, it is obvious that frequency (wavelength) shift is significant.

Due to the easier comparison with Table A.2, the inverse ratio of ω_i/ω_s is depicted in Table A.3. The same angles θ_i and θ_s are used as for the calculation in the previous Section. One can see that for the energy of 100 keV the reduction factor is around 2, but for energies above 1 MeV it is higher than 10. However, the reduction factor estimated here is smaller

θ_s \ W:	10 keV	100 keV	1 MeV	10 MeV	30 MeV
1.8°	1.20-1.28	2.02-2.40	14.4-19.3	503-690	1330-1820
9°	1.20-1.28	1.99-2.37	12.1-16.3	62.6-85.8	67.8-92.9
18°	1.99-1.26	1.91-2.27	8.12-10.9	16.8-23.1	17.2-23.6

Table A.3: The ratio between the incident ω_i and the scattered ω_s frequencies, as a factor of the photon number reduction with increasing RE energy. Left and right values in the same column correspond to the incident angles $\theta_i = 81°$ and $\theta_i = 99°$, respectively.

than the power radiation enlargement from Table A.2, meaning that the tangential measurement of ITS from REs should still have enhanced signal. Note that this is not the case around $W = 100\,\mathrm{keV}$ for $\theta_s = 9°$ due to the very small value of the geometrical factor.

A.2.6 Summary for ITS

Incoherent Thomson scattering could be a useful diagnostic tool for direct measurement of the RE distribution function over a wide energy range. Moreover, the diagnostic technique itself is non-perturbative and very well localised. Therefore, basic physical calculations are reported here to investigate the feasibility of the concept.

To overcome the significantly lower number of REs in comparison to the thermal electrons, it would be best to make observation of the incident ITS laser in the tangential direction to the tokamak plasma. The geometrical factor of radiated power in the tangential direction is calculated. The reason for selection of the tangential view should be used is clear from numbers reported in Table A.2 However, the number of scattered photons would decrease with the increasing RE energy. Even though the decreasing factor of detected photons is smaller than the increasing factor of radiated power, the detectors do have a lower limit of photon counts. Therefore, for RE studies more powerful laser than for thermal plasma should be used. While this is possible in theory, purchasing the stronger laser would be very expensive. The spectrum range in tangential view on ITS laser would spread from visible to SXR region. Hence, there would not be a need for the sophisticated detector with the high wavelength resolution. On the other hand, there are many other sources of radiation from tokamak in those parts of spectra. Thus the full calculation of power spectrum from ITS on RE and background plasma should be performed for better prediction.

Moreover, the exact calculation of the power spectrum is not the only challenge for ITS as a RE diagnostic. The theory behind this estimate should be also developed specially using realistic distribution function with thermal electrons and RE in the tokamak, as Palastrao [175] derived power spectrum for Maxwell-Jüttner distribution function. Finally, as already mentioned in Section 2.3.6, the final transit time effect assumption could be inapplicable for the measurements of the REs with ITS, as it assumes constant electron population in the observed volume during the measurement.

Appendix B

Justifying the Neutron Detector Purchase

One of the author's undertakings was the purchase of a new neutron detector for the COMPASS tokamak. The task lasted more than a year - from the first requests to the first test. Therefore, a justification of the choice made will be detailed here. Beside the justification, other details useful for future are reported. Note that no details on any detector design or principle will be done, as it would require too much space and time for something far away from the scope of the topic. For that, the reader is referred to Ref. [179] and [180].

The Appendix starts with motivation and introduction to the matter. Next Section describes advantages and disadvantages of the different neutron detectors for our purpose. At the end, a summary is made and the final choice of the detector is given, including the rationale for this choice.

B.1 Motivation

The process of neutron origin from RE is described in Section 2.3.3. In short, detection of neutrons gives valuable information on the dynamic of high energy RE losses. Additionally, neutrons are also coming from fusion reactions, increasing the importance of having a reliable measurement of neutrons.

On the other hand, as described in Section 3.3.2, the scintillator used for neutron detection at COMPASS is also sensitive to strong fluxes of HXR, although the detector is shielded by 10 cm of Pb. This combined detection of neutrons and photons (HXR and γ-rays) makes measurements impractical for any quantitative study as discrimination between neutron and photon signals seems to be unfeasible for our Shielded HXR detector due to very high overlay of pulses. Henceforth, we decided to purchase a new neutron

detector, that either would have been weakly sensitive to γ-rays or would have signal convenient for the γ-discrimination.

B.2 Introduction to Fast Neutron Detection

Moving neutrons are usually divided into "slow" and "fast" ones with the threshold being defined as Cd cut-off energy that is equal to 0.5 eV. Obviously, neutrons in tokamak environment are **fast** as they have keV and MeV energies.

Secondary (i.e. detected) radiation from neutrons is (almost always) a heavy charged particle, which is contrary to γ-rays detection principles (often based on the Compton scattering). This makes detection somewhat easier, but slower and more difficult to unfold. Furthermore, the neutron spectrum can be measured only when the Q-value[1] is not too large in comparison to the neutron energy. For tokamaks, this means that neutrons should have energies above $10 - 100$ keV.

For fast neutrons, scattering is more important than nuclear reactions, due to the relatively high energy transfer in one collision, creating a recoil nuclei. Recoil nuclei energy cannot be omitted for neutrons with an energy of a few keV and higher, hence this effect is important for studies of neutrons from a tokamak.

To detect a significant amount of fast neutrons that have a few keV and higher energies, they have to be slowed down. This is done with so-called *moderators*. Hydrogen is shown to be by far the best moderator, which is the reason why the most commonly used moderators are made out of different kinds of plastic materials. However, the thickness of the moderator should be optimised, as a thick moderator increases the chance for neutron moderation but decreases the chance of detection (because the volume ratio between the detector and the moderator is smaller). For example, several tens of centimeters are needed for moderation of the MeV neutrons. Moreover, moderation extracts the energy information of the initial neutron making estimation of neutron energy spectra impossible or at least very difficult and with large uncertainties. Additionally, moderators slow down the detection time significantly - from a few nanoseconds necessary for direct observation to the order of $10 - 100\,\mu$s.

Gas detectors with ^{3}He as the working gas have the highest neutron sensitivity. Those detectors were and are often used in airports, and borders checks for the control of nuclear weapon smuggling. Unfortunately, the amount of ^{3}He on Earth is depleted. After September 11 Attack in USA demand for ^{3}He-detectors increased, leading to the ^{3}He shortage in 2008. Consequently, ^{3}He price skyrocketed - i.e. from $40-80$ \$/l before to 1000 \$/l after the shortage. BF_3-detectors are the most common substitute to the ^{3}He ones, as their price is lower.

[1] Q-value represents the energy lost during a nuclear reaction.

It should be mentioned that ^{3}He-detector was already used in COMPASS and the preliminary results are reported in [181]. However, measurements were done with the detectors outside the hall, as inside the signal would saturate. At the time, the estimated neutron flux was 5×10^9 neutrons/s.

B.3 Fast Neutron Detectors

Even though detectors based on ^{3}He are the best choice for fast neutrons, here we will go through all options that were encountered during the decision making.

Fission chamber can be used as very reliable neutron counter, but no energy spectra can be expected from it. It has the lowest sensitivity to γ-ray compared to all other detectors and a very high dynamic range, but also smaller neutron detection efficiency.

Activation counters are not suitable for our application, as there is no prompt (or at least fast enough) signal because unfolding (post-processing) is needed. Also neutron fluence is a bit low on COMPASS due to short pulse.

A good option for fast neutron detection is the **LiI scintillator** (usually doped with Eu). However, its response could be non-linear. This detection issue can be solved by cooling, but that increases the price significantly. Another type of scintillator - the proton recoil - could also be used for measurement of fast neutrons. Usually it is made from H-containing (organic) material, therefore being self-moderator. Detectors with CH_4 are one of the fastest on the market, but their cross-section with neutrons is significantly lower than for ^{3}He or even boron-containing detectors. In general, the benefit of all scintillators is their fast response and modest cost, while they are usually too sensitive to γ-radiation. The last point is highly relevant for the RE COMPASS studies, as explained in the Motivation Section B.1.

The conventional **BF_3 tubes** have a low detection efficiency for fast neutrons and consequently are almost never used for this purpose. However, moderated BF_3 tube can be used for this function. Another way of using good boron reactivity with neutrons is having a chamber coated with thin layer of ^{10}B. Those are so-called **B-lined** detectors. Its neutron detection efficiency is higher than for fission chamber but lower than for BF_3 and ^{3}He. However, it has higher γ-insensitivity than ^{3}He and BF_3, while lower than the fission chamber has. The B-line detectors are very fast, as nuclear reaction with neutron does not occur with filled gas, but on the inner detector wall. Moreover, lower pressures and voltages are needed for B-lined than for BF_3 detectors, while they are even lower for ^{3}He detectors.

Finally, a few detector types based on ^{3}He are mentioned here. ^{3}He proportional counter (sometimes mixed with another inert gas) features very good performance in high γ-flux environment. The ^{3}He ionisation chamber has a better energy resolution, but slower and noisier signal than

the previous detectors. He scintillator (usually doped with Xe+N or p-terphenyl) has very fast detection, but very poor energy resolution.

B.4 Overview and Decision

As the Shielded HXR is sensitive to both, neutrons and γ-rays, without the possibility to discriminate between the two, we had to purchase a new neutron detector. To do so, the author had to look for the more suitable and the most economical solution. The main point of this Appendix was to summarise the advantages and disadvantages of the different neutron detectors offered on the market.

In a nutshell, the most commonly used alternatives for ^{3}He tubes are Li scintillators, B-lined tubes and BF_3 tubes that meet close enough the required neutron detection efficiency and γ-ray discrimination. However, the former two are rather expensive, as both - ^{6}Li and ^{10}B - are export controlled materials. Therefore, even though BF_3 is a hazardous material, it seemed to present the best alternative to the ^{3}He detector.

Despite that our choice was the BF_3 detector, after communicating with the Manufacturer we purchased the ^{3}He detector as the price difference was rather negligible due to the low amount of the detection gas. In Ref. [181], the gas pressure was around 500 kPa of ^{3}He that lead to signal saturation. After realising the relatively low cost, we purchased two ^{3}He detectors with a ^{3}He pressure around 10 kPa to reduce detector sensitivity due to the large fluxes. Additionally, a set of 5 high-density polyethylene (HDPE) moderators of different thickness were bought. When the first tests of the detectors were finally performed, it was almost time for the author to leave the COMPASS facility, showing how long this kind of process can be. Thus, the new results will be reported in another document in the near future.

Appendix C

Calibration of the Massive Gas Injection Valve

As already mentioned in this Thesis, the MGI experiments on COMPASS were achieved using solenoid valves. Their location is depicted in Fig. 3.3 and their installation among RE campaigns is elaborated in Section 3.3.3. The parameter of importance for the gas injection is the back pressure P_{back}. However, more physically meaningful parameters are the number of injected particles and the particle flow through the pipes between the valve and the vacuum vessel. For that reason, the calibration for transforming P_{back} to the particle flow rate $\mathrm{d}N/\mathrm{d}t$ is reported here, the necessary measurements and corresponding results for each of three solenoid valve are also given.

The calibration was performed outside the tokamak operation time for Ar gas, but tokamak was under vacuum with stopped pumping while injections were operated. Injections were realised for different valve opening times τ_v and back pressures P_{back}, 10 times in a raw with the exact same setup to reduce statistical errors. Pressure inside the tokamak was measured with a Pirani gauge after each injection. The measured values are presented in Tables C.1, C.3 and C.5. The gauge being calibrated for hydrogen/deuterium, the pressure was converted to Ar pressure using abacus provided in the gauge's documentation. The converted values are presented in Tables C.2, C.4 and C.6.

Knowing the final gas pressure inside the vacuum vessel P_{vv} after injection, one can deduce number of injected particles N_{vv} through the ideal gas law assuming that the initial pressure in the vacuum vessel is much smaller than P_{vv}

$$N_{vv}[\text{particles}] = \frac{P_{vv}V_{vv}}{k_B T_{vv}} \approx 2.4155 \times 10^{20} P_{vv}[\text{Pa}], \tag{C.1}$$

where k_B is the Boltzmann constant, the volume of the vacuum vessel V_{vv} is approximately $1\,\mathrm{m}^3$ and the room temperature $\sim 300\,\mathrm{K}$ is assumed inside

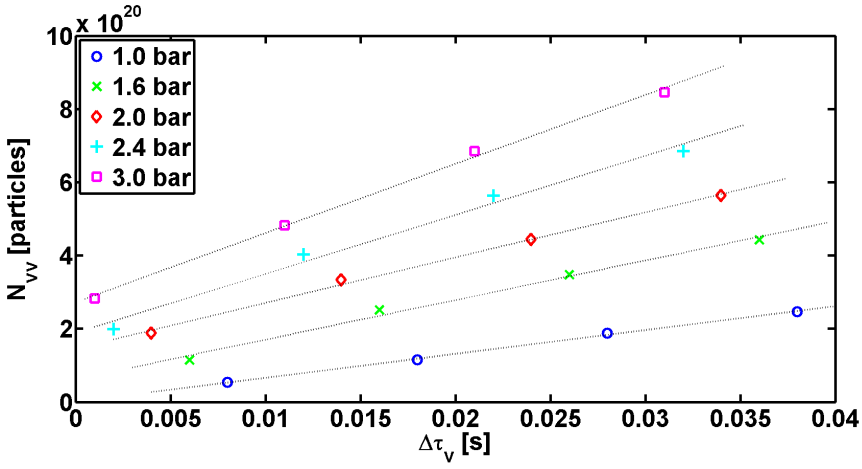

Figure C.1: The number of particles in vacuum vessel N_{vv} versus the time that valve is opened $\Delta\tau_v$ for different P_{back} - 1.0 bars (blue circles), 1.6 bars (green exmarks), 2.0 bars (red diamonds), 2.4 bars (cyan pluses), and 3.0 bars (magenta squares). The black doted lines correspond to the Q_{eff} fit for each P_{back}.

the vacuum vessel and the pipes T_{vv}. With the knowledge of N_{vv} one can estimate the volumetric particle flow rate

$$Q_{eff} = \frac{N_{vv} V_{vv}}{\Delta\tau_v} \tag{C.2}$$

for each P_{back}, where $\Delta\tau_v$ is the time for how long the valve is opened. An example of Q_{eff} fitting is given in Fig. C.1 for the EAST valve. The $\Delta\tau_v$ is estimated via formula:

$$\Delta\tau_v = \tau_v - t_{opening} \tag{C.3}$$

where τ_v is the length of a rectangular triggering signal going through the valve and $t_{opening}$ the time needed for the valve to open, i.e. the reacting time. The opening moment occurs when the solenoid in the valve reaches certain voltage after the triggering signal. We found that $t_{opening}$ is not constant and that it depends on the P_{back}:

$$t_{opening}[\text{ms}] = a_v P_{back}[\text{bars}] + b_v \tag{C.4}$$

where the fitting coefficients are depicted in the Table C.7 for the each valve.

Furthermore, a capacitance of the valve-piping system C_v can be deduced

$$C_v = \frac{Q_{eff}}{P_{back}}. \tag{C.5}$$

As C_v should be independent on the P_{back}, we used small discrepancies for the estimation of statistical errors of the calibration method. Finally, particle flow rate for each of three valves can be calculated via expression:

$$\frac{\mathrm{d}N}{\mathrm{d}t} = \frac{C_v * P_{back}}{V_{vv}} \approx C_v * P_{back}[\mathrm{bars}], \tag{C.6}$$

as V_{vv} is approximately $1\,\mathrm{m}^3$ for the COMPASS tokamak. The C_v and their corresponding errors are enlisted in Table C.7 for the each valve.

To obtain a number of particles at the certain moment one needs simply to multiple flow rate with the time for how long the valve was open until that moment.

TABLES

Table C.1: Measured P_{vv} with the gauge calibrated for H injecting with the EAST valve. The values of P_{vv} are in bars. The first column was used for the estimation of the valve opening time and therefore τ_v is not constant - $\tau_{v,min} = 18$, 20 and 22 ms for $P_{back} = 1.0$, 1.6, and 2.0 bars, respectively.

$P_{back} \setminus \tau_v$	$\tau_{v,min}$	25 ms	35 ms	45 ms	55 ms
1.0 bars	0.15	0.31	0.43	0.55	0.66
1.6 bars	0.22	0.43	0.67	0.88	1.1
2.0 bars	0.38	0.55	0.85	1.1	1.4
2.4 bars	-	0.57	1.0	1.4	1.7
3.0 bars	-	0.74	1.2	1.7	2.1

Table C.2: Effective P_{vv} converted for Ar from the measured P_{vv} reported in Table C.1.

$P_{back} \setminus \tau_v$	$\tau_{v,min}$	25 ms	35 ms	45 ms	55 ms
1.0 bars	0.07	0.22	0.48	0.78	1.0
1.6 bars	0.12	0.48	1.0	1.4	1.8
2.0 bars	0.36	0.78	1.4	1.8	2.3
2.4 bars	-	0.83	1.7	2.3	2.8
3.0 bars	-	1.2	2.0	2.8	3.5

Table C.3: Measured P_{vv} with the gauge calibrated for H injecting with the NORTH valve. The values of P_{vv} are in bars. The first column was used for the estimation of the valve opening time and therefore τ_v is not constant - $\tau_{v,min} = 13$ ms for $P_{back} = 1.0$, 1.6, and 2.0 bars and $\tau_{v,min} = 14$ ms for $P_{back} = 2.4$ and 3.0 bars.

$P_{back} \setminus \tau_v$	$\tau_{v,min}$	25 ms	35 ms	45 ms	55 ms
1.0 bars	0.17	0.44	0.59	0.74	0.89
1.6 bars	0.26	0.68	0.92	1.1	1.4
2.0 bars	0.31	0.84	1.1	1.4	1.7
2.4 bars	0.43	1.0	1.4	1.7	2.1
3.0 bars	0.51	1.2	1.7	2.1	2.6

Table C.4: Effective P_{vv} converted for Ar from the measured P_{vv} reported in Table C.3.

$P_{back} \setminus \tau_v$	$\tau_{v,min}$	25 ms	35 ms	45 ms	55 ms
1.0 bars	0.08	0.50	0.88	1.2	1.5
1.6 bars	0.16	1.1	1.5	1.8	2.3
2.0 bars	0.22	1.4	1.8	2.3	2.8
2.4 bars	0.48	1.7	2.3	2.8	3.5
3.0 bars	0.68	2.0	2.8	3.5	4.3

Table C.5: Measured P_{vv} with the gauge calibrated for H injecting with the WEST valve. The values of P_{vv} are in bars. The first column was used for the estimation of the valve opening time and therefore τ_v is not constant - $\tau_{v,min} = 9$ ms for $P_{back} = 1.0$ and 1.6 bars and $\tau_{v,min} = 10$ ms for $P_{back} = 2.0$, 2.4, and 3.0 bars.

$P_{back} \setminus \tau_v$	$\tau_{v,min}$	25 ms	35 ms	45 ms	55 ms
1.0 bars	0.60	0.88	1.1	1.35	1.55
1.6 bars	0.93	1.45	1.85	2.2	2.55
2.0 bars	1.25	1.8	2.3	2.8	3.2
2.4 bars	1.5	2.15	2.8	3.25	3.8
3.0 bars	1.7	2.6	3.8	4.1	4.8

Table C.6: Effective P_{vv} converted for Ar from the measured P_{vv} reported in Table C.5.

$P_{back} \setminus \tau_v$	$\tau_{v,min}$	25 ms	35 ms	45 ms	55 ms
1.0 bars	0.9	1.4	1.8	2.25	2.6
1.6 bars	1.5	2.4	3.1	3.7	4.25
2.0 bars	2.1	3.0	3.8	4.7	5.3
2.4 bars	2.5	3.6	4.7	5.4	6.3
3.0 bars	2.8	4.3	6.3	6.8	8.0

Table C.7: The results of the calibration - the valve-pipes system capacitance C_v, its relative error $\delta(C_v)$ and coefficients a_v and b_v from Eq. C.4.

valve	C_v $[\times 10^{21}]$	$\delta_r(C_v)$ [%]	a_v	b_v
EAST	6.5	3.9	3.7	13.4
NORTH	6.4	10.9	0.73	10.73
WEST	9.4	3.2	0.82	6.8

Bibliography

[1] C. M. Braams and P. E. Stott. *Nuclear Fusion - Half a Century of Magnetic Confinement Fusion Research*. Institute of Physics Publishing, 2002, ISBN: 978-0750307055.

[2] Henri Poincaré. *Sur les courbes définies par une équation différentielle*. Comptes rendus hebdomadaires de l'Académie des sciences de Paris, 90:673–675, 1880.

[3] D. van Houtte, G. Martin, A. Bécoulet, J. Bucalossi, G. Giruzzi, G.T. Hoang, Th. Loarer, B. Saoutic, and the Tore Supra Team. *Recent fully non-inductive operation results in Tore Supra with 6min, 1GJ plasma discharges*. Nuclear Fusion, 44(5):L11, 2004.

[4] *Down to Earth*. https://www.iter.org/newsline/53/1589, October 2008. [cit. August 2017].

[5] *All-the-World's Tokamaks*. www.tokamak.info, December 2016. [cit. August 2017].

[6] *Renewable Energy Sources in Figures*. http://www.bmwi.de/Redaktion/EN/Publikationen/renewable-energy-sources-in-figures.html, September 2016. [cit. August 2017].

[7] T.C. Hender, J.C Wesley, J. Bialek, A. Bondeson, A.H. Boozer, R.J. Buttery, A. Garofalo, T.P Goodman, R.S. Granetz, Y. Gribov, O. Gruber, M. Gryaznevich, G. Giruzzi, S. Gnter, N. Hayashi, P. Helander, C.C. Hegna, D.F. Howell, D.A. Humphreys, G.T.A. Huysmans, A.W. Hyatt, A. Isayama, S.C. Jardin, Y. Kawano, A. Kellman, C. Kessel, H.R. Koslowski, R.J. La Haye, E. Lazzaro, Y.Q. Liu, V. Lukash, J. Manickam, S. Medvedev, V. Mertens, S.V. Mirnov, Y. Nakamura, G. Navratil, M. Okabayashi, T. Ozeki, R. Paccagnella, G. Pautasso, F. Porcelli, V.D. Pustovitov, V. Riccardo, M. Sato, O. Sauter, M.J. Schaffer, M. Shimada, P. Sonato, E.J. Strait, M. Sugihara, M. Takechi, A.D. Turnbull, E. Westerhof, D.G. Whyte,

R. Yoshino, H. Zohm, Disruption the ITPA MHD, and Magnetic Control Topical Group. *Chapter 3: MHD stability, operational limits and disruptions.* Nuclear Fusion, 47(6):S128, 2007.

[8] H. Knoepfel and D.A. Spong. *Runaway electrons in toroidal discharges.* Nuclear Fusion, 19(6):785, 1979.

[9] C.T.R. Wilson. *The Acceleration of β-particles in Strong Electric Fields such as those of Thunderclouds.* Mathematical Proceedings of the Cambridge Philosophical Society, 22:534–538, 3 1925.

[10] M.A. F. Hoyle. *Some Recent Research in Solar Physics.* Cambridge University Press, Cambridge, UK, 1949, ISBN: 978-1107418929.

[11] Timothy F. Bell, Victor P. Pasko, and Umran S. Inan. *Runaway electrons as a source of red sprites in the mesosphere.* Geophysical Research Letters, 22(16):2127–2130, 1995.

[12] V. I. Shevchenko and V. L. Galinsky. *Stability of the strahl electron distribution function and its dynamics.* Nonlinear Processes in Geophysics, 17(5):593–597, 2010.

[13] A. V. Gurevich, J. A. Valdivia, G. M. Milikh, and K. Papadopoulos. *Runaway electrons in the atmosphere in the presence of a magnetic field.* Radio Science, 31(6):1541–1554, 1996.

[14] G.I. Budker. *Relativistic stabilized electron beam.* The Soviet Journal of Atomic Energy, 1(5):673–686, 1956.

[15] Allen H. Boozer. *Theory of runaway electrons in ITER: Equations, important parameters, and implications for mitigation.* Physics of Plasmas, 22(3):032504, 2015.

[16] H. P. Furth and P. H. Rutherford. *Ion Runaway in Tokamak Discharges.* Phys. Rev. Lett., 28:545–548, Feb 1972.

[17] P Helander and DJ Ward. *Positron creation and annihilation in tokamak plasmas with runaway electrons.* Phys. Rev. Lett., 90(13):135004, April 2003.

[18] H. Dreicer. *Electron and Ion Runaway in a Fully Ionized Gas. I.* Phys. Rev., 115:238–249, Jul 1959.

[19] H. Dreicer. *Electron and Ion Runaway in a Fully Ionized Gas. II.* Phys. Rev., 117:329–342, Jan 1960.

[20] J.W. Connor and R.J. Hastie. *Relativistic limitations on runaway electrons.* Nuclear Fusion, 15(3):415, 1975.

[21] H.H. Fleischmann and S.J. Zweben. *Evaluation of Potential Runaway Generation in Large-Tokamak Disruptions.* Technical report PPPL-2914, Princeton Plasma Physics Laboratory, Princeton University, 1993.

[22] R. W. Harvey, V. S. Chan, S. C. Chiu, T. E. Evans, M. N. Rosenbluth, and D. G. Whyte. *Runaway electron production in DIII-D killer pellet experiments, calculated with the CQL3D/KPRAD model.* Physics of Plasmas, 7(11):4590–4599, 2000.

[23] H. Smith, P. Helander, L.-G. Eriksson, and T. Fülöp. *Runaway electron generation in a cooling plasma.* Physics of Plasmas, 12(12):122505, 2005.

[24] H. M. Smith and E. Verwichte. *Hot tail runaway electron generation in tokamak disruptions.* Physics of Plasmas (1994-present), 15(7):072502, 2008.

[25] I. A. Sokolov. *'Multiplication' of accelerated electrons in a tokamak.* ZhETF Pisma Redaktsiiu, 29:244–246, February 1979.

[26] M.N. Rosenbluth, D. Post, S. Putvinski, P.B. Parks, H.A. Scott, and Putvinskaya N. *Runaway electrons and fast plasma shutdown.* In Proceedings of the IAEA International Conference on Fusion Energy, Montreal, Canada, pages 979–986, Vienna, Austria, 1997. International Atomic Energy Agency.

[27] E. Nilsson, J. Decker, Y. Peysson, R. S. Granetz, F. Saint-Laurent, and M. Vlainic. *Kinetic modelling of runaway electron avalanches in tokamak plasmas.* Plasma Physics and Controlled Fusion, 57(9):095006, September 2015.

[28] M.N. Rosenbluth and S.V. Putvinski. *Theory for avalanche of runaway electrons in tokamaks.* Nuclear Fusion, 37(10):1355, 1997.

[29] E. Nilsson, J. Decker, N. J. Fisch, and Y. Peysson. *Trapped-electron runaway effect.* Journal of Plasma Physics, 81(4):475810403, August 2015.

[30] A. Stahl, E. Hirvijoki, J. Decker, O. Embréus, and T. Fülöp. *Effective Critical Electric Field for Runaway-Electron Generation.* Phys. Rev. Lett., 114:115002, Mar 2015.

[31] Ruili Zhang, Jian Liu, Hong Qin, Yulei Wang, Yang He, and Yajuan Sun. *Volume-preserving algorithm for secular relativistic dynamics of charged particles.* Physics of Plasmas, 22(4):044501, 2015.

[32] Xiaoyin Guan, Hong Qin, and Nathaniel J. Fisch. *Phase-space dynamics of runaway electrons in tokamaks.* Physics of Plasmas, 17(9):092502, 2010.

[33] P Helander, L-G Eriksson, and F Andersson. *Runaway acceleration during magnetic reconnection in tokamaks.* Plasma Physics and Controlled Fusion, 44(12B):B247, 2002.

[34] J. Decker and Y. Peysson. *DKE: A Fast Numerical Solver for the 3-D Relativistic Bounce-Averaged Electron Drift Kinetic Equation.* Technical report EUR-CEA-FC-1736, CEA Cadrache, 2004.

[35] J.F. Artaud, V. Basiuk, F. Imbeaux, M. Schneider, J. Garcia, G. Giruzzi, P. Huynh, T. Aniel, F. Albajar, J.M. Ané, A. Bécoulet, C. Bourdelle, A. Casati, L. Colas, J. Decker, R. Dumont, L.G. Eriksson, X. Garbet, R. Guirlet, P. Hertout, G.T. Hoang, W. Houlberg, G. Huysmans, E. Joffrin, S.H. Kim, F. Köchl, J. Lister, X. Litaudon, P. Maget, R. Masset, B. Pégourié, Y. Peysson, P. Thomas, E. Tsitrone, and F. Turco. *The CRONOS suite of codes for integrated tokamak modelling.* Nuclear Fusion, 50(4):043001, 2010.

[36] R. W. Harvey and M. G. McCoy. *The CQL3D Fokker-Planck Code.* In Proceedings of the IAEA Technical Committee Meeting on Advances in Simulation and Modeling of Thermonuclear Plasmas, Montreal, Canada, pages 489–526, Vienna, Austria, 1993. International Atomic Energy Agency.

[37] Matt Landreman, Adam Stahl, and Tünde Fülöp. *Numerical calculation of the runaway electron distribution function and associated synchrotron emission.* Computer Physics Communications, 185(3):847 – 855, 2014.

[38] A. Stahl, M. Landreman, O. Embréus, and T. Fülöp. *NORSE: A solver for the relativistic non-linear Fokker–Planck equation for electrons in a homogeneous plasma.* Computer Physics Communications, 212:269 – 279, 2017.

[39] G T A Huysmans, S Pamela, E van der Plas, and P Ramet. *Non-linear MHD simulations of edge localized modes (ELMs).* Plasma Physics and Controlled Fusion, 51(12):124012, 2009.

[40] C. Sommariva, E. Nardon, A. Fil, P. Beyer, G.T.A. Huysmans, M. Hoelzl, D. van Vugt, K. Sarkimaki, and JET Contributors. *Simulating runaway electrons during disruptions with test particles in the JOREK code.* In 43rd EPS Conference on Plasma Physics, Leuven, Belgium, ECA Vol. 40A, Mulhouse, France, 2016. European Physical Society.

[41] M. Drevlak. *Thermal Load on the W7-X Vessel from NBI Losses.* In 36nd EPS Conference on Plasma Physics, Sofia, Bulgaria, ECA Vol. 33E, Mulhouse, France, 2009. European Physical Society.

[42] R.R. Khayrutdinov and V.E. Lukash. *Studies of Plasma Equilibrium and Transport in a Tokamak Fusion Device with the Inverse-Variable Technique.* Journal of Computational Physics, 109(2):193 – 201, 1993.

[43] H. Smith, P. Helander, L.-G. Eriksson, D. Anderson, M. Lisak, and F. Andersson. *Runaway electrons and the evolution of the plasma current in tokamak disruptions.* Physics of Plasmas, 13(10):102502, 2006.

[44] S A Bozhenkov, M Lehnen, K H Finken, M W Jakubowski, R C Wolf, R Jaspers, M Kantor, O V Marchuk, E Uzgel, G Van Wassenhove, O Zimmermann, D Reiter, and the TEXTOR team. *Generation and suppression of runaway electrons in disruption mitigation experiments in TEXTOR.* Plasma Physics and Controlled Fusion, 50(10):105007, 2008.

[45] A. Stahl, M. Landreman, G. Papp, E. Hollmann, and T. Fülöp. *Synchrotron radiation from a runaway electron distribution in tokamaks.* Physics of Plasmas (1994-present), 20(9):093302, 2013.

[46] A. Fil, E. Nardon, P. Beyer, M. Becoulet, G. Dif-Pradalier, V. Grandgirard, R. Guirlet, M. Hoelzl, G.T.A Huijsmans, G. Latu, M. Lehnen, A. Loarte, F. Orain, S. Pamela, C. Passeron, C. Reux, F. Saint-Laurent, P. Tamain, and JET EFDA Contributors. *Modeling of disruption mitigation by massive gas injection.* In 41nd EPS Conference on Plasma Physics, Berlin, Germany, ECA Vol. 38F, Mulhouse, France, 2014. European Physical Society.

[47] G. Papp, A. Stahl, M.Drevlak, T. Fulop, Ph. W. Lauber, and G. I. Pokol. *Towards self-consistent runaway electron modeling.* In 42nd EPS Conference on Plasma Physics, Lisbon, Portugal, ECA Vol. 39E, Mulhouse, France, 2015. European Physical Society.

[48] R. S. Granetz, B. Esposito, J. H. Kim, R. Koslowski, M. Lehnen, J. R. Martin-Solis, C. Paz-Soldan, T. Rhee, J. C. Wesley, L. Zeng, and ITPA MHD Group. *An ITPA joint experiment to study runaway electron generation and suppressiona).* Physics of Plasmas, 21(7):072506, 2014.

[49] C. Paz-Soldan, N. W. Eidietis, R. Granetz, E. M. Hollmann, R. A. Moyer, J. C. Wesley, J. Zhang, M. E. Austin, N. A. Crocker, A. Wingen, and Y. Zhu. *Growth and decay of runaway electrons above the critical electric field under quiescent conditions.* Physics of Plasmas, 21(2):022514, 2014.

[50] Z. Popovic, B. Esposito, J. R. Martin-Solis, W. Bin, L. Boncagni, D. Carnevale, M. Gospodarczyk, D. Marocco, G. Ramogida, and M. Riva. *Runaway Electron Dynamics and Critical Electric Field*

for Runaway Generation in the FTU Tokamak. In 42nd EPS Conference on Plasma Physics, Lisbon, Portugal, ECA Vol. 39E, Mulhouse, France, 2015. European Physical Society.

[51] L. Rodriguez-Rodrigo. *TJ-II:Paddle.* http://fusionwiki.ciemat.es/wiki/TJ-II:Paddle, April 2011. [cit. August 2017].

[52] B. Lloyd, G.L. Jackson, T.S. Taylor, E.A. Lazarus, T.C. Luce, and R. Prater. *Low voltage Ohmic and electron cyclotron heating assisted startup in DIII-D.* Nuclear Fusion, 31(11):2031, 1991.

[53] B. Coppi, G. Lampis, F. Pegoraro, L. Pieroni, and S. Segre. *Quasi-resistive regimes in magnetically confined plasmas.* Physics Letters A, 55(4):221 – 224, 1975.

[54] G. Fussmann, G. Becker, K. Behringer, K. Bernhardi, K. Buchl, D. Campbell, A. Eberhagen, W. Engelhardt, O. Gehre, J. Gernhardt, G. v. Gierke, E. Glock, G. Haas, M. Huang, F. Karger andM. Keilhacker, S. Kissel, 0. Kliiber, M. Kornherr, K. Lackner, G. Lisitano, G.G. Lister, H.M. Mayer, D. Meisel, E.R. Muller, H. Murmann, H. Niedermeyer, W. Poschenrieder, H. Rapp, H. Rohr, F. Schneider, G. Siller, P. Smeulders, F. Soldner, E. Speth, A. Stabler, K.H. Steuer, G. Venus, 0. Vollmer, F. Wagner, and Z. Yu. *Investigation of suprathermal discharges in the ASDEX tokamak.* In Proceedings of the 9th International Conference on Plasma Physics and Controlled Fusion, Baltimore, USA, pages 295–307, Vienna, Austria, 1983. International Atomic Energy Agency.

[55] G. Fussmann, D. Campbell, A. Eberhagen, W. Engelhardt, F. Karger, M. Keilhacker, O. Klüber, K. Lackner, S. Sesnic, F. Wagner, K. Behringer, O. Gehre, J. Gernhardt, E. Glock, G. Haas, M. Kornherr, G. Lisitano, H. M. Mayer, D. Meisel, R. Müller, H. Murmann, H. Niedermeyer, W. Poschenrieder, H. Rapp, N. Ruhs, F. Schneider, G. Siller, and K. H. Steuer. *Long-Pulse Suprathermal Discharges in the ASDEX Tokamak.* Phys. Rev. Lett., 47:1004–1007, Oct 1981.

[56] Z.Y. Chen, W.C. Kim, S.W. Yoon, A.C. England, K.D. Lee, J.W. Yoo, Y.K. Oh, J.G. Kwak, and M. Kwon. *Characteristic of slide away discharges in the KSTAR tokamak.* Physics Letters A, 376(47–48):3638 – 3640, 2012.

[57] Bao Nian Wan Zhong Yong Chen and Yue Jiang Shi. *Observation of the Trapping of Runaway Electrons into Local Magnetic Mirrors during Slide-away Discharges in the HT-7 Tokamak.* Journal of the Korean Physical Society, 59(2):271 – 274, 2011.

[58] G. Martin, M. Chatelier, and C. Doloc. *New insight into runaway electrons production and confinement.* In 22nd EPS Conference on

Plasma Physics, ECA Vol. 19C, Bournemouth, United Kingdom, 1995. Plasma Physics and Controlled Fusion 37, 11A.

[59] R. Yoshino, S. Tokuda, and Y. Kawano. *Generation and termination of runaway electrons at major disruptions in JT-60U.* Nuclear Fusion, 39(2):151, 1999.

[60] R.D. Gill, B. Alper, M. de Baar, T.C. Hender, M.F. Johnson, V. Riccardo, and contributors to the EFDA-JET Workprogramme. *Behaviour of disruption generated runaways in JET.* Nuclear Fusion, 42(8):1039, 2002.

[61] Z Y Chen, W C Kim, Y W Yu, A C England, J W Yoo, S H Hahn, S W Yoon, K D Lee, Y K Oh, J G Kwak, and M Kwon. *Study of runaway current generation following disruptions in KSTAR.* Plasma Physics and Controlled Fusion, 55(3):035007, 2013.

[62] T. Fulop, H. M. Smith, and G. Pokol. *Magnetic field threshold for runaway generation in tokamak disruptions.* Physics of Plasmas, 16(2):022502, 2009.

[63] E. M. Hollmann, M. E. Austin, J. A. Boedo, N. H. Brooks, N. Commaux, N. W. Eidietis, D. A. Humphreys, V. A. Izzo, A. N. James, T. C. Jernigan, A. Loarte, J. R. Martín-Solís, R. A. Moyer, J. M. Mu ooz Burgos, P.B. Parks, D.L. Rudakov, E. J. Strait, C. Tsui, M. A. Van Zeeland, J. C. Wesley, and J. H. Yu. *Control and dissipation of runaway electron beams created during rapid shutdown experiments in DIII-D.* Nuclear Fusion, 53(8):083004, 2013.

[64] F. Saint-Laurent, C. Reux, J. Bucalossi, A. Loarte, S. Bremond, C. Gil, and P. Moreau. *Control of Runaway Electron Beams on Tore Supra.* In 36th EPS Conference on Plasma Physics, ECA Vol. 33E, Sofia, Bulgaria, 2009. Plasma Physics and Controlled Fusion.

[65] G. Papp, G. Pautasso, J. Decker, M. Gobbin, P.J. McCarthy, P. Blanchard, D. Carnevale, D. Choi, S. Coda, B. Duval, R. Dux, B. Erdos, B. Esposito, O. Ficker, R. Fischer, C. Fuchs, C. Galperti, L. Giannone, A. Gude, B. Labit, K. Lackner, T. Lunt, L. Marelli, P. Martin, A. Mlynek, M. Maraschek, P. Marmillod, M. Nocente, Y. Peysson, P. Piovesan, V.V. Plyusnin, G.I. Pokol, P.Zs. Poloskei, S. Potzel, C. Reux, F. Saint-Laurent, O. Sauter, B. Sieglin, U. Sheikh, C. Sommariva, W. Suttrop, G. Tardini, D. Testa, W. Treutterer, M. Valisa, ASDEX Upgrade Team, TCV Team, and the EUROfusion MST1 Team. *Runaway electron generation and mitigation on the European medium sized tokamaks ASDEX Upgrade and TCV.* In 26th IAEA Fusion Energy Conference, number EX/9-4 in Kyoto (2016), Kyoto, Japan, 2016. [cit. August 2017].

[66] V.V. Plyusnin, C. Reux, V.G. Kiptily, A.E. Shevelev, J. Mlynar, M. Lehnen, P.C. de Vries, E.M. Khilkevitch, A. Huber, G. Sergienko, R.C. Pereira, D. Alves, B. Alper, U. Kruezi, S. Jachmich, A. Fernandes, M. Brix, V. Riccardo, L. Giacomelli, C. Sozzi, S. Gerasimov, A. Manzanares, E. de La Luna, A. Boboc, G. F. Matthews, and JET contributors. *Parameters of Runaway Electrons in JET.* In 25th IAEA Fusion Energy Conference, number EX/P5-23 in Saint Petersburg (2014), Saint Petersburg, Russia, 2014. pre-print EFDA-JET-CP(14)06/34 at http://www.euro-fusionscipub.org/jetarchive. [cit. August 2017].

[67] T. Fulop and S. Newton. *Alfvénic instabilities driven by runaways in fusion plasmas.* Physics of Plasmas, 21(8):080702, 2014.

[68] T. Fülöp and G. Papp. *Runaway Positrons in Fusion Plasmas.* Phys. Rev. Lett., 108(22):225003, May 2012.

[69] H P Zehrfeld, G Fussmann, and B J Green. *Electric field effects on relativistic charged particle motion in Tokamaks.* Plasma Physics, 23(5):473, 1981.

[70] R. Jaspers. *Relativistic runaway electrons in Tokamak Plasmas.* PhD thesis, Technische Universiteit van Eindhoven, Eindhoven, The Netherlands, 1995.

[71] J. R. Myra, Peter J. Catto, H. E. Mynick, and R. E. Duvall. *Quasilinear diffusion in stochastic magnetic fields: Reconciliation of driftorbit modification calculations.* Physics of Fluids B, 5(4):1160–1163, 1993.

[72] S. S. Abdullaev, K. H. Finken, and M. Forster. *New mechanism of runaway electron diffusion due to microturbulence in tokamaks.* Physics of Plasmas, 19(7), 2012.

[73] B. Kurzan, K. H. Steuer, and G. Fussmann. *Dynamics of Runaway Electrons in the Magnetic Field of a Tokamak.* Phys. Rev. Lett., 75:4626–4629, Dec 1995.

[74] J. R. Martin-Solis, R. Sanchez, and B. Esposito. *Effect of magnetic and electrostatic fluctuations on the runaway electron dynamics in tokamak plasmas.* Physics of Plasmas, 6(10):3925–3933, 1999.

[75] L. Laurent and J. M. Rax. *Stochastic Instability of Runaway Electrons in Tokamaks.* EPL (Europhysics Letters), 11(3):219, 1990.

[76] M. Lehnen, S. A. Bozhenkov, S. S. Abdullaev, and M. W. Jakubowski. *Suppression of Runaway Electrons by Resonant Magnetic Perturbations in TEXTOR Disruptions.* Phys. Rev. Lett., 100(25):255003, Jun 2008.

[77] T. Fulop, G. Pokol, P. Helander, and M. Lisak. *Destabilization of magnetosonic-whistler waves by a relativistic runaway beam.* Physics of Plasmas, 13(6):062506, 2006.

[78] V.V. Parail and O.P. Pogutse. *The kinetic theory of runaway electron beam instability in a tokamak.* Nuclear Fusion, 18(3):303, 1978.

[79] R.A. Moyer, C. Paz-Soldan, E.M. Hollmann, N.W. Eidietis, N. Commaux, R.S. Granetz, and P.B. Parks. *Impact of Core Modes, Islands, and Instabilities on Runaway Electron Confinement.* In 25th IAEA Fusion Energy Conferencein Saint Petersburg, Russia, number EX/P2-23 . Pre-print EFDA-JET-CP(14)06/34 at http://www.euro-fusionscipub.org/jetarchive (Only Abstract), 2014.

[80] J. D. Jackson. *Classical Electrodynamics.* John Wiley and Sons, 1999, ISBN: 978-0-471-30932-1.

[81] J. H. Yu, E. M. Hollmann, N. Commaux, N. W. Eidietis, D. A. Humphreys, A. N. James, T. C. Jernigan, and R. A. Moyer. *Visible imaging and spectroscopy of disruption runaway electrons in DIII-D.* Physics of Plasmas (1994-present), 20(4):042113, 2013.

[82] M. Bakhtiari, G. J. Kramer, and D. G. Whyte. *Momentum-space study of the effect of bremsstrahlung radiation on the energy of runaway electrons in tokamaks.* Physics of Plasmas, 12(10):102503, 2005.

[83] *Generating runaway electrons in JET to benefit ITER.* https://www.euro-fusion.org/2015/06/generating-runaway-electrons-in-jet-to-benefit-iter/, June 2015. [cit. August 2017].

[84] J.R. Martín-Solís, A. Loarte, E.M. Hollmann, B. Esposito, V. Riccardo, FTU, DIII-D Teams, and JET EFDA Contributors. *Intermachine comparison of the termination phase and energy conversion in tokamak disruptions with runaway current plateau formation and implications for ITER.* Nuclear Fusion, 54(8):083027, 2014.

[85] E. M. Hollmann, P. B. Aleynikov, T. Fülöp, D. A. Humphreys, V. A. Izzo, M. Lehnen, V. E. Lukash, G. Papp, G. Pautasso, F. Saint-Laurent, and J. A. Snipes. *Status of research toward the ITER disruption mitigation system.* Physics of Plasmas, 22(2):021802, 2015.

[86] M. Lehnen, S. S. Abdullaev, G. Arnoux, S. A. Bozhenkov, M. W. Jakubowski, R. Jaspers, V. V. Plyusnin, V. Riccardo, U. Samm, Jet Efda Contributors, and Textor Team. *Runaway generation during disruptions in JET and TEXTOR.* Journal of Nuclear Materials, 390:740–746, June 2009.

[87] C. Reux, V. Plyusnin, B. Alper, D. Alves, B. Bazylev, E. Belonohy, A. Boboc, S. Brezinsek, I. Coffey, J. Decker, P. Drewelow, S. Devaux, P.C. de Vries, A. Fil, S. Gerasimov, L. Giacomelli, S. Jachmich, E.M. Khilkevitch, V. Kiptily, R. Koslowski, U. Kruezi, M. Lehnen, I. Lupelli, P.J. Lomas, A. Manzanares, A. Martin De Aguilera, G.F. Matthews, J. Mlynář, E. Nardon, E. Nilsson, C. Perez von Thun, V. Riccardo, F. Saint-Laurent, A.E. Shevelev, G. Sips, C. Sozzi, and JET contributors. *Runaway electron beam generation and mitigation during disruptions at JET-ILW.* Nuclear Fusion, 55(9):093013, 2015.

[88] M. Lehnen, A. Alonso, G. Arnoux, N. Baumgarten, S.A. Bozhenkov, S. Brezinsek, M. Brix, T. Eich, S.N. Gerasimov, A. Huber, S. Jachmich, U. Kruezi, P.D. Morgan, V.V. Plyusnin, C. Reux, V. Riccardo, G. Sergienko, M.F. Stamp, and JET EFDA contributors. *Disruption mitigation by massive gas injection in JET.* Nuclear Fusion, 51(12):123010, 2011.

[89] F. Santini, E. Barbato, F. De Marco, S. Podda, and A. Tuccillo. *Anomalous Doppler Resonance of Relativistic Electrons with Lower Hybrid Waves Launched in the Frascati Tokamak.* Phys. Rev. Lett., 52:1300–1303, Apr 1984.

[90] J.R. Martin-Solis, B. Esposito, R. Sanchez, and G. Granucci. *Runaway electron behaviour during electron cyclotron resonance heating in the Frascati Tokamak Upgrade.* Nuclear Fusion, 44(9):974, 2004.

[91] M. Lehnen, K. Aleynikova, P.B. Aleynikov, D.J. Campbell, P. Drewelow, N.W. Eidietis, Yu. Gasparyan, R.S. Granetz, Y. Gribov, N. Hartmann, E.M. Hollmann, V.A. Izzo, S. Jachmich, S.-H. Kim, M. Kočan, H.R. Koslowski, D. Kovalenko, U. Kruezi, A. Loarte, S. Maruyama, G.F. Matthews, P.B. Parks, G. Pautasso, R.A. Pitts, C. Reux, V. Riccardo, R. Roccella, J.A. Snipes, A.J. Thornton, and P.C. de Vries. *Disruptions in ITER and strategies for their control and mitigation.* Journal of Nuclear Materials, 463:39 – 48, 2015. PLASMA-SURFACE INTERACTIONS 21, Proceedings of the 21st International Conference on Plasma-Surface Interactions in Controlled Fusion Devices Kanazawa, Japan May 26-30, 2014.

[92] L. Boncagni, D. Carnevale, C. Cianfarani, B. Esposito, G. Granucci, G. Maddaluno, D. Marocco, J.R. Martin-Solis, G. Pucella, C. Sozzi, G. Varano, V. Vitale, and L. Zaccarian. *A first approach to runaway electron control in FTU.* Fusion Engineering and Design, 88(6–8):1109 – 1112, 2013. Proceedings of the 27th Symposium On Fusion Technology (SOFT-27); Liège, Belgium, September 24-28, 2012.

[93] D. Carnevale, M. Gospodarczyk, B. Esposito, L. Boncagni, M. Sassano, S. Galeani, W. Bin, P. Buratti, G. Calabro, C. Cianfarani,

A. Gabrielli, G. Ferro, G. Granucci, D. Marocco, J.R. Martin-Solis, F. Martinelli, L. Panaccione, Z. Popovic, G. Pucella, G. Ramogida, M. Riva, O. Tudisco, and FTU team. *Control-oriented dynamical model of disruption generated RE beam.* In 42nd EPS Conference on Plasma Physics, Lisbon, Portugal, ECA Vol. 39E, Mulhouse, France, 2015. European Physical Society.

[94] R. D. Gill, B. Alper, A. W. Edwards, L. C. Ingesson, M. F. Johnson, and D. J. Ward. *Direct observations of runaway electrons during disruptions in the JET tokamak.* Nuclear Fusion, 40(2):163, 2000.

[95] D. Marocco, B. Esposito, M. Riva, F. Belli, S. Podda, and L. Panaccione. *First results on runaway electron studies using the FTU neutron camera.* Fusion Engineering and Design, 96–97:852 – 855, 2015. Proceedings of the 28th Symposium On Fusion Technology (SOFT-28).

[96] Yves Peysson and Frédéric Imbeaux. *Tomography of the fast electron bremsstrahlung emission during lower hybrid current drive on TORE SUPRA.* Review of Scientific Instruments, 70(10):3987–4007, 1999.

[97] J. Kamleitner, S. Gnesin, S. Coda, Ph. Marmillod, and J. Decker. *A new hard x-ray spectrometer for suprathermal electron studies in TCV.* In 39nd EPS Conference on Plasma Physics, Stockholm, Sweden, ECA Vol. 36F, Mulhouse, France, 2012. European Physical Society.

[98] A.E. Shevelev, E.M. Khilkevitch, V.G. Kiptily, I.N. Chugunov, D.B. Gin, D.N. Doinikov, V.O. Naidenov, A.E. Litvinov, I.A. Polunovskii, and JET-EFDA Contributors. *Reconstruction of distribution functions of fast ions and runaway electrons in fusion plasmas using gamma-ray spectrometry with applications to ITER.* Nuclear Fusion, 53(12):123004, 2013.

[99] S. S. Medley, S. D. Scott, A. L. Roquemore, and F. E. Cecil. *Performance of the fusion gamma diagnostic on TFTR.* Review of Scientific Instruments, 61(10):3226–3228, 1990.

[100] E.D. Fredrickson, M.G. Bell, G. Taylor, and S.S. Medley. *Control of disruption-generated runaway plasmas in TFTR.* Nuclear Fusion, 55(1):013006, 2015.

[101] B Esposito, L Bertalot, Yu.A Kaschuck, D.V Portnov, and J.R Martin-Solis. *A gamma-ray spectrometer system for fusion applications.* Nuclear Instruments and Methods in Physics Research Section A: Accelerators, Spectrometers, Detectors and Associated Equipment, 476(1–2):522 – 526, 2002. Int. Workshop on Neutron Field Spectrometry in Science, Technology and Radiation Protection.

[102] H. W. Piekaar and W. R. Rutgers. *Cyclotron Radiation From Thermal and Nonthermal Electrons in the Wega Stellarator.* Technical Report Rijnhuizen-80-128, FOM-INSTITUUT VOOR PLASMAFYSICA, 1980.

[103] R. W. Harvey, M. R. O'Brien, V. V. Rozhdestvensky, T. C. Luce, M. G. McCoy, and G. D. Kerbel. *Electron cyclotron emission from nonthermal tokamak plasmas.* Physics of Fluids B, 5(2):446–456, 1993.

[104] K.H. Finken, J.G. Watkins, D. Rusbüldt, W.J. Corbett, K.H. Dippel, D.M. Goebel, and R.A. Moyer. *Observation of infrared synchrotron radiation from tokamak runaway electrons in TEXTOR.* Nuclear Fusion, 30(5):859, 1990.

[105] R. Jaspers, N. J. Lopes Cardozo, A. J. H. Donné, H. L. M. Widdershoven, and K. H. Finken. *A synchrotron radiation diagnostic to observe relativistic runaway electrons in a tokamak plasma.* Review of Scientific Instruments, 72(1):466–470, 2001.

[106] L. Pieroni and S. E. Segre. *Observation of Non-Maxwellian Electron Distribution Functions in the Alcator Device by Means of Thomson Scattering and Their Interpretation.* Phys. Rev. Lett., 34:928–930, Apr 1975.

[107] John Sheffield, Dustin Froula, Siegfried H. Glenzer, and Jr Neville C. Luhmann. *Plasma Scattering of Electromagnetic Radiation.* Elsevier, Amsterdam, The Netherlands, 2011, ISBN: 978-0-12-374877-5.

[108] M. J. Sadowski, L. Jakubowski, and A. Szydlowski. *Adaptation of selected diagnostic techniques to magnetic confinement fusion experiments.* Czechoslovak Journal of Physics, 54(3):C74–C81, 2004.

[109] L. Jakubowski, M.J. Sadowski, J. Stanislawski, K. Malinowski, J. Zebrowski, M. Jakubowski, V. Weinzettl, J. Stockel, M. Vacha, and M. Peterka. *Application of Cherenkov Detectors for Fast Electron Measurements in CASTOR-Tokamak.* In 34th EPS Conference on Plasma Physics, Warsaw, Poland, ECA Vol. 31F, Mulhouse, France, 2007. European Physical Society.

[110] V. V. Plyusnin, L. Jakubowski, J. Zebrowski, H. Fernandes, C. Silva, K. Malinowski, P. Duarte, M. Rabinski, and M. J. Sadowski. *Use of Cherenkov-type detectors for measurements of runaway electrons in the ISTTOK tokamak.* Review of Scientific Instruments, 79(10):10F505, 2008.

[111] L. Jakubowski, M. J. Sadowski, J. Zebrowski, M. Rabinski, K. Malinowski, R. Mirowski, Ph. Lotte, J. Gunn, J-Y. Pascal, G. Colledani,

V. Basiuk, M. Goniche, and M. Lipa. *Cherenkov-type diamond detectors for measurements of fast electrons in the TORE-SUPRA tokamak.* Review of Scientific Instruments, 81(1):013504, 2010.

[112] L. Jakubowski, V. V. Plyusnin, M. J. Sadowski, J. Zebrowski, K. Malinowski, M. Rabinski, H. Fernandes, C. Silva, P. Duarte, and M. Jakubowski. *Estimation of ISTTOK runaway-electrons energies by means of a Cherenkov-type probe with modified AlN radiators.* Nukleonika, 57(2):171–175, 2012.

[113] J.A. Romero, J.-M. Moret, S. Coda, F. Felici, and I. Garrido. *Development and validation of a tokamak skin effect transformer model.* Nuclear Fusion, 52(2):023019, 2012.

[114] V. D. Shafranov. *Equilibrium of a toroidal pinch in a magnetic field.* Soviet Atomic Energy, 13(6):1149–1158, 1962.

[115] K. Wongrach, K. H. Finken, S. S. Abdullaev, O. Willi, L. Zeng, and Y. Xu. *Structure of the runaway electron loss during induced disruptions in TEXTOR.* Physics of Plasmas, 22(10):102508, 2015.

[116] Jr. Stanley Humphries. *Principles of Charged Particle Acceleration.* John Wiley and Sons, New York, USA, 1999, ISBN: 0-471-87878-2.

[117] R. Pánek, J. Adámek, M. Aftanas, P. Bílková, P. Böhm, P. Cahyna, J. Cavalier, R. Dejarnac, M. Dimitrova, O. Grover, P. Háček, J. Havlíček, A. Havránek, J. Horáček, M. Hron, M. Imríšek, F. Janky, M. Komm, K. Kovařík, J. Krbec, L. Kripner, T. Markovič, K. Mitošinková, J. Mlynář, D. Naydenkova, M. Peterka, J. Seidl, , J. Stöckel, E. Štefániková, M. Tomeš, J. Urban, P. Vondráček, M. Varavin, J. Varju, V. Weinzettl, J. Zajac, and the COMPASS Team. *Status of the COMPASS tokamak and characterization of the first H-mode.* Plasma Physics and Controlled Fusion, 58(1):014015, 2016.

[118] J. Mlynar, O. Ficker, M. Vlainic, V. Weinzettl, M. Imrisek, R. Paprok, M. Rabinski, M. Jakubowski, and the COMPASS Team. *Effects of Plasma Control on Runaway Electrons in COMPASS Tokamak.* In In 42nd EPS Conference on Plasma Physics in Lisbon, Portugal, number P4.102 in ECA Vol. 39E, Mulhouse, France, 2015. European Physical Society.

[119] J. Havlíček and O. Hronová. *Magnetic Diagnostics of COMPASS Tokamak: http://www.ipp.cas.cz/Tokamak/euratom/index.php/en/compass-diagnostics/magnetic-diagnostics*, July 2010. [cit. August 2017].

[120] C. Gormezano, A.C.C. Sips, T.C. Luce, S. Ide, A. Becoulet, X. Litaudon, A. Isayama, J. Hobirk, M.R. Wade, T. Oikawa,

R. Prater, A. Zvonkov, B. Lloyd, T. Suzuki, E. Barbato, P. Bonoli, C.K. Phillips, V. Vdovin, E. Joffrin, T. Casper, J. Ferron, D. Mazon, D. Moreau, R. Bundy, C. Kessel, A. Fukuyama, N. Hayashi, F. Imbeaux, M. Murakami, A.R. Polevoi, and H.E. St John. *Chapter 6: Steady state operation.* Nuclear Fusion, 47(6):S285, 2007.

[121] H J Hartfuss, T Geist, and M Hirsch. *Heterodyne methods in millimetre wave plasma diagnostics with applications to ECE, interferometry and reflectometry.* Plasma Physics and Controlled Fusion, 39(11):1693, 1997.

[122] G. P. Ermak, A. V. Varavin, A. S. Vasilev, M. Stumbra, A. S. Fateev, F. Zacek, J. Zajac, N. Varavin, and V. Shevchenko. *Two-wavelength millimeter wave "unambiguous" heterodyne interferometer.* In Physics and Engineering of Microwaves, Millimeter and Submillimeter Waves (MSMW), 2013 International Kharkov Symposium on, pages 529–531, June 2013.

[123] V. Weinzettl, D.I. Naydenkova, D. Sestak, J. Vlcek, J. Mlynar, R. Melich, D. Jares, J. Malot, D. Sarychev, and V. Igochine. *Design of multi-range tomographic system for transport studies in tokamak plasmas.* Nuclear Instruments and Methods in Physics Research Section A: Accelerators, Spectrometers, Detectors and Associated Equipment, 623(2):806 – 808, 2010. 1st International Conference on Frontiers in Diagnostics Technologies.

[124] Petra Bilkova, Milan Aftanas, Petr Bohm, Vladimir Weinzettl, David Sestak, Radek Melich, Jan Stockel, Rory Scannell, and Mike Walsh. *Design of new Thomson scattering diagnostic system on COMPASS tokamak.* Nuclear Instruments and Methods in Physics Research Section A: Accelerators, Spectrometers, Detectors and Associated Equipment, 623(2):656 – 659, 2010. 1rs International Conference on Frontiers in Diagnostics Technologies.

[125] R Paprok, M Vlainic (presenting), J Mlynar, V Weinzettl, M Varavin, J Varju, O Ficker, M Imrisek, , and the COMPASS Team. *CsI(Tl) Semiconductor Detectors for Hard X-Ray Diagnostics at COMPASS Tokamak.* In Proceedings of 1st EPS Conference on Plasma Diagnostics, Frascati, Italy, 2015.

[126] X. Llopart, R. Ballabriga, M. Campbell, L. Tlustos, and W. Wong. *Timepix, a 65k programmable pixel readout chip for arrival time, energy and/or photon counting measurements.* VCI 2007 Proceedings of the 11th International Vienna Conference on Instrumentation. Nuclear Instruments and Methods in Physics Research Section A: Accelerators, Spectrometers, Detectors and Associated Equipment, 581(1–2):485 – 494, 2007.

[127] J. Horacek, P. Vondracek, R. Panek, R. Dejarnac, M. Komm, R.A. Pitts, M. Kocan, R.J. Goldston, P.C. Stangeby, E. Gauthier, P. Hacek, J. Havlicek, M. Hron, M. Imrisek, F. Janky, and J. Seidl. *Narrow heat flux channels in the COMPASS limiter scrape-off layer.* Journal of Nuclear Materials, 463:385 – 388, 2015. PLASMA-SURFACE INTERACTIONS Proceedings of the 21st International Conference on Plasma-Surface Interactions in Controlled Fusion Devices Kanazawa, Japan May 26-30, 2014.

[128] Milos Vlainic, Jan Mlynar, Ondrej Ficker, Jakub Urban, Josef Havlicek, Vladimir Weinzettl, Martin Imrisek, Radomir Panek, Jean-Marie Noterdaeme, and the COMPASS Team. *Influence of Runaway Electrons on Discharge Start-Up in COMPASS.* In Controbuted Papers & Abstracts of Invited Lecturers, Topical Invited Lecturers, Progress Reports and Workshop Lecturers, number P4.1. Serbian Academy of Science and Arts, University of Belgrade, 2016.

[129] Ondrej Ficker. *Generation, losses and detection of RE in tokamaks.* diploma thesis, Faculty of Nuclear Sciences and Physical Engineering, 2015. http://physics.fjfi.cvut.cz/publications/FTTF/DP_Ondrej_Ficker.pdf, [cit. August 2017].

[130] O. Ficker, J. Mlynar, M. Vlainic, E. Macusova, P. Vondracek, V. Weinzettl, J. Urban, J. Cerovsky, J. Cavalier, J. Havlicek, R. Paprok, A. Havranek, M. Hron, R. Panek, J. Decker, Y. Peysson, and the COMPASS team. *Long slide-away discharges in the COMPASS tokamak.* In 58th Annual Meeting of the APS Division of Plasma Physics, San Jose (CA), USA, volume 61(18):GP10.00101.

[131] I T Chapman. *Controlling sawtooth oscillations in tokamak plasmas.* Plasma Physics and Controlled Fusion, 53(1):013001, 2011.

[132] O. Ficker, J. Mlynar, M. Vlainic, J. Cerovsky, J. Urban, P. Vondracek, V. Weinzettl, E. Macusova, J. Decker, M. Gospodarczyk, P. Martin, E. Nardon, G. Papp, V.V. Plyusnin, C. Reux, F. Saint-Laurent, C. Sommariva, J. Cavalier, J. Havlicek, A. Havranek, O. Hronova, M. Imrisek, T. Markovic, J. Varju, R. Paprok, R. Panek, M. Hron, and The COMPASS Team. *Losses of runaway electrons in MHD-active plasmas of the COMPASS tokamak.* Nuclear Fusion, 57(7):076002, 2017.

[133] O. Ficker, J. Mlynar, M. Vlainic, J. Havlicek, M. Imrisek, O. Hronova, V. Weinzettl, R. Paprok, and T. Markovic. *Runaway electron losses induced by various MHD events in the COMPASS tokamak.* In Poster at the 5th FuseNet PhD Event in Prague, Czech Republic, 2015.

[134] T. Markovic, J. Seidl, A. Melnikov, P. Haccek, J. Havlicek, A. Havranek, M. Hron, O. Hronova, M. Imrisek, F. Janky, K. Kovarik, O. Mikulín, R. Panek, R. Paprok, J. Pipek, P. Vondracek, and V. Weinzettl. *Alfvén-wave character oscillations in tokamak COMPASS plasma.* In In 42nd EPS Conference on Plasma Physics in Lisbon, Portugal, number P4.104 in ECA Vol. 39E, Mulhouse, France, 2015. European Physical Society.

[135] P. Cahyna, R. Pánek, V. Fuchs, L. Krlín, M. Bécoulet, G. Huysmans, and E. Nardon. *The optimization of resonant magnetic perturbation spectra for the COMPASS tokamak.* Nuclear Fusion, 49(5):055024, May 2009.

[136] Milos Vlainic, J. Mlynar, J. Cavalier, V. Weinzettl, R. Paprok, M. Imrisek, O. Ficker, M. Varavin, P. Vondracek, and J.-M. Noterdaeme. *Post-disruptive runaway electron beams in the COMPASS tokamak.* Journal of Plasma Physics, 81(05):475810506, October 2015.

[137] V.V. Plyusnin, C. Reux, V.G. Kiptily, P. Lomas, V. Riccardo, G. Pautasso, J. Decker, G. Papp, J. Mlynar, S. Jachmich, A.E. Shevelev, E. Khilkevitch, S. Coda, B. Alper, Y. Martin, V. Weinzettl, R. Dux, C. Fuchs, B. Duval, M. Brix, M. Maraschek, W. Treutterer, L. Giannone, G. Tardini, U. Kruezi, A. Mlynek, A. Fernandes, S. Gerasimov, P. Martin, A. Boboc, K. Lackner, P. J. McCarthy, O. Ficker, M. Imrisek, R. Paprok, J. Havlicek, S. Potzel, M. Nocente, L. Giacomelli, M. Vlainic, A. Kallenbach, COMPASS team, TCV team, ASDEX Upgrade team, EUROFusion MST1 Team, , and JET contributors. *Comparison of Runaway Electron Generation Parameters in Small, Medium-sized and Large Tokamaks - A Survey of Experiments in COMPASS, TCV, ASDEX-Upgrade and JET.* Nuclear Fusion, 2017. Status: Submitted for Revision.

[138] S. S. Abdullaev, K. H. Finken, K. Wongrach, M. Tokar, H. R. Koslowski, O. Willi, and L. Zeng. *Mechanisms of plasma disruption and runaway electron losses in the TEXTOR tokamak.* 81(5):475810501, October 2015.

[139] I. M. Pankratov. *Analysis of the synchrotron radiation spectra of runaway electrons.* Plasma Physics Reports, 25:145–148, February 1999.

[140] Internal communication with V. Weinzettl and D. Naydenkova, IPP Prague.

[141] M. Aftanas, P. Bohm, P. Bilkova, V. Weinzettl, J. Zajac, F. Zacek, J. Stockel, M. Hron, R. Panek, R. Scannell, and M. J. Walsh.

High-resolution Thomson scattering system on the COMPASS tokamak: Evaluation of plasma parameters and error analysisa). Review of Scientific Instruments, 83(10), 2012.

[142] Takaaki Fujita, Yasutaka Fuke, Zensho Yoshida, Nobuyuki Inoue, Takeo Tanihara, Ken ichi Mori, Masayuki Fukao, Yukihiro Tomita, and Akihiro Mohri. *High-Current Runaway Electron Beam in a Tokamak Plasma.* Journal of the Physical Society of Japan, 60(4):1237–1246, 1991.

[143] J. Havlicek. *Study of Equilibrium Magnetic Configuration in Tokamak Type Devices.* PhD thesis, Charles University in Prague, Prague, Czech Republic, 2015.

[144] J. A. Romero, S. Coda, F. Felici, J. M. Moret, J. Paley, G. Sevillano, I. Garrido, and H. B. Le. *Sliding mode control of a tokamak transformer.* In 2012 IEEE 51st IEEE Conference on Decision and Control (CDC), pages 386–393, Dec 2012.

[145] J.A. Romero and JET-EFDA Contributors. *Plasma internal inductance dynamics in a tokamak.* Nuclear Fusion, 50(11):115002, 2010.

[146] M. Vlainić, J. Mlynář, V. Weinzettl, R. Papřok, M. Imrísek, O. Ficker, P. Vondráček, and J. Havlíček. *First Dedicated Observations of Runaway Electrons in COMPASS Tokamak.* Nukleonika, 60(2):249–255, 2015.

[147] Z. Yoshida. *Numerical analysis of runaway tokamak equilibrium.* Nuclear Fusion, 30(2):317, 1990.

[148] V.S. Mukhovatov and V.D. Shafranov. *Plasma equilibrium in a Tokamak.* Nuclear Fusion, 11(6):605, 1971.

[149] Alfred Mondelli and Edward Ott. *Straight and toroidal plasma equilibria with an intense relativistic electron current component.* Physics of Fluids, 17(5):1017–1025, 1974.

[150] Leslie Colin Woods. *Theory of Tokamak Transport.* John Wiley and Sons, Weinheim, Germany, 2006, ISBN: 3-527-40625-5.

[151] J Decker, E Hirvijoki, O Embreus, Y Peysson, A Stahl, I Pusztai, and T Fülöp. *Numerical characterization of bump formation in the runaway electron tail.* Plasma Physics and Controlled Fusion, 58(2):025016, 2016.

[152] M. Vlainic, P. Vondracek, J. Mlynar, V. Weinzettl, O. Ficker, M. Varavin, R. Paprok, M. Imrisek, J. Havlicek, R. Panek, J.-M. Noterdaeme, and the COMPASS Team. *Synchrotron Radiation from Runaway Electrons in COMPASS Tokamak.* In In 42nd EPS Conference

on Plasma Physics in Lisbon, Portugal, number P4.108 in ECA Vol. 39E, Mulhouse, France, 2015. European Physical Society.

[153] Julian Schwinger. *On the Classical Radiation of Accelerated Electrons.* Phys. Rev., 75:1912–1925, Jun 1949.

[154] B.A. Trubnikov and U.S. Atomic Energy Commission. *Magnetic Emission of High Temperature Plasma.* AEC-tr. United States Atomic Energy Commission, Technical Information Service, 1960.

[155] G. Bekefi. *Radiation processes in plasmas.* Wiley series in plasma physics. Wiley, 1966, ISBN: 978-0471063506.

[156] L.D. Landau and Lifshitz E.M. *The Classical Theory of Fields.* Textbook Publishers, 2003, ISBN: 978-0758164865.

[157] E. Hirvijoki, I. Pusztai, J. Decker, O. Embréus, A. Stahl, and T. Fülöp. *Radiation reaction induced non-monotonic features in runaway electron distributions.* 81(5):475810502, 10 2015.

[158] I. M. Pankratov. *Analysis of the synchrotron radiation emitted by runaway electrons.* Plasma Physics Reports, 22(6):535–538, 1996.

[159] R. J. Zhou, I. M. Pankratov, L. Q. Hu, M. Xu, and J. H. Yang. *Synchrotron radiation spectra and synchrotron radiation spot shape of runaway electrons in Experimental Advanced Superconducting Tokamak.* Physics of Plasmas, 21(6):063302, 2014.

[160] S. S. Abdullaev, K. H. Finken, K. Wongrach, M. Tokar, H. R. Koslowski, O. Willi, and L. Zeng. *Mechanism of runaway electron beam formation during plasma disruptions in tokamaks.* Physics of Plasmas, 22(4):040704, 2015.

[161] C. Reux, V. Plyusnin, B. Alper, D. Alves, B. Bazylev, E. Belonohy, S. Brezinsek, J. Decker, S. Devaux, P. de Vries, A. Fil, S. Gerasimov, I. Lupelli, S. Jachmich, E.M. Khilkevitch, V. Kiptily, R. Koslowski, U. Kruezi, M. Lehnen, A. Manzanares, J. Mlynář, E. Nardon, E. Nilsson, V. Riccardo, F. Saint-Laurent, A.E. Shevelev, and C. Sozzi. *Runaway beam studies during disruptions at JET-ILW.* Journal of Nuclear Materials, 463:143 – 149, 2015.

[162] I. Entrop, N. J. Lopes Cardozo, R. Jaspers, and K. H. Finken. *Scale Size of Magnetic Turbulence in Tokamaks Probed with 30-MeV Electrons.* Phys. Rev. Lett., 84:3606–3609, Apr 2000.

[163] S. S. Abdullaev, K. H. Finken, T. Kudyakov, and M. Lehnen. *Asymptotical Theory of Runaway Electron Diffusion Due to Magnetic Turbulence in Tokamak Plasmas.* Contributions to Plasma Physics, 50(10):929–941, 2010.

[164] L. Zeng, H. R. Koslowski, Y. Liang, A. Lvovskiy, M. Lehnen, D. Nicolai, J. Pearson, M. Rack, H. Jaegers, K. H. Finken, K. Wongrach, Y. Xu, and the TEXTOR team. *Experimental Observation of a Magnetic-Turbulence Threshold for Runaway-Electron Generation in the TEXTOR Tokamak.* Phys. Rev. Lett., 110:235003, Jun 2013.

[165] K. Wongrach, K.H. Finken, S.S. Abdullaev, R. Koslowski, O. Willi, L. Zeng, and the TEXTOR Team. *Measurement of synchrotron radiation from runaway electrons during the TEXTOR tokamak disruptions.* Nuclear Fusion, 54(4):043011, 2014.

[166] Pavel Aleynikov. *Mitigation of runaway electrons in ITER*, June 2014. Presentation at Runaway Electron Meeting Workshop in Gothenburg, Sweden.

[167] Kosuke Kato. PhD thesis, Massachusetts Institute of Technology, Cambridge (MA), USA, 1986.

[168] Kenro Miyamoto. *Controlled Fusion and Plasma Physics.* Taylor Francis, Milton Park, UK, 2006, ISBN: 978-1584887096.

[169] C.M. Celata and D.A. Boyd. *Cyclotron radiation as a diagnostic tool for tokamak plasmas.* Nuclear Fusion, 17(4):735, 1977.

[170] Eric Hollmann. *Measurements of RE f(E) evolution following MGI into RE plateau*, June 2014. Presentation at Runaway Electron Meeting Workshop in Gothenburg, Sweden.

[171] A.C.A.P. Van Lammeren, C.J. Barth, Q.C. van Est, and F.C. Schuller. *Non-Maxwellian electron velocity distributions observed with Thomson scattering in the TORTUR tokamak.* Nuclear Fusion, 32(4):655, 1992.

[172] John Sheffield. *Plasma Scattering of Electromagnetic Radiation.* Academic Press, New York, USA, 1975. ISBN: 978-1483220222.

[173] Tohru Matoba, Tokiyoshi Itagaki, Toshihiko Yamauchi, and Akimasa Funahashi. *Analytical Approximations in the Theory of Relativistic Thomson Scattering for High Temperature Fusion Plasma.* Japanese Journal of Applied Physics, 18(6):1127, 1979.

[174] O. Naito, H. Yoshida, and T. Matoba. *Analytic formula for fully relativistic Thomson scattering spectrum.* Physics of Fluids B: Plasma Physics (1989-1993), 5(11):4256–4258, 1993.

[175] J. P. Palastro, J. S. Ross, B. Pollock, L. Divol, D. H. Froula, and S. H. Glenzer. *Fully relativistic form factor for Thomson scattering.* Phys. Rev. E, 81:036411, Mar 2010.

[176] Robert D. Guenther. *Modern Optics*, chapter Chapter 2: Electromagnetic Theory, pages 25–36. John Wiley & Sons, New York, USA, 1990. ISBN: 978-0471605386.

[177] John David Jackson. *Classical Electrodynamics*, chapter Chapter 14: Radiation by Moving Charges, pages 661–708. John Wiley & Sons, New York, USA, 1999. ISBN: 978-0471309321.

[178] Ian H. Hutchinson. *Principles of Plasma Diagnostics*, chapter 7 Scattering of Electromagnetic Radiation, pages 273–321. Cambridge University Press, New York, USA, 2002. ISBN: 978-0521675741.

[179] Glenn F. Knoll. *Radiation Detection and Measurements*. John Wiley and Sons, 2000, ISBN: 978-0471073383.

[180] Hastings Smith Jr. Doug Reilly, Norbert Ensslin and Sarah Kreiner. *Passive Nondestructive Assay of Nuclear Materials*, chapter 13 Neutron Detectors by T. W. Crane and M. P. Baker, pages 379–405. US Nuclear Regulatory Commission, Los Alamos, USA, 1991, ISBN: 978-0160327247.

[181] J. Dankowski, F. Janky, A. Kurowski, J. Stockel, and D. Twarog. *Preliminary measurements of neutrons from the D-D reaction in the COMPASS tokamak*. AIP Conference Proceedings, 1612(1):109–112, 2014.

List of Publications and Presentations

Publications:

M. Vlainic, J. Mlynar, J. Cavalier, V. Weinzettl, R. Paprok, M. Imrisek, O. Ficker, M. Varavin, P. Vondracek, J.-M. Noterdaeme and the COMPASS Team
Post-disruptive runaway electron beam in COMPASS Tokamak
J. Plasma Phys. (2015), Vol. 81(475810506)
doi:10.1017/S0022377815000914

M. Vlainic, J. Mlynar, V. Weinzettl, R. Paprok, M. Imrisek, O. Ficker, P. Vondracek, J. Havlicek
First dedicated observations of runaway electrons in the COMPASS tokamak
NUKLEONIKA (2015), Vol. 60(2), p. 249-255
doi:10.1515/nuka-2015-0052

E. Nilsson, J. Decker, Y. Peysson, R.S. Granetz, F. Saint-Laurent and M. Vlainic
Kinetic modelling of runaway electron avalanches in tokamak plasmas
Plasma Phys. Control. Fusion (2015), Vol. 57(095006)
doi:10.1088/0741-3335/57/9/095006

O. Ficker, J. Mlynar, M. Vlainic, J. Cerovsky, J. Urban, P. Vondracek, V. Weinzettl, E. Macusova, J. Decker, M. Gospodarczyk, P. Martin, E. Nardon, G. Papp, V.V. Plyusnin, C. Reux, F. Saint-Laurent, C. Sommariva, J. Cavalier, J. Havlicek, A. Havranek, O. Hronova, M. Imrisek, T. Markovic, J. Varju, R. Paprok, R. Panek, M. Hron, and The COMPASS Team
Losses of runaway electrons in MHD-active plasmas of the COMPASS tokamak
Nuclear Fusion (2017), Vol. 57(7), p. 076002
doi:10.1088/1741-4326/aa6aba

V.V. Plyusnin, C. Reux, V.G. Kiptily, P. Lomas, V. Riccardo, G. Pautasso, J. Decker, G. Papp, J. Mlynar, S. Jachmich, A.E. Shevelev, E. Khilkevitch, S. Coda, B. Alper, Y. Martin, V. Weinzettl, R. Dux, C. Fuchs, B. Duval, M. Brix, M. Maraschek, W. Treutterer, L. Giannone, G. Tardini, U. Kruezi, A. Mlynek, A. Fernandes, S. Gerasimov, P. Martin, A. Boboc, K. Lackner, P. J. McCarthy, O. Ficker, M. Imrisek, R. Paprok, J. Havlicek, S. Potzel, M. Nocente, L. Giacomelli, M. Vlainic, A. Kallenbach, COMPASS team, TCV team, ASDEX Upgrade team, EUROFusion MST1 Team, and JET contributors.
Comparison of runaway electron generation parameters in small, medium-sized and large tokamaks - a survey of experiments in COMPASS, TCV, ASDEX-Upgrade and JET
Nuclear Fusion - Status: Submitted for Revision

Oral Presentations...

...as Speaker:

13th Kudowa Summer School "Towards fusion energy", *Detection of runaway electrons in tokamaks*, June 2014, Kudowa (Poland)

COMPASS Programmatic Conference and IBA meeting, *Study of runaways on COMPASS*, September 2014, Prague (Czech Republic)

3rd Runaway Electron Meeting Workshop, *Infrared radiation from RE in COMPASS tokamak*, June 2015, Pertuis (France)

...as Contributor:

2nd Runaway Electron Meeting Workshop, *Some preliminary results from the first re campaign on COMPASS*, June 2014, Gothenburg (Sweden)

EUROfusion Management visit to COMPASS, *Runaway electron studies at COMPASS under the MST2-9 project*, March 2015, Prague (Czech Republic)

3rd Runaway Electron Meeting Workshop, *Recent experimental results from the RE studies at COMPASS tokamak*, June 2015, Pertuis (France)

COMPASS Programmatic Conference and IBA meeting, *Recent experimental results from the RE studies at COMPASS tokamak*, September 2015, Prague (Czech Republic)

MST1 Task Force Meeting, *Runaway electron studies at COMPASS*, February 2016, Gothenburg (Sweden)

4th Runaway Electron Meeting Workshop, *Status of Runaway Electron Experiments in Prague*, June 2016, Pertuis (France)

COMPASS Programmatic Conference and IBA meeting, *Mitigation of runaways, validation of runaway generation models*, September 2016, Prague (Czech Republic)

5th Runaway Electron Meeting Workshop, *Post-disruptive RE beams in COMPASS and related diagnostics*, June 2017, Prague (Czech Republic)

5th Runaway Electron Meeting Workshop, *Runaway electron studies during the flattop phase in COMPASS*, June 2017, Prague (Czech Republic)

Poster Presentations...

...as Presenter:

4th FuseNet PhD Event, *Preliminary results of data analyses for the first dedicated runaway electron discharges in COMPASS tokamak*, November 2014, Lisbon (Portugal)

1st EPS Conference on Plasma Diagnostics, *CsI(Tl) semiconductor detectors for hard X-ray diagnostics at COMPASS tokamak*, April 2015, Frascati (Italy)

42nd EPS Conference on Plasma Physics, *Synchrotron Radiation from Runaway Electrons in COMPASS Tokamak*, June 2015, Lisbon (Portugal) Europhysics Conference Abstracts 39E, P4.108

5th FuseNet PhD Event, *Potential of ECE diagnostics for runaway electrons studies*, November 2015, Prague (Czech Republic)

...as Contributor:

42nd EPS Conference on Plasma Physics, *Effects of Plasma Control on Runaway Electrons in COMPASS Tokamak*, June 2015, Lisbon (Portugal) Europhysics Conference Abstracts 39E, P4.102

5th FuseNet PhD Event, *Runaway electron losses induced by various MHD events in the COMPASS tokamak*, November 2015, Prague (Czech Republic)

26th IAEA Fusion Energy Conference, *Losses of runaway electrons in MHD-active plasmas of the COMPASS tokamak*, October 2016, Kyoto (Japan)

26$^{\text{th}}$ IAEA Fusion Energy Conference, *Comparison of runaway electron generation parameters in small, medium-sized and large tokamaks - a survey of experiments in COMPASS, TCV, ASDEX-Upgrade and JET*, October 2016, Kyoto (Japan)

58$^{\text{th}}$ Annual Meeting of the APS Division of Plasma Physics, *Long slide-away discharges in the COMPASS tokamak*, November 2016, San Jose-CA (USA)

Acknowledgments

As I am not man of too many written words (even though length of this Thesis would not confirm that), I will try to keep this part as short as possible.

Firstly and most importantly I would like to thank my supervisor docent Jan Mlynář who has guided me all the time and giving me support even when I was doubting myself. Secondly, I am enormously thankful to my very best colleagues and good friends Ondřej Ficker and Jordan Cavalier with whom I learned a lot and who helped me when ever they could. Next, I would like to thank the whole COMPASS tokamak community for its openness and friendliness. I only wish them to keep their unique atmosphere and team chemistry. I do also appreciate a lot the communication with Adam Stahl, who helped me a lot on running SYRUP and NORSE. Furthermore, I would like to thank my promotor Prof. Jean-Marie Noterdaeme for his support and academic advising. The support role of Prof. Igor Jex and Prof. Geert Verdoolaege is also acknowledged. Of course, nothing of this would be possible without the understanding and support of my family and close friends - therefore I want them to know how I appreciate it a lot.

Regarding the institutions I would like to mention: (1) Erasmum Mundus Joint Doctoral Collage in Fusion Science and Engineering (often abbreviated as "Fusion-DC") that provided me the necessary infrastructure for the studies; (2) IPP Prague whose infrastructure I used for my research, especially in the frame of the project MSMT LM2011021 that supported COMPASS operation; (3) Ghent University and Czech Technical University who accepted me as a student and managed my Cotutelle in a timely manner; and (4) EUROfusion who granted the WP14-MST2-9 project to the COMPASS tokamak. Regarding the latter, I am obliged to write that the views and opinions expressed in this work do not necessarily reflect those of the European Commission.